12-18-2018

Temperature Transient Analysis for Reservoir Characterization

Yilin Mao
Louisiana State University and Agricultural and Mechanical College

TEMPERATURE TRANSIENT ANALYSIS FOR RESERVOIR CHARACTERIZATION

A Dissertation

Submitted to the Graduate Faculty of the
Louisiana State University and
Agricultural and Mechanical College
in partial fulfillment of the
requirements for the degree of
Doctor of Philosophy

in

The Craft and Hawkins Department of Petroleum Engineering

by
Yilin Mao
B.S., Fudan University, 2008
M.S., Missouri University of Science and Technology, 2014
May 2019

Acknowledgments

Time flies and flies faster as a doctorate candidate facing challenges, discoveries, and struggles every day. It is hard to imagine my life would be without all the helpers around me.

Among them, I want to firstly thank my supervisor, Dr. Mehdi Zeidouni, whose maddening attention to deep-thinking drove me to finally learn to avoid superficial. Your selfless time and effort were sometimes all that kept me going. Many thanks to Professor Zeidouni, I am very fortunate and honored to be your first Ph.D. student.

I would also like to express my gratitude to my committee members, Dr. Kunlun Ding, Dr. Richard Hughes, Dr. Karsten Thompson, and Dr. Frank Tsai, for your effort and time on improving my research and dissertation. Furthermore, my thanks are sent to my wonderful colleagues, Oscar Molina, Mojtaba Mosaheb, Kewei Shi, Nam Tran, Refaat Galal, for all the late nights we spent and the lights we shared. More recently, I want to thank Caroline Godefroy and Dr. Michel Gysen in Interpretive Software Products. You trained and linked my research to the very need of the industry. I am also thankful to the Craft and Hawkins Department of Petroleum Engineering for providing the funding and software (CMG, KAPPA, IHS, COMSOL) for my research.

Last but definitely not the least, the special thanks go to my family. I am in-debted to my parents, Dan Zhu and Dr. Zhiqiang Mao, for raising me from a boy to a man, and for trusting my academic potential when I almost gave it up on myself. This journey would not have been possible without your determined effort to drag me from middle of the desert. My wife, Shui Yu, never bothered me while working and took care of almost everything in our house. It is entirely possible that I would have eaten fast food through my Ph.D. had you not been willing to feed me every day, that I would have been miserable had you not been there to cheer me up, and that our dearest daughter, Audrey, definitely have never happened had you not been as important a part of my life.

Thank you, all of you, who have guided me, taught me, criticized me, and helped me.

Table of Contents

List of Tables

List of Figures

Nomenclature

a	parameter defined in Equation 6.3 (casing wall temperature)
B	wellbore fluid formation volume factor
$\hat{c}_r$, $\hat{c}_o$, $\hat{c}_t$	rock, oil, and total compressibility of the fluid saturated porous media, respectively, $m^{-1}Lt^2$, 1/Pa
c_f, c_m, c_s, c_w	specific heat capacity of the fluid phase, fluid saturated porous medium, solid phase, and water phase, respectively, L^2/t^2T, J/(kg·K)
C	wellbore storage coefficient, $m^{-1}L^4t^2$, m^3/Pa
E_1	En-function with n=1, and $E_1(x)=-E_i(-x)$
E_i	function of exponential integral
Fo	Forchheimer number
g	standard gravity, Lt^{-2}, 9.8 m/s^2
g_c	conversion factor defined in Hasan, Kabir, and Lin (2005)
H	reservoir thickness, L, m
$\hat{H}$	enthalpy, L^2/t^2, J/kg
h_i	i layer thickness, L, m
J	conversion factor defined in Hasan, Kabir, and Lin (2005)
k	reservoir permeability, L^2, m^2
k_r, k_s, k_i	relative permeability, permeability of the damaged zone, and i layer permeability, respectively
K_0, K_1	modified Bessel functions of the second kind of order 0 and 1, respectively
L	half of the fracture interval, L, m
L_R	relaxation factor defined in Hasan, Kabir, and Lin (2005)
p	pressure, $mL^{-1}t^{-2}$, Pa
p_s	pressure at the edge of the damaged zone, m/Lt^2, Pa
q	downhole production rate, L^3t^{-1}, m^3/s
q_i	ILPR, L^3/t, m^3/s
q_{sf}	volumetric after-flow rate, L^3t^{-1}, m^3/s
r	radius, L, m
r_i, r_s, r_w, r_e, r_{sf}	radius of investigation, damaged zone radius, production wellbore radius, outer closed boundary radius, and sandface radius, respectively, L, m
S_{wr}	saturation of the residual water
t	time, t, s
t_p, t_{pss}	end of production time and start of pseudo-steady state fluid period, respectively, t, s
T	temperature, T, K
T_i, T_s, T_{sf}	initial reservoir temperature, the temperature at the edge of the damaged zone, and sandface temperature, respectively, T, K
T_f, T_p, T_{ei}, T_{inflow}	wellbore fluid temperature, producing fluid temperature before the shut-in, casing wall temperature illustrated in Figure 6.9, inflow fluid temperature for each fracture, respectively, T, K
u	average linear (Darcy) velocity, L/t, m/s
U	specific internal energy, L^2/t^2, J/kg
U'	Heaviside's unit function
v	actual local (superficial) velocity, L/t, m/s
x	distance in flow direction, L, m
α	thermal diffusivity of the fluid saturated porous medium, L^2/t, m^2/s

β	thermal expansion coefficient of the fluid, 1/T, 1/K
β_{ND}	non-Darcy flow coefficient, $1/L^2$, $1/m^2$
η	pressure diffusivity coefficient, L^2/t^2, m^2/s^2
η_a	AE coefficient of the fluid, Lt^2T/m, K/Pa
θ	well inclination from horizontal
ϕ	average porosity in the porous medium
ϕ'	a lumped parameter defined in Equation 6.2
γ	Euler's constant
λ	thermal conductivity, $MLt^{-3}T^{-1}$, W/(m·K)
λ_f, λ_m, λ_s, λ_w	thermal conductivity of the fluid phase, fluid saturated porous medium, solid phase, and water phase, respectively, $MLt^{-3}T^{-1}$, W/(m·K)
μ	fluid viscosity, $mL^{-1}t^{-1}$, Pa·s
μ_{JT}	JT coefficient of the fluid, Lt^2T/m, K/Pa
ρ	density, mL^{-3}, kg/m^3
ρ_f, ρ_s, ρ_w	density of the fluid phase, solid phase, and water phase, respectively, mL^{-3}, kg/m^3
τ	shear stress, $mL^{-1}t^{-2}$, Pa

Abstract

Recent developments in downhole temperature measurements open new alternatives contributing to reservoir characterization. In this dissertation, novel forward and inverse models to analyze production- and injection-induced temperature signals are developed for conventional and unconventional reservoir applications. Important limitations of the proposed models are addressed by accounting for fluid property variations and complex production strategies.

Forward modeling approaches involve making relevant assumptions that allow rigorous analytical solutions to be constructed using Laplace transform, Method of Characteristics, and control volume analysis. Our results of the analytical models are benchmarked with those from commercial numerical simulation software. Multiple possible scenarios of conventional reservoirs are addressed including single-layer reservoir, multi-layer reservoir, near-wellbore damaged zone, and non-Darcy flow effect. To treat temperature signals associated with complex production history, we introduce methods with underlying theories of superposition principle and production rate normalization borrowed from pressure transient analysis while developing a new analytical approach when these theories are not applicable. Besides the transient flow period, boundary dominated flow is incorporated to extend the application of the proposed temperature transient analysis. We further extend the temperature transient analysis to fracture diagnostics during production and flow-back periods for unconventional reservoirs and CO_2 leakage detection and characterization from storage zones.

From the analysis results, we identify major mechanisms for thermal signals associated with production/injection of fluids from/into the subsurface: Joule-Thomson (JT) effect, adiabatic expansion/compression, heat conduction, and advection. We determine the significance of these mechanisms depending on the application of interest and the dominating flow regime (transient versus boundary dominated). For conventional reservoir production cases with high drawdown and strong temperature signals, the developed fluid property correction method improves the accuracy of the forward models. The interpretation and inversion processes are mainly conducted on semi-log plots with temporal temperature signals. For conventional reservoirs, the inverse modeling estimates permeability, porosity, damaged zone permeability and radius, non-Darcy flow coefficient, drainage area, and reservoir shape. Other outputs from the inversion procedures include leakage rate and transmissibility for CO_2 leakage, and inflow fluid temperature, surrounding temperature field, and after-flow velocity of each fracture during unconventional reservoir production and flow-back.

Chapter 1. Introduction

1.1 Background and Research Motivations

Reservoir characterization plays the fundamental role of successful reservoir engineering. A better understanding of the reservoir and estimating of the reservoir properties help to manage and optimize its lifetime performance. To minimize the associated uncertainties with estimated properties, various data sources are individually/jointly analyzed. Common techniques to characterize the reservoir include wireline formation testing, log-derived reservoir properties estimates, core analysis, and well testing. Conventional well testing focus on exploiting and interpreting the pressure transient data to identify the reservoir models, and estimate the reservoir properties. The progress on the downhole monitoring systems, which provide continuous and accurate downhole pressure measurements, enlarged the scope of the conventional well testing to incorporate and improve the quality of multi-rate, and permanent monitoring pressure transient analysis (PTA).

Temperature measurements are more common in downhole monitoring systems, with longer coverage and higher accuracy compared to the pressure measurements. Until recently, the applications of the temperature measurements in the industry were restricted to calibrate the downhole monitoring system and to compare with geothermal temperature profile to qualitatively identify the potentials of wellbore leakage and downhole activities (Prensky 1999). Reservoir modeling was often performed with isothermal conditions due to the small temperature changes associated with fluid flow, and slow-moving thermal front in multi-phase flow conditions. With the improvements in the temperature monitoring techniques, even small temperature changes associated with the fluid flow can be identified and analyzed to obtain useful reservoir information, similar to those in PTA.

Another advantage of the temperature measurements is its independence from pressure and other production parameters, which currently are the major reservoir characterization techniques. This independence can be very useful in certain conditions. For example, multilayer characterization from PTA remains a challenge due to the pressure dependency of the multiple layers. Given their depositional environment, many reservoirs are composed of multiple layers with different properties. Despite the cases of the multiple tubing completion with zonal separation, production wells in such reservoirs may penetrate and perforate multiple layers. Pressure behavior, which is an average response to the fluid behavior in the system, seldom reveals more than the average properties of the entire system. To obtain individual layer properties, pressure transient test for multilayer reservoirs remains a challenge due to time-consuming and complex steps to acquire multiple sets of pressure and production rate data. This is not an issue for the temperature measurements. With one production rate, the inflow temperatures for each layer are different and can be analyzed to obtain the reservoir properties for that layer. A similar situation occurs in characterizing multi-stage hydraulic fracturing well production performance. By analyzing the temperature data at each perforation, we can estimate the inflow performance for each stage.

As an evolving reservoir characterization technique, temperature transient analysis (TTA) can also lend the concept from existing approaches (e.g. reservoir limit testing, decline curve analysis, rate transient analysis) for more applications. Investigating boundary dominated flow (BDF) in reservoir limit testing estimates the reservoir boundary and original oil/gas in place through rate decline analysis. This flow regime is critical since most of the hydrocarbon is recovered during this period compared to the preceding transient period. To extend the applications of PTA to field data with complex production history, several approaches are implemented, which include superposition principle and production rate normalization. The

proposed TTA can explore more applications and extend the scope by lending the underlying theories behind these approaches.

Other potential applications for the temperature measurements include the shale reservoir characterization and leakage detection in CO_2 storage project. The limitations to apply conventional PTA on shale reservoir are due to the extremely low permeability, shortened radius of investigation, and longer testing period in shale reservoir. Contrary to the pressure propagation wave, the temperature propagates based on multiple physical processes. Conductive heat transfer, the propagating speed of which is not a function of the testing medium permeability, in low permeability reservoir are more significant than other factors affecting the temperature measurements in shale reservoir. Therefore, it is particularly encouraging to apply TTA to characterize shale reservoirs. The temperature variations caused by fluid flow is a function of the thermal properties of the flowing fluids. In multi-phase flow scenario, this functionality is very promising to identify the saturation front and leakage fluid type by temperature measurements.

These limitations with the current PTA to interpret unconventional reservoir, and the potential to apply temperature measurements as a testing technique to characterize reservoir properties, motivated this research. Other applications of this research can be expanded to investigate the leakage rate and pathway properties for CO_2 storage zone, multi-layer reservoir, and hydraulic fracturing evaluation.

1.2 Problem Statement

This research aims to investigate the potential to develop TTA techniques in order to obtain reservoir properties. In details, the following problems will be addressed in this research:

1. To develop forward models for profiling the temperature distribution in conventional reservoirs. The methodology to develop this forward model can be analytical, semi-analytical, and numerical. The preferred forward model is analytical, while semi-analytical and numerical models will be the alternatives when analytical modeling is not feasible. To validate these models, other available models and field data need to be presented to compare with the developed models.
2. To develop forward models predicting the temperature distribution during production and characterizing the hydraulic fractures and reservoir in the flow-back periods. These models will be based on the forward model for the conventional reservoir, where similar validation methods are applied to examine these forward models.
3. To apply the forward models to the scenarios of interest (near wellbore properties, multi-layer reservoir, and leakage detection in CO_2 storage projects). Sensitivity analysis are required to investigate the relationship between the temperature signals and reservoir/leakage properties, and the potentials to apply inverse modeling to extract the reservoir/leakage properties from the temperature signals.
4. To develop inverse models to extract the reservoir properties from the temperature signals. The degrees of uncertainty in the scenarios of interest determine the methodology for the selected forward models.

1.3 Governing Equations

To understand the physics behind the temperature signal induced by fluid flow in a porous medium, the governing equation for heat transfer need to be developed for the porous medium in the first place. The derivation of the governing equations for heat transfer in a porous medium begins with the conservation of mass, momentum, and energy. By combining these

three conservation laws, the heat transfer governing equation (energy balance equation) for single-phase flow in a porous medium is constructed. Thereafter, the governing equation for multi-phase flow in a porous medium is implemented by applying the volumetric averaging technique to complete this derivation.

1.3.1 Conservation Laws

The three conservation laws to derive the energy balance equation are the continuity equation (conservation of mass), the equation of motion (conservation of momentum), and the conservation of energy.

The continuity equation (conservation of mass) is to conserve the mass in the system. The accumulation of mass is identical to the rate differences between the mass entering and leaving the system. Considering those rates in a control volume, the differential form of the continuity equation becomes:

$$\frac{\partial \rho}{\partial t} = -\nabla(\rho v) \tag{1.1}$$

The velocity should be a vector in a system with multiple dimensions. The direction of fluid flow in this research is in one dimension, therefore the velocity vector is simplified to a velocity scalar.

The equation of motion (conservation of momentum) is to conserve the momentums and the forces in the system. Based on the equation of motion, the incremental rate of momentum results from the rate differences between momentum entering and leaving the system, and with the external forces acting on the system. In the same control volume, the differential form of the conservation of momentum becomes:

$$\frac{\partial(\rho v)}{\partial t} = -\nabla\left[(\rho v \cdot v) + \tau\right] - \nabla p + \rho g \tag{1.2}$$

Again, the shear stress tensor is simplified to a scalar in the one-dimensional system.

The conservation of energy is another form of the first law of thermodynamics, which defines the changes in the internal energy of a closed system. The internal energy is affected by the thermal energy variation in the system and the work done on the system. The increasing rates of the kinetic and internal energy are divided into four categories, namely: (1) kinetic and internal energy addition from convective transport; (2) heat addition from molecular transport (conduction); (3) work done on system by molecular mechanisms (i.e., by stresses); and (4) work done on system by external and body forces (e.g., by gravity). In a control volume, the differential form of the conservation of energy becomes:

$$\frac{\partial}{\partial t}\left(\frac{1}{2}\rho v^2 + \rho U\right) = -\nabla\left[\left(\frac{1}{2}\rho v^2 + \rho U\right)v + pv + \tau v\right] + \nabla(\lambda \nabla T) + \rho(vg) \tag{1.3}$$

1.3.2 Single-Phase Energy Balance Equation

We will derive the energy balance equation for the fluid phase from the three conservation laws in this section. Thereafter, certain modifications are made to obtain the energy balance equation for the solid phase. Two assumptions need to be made to apply the three conservation laws, which are no chemical reaction, and homogeneous porous media.

Multiplying the equation of motion (1.2) by the actual local velocity gives:

$$\frac{\partial}{\partial t}\left(\frac{1}{2}\rho v^2\right) = -\nabla\left(\frac{1}{2}\rho v^2 \cdot v\right) - v\nabla p - v(\nabla \tau) + \rho(vg) \tag{1.4}$$

Equation 1.5 is the difference between equations 1.3 and 1.4:

$$\frac{\partial}{\partial t}(\rho U) = -\nabla\left[(\rho U)v - \lambda\nabla T\right] - p\nabla v - \tau\nabla v \tag{1.5}$$

Applying the definition of internal energy $U = \hat{H} - \frac{p}{\rho}$, equation 1.5 becomes:

$$\frac{\partial}{\partial t}\left(\rho\hat{H}\right) - \frac{\partial p}{\partial t} = -\nabla\left[\left(\rho\hat{H}\right)v\right] + \nabla\left(\lambda\nabla T\right) + v\nabla p - \tau\nabla v \tag{1.6}$$

Equation 1.7 is the result of applying conservation of mass (equation 1.1) to equation 1.6:

$$\rho\frac{\partial\hat{H}}{\partial t} - \frac{\partial p}{\partial t} = -\rho v\nabla\hat{H} + \nabla\left(\lambda\nabla T\right) + v\nabla p - \tau\nabla v \tag{1.7}$$

Equation 1.7 becomes equation A8 after applying the definition of enthalpy:

$d\hat{H} = \frac{\partial\hat{H}}{\partial T}dT + \frac{\partial\hat{H}}{\partial p}dp = c_p dT + \left[\frac{1}{\rho} - T\frac{\partial\left(\frac{1}{\rho}\right)}{\partial T}\right]dp$ on the left-hand side (LFS) of equation 1.7

and the definition of the thermal expansion coefficient: $\beta = -\frac{1}{\rho}\left(\frac{\partial\rho}{\partial T}\right)_p$ on the right-hand side (RHS) of equation 1.7:

$$\rho c_p\frac{\partial T}{\partial t} - T\beta\frac{\partial p}{\partial t} = -\rho c_p v\nabla T + \nabla\left(\lambda\nabla T\right) + T\beta v\nabla p - \tau\nabla v \tag{1.8}$$

Equation 1.8 is the energy balance equation for the fluid phase derived from the conservation of energy, the equation of motion and continuity.

The solid phase energy balance equation is modified from equation 1.8 with two simplifications. The first simplification is to neglect the thermal expansion for the solid phase. The magnitudes of the thermal expansions for solid, liquid, and gas phase are in the order of 10^{-5}, 10^{-3}, 10^{-1} degC^{-1}, respectively. The thermal expansion for the solid phase is negligible compared to the other two phases. The second simplification is based on the zero velocity for the solid phase. Applying these two simplifications, equation 1.8 becomes equation 1.9, which is the solid phase energy balance equation.

$$\rho c_p\frac{\partial T}{\partial t} = \nabla\left(\lambda\nabla T\right) \tag{1.9}$$

Two assumptions need to be made to apply these two equations to develop the energy balance equation for single-phase flow. The first assumption is that the solid and fluid phases are in local thermal equilibrium and with the same temperature. This assumption is valid considering the very small Reynold number in Darcy flow. And the second simplification is no heat generation or dissipation in the system.

The theory and procedures to derive the energy balance equation for single-phase flow in a porous medium are to combine equations 1.8 (fluid phase) and 1.9 (solid phase) to construct a representative governing equation. The average porosity in the porous medium is defined as ϕ. Considering the whole system, the solid phase (grains) is occupying $1-\phi$ of the total volume, and the fluid phase is occupying ϕ of the total volume. By merging equations 1.8 and 1.9, a volumetric average of the energy balance equations for fluid and solid phases are required. Volumetric averaging requires that equation 1.9 is multiplied by $1-\phi$, and equation 1.8 is multiplied by ϕ. The sum of the resulting equations gives equation 1.10, which is the energy balance equation of single-phase flow in a porous medium:

$$\left[\phi\rho_f c_f + (1-\phi)\rho_s c_s\right]\frac{\partial T}{\partial t} - T\phi\beta_f \frac{\partial p}{\partial t} = \\ -\phi\rho_f c_f v_f \nabla T + \left[\phi\lambda_f + (1-\phi)\lambda_s\right]\nabla^2 T + \phi T\beta_f v_f \nabla p - \phi\tau_f \nabla v_f \tag{1.10}$$

The average linear (Darcy) velocity *u* is defined as the flow rate per unit cross-sectional area of the porous medium. Therefore, the average linear velocity can be obtained from Darcy's law or from the volumetric injection rate. The average linear velocity can be represented by multiplying the actual local velocity *v* with the percentage of the fluid phase on the cross-sectional area, which is ϕ in this case. Applying $v\phi = u$, equation 1.10 becomes:

$$\left[\phi\rho_f c_f + (1-\phi)\rho_s c_s\right]\frac{\partial T}{\partial t} - T\phi\beta_f \frac{\partial p}{\partial t} = \\ -\rho_f c_f u_f \nabla T + \left[\phi\lambda_f + (1-\phi)\lambda_s\right]\nabla^2 T + T\beta_f u_f \nabla p - \tau_f \nabla u_f \tag{1.11}$$

The viscous dissipation term ($\tau_f \nabla u_f$) can be written as $u_f \nabla p$ in Darcy's flow (Nield and Bejan 2013). Equation 1.11 becomes:

$$\left[\phi\rho_f c_f + (1-\phi)\rho_s c_s\right]\frac{\partial T}{\partial t} - T\phi\beta_f \frac{\partial p}{\partial t} = \\ -\rho_f c_f u_f \nabla T + \left[\phi\lambda_f + (1-\phi)\lambda_s\right]\nabla^2 T + T\beta_f u_f \nabla p - u_f \nabla p \tag{1.12}$$

Equation 1.12 can be re-written as:

$$\frac{\partial T}{\partial t} + C u_f \nabla T = \eta\phi C \frac{\partial p}{\partial t} + \alpha\nabla^2 T + \mu_{JT} C u_f \nabla p \\ c_m = \phi\rho_f c_f + (1-\phi)\rho_s c_s \\ \lambda_m = \phi\lambda_f + (1-\phi)\lambda_s \\ \alpha = \frac{\lambda_m}{c_m} \\ C = \frac{\rho_f c_f}{c_m} \\ \mu_{JT} = \frac{T\beta - 1}{\rho_f c_f} \\ \eta = \frac{T\beta}{\rho_f c_f} \tag{1.13}$$

1.3.3 Multi-Phases Energy Balance Equation

The theory and procedures to derive the energy balance equation for two-phase flow in a porous medium are similar to the one for single-phase flow. We need to combine one more equation 1.8 (fluid phase) to represent another fluid phase. Subscript *1* indicates the first fluid phase, and subscript *2* indicates the second fluid phase. Therefore, the saturation of the first fluid phase is S_1, and the saturation of the second fluid phase is therefore S_2. Considering the whole system, the solid phase (grains), first fluid phase, and the second fluid phase are occupying $1-\phi$, $S_1\phi$, and $S_2\phi$ of the total volume, respectively. The same volumetric average of the energy balance equations for fluid and solid phases are required that equation 1.9 is multiplied by $1-\phi$, and equation 1.8 is multiplied by $S_1\phi$ and $S_2\phi$. The sum of the resulting equations gives equation 1.14, which is the energy balance equation of two-phase flow in a porous medium:

$$\begin{aligned}&\left\{\phi\left[\rho_1 c_1 S_1+\rho_2 c_2 S_2\right]+(1-\phi)\rho_s c_s\right\}\frac{\partial T}{\partial t}-T\phi\left(S_1\beta_1+S_2\beta_2\right)\frac{\partial p}{\partial t}=\\&-\phi\left(\rho_1 c_1 v_1 S_1+\rho_2 c_2 v_2 S_2\right)\nabla T+\left\{\phi\left[\lambda_1 S_1+\lambda_2 S_2\right]+(1-\phi)\lambda_s\right\}\nabla^2 T\\&+\phi T\left(S_1\beta_1 v_1+S_2\beta_2 v_2\right)\nabla p-\phi\left(\tau_1 S_1\nabla v_1+\tau_2 S_2\nabla v_2\right)\end{aligned}\tag{1.14}$$

The average linear velocities of two fluid phases can be calculated by multiplying the actual local velocity v_1 and v_2 with the percentage of the two fluid phases on the cross-sectional area, which are $S_1\phi$ and $(1\text{-}S_1)\phi$ respectively. Applying $v_1 S_1\phi=u_1; v_2 S_2\phi=u_2$, equation 1.14 becomes:

$$\begin{aligned}&\left\{\phi\left[\rho_1 c_1 S_1+\rho_2 c_2 S_2\right]+(1-\phi)\rho_s c_s\right\}\frac{\partial T}{\partial t}-T\phi\left(S_1\beta_1+S_2\beta_2\right)\frac{\partial p}{\partial t}=\\&-\left(\rho_1 c_1 u_1+\rho_2 c_2 u_2\right)\nabla T+\left\{\phi\left[\lambda_1 S_1+\lambda_2 S_2\right]+(1-\phi)\lambda_s\right\}\nabla^2 T\\&+T\left(\beta_1 u_1+\beta_2 u_2\right)\nabla p-\left(\tau_1\nabla u_1+\tau_2\nabla u_2\right)\end{aligned}\tag{1.15}$$

Applying the viscous dissipation representation for two fluid phases, equation 1.15 becomes:

$$\begin{aligned}&\left\{\phi\left[\rho_1 c_1 S_1+\rho_2 c_2 S_2\right]+(1-\phi)\rho_s c_s\right\}\frac{\partial T}{\partial t}-T\phi\left(S_1\beta_1+S_2\beta_2\right)\frac{\partial p}{\partial t}=\\&-\left(\rho_1 c_1 u_1+\rho_2 c_2 u_2\right)\nabla T+\left\{\phi\left[\lambda_1 S_1+\lambda_2 S_2\right]+(1-\phi)\lambda_s\right\}\nabla^2 T\\&+T\left(\beta_1 u_1+\beta_2 u_2\right)\nabla p-\left(u_1+u_2\right)\nabla p\end{aligned}\tag{1.16}$$

Further rearrangements and manipulations of equation 1.16 give:

$$\begin{aligned}&\frac{\partial T}{\partial t}+\tilde{u}_m\nabla T=\tilde{\eta}\phi\frac{\partial p}{\partial t}+\tilde{\alpha}\nabla^2 T+\tilde{J}\nabla p\\&\tilde{u}_m=\frac{\rho_1 c_1 u_1+\rho_2 c_2 u_2}{\phi\left[\rho_1 c_1 S_1+\rho_2 c_2 S_2\right]+(1-\phi)\rho_s c_s}\\&\tilde{\alpha}=\frac{\phi\left[\lambda_1 S_1+\lambda_2 S_2\right]+(1-\phi)\lambda_s}{\phi\left[\rho_1 c_1 S_1+\rho_2 c_2 S_2\right]+(1-\phi)\rho_s c_s}\\&\tilde{J}=\frac{u_1\left(\beta_1 T-1\right)+u_2\left(\beta_2 T-1\right)}{\phi\left[\rho_1 c_1 S_1+\rho_2 c_2 S_2\right]+(1-\phi)\rho_s c_s}=\frac{u_1\rho_1 c_1\mu_{JT1}+u_2\rho_2 c_2\mu_{JT2}}{\phi\left[\rho_1 c_1 S_1+\rho_2 c_2 S_2\right]+(1-\phi)\rho_s c_s}\\&\mu_{JT}=\frac{T\beta-1}{\rho_f c_f}\\&\tilde{\eta}=\frac{T\phi\left(S_1\beta_1+S_2\beta_2\right)}{\phi\left[\rho_1 c_1 S_1+\rho_2 c_2 S_2\right]+(1-\phi)\rho_s c_s}=\frac{\phi\left(S_1\rho_1 c_1\eta_1+S_2\rho_2 c_2\eta_2\right)}{\phi\left[\rho_1 c_1 S_1+\rho_2 c_2 S_2\right]+(1-\phi)\rho_s c_s}\end{aligned}\tag{1.17}$$

where J is the JT coefficient of the fluid, and the tilde accent represents the effective average of the corresponding parameter based on the two-phase fluid.

To verify the derived governing equations, the results are compared and validated with several equations in the literature. Equations 1.12, 1.13, and 1.17 are identical with equation 2.33, 2.43. 2.63 in Duru (2011), respectively. Applying the assumption incompressible flow and the fractional flow definition, equation 1.17 can be converted to equation A6 in LaForce, Ennis-King, and Paterson (2014). Implementing another assumption of no heat conduction, equation 1.17 is the same with equation 3 in Sumnu-Dindoruk and Dindoruk (2008).

1.4. Modeling Approaches

With the developed governing equation, we can develop forward models by solving the equation under appropriate initial and boundary conditions and analyze heat transfer in the reservoir. Two main types of methods to construct the forward models are analytical and numerical. The semi-analytical model can be useful in certain problems where part of the model can be solved analytically, and the rest is solved numerically. In this section, we will introduce these two methods and mathematical tools to apply these methods.

1.4.1 Analytical Model

The analytical model is the traditional way to solve the governing equation. Analytical models can obtain the temperature distribution without the need for time and space discretization and computationally expensive iterative approaches. More importantly, analytical models can explicitly relate the temperature variation to reservoir properties which will be extremely useful for the development of temperature-based reservoir characterization methods. Such approaches are analogous to conventional PTA which is based on analytical solutions obtained for the pressure diffusivity equation. Also, temperature inversion using analytical solutions is stable and easy to compute.

The governing equation (equation 1.17) is a non-linear second-order partial differential equation (PDE). To solve it analytically, mathematical techniques need to be applied. Laplace transform can be used to develop the analytical solution for the conventional reservoir, which is a very useful tool that can simplify PDE to ordinary differential equation (ODE). Fourier transform is another widely used mathematical tool to solve PDEs. Similar to Laplace transform, Fourier transform solve PDEs by reducing its dimensions. By applying Laplace and Fourier transform together, we can transform a two-dimensional PDE into ODE, and solve it. These mathematical tools are essential to obtain the analytical solutions for heat transfer in hydraulic fracturing.

1.4.2 Numerical Simulation

Numerical simulation has been evolved with the development of computational speed to solve complex physical problems in recent years. This method solves the governing equations for heat and mass flow in porous media by finding the numerical approximation in time and space discretization of the whole system. Such discretization can be very fine to improve the accuracy of the simulation on time and space, which is valuable especially for non-linear fluid properties, the complex set of boundary conditions, and heterogeneous reservoir. More importantly, the numerical simulation can obtain the temperature distribution without the need for certain assumptions to simplify the problem. Rigid and precise solutions can be obtained from the numerical simulation, which can be used to complement and validate analytical solutions.

In this research, we investigate the temperature signals in the reservoir to characterize it. Thermal reservoir simulations are used to solve the governing equations and predict the temperature signals. We use the thermal model in CMG-GEM (2015), CMG-STARS (2015), KAPPA-RUBIS (2015) to perform thermal reservoir simulations, which apply finite difference method to numerically solve the coupled heat and flow equations.

Finite element method is similar to the finite difference method on the discretization of the problem, which is named as a finite element. The globe solutions acquired from finite element method are based on the solutions from each node. Therefore, it can represent complex material properties and geometry more accurately, by capturing the local effects. In another

hand, the accuracy requires more computational capacities. In this research, we investigate the heat transfer in the wellbore using the finite element method (COMSOL 2015).

1.5 Review of Chapters

Below is an overview of the upcoming chapters in this dissertation:

Chapter 2 reviews the current research state of the subjects studied, which includes the developments of downhole monitoring systems, and temperature forward and inverse modeling in conventional and unconventional reservoirs. In addition, literature review on fracture diagnostic and CO_2 storage leakage detection and rate estimation are conducted with special focus on using thermal approaches.

Chapter 3 presents the forward thermal modeling in the producing conventional reservoir using newly derived analytical solutions. Various reservoir types are investigated considering single-layer reservoir, multi-layer reservoir, near-wellbore damaged zone, and non-Darcy flow effect. Moreover, both transient and boundary dominated flow regimes are investigated to reveal different production induced thermal signals.

Chapter 4 illustrates the reservoir characterization through detailed temperature inversion procedures in a producing conventional reservoir. Temperature interpretation techniques are provided based on semi-log and Cartesian graphical analysis using the synthetic temperature data obtained from production and monitoring wells. For each scenario mentioned in chapter 3, specific outputs are produced from the associated analytical solutions, which include permeability, porosity, damaged zone properties, non-Darcy flow coefficient, reservoir drainage area, and reservoir shape.

Chapter 5 extends the scope of TTA by addressing two main assumptions made in Chapter 3: constant fluid property and production rates. Fluid property correction methods and four approaches to account for production rate and pressure variations are developed in this chapter. Applications of these approaches significantly improve the estimation accuracy compared with those in Chapter 4.

Chapter 6 introduces the forward and inverse thermal modeling in unconventional reservoirs. Two cases are presented in this chapter: a numerical model to simulate thermal signals from producing multi-stage hydraulic fractured horizontal well (MFHW) and an analytical model to analyze flow-back temperature data. The outputs of this thermal modeling include inflow fluid temperature, surrounding temperature field, and after-flow velocity of each fracture.

Chapter 7 discusses the applications of TTA to characterization of CO_2 leakage from storage zones. We investigate the strength of the temperature signals for two scenarios in which leakage occurs either through a leaky well or a leaky fault. In addition, we investigate the strength of the temperature signal as a function of leakage rate and develop a control volume analysis to relate these two in the complex two-phase leakage conditions. This analytical thermal model for CO_2 leakage enables quick analysis with sufficient accuracy to estimate the leakage rate.

Finally, conclusions and recommendations for future work are presented in Chapter 8.

Chapter 2. Literature Review

2.1 Developments in Downhole Monitoring Systems

The temperature data from production logging has been recorded since 1920's (Sclater and Stephenson 1929) which can be used to qualitatively identify fluid entry/leakage and evaluate the integrity of well completions. For reservoir characterization purposes, temperature measurements are not prevailing as pressure since the main approach for temperature monitoring is through well logging (Quintero et al. 1993). Recent developments on intelligent well systems open new alternatives contributing to reservoir management by acquiring information on the reservoir properties (Denney 2015). The monitoring systems on a typical intelligent well include pressure and temperature permanent downhole gauges (PDG), Distributed Temperature Sensing (DTS) or Array Temperature Sensing (Prats and Vogiatzis) real-time system, multi-phase flowmeters (Bostick 2003), and Fiber Bragg Grating (FBG) real-time system (Li et al. 2017). These evolving technologies are cost-effective, with relatively high resolution (as high as 0.01 degC (Muradov and Davies 2012b)), and profiling the temperature signals both temporally and spatially (DTS and FBG). Meanwhile, the flexibility of DTS and FBG allows their implementations embedded in the cement to minimize the wellbore thermal effects (Glasbergen et al. 2009). As a result, temperature data obtained from such systems can be assumed as the sandface temperature signal, which is a strong function of reservoir properties and production constraints. The advent of the DTS system demands the development of new forward and inverse models to enable interpretation of the acquired temperature data.

2.2 Temperature Modeling in Conventional Reservoirs

Numerical modeling of reservoir temperature variation has been the focus of several studies (Sui et al. 2008a, Sui et al. 2008b, App 2017, App 2010, App 2016, App and Yoshioka 2013, Duru and Horne 2010a, 2011a), which revealed the potential of using the temperature data to derive information on the reservoir. Analytical modeling is another approach to evaluate the reservoir temperature. Early attempts to analytically investigate the heat transfer in reservoirs can be traced back to (Edwardson et al. 1962, Chekalyuk 1965, Atkinson and Ramey 1977). Edwardson et al. (1962) developed an analytical solution to calculate the temperature changes in both the wellbore and the reservoir due to mud circulation during drilling operations. To determine the reservoir temperature, they solved the heat conduction differential equation. Atkinson and Ramey (1977) derived a solution to estimate the temperature distribution considering heat conduction and convection. Both of these studies neglected the temperature changes caused by the baro-thermal effects (i.e. those due to viscous dissipation and compressibility).

Several recent studies focused on the development of analytical models for reservoir temperature variation. Ramazanov and Parshin (2006) obtained an analytical solution for the temperature distribution in an oil reservoir assuming steady-state pressure distribution. Ramazanov and Nagimov (2007) extended this solution by including the pressure transient response to the analytical solution. Ramazanov et al. (2010) obtained an analytical solution for the reservoir temperature using the Method of Characteristics. The skin-related temperature slope changes were investigated, and the skin was estimated from field bottom-hole temperature data. However, the first two solutions accounted for the baro-thermal effects by a pre-defined varying bottom-hole pressure instead of including a rigorous pressure response, and the adiabatic expansion (AE) effect in the third solution is not well represented due to the usage of the steady-state pressure equation.

Muradov and Davies (2011), Muradov and Davies (2012a) presented asymptotic analytical solutions to calculate the reservoir temperature profile in producing horizontal wells. The asymptotic solutions accounted for convection, heat loss to surrounding layers, and JT effects and were compared with the results from numerical simulation. The AE effect was separately accounted for by considering initial, pressure-induced temperature changes (jumps) into the temperature profile. Similar bottom-hole temperature jumps can occur after rate changes associated with the AE of the reservoir fluid (App 2009, App 2010). Nevertheless, the AE effect is generally not only an early-time effect in the bottom-hole location. For the proposed forward modeling in the conventional reservoir, we will build on these findings and derive a transient temperature analytical solution to identify the far-field AE effect.

App and Yoshioka (2013) presented a steady-state analytical solution and a transient numerical simulation to evaluate the impact of reservoir permeability on sand-face temperature. In a high permeability reservoir, Peclet number (the ratio of heat transfer by convection to that by conduction) is higher, which implies that the convection dominates over conduction. The proposed forward model in section 3.1 builds on these findings and develops a transient analytical solution to model the temperature profiles in the conventional reservoir.

Onur and Çinar (2016) presented semi-log and log-log interpretation methods to analyze the temperature transient data from drawdown and buildup tests. Their methods account for JT, AE effects, and damaged zone. However, the propagation speeds of JT and AE effects seem to be the same with PTA, which are in contradiction with the previous studies.

Other analytical solutions for reservoir temperature profile had been developed for multi-phase systems. Meyer (1989) presented an analytical model of reservoir temperature profile considering a vertical fracture propagating in the reservoir. Sumnu-Dindoruk and Dindoruk (2008) solved the non-isothermal two-phase flow equation using fractional flow modeling approach. The solution involved a thermal shock obtained by plotting a tangent line on the fractional-flow curves similar to the solution construction for the isothermal Buckley-Leverett problem (Buckley and Leverett 1942). LaForce, Ennis-King, and Paterson (2014) extended the model in Sumnu-Dindoruk and Dindoruk (2008) to account for the heat loss from the reservoir. The JT and AE effects were ignored in all the above two-phase analytical models. Mathias et al. (2010) derived an analytical solution for a two-phase system involving the CO_2 injection in a saline aquifer considering JT effect. However, their solution is based on approximating the two-phase system by single-phase assuming that the non-isothermal behavior only occurs in the single-phase zone. Later, Mathias, McElwaine, and Gluyas (2014) extended the solution in Mathias et al. (2010) to account for non-Darcy flow effect in a two-layer depleted gas reservoir.

2.3 Multi-layer Reservoir Modeling

Sui et al. (2012) presented a numerical model to evaluate the individual layer permeability and skin from transient temperature measurements of a commingled production well penetrating a multilayer gas reservoir. Under the condition of no layers communication, they found that the temperature response is sensitive to the damaged zone radius and permeability. Valiullin et al. (2014) applied similar models to compare the numerical results with field data, as well as the data obtained from deviated wells. The inversion process to achieve multilayer reservoir characterization required all available field data. However, the disagreements between field and numerically modeled data still exist. In section 3.5, we address this problem with an analytical solution, which significantly reduces the computational cost of the inversion and provides straightforward graphical interpretation techniques. In addition, the proposed work focuses on the multilayer reservoirs with layer cross-flow, which

is more common in practice and can reveal more information compare to those without layers communication.

Baro-thermal (pressure-induced non-isothermal) effect is an important cause for the temperature signals in the reservoir. Thus, it is important to correctly capture the pressure behavior before modeling the temperature signals in multilayer reservoirs. Investigations on pressure signals and fluid flow behaviors associated with producing multilayer reservoirs start from the early 1960s. Lefkovits et al. (1961) derived an analytical solution for pressure transient behavior in a two-layered reservoir. Bourdet (1985) extended this model to incorporate cross-flow, wellbore storage, and skin effect. In the 1980s, the advances of logging techniques provided the opportunity to acquire continuous pressure and flow rate signals downhole, which brought up another round of extensive studies. Ehlig-Economides and Joseph (1987) thoroughly reviewed the previous works and extended the two-layered to the multilayered system. The early time and late time behaviors of individual layer production rates (ILPR) were investigated and late summarized in Park (1989). We implement the above-mentioned works on layer pressure and production rate performances to construct the multilayer reservoir transient temperature analytical solution.

2.4 Near Wellbore Damage and Non-Darcy Flow Effect Modeling

Sui et al. (2008a) presented a numerical model to evaluate the individual layer permeability and skin for multiple layers from transient temperature measurements. They found that the temperature response is sensitive to the damaged zone radius and permeability. App (2010) modeled non-isothermal productivity for high-pressure reservoirs and showed that the large pressure gradient in the near-wellbore region induces a significant Joule-Thomson (JT) effect that can cause substantial temperature changes in the bottom-hole location. Duru and Horne (2011b) used the Method of Characteristics to solve the advection part of the energy balance equation, obtained the characteristic velocity, and validated this velocity with the experimental results. This model was further extended to estimate the radius of the damaged/stimulated zone, and determine whether a reservoir is composite.

In investigating the effect of the non-Darcy flow on TTA, we start with its associated pressure response. High fluid velocity encountered in the near wellbore region may result in the violation of Darcy's law. Forchheimer (1901) modeled this scenario using Darcy's law with an additional term, which is a function of the non-Darcy flow coefficient. The effect of non-Darcy flow is most commonly encountered in producing gas wells, but also possible in oil wells. Su (2004) extended Forchheimer formulation from the single phase to a three-phase system, where the non-Darcy flow coefficients of oil were reviewed and reported by Li and Engler (2001). According to these two studies, the non-Darcy flow coefficients of oil ranged from 10^8 to 10^{12} 1/m. The initiation of non-Darcy flow effect can be estimated by the magnitude of Reynold's number or Forchheimer number (Salina Borello et al. 2016). Zeng and Grigg (2006) reported the better way to identify this criterion by evaluating Forchheimer number. Considering a 10% non-Darcy flow effect, the critical Forchheimer number is 0.11. In sections 3.3 and 4.3, we consider and model the damaged zone and non-Darcy flow effect in TTA, and evaluate the damaged zone properties, as well as the critical Forchheimer number from the current temperature monitoring system.

2.5 Variation of Fluid Properties

Introducing corrections on the variable properties is an effective approach to account for the effect of the property variations on the modeling process. Vilarrasa et al. (2010) introduced a correction to account for CO_2 compressibility (density) and viscosity variations,

and apply this correction to analytical solutions to predict the interface position for the CO_2 plume. This correction is based on the volumetric average of varying properties, which is validated with numerical simulation results. In the petroleum industry, we often simplify the heterogeneous and non-uniform reservoir properties by introducing average values, e.g. average permeability (Tiab and Donaldson 2015). This averaging approach is based on three standard techniques: arithmetic, geometric, and harmonic averages for different ranges of the Dykstra-Parsons coefficient (Dykstra and Parsons 1950). This theory has evolved for reservoir property upscaling when modeling heterogeneous reservoirs. In section 5.1, we develop a method to account for fluid property variations in temperature and PTA considering practical conditions.

2.6 Modeling Boundary Dominated Flow and Variable Rate and Pressure Conditions

Investigating BDF has been an important aspect of PTA since the 1960's (Slider 1966). One major application of BDF is to estimate the original oil/gas in place through rate decline analysis (Fetkovich 1980, Palacio and Blasingame 1993, Agarwal et al. 1999, Mattar and Anderson 2003, Mattar, Anderson, and Stotts 2006). If the BDF is in radial flow regime, most of the hydrocarbon is recovered during this period compared to the preceding transient period (Zhang, Singh, and Ayala 2016). Therefore, in this thesis, we incorporate the radial BDF into the evolving TTA, as an emerging reservoir characterization and production analysis technique.

As a currently dominating method for reservoir characterization, PTA faces similar assumptions and has been evolved to address comparable challenges. A rigorous method to account for the production rate variation for PTA is introduced by Bourdet, Ayoub, and Pirard (1989) using the superposition principle. This superposition function is the constant rate analog for analysis of variable-rate production and can be used to treat finite production rate changes (Blasingame, McCray, and Lee 1991). For cases with infinite and small production rate changes, such as constant pressure production, a more practical approach is based on variable production rate normalization (Winestock and Colpitts 1965). This type of analysis is named as rate transient analysis (RTA), comparable to PTA. Traditionally, RTA is primarily applied when BDF is established and presents decent results to estimate the drainage area through reservoir limiting test (Blasingame and Lee 1986). Recently, RTA has gained popularity to analyze the production data from producing unconventional low-permeability oil and gas reservoirs (Bello and Wattenbarger 2010, Nobakht, Clarkson, and Kaviani 2012). In sections 3.4 and 4.4, we lend the underlying theories behind the superposition principle and production rate normalization to TTA, addressing the variable rate challenge faced by current analytical TTA approaches.

2.7 Hydraulic Fracturing Evaluation and Reservoir Characterization in Shale Reservoir

Recent developments in horizontal well drilling and hydraulic fracturing make the exploration of shale reservoir technically feasible. The evaluations on the fractures are critical to determining the production strategies for each well. Micro-seismic monitoring can reveal the source locations, timing, and mechanisms of the induced seismic events to make inferences about the associated fracture activities (Maxwell et al. 2010). The traditional well testing techniques are applied to hydraulic fractured horizontal wells to investigate the flow potentials of the fractures. However, the results are generally an average of all the fractures performance instead of the individual fracture. Information on individual fractures is useful to determine whether the fracturing job was successful and/or whether re-fracturing is required. Therefore, the industry is exploiting new method to evaluate the characteristics per individual fracturing stage.

The usage of temperature measurements to characterize the hydraulic fractures can be traced back to the 1970's. Early attempts for this applications were presented by Hannah, Harrington, and Anderson (1977), Harrington, Hannah, and Robert (1978). However, the applications are based on the early flow-back temperature at the surface, and relatively qualitative. Recent developments in downhole temperature monitoring system show great potentials to further exploit temperature measurements. Field examples from the industry have proved this potential. Sierra et al. (2008) presented field experiences of transient DTS data acquired during multi-stage hydraulic fracturing in vertical, deviated, and horizontal wells. They compared two cases where DTS monitoring systems are implemented inside the casing or cemented. Huckabee (2009) summarized applications of DTS technology for hydraulic fracturing stimulation diagnostics and well performance evaluation in unconventional gas well completions. Field examples are provided with applications on vertical and horizontal well stimulation diagnostics.

Triggered by these field cases, research has been conducted to investigate the temperature profiles during the early flow-back and production periods to characterize the fractures. Tabatabaei and Zhu (2012) developed a thermal model to simulate the temperature behavior along the horizontal wells during the hydraulic fracturing to evaluate the fracture properties. This model couples a near-wellbore thermal conduction model with the radial flow of an incompressible fluid, and a wellbore convection model. The energy balance equation is solved numerically with the finite-difference method. Ribeiro and Horne (2016) presented the modeling and analysis of temperature signal during and after the multiple hydraulic fracturing along horizontal wellbore. This model accounts for fracture growth and closure, wellbore effects, and interaction between multiple fractures. On the other hand, the temperature signals obtained during the production can be analyzed to characterize the reservoir. Yoshida, Zhu, and Hill (2014) developed numerical flow and thermal models for transverse fractures in horizontal wells under single-phase gas flow conditions. The reservoir thermal model, solved by a finite-difference method, considers viscous dissipation and temperature variation caused by fluid expansion, heat conduction and convection. A similar model was developed in Sun, Yu, and Sepehrnoori (2017). Cui, Zhu, and Jin (2015) presented fracture flow and thermal models to predict temperature and pressure behavior in multiple-fracture horizontal wells during production, in which the fracture flow model is solved semi-analytically. Shortly after that, they adopted the fast marching method (FMM) to simulate the same problem more efficiently (Cui et al. 2016).

The current research phase of using temperature data to evaluate the hydraulic fractures and reservoir is developing forward numerical and semi-analytical models to predict the temperature profiles during fracturing and during production. However, the study on temperature signals from the flow-back period between fracturing and production is underwhelming due to the complexity of its nature. Shortly after hydraulic fracturing, the temperature in the fracture stimulated region is still lower than the non-fractured region. The JT effect under linear flow through the fracture can be masked by the heterogeneous surrounding temperature. Therefore, analyzing production temperature signals from flow-back period to evaluate fracture efficiency and quantify inflow profile can be tricky.

The theory of estimating inflow profile from production temperature signals can be mainly attributed to thermal production-logging-tool (PLT), which started from 1960's with the initial focus on locating production zone with phase identification from JT effect (Peacock 1965). With the development of PLT and DTS, faster and more accurate temperature measurements can be recorded during production, which enables other applications including inflow profile and rate estimation. For conventional reservoir, these applications are achieved by: (1) modeling temperature profile in wellbore subject to rate variation and conduction effect through wellbore to surrounding formation (Hasan and Kabir 1991, Hasan, Kabir, and Lin

2005, Hasan, Kabir, and Wang 2013, Kabir et al. 1996, Kabir et al. 2002, Nojabaei, Hasan, and Kabir 2014), and (2) energy balance in the wellbore with accurate inflow rate and fluid temperature from each perforation (App 2017, Gysen et al. 2010, Quintero et al. 1993, Wisian et al. 1998). These analyses require precise estimation of inflow temperature, which is the combined effect of baro-thermal (mainly JT and adiabatic expansion effects) and geothermal temperature for each layer. In section 6.2, we develop a method to estimate the inflow temperature from each of the fracture during the flow-back period of an unconventional reservoir.

2.8 Inverse Modeling for Temperature Measurements

The objective of the inversion process is to obtain the fracture and reservoir properties from the temperature data. One of the simple methods to achieve this goal is the stochastic method, which minimizes the least-square difference between the data from the field and the forward model. This method is reliable in the non-linear problem but could be time-consuming in a complicated situation. Cui, Zhu, and Jin (2015) applied a random-based manual searching inversion technique, which is completed by minimizing the temperature difference between the forward model and field data. Similar techniques were applied in Duru and Horne (2010a), Tan et al. (2012), Tardy et al. (2012). Shortly after that, FMM was introduced in the forward modeling, which significantly reduces the complexity of the inversion. Zhang and Zhu (2017) reported this inverse model which estimated the production rate and fracture conductivity from each fracture.

Another type of inversion methods focuses on improving the convergence by minimizing the difference between the measured profiles with the calculated profiles from the forward model. Gauss-Newton or other gradient-based methods can be fast to converge but may cause difficulty to minimize the error facing the non-linear problem. Tabatabaei and Zhu (2012) compared this method with the stochastic method to invert the temperature data to characterize the fractures. Both methods work fine in the specific problems of their paper. Levenberg-Marquardt algorithm (Marquardt 1963) based inversion method was applied to predict the flow-rate profiles along horizontal wells (Yoshioka et al. 2009). This method successfully inverted pressure and temperature profiles from synthetic and filed examples, which matched the flowmeter-derived profiles.

The theory of another type of more complicated inversion method characterizes the posterior probability density function (PDF) of the uncertain parameters by combining their prior PDF with the observed data, through a likelihood function. The advantages of this type of inversion method include more accurate results and better eliminating the noise. Duru and Horne (2011a) improved the data de-noising to interpret field data and synthetic data with 10% noise by implementing the Bayesian method. Combined with Ensemble Kalman Filter for data assimilation, Duru and Horne (2010b) show that temperature measurements can characterize the reservoir porosity more accurately compare to the conventionally used production data. Zhang and Jafarpour (2013) consider the Maximum A-Posteriori (MAP) estimation approach for joint inversion of flow and temperature data and apply the Randomized Maximum Likelihood (RML) method for uncertainty quantification. The results showed the temperature data is sensitive to the permeability variation with depth, which cannot be predicted from the production data.

2.9 CO_2 Storage Leakage Detection and Characterization with Temperature Signals

Underground storage of carbon dioxide (CO_2) is a promising method to mitigate anthropogenic CO_2 emissions. To ensure the effectiveness of this process, the containment of

the injected CO_2 in the storage zone should be investigated. Candidate storage sites may be depleted oil/gas reservoirs and/or saline aquifers that have been intensely drilled or intersected by wells for exploration and production of underground fluids (IPCC 2005). Ten to hundred thousands of wells were drilled in mature sedimentary basins of North America. Defective wells have been estimated to be as high as 10% of the total wells in a given field (Nygaard et al. 2014). Such wells can provide leakage pathways for CO_2 that may not self-seal, and can persist for long times (Evans et al. 2004). Some of these wells date back to as early as the second half of the nineteenth century (Nordbotten, Celia, and Bachu 2004, King and Valencia 2014). Many of these older wells were not properly completed and/or abandoned, and in many cases records on well locations and abandonment strategy are nonexistent (Gass, Lehr, and Heiss 1977). For other wells that are cemented upon abandonment, changing temperature and pressure conditions during cementation can result in micro-annuli in the cement annulus (Thiercelin et al. 1998). For geologically stored CO_2, these micro-annuli can become migration pathways compromising the integrity of the storage site. As a result, leaking wells are widely identified as the main potential leakage pathways for the injected CO_2. Various monitoring techniques have been proposed to assure storage quality and to detect and characterize leakage pathways.

The pressure monitoring methods included investigations on injection zone (IZ) pressure profiles (Mathias, McElwaine, and Gluyas 2014), Above-Zone (AZ) pressure signals, pulse pressure testing (Sun et al. 2016, Shakiba and Hosseini 2016), sustained casing pressure (Tao et al. 2014), and vertical interference test (Gasda et al. 2013). The leakage of CO_2, brine, and their mixture can induce pressure changes in an AZ that is separated from the IZ by a sealed confining layer. Analytical and numerical models were developed to enable inverting the pressure perturbations in the IZ and AZ to determine the leakage characteristics (Zeidouni and Pooladi-Darvish 2012a, b, Sun et al. 2013, Jung, Zhou, and Birkholzer 2013, Wang and Small 2014, Zeidouni 2016, Zeidouni and Vilarrasa 2016, Mosaheb and Zeidouni 2017c, a, b, Mosaheb and Zeidouni 2018, Mosaheb, Zeidouni, and Shakiba 2018). However, pressure monitoring and testing procedures can be time-consuming and expensive since the pressure measurements are more complex and less flexible than other measurements such as temperature and strain. For example, temperature monitoring techniques can be implemented on both inside and outside of the casing for wellbore leakage detection purposes. Also, it may be risky to rely on pressure monitoring alone for leakage characterization because inversion of diffusive pressure signals is highly unstable and may introduce huge errors in leakage rate estimation (Zeidouni and Pooladi-Darvish 2012a, b). Introducing other measurements to complement the results from pressure-based models or replace it is one of the motivations of this study. Conclusions drawn from section 7.2 suggest that the leakage rate detection range by temperature and pressure monitoring can be different. Outputs of the analytical thermal model developed in section 7.2 provide an alternative approach to estimate the rate and transmissibility of leakage pathways from measured temperature anomalies.

With the advancements of downhole temperature monitoring system introduced in section 2.1, it has been implemented in injection and observation wells of several pilot CO_2 storage projects (Doughty and Freifeld, 2013; Liebscher et al., 2013; Wiese, 2014; Zhang and Bachu, 2011). For the issue of existing well leakage characterization investigated in this study, Nuñez-Lopez et al. (2014) presented the temperature monitoring data using DTS and PDG from two observation wells in Cranfield CO_2 storage project. During the four-year monitoring period after CO_2 injection, temperature signals in the AZ were quite stable (less than 0.5 degC perturbations) despite several abrupt changes due to instrument drift and workover operations. The cooling front of the injected CO_2 in the IZ traveled more than 10 times slower compared to the saturation front, as expected theoretically (e.g. based on LaForce et al., 2014). As a result, if the cooling signal due to CO_2 wellbore leakage is significant, field data should be useful for

leakage detection and characterization given the time window of stable temperature signals (months to years) after CO_2 arrival at the leakage path.

More recent works investigated the potential for leakage detection based on AZ's temperature signal (Zeidouni, Nicot, and Hovorka 2014b, Pruess 2011, Lu et al. 2012). The CO_2 migration in a vertical fault exhibits strong cooling effects due to the expansion of gaseous phase CO_2, and a possible phase change from liquid/supercritical to gas CO_2 (Pruess 2005). Several other processes controlling the thermal signal includes the Joule-Thomson (JT) effect, heat from dissolution/vaporization of CO_2/water, the temperature discrepancy between the injected and native fluids, geothermal gradient, and heat exchange with the surrounding rock-fluid system (Lu et al. 2012, Mathias et al. 2010, Zhang et al. 2018). The magnitude of the JT effect, which has a strong contribution to those processes, is determined by the fluid properties (mainly JT coefficient), and the pressure gradient. Therefore, the temperature signal for leakage detection can identify the leaking fluid (CO_2 versus brine) (Zeidouni, Nicot, and Hovorka 2014a), which is difficult to detect by the pressure signal. The leakage temperature signals from a secondary CO_2 accumulation site (shallow storage reservoir, e.g. groundwater aquifer) to the land surface have been modeled by Pruess (2007), Pruess (2008). The cooling effects associated with decompression of CO_2 and JT effect have minor impacts on the possibility of discharging CO_2 to the land surface but are significant enough to be detected. Similarly, the leakage temperature signals from a primary CO_2 storage reservoir are expected to be significant too and captured by the downhole temperature monitoring system. Zeng, Zhao, and Zhu (2012) developed a single phase heat transfer numerical model to simulate the leakage thermal signals which resulted in an empirical equation to relate the leakage rates to maximum temperature signals. In this work, we investigate the driving mechanisms that control leakage temperature signal for two-phase leakage system. An analytical leakage thermal model is constructed in section 7.2 considering both steady and transient conditions that can be used to estimate the wellbore leakage rate as well as the transmissibility of the wellbore leak from temperature data, the results of which will be compared with those obtained from the approach presented by Zeng, Zhao, and Zhu (2012).

With careful site characterization, it is likely that the injection well is located far from potential leakage pathways. When CO_2, traveling in the IZ, reaches the leakage pathway distant from the injection well, the fluid and matrix are already in local thermal equilibrium (Nield and Bejan 2013). This equilibrium is mainly due to the high heat capacity of the rock-fluid system, which maximizes heat absorption from the injected CO_2. CO_2 dissolution in the brine may cause minor temperature increase on the CO_2 front which is negligible compared to the leakage-induced thermal signal mainly controlled by the JT effect. The CO_2 front is therefore ahead of the thermal signal front (Sumnu-Dindoruk and Dindoruk 2008, LaForce, Ennis-King, and Paterson 2014). These physical behaviors of the CO_2 injection process give itself a perfect candidate to monitor the temperature signals for leakage.

In general, leakage pathways, which can be cracks/fractures, are different media than the reservoir regarding fluid flow properties. To simulate the leakage pathways, the cracks/fractures can be treated as a high permeability region in a cap-rock (single-porosity model) (Pruess 2008, 2011, Lu et al. 2012), or more realistically, as a different pore structures with a distinct set of permeability and porosity (dual-porosity/dual-permeability models) to represent the fracture system (Rohmer and Seyedi 2010, Zhang et al. 2011, Wang et al. 2013). Dual-porosity/dual-permeability approaches (Hill and Thomas 1985, Blaskovich et al. 1983) honor the different flow characteristics of the fracture and matrix systems. The dual-permeability approach is an extension of the dual-porosity model presented by Warren and Root (Warren and Root 1963) and Kazemi et al. (Kazemi et al. 1979). Fluid exchanges between matrix and fracture blocks are accommodated using the dual-porosity approach. The dual-permeability model also accounts for additional fluid exchanges between matrixes. The matrix

and fracture flow domains are coupled using a shape factor transfer term. Moreover, naturally fractured reservoirs present significant CO_2 storage capacities, especially in depleted oil and gas reservoirs (Cicek 2003). The naturally fractured reservoirs are not only complicated but also hard to verify their integrity (Trivedi and Babadagli 2009). In section 7.1, we investigate the temperature signals from the leakage pathways using the two major types of simulation models, as well as in the naturally fractured reservoirs.

Chapter 3. Forward Modeling in Conventional Reservoir

In this chapter, novel analytical solutions are derived to predict the temperature signal associated with the production of slightly-compressible hydrocarbon from a fully penetrating vertical well and applied to the production from oil and gas reservoirs. Various reservoir types and flow conditions are considered in the forward modeling, which include single layer reservoir under transient flow with homogeneous properties, near wellbore damaged zone, near wellbore non-Darcy effect, under BDF, and multi-layer reservoir.

3.1 Single Layer Homogeneous Reservoir under Transient Flow

Based on the current state of literature, new developments on analytical modeling of temperature transient in the reservoir is required. The analytical solution of interest should be applicable to calculate the temperature profile over the whole transient period and on the reservoir scale. We limit the scope of this study to development of analytical solutions for transient flow considering slightly-compressible hydrocarbons produced from vertical wells. Temperature profiles obtained from the analytical solutions are presented for two example problems and compared with the results from numerical simulation.

3.1.1 Problem Description and Analytical Solution

The first step to develop this forward model is to identify the governing equation for this problem. For a case of a fully penetrating vertical well producing at a constant rate from a cylindrical, homogenous, and isotropic reservoir (a schematic of this model is illustrated in Figure 1), Equation 2.17 becomes:

$$\begin{aligned}&\left\{\phi\left[\rho_w c_w S_{wr}+\rho_f c_f\left(1-S_{wr}\right)\right]+\left(1-\phi\right)\rho_s c_s\right\}\frac{\partial T}{\partial t}\\&=\frac{q\rho_f c_f}{2\pi rH}\left[\frac{\partial T}{\partial r}-\mu_{JT}\frac{\partial p}{\partial r}\right]+\phi\left(\rho_f c_f \mu_{JT}+1\right)\frac{\partial p}{\partial t}\end{aligned} \tag{3.1}$$

The initial condition and the outer boundary condition represented by the reservoir initial temperature are given by.

$$T=T_i, r\geq r_w, t=0 \tag{3.2}$$

$$T=T_i, r\to\infty, t>0 \tag{3.3}$$

With the derived governing equation and boundary conditions, the analytical solutions can be derived and analyzed. To derive an analytical solution from Equation 3.1, pressure derivatives with respect to time and space should be first evaluated and replaced. The transient pressure response for slightly compressible fluid (e.g. oil) subject to constant rate production is used to evaluate the pressure derivatives. The gas phase can be treated as slightly compressible fluid as long as the pressure drawdown is within 10% of the initial reservoir pressure (Spivey and Lee 2013). The transient pressure solution for slightly compressible fluid considering constant rate production is (Theis 1935):

$$p(r,t)-p_i=\frac{\mu q}{4\pi Hk_r k}Ei\left(\frac{\phi\mu c_t r^2}{4kt}\right) \tag{3.4}$$

The resulting pressure derivatives are given by:

$$\frac{\partial p}{\partial t}=-\frac{\mu q}{4\pi tHk_r k}\exp\left(-\frac{\phi\mu c_t r^2}{4kk_r t}\right) \tag{3.5}$$

$$\frac{\partial p}{\partial r}=\frac{\mu q}{2\pi rHk_r k}\exp\left(-\frac{\phi\mu c_t r^2}{4kk_r t}\right) \tag{3.6}$$

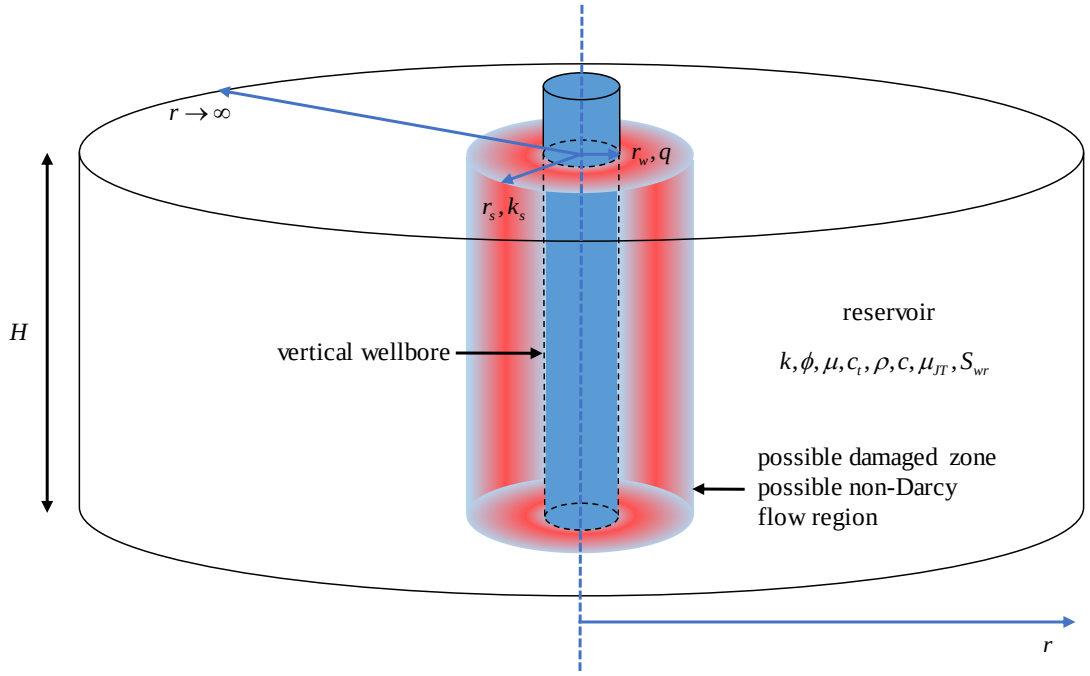

Figure 3. 1. Model description for single layer reservoir under transient flow.

As a result, the energy balance equation and corresponding initial and boundary conditions in dimensionless form are:

$$\frac{\partial T_D}{\partial t_D}=\frac{1}{r_D}\left[\frac{\partial T_D}{\partial r_D}-\frac{1}{r_D}\exp\left(-\frac{C_2 r_D^2}{4t_D}\right)\right]-\frac{C_1}{t_D}\exp\left(-\frac{C_2 r_D^2}{4t_D}\right) \tag{3.7}$$

$$T_D=0, r_D\geq 1, t_D=0 \tag{3.8}$$

$$T_D=0, r_D\to\infty, t_D>0 \tag{3.9}$$

where

$$r_D=\frac{r}{r_w} \tag{3.10}$$

$$t_D=\left\{\frac{\rho_f c_f}{\phi\left[\rho_w c_w S_{wr}+\rho_f c_f\left(1-S_{wr}\right)\right]+\left(1-\phi\right)\rho_s c_s}\right\}\frac{tq}{2\pi r_w^2 H} \tag{3.11}$$

$$T_D=\frac{2\pi Hk_r k\left(T-T_i\right)}{\mu_{JT}\mu q} \tag{3.12}$$

$$C_1=\frac{\phi\left(\rho_f c_f \mu_{JT}+1\right)}{2\mu_{JT}\left\{\phi\left[\rho_w c_w S_{wr}+\rho_f c_f\left(1-S_{wr}\right)\right]+\left(1-\phi\right)\rho_s c_s\right\}} \tag{3.13}$$

$$C_2=\left\{\frac{\rho_f c_f}{\phi\left[\rho_w c_w S_{wr}+\rho_f c_f\left(1-S_{wr}\right)\right]+\left(1-\phi\right)\rho_s c_s}\right\}\frac{q}{2\pi H}\frac{\phi\mu c_t}{kk_r} \tag{3.14}$$

Applying Laplace transform, implementing the integrating factor, and Laplace inversion gives (the details of the derivation is given in Appendix A):

$$T_D = -0.5\ln\left(1+\frac{2t_D}{r_D^2}\right)+C_1\ln\left(1+\frac{2t_D}{r_D^2}\right)+C_1 Ei\left(-\frac{C_2 r_D^2}{4t_D}\right) \quad (3.15)$$

The following can be implied from inspecting the above solution:

i. The derivation process indicates that the temperature signal due to the JT effect is presented by the first term of Equation 3.15 only. Therefore, the second and third terms on the RHS of Equation 3.15 represent the temperature changes corresponding to the AE effect.

ii. The first and second terms on the RHS of Equation 3.15 diminish for large radial distances. Thus, the temperature signal far from the wellbore is dominated by the third term (due to the AE effect). The third term is analogous to the pressure transient solution (Theis 1935), for which the radius of investigation can be determined by making the argument of the *Ei* function equal to unity (Lee 1982). Therefore, the radius of investigation (r_i) considering AE effect is $(4\eta t)^{0.5}$. In other words, the far-field temperature propagates with a diffusivity coefficient, $\eta=kk_r/(\phi\mu c_t)$, which is identical to the diffusivity coefficient for the pressure propagation. Without the AE effect, r_i is $(r_w^2+2C_2\eta t)^{0.5}$ (Ramazanov et al. 2010, Duru and Horne 2011b). Compared to the radius of investigation without the AE effect, the radius of investigation considering AE effect is much more far-reaching and identical to the radius of investigation for transient pressure response.

iii. The result of the temperature profile is affected by the dimensionless time and radius. From Equation 3.15, a similarity variable (r^2/t) is the only variable required to obtain the dimensionless temperature.

This analytical solution (Equation 3.15) is similar to the solutions in Ramazanov et al. (2010) and Palabiyik et al. (2016), with a different approach. The temperature responses modeled by Equation 16 would be identical to those in Ramazanov et al. (2010) for the JT effect, with a different form for AE effect due to the use of steady-state pressure profiles in Ramazanov et al. (2010). Applying Boltzmann transformation in Palabiyik et al. (2016) allows obtaining the solution in terms of *Ei* function only. The temperature modeling using Equation 3.15 and corresponding solution in Palabiyik et al. (2016) are very similar because the *Ei* function can be approximated by the logarithmic function shown in Equation 3.15.

3.1.2 Results

Here, we obtain the temperature profile from our derived analytical solutions and compare results to those from the numerical simulation. The temperature profiles will be presented for two cases. The first case is a gas reservoir presented by Oldenburg (2007), and the second case is an oil reservoir presented by App (2010). The results of the temperature profiles will be presented in the following sequence. The results of the temperature profiles from the analytical solutions are analyzed and compared with the results from numerical simulation in two cases. The numerical simulations are performed using a commercial reservoir simulation software (CMG-GEM 2015), where the procedure details were introduced in Zeidouni, Nicot, and Hovorka (2014a).

The temperature profiles calculated by the analytical solutions are benchmarked with the results from numerical simulation to validate the analytical solutions. The input reservoir properties are presented in Table 3.1. The thermo-physical properties at the initial reservoir conditions obtained from Linstrom and Mallard (2008) are presented in Table 3.2, and used only in analytical solutions. The gas reservoir drawdown is limited to below 10% of the initial reservoir pressure to ensure that the gas can be treated as a slightly compressible fluid.

With the provided reservoir properties and thermo-physical properties of oil and gas, the temperature profiles from the analytical solutions and numerical simulations are presented in Figures 3.2a and 3.2b for both cases. The gas reservoir is producing for up to one year, and the oil reservoir is producing for up to 50 days. In both cases, the simulation results for different production time periods provide very close agreement, which proves that the similarity variable is the only variant to determine the temperature profile in the undamaged reservoir. The basic analytical solution shows good agreement with the numerical simulation in both cases.

Table 3. 1. Selected reservoir properties for two reservoir cases.

	Gas Reservoir	Oil Reservoir
Reservoir pressure (MPa)	5	144.8
Porosity (-)	0.3	0.25
Downhole production rate (m^3/day)	1000	347
Reservoir thickness (m)	50	30.48
Permeability (mD)	10	20
Damaged zone permeability (mD)	5	10
Damaged zone radius (m)	1.27	1.32
Reservoir temperature (degC)	80	150
Residue water saturation (-)	0	0
Rock density (kg/m^3)	2600	2643
Rock specific heat (J/kg/K)	1000	1000
Production well radius (m)	0.0762	0.125
Relative permeability (-)	1	1

Table 3. 2. Thermo-physical properties at the initial reservoir conditions for two reservoir cases.

	Gas Reservoir	Oil Reservoir
Specific heat (J/kg/K)	2575	3830
Density (kg/m^3)	28	751.7
JT coefficient (K/MPa)	2.7	-0.28
Fluid viscosity (μPa·s)	13.6	2352

The modeled transient temperature signals in Figure 3.2 demonstrate the characteristics of JT and AE effects discussed in section 3.1.1. The AE effect induces minor temperature drop far from the production well, and the JT effect dominates the near wellbore region by raising or reducing the temperature depending on the JT coefficient of the producing fluid. The slopes

on the semi-log graph of the temperature profiles versus the similarity variables caused by AE and JT effects can be used to achieve interpretation techniques similar to those for PTA. From Equation 3.15, we can determine the slope of the near wellbore temperature profiles (m_1) is $1.152\mu_{JT}\mu q/(2\pi Hkk_r)$, and the slope of the far-field temperature profiles (m_2) is $2.303C_1\mu_{JT}\mu q/(2\pi Hkk_r)$, which is also enlarged in the subplot. The slope values calculated from these equations are compared with numerical temperature data from Figure 3.2which confirm the decent match (Table 3.3). The procedures to obtain reservoir properties from these slopes are provided in section 4.1.

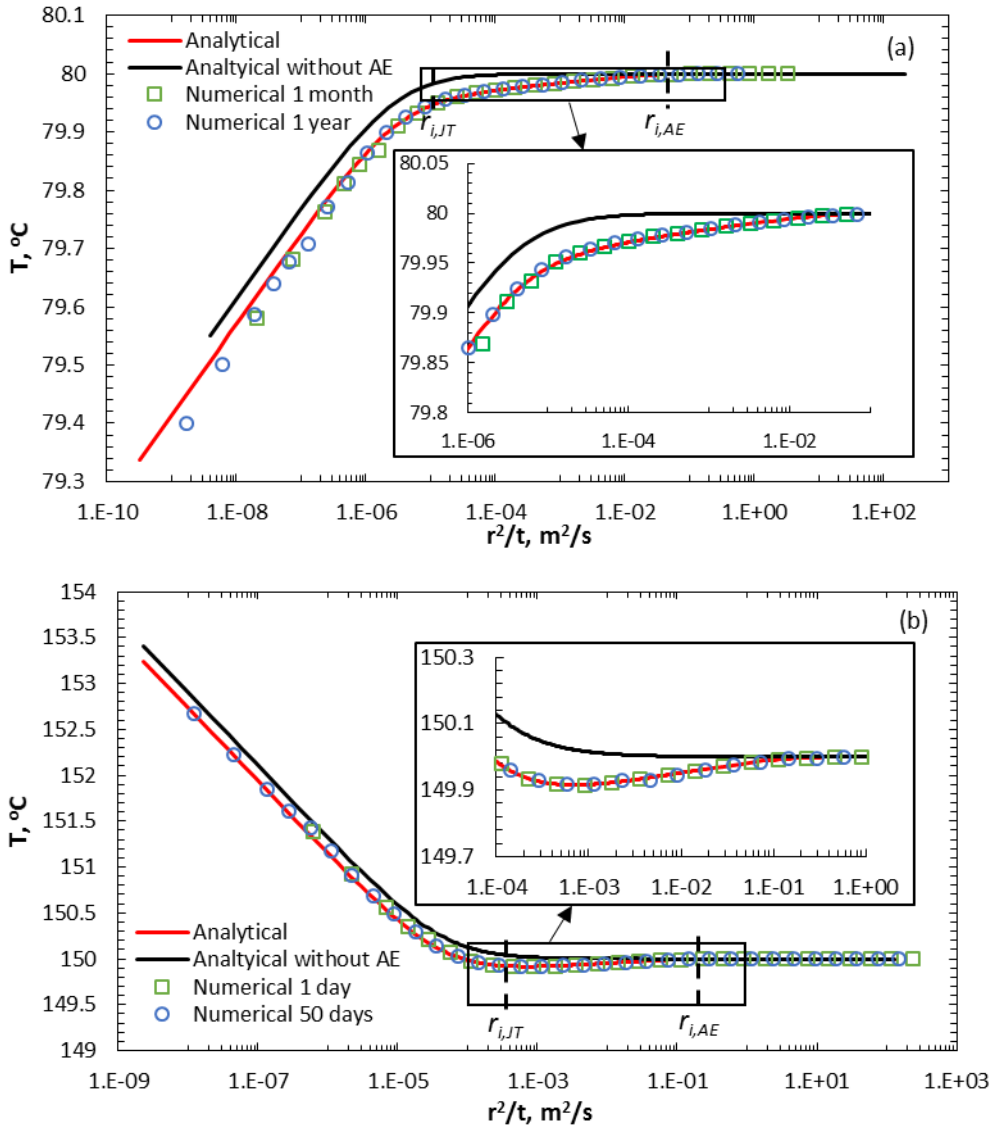

Figure 3. 2. Comparison of temperature profiles between the basic analytical solution and numerical simulation for (a) gas reservoir and (b) oil reservoir. The squares and circles indicate the results from numerical simulation and solid lines indicate the results from analytical solutions. The dashed lines indicate the radius of investigations for JT and AE effects. Sections of the temperature profiles dominated by AE effect are enlarged in the subplots.

In both cases, the temperature profiles neglecting the AE effect deviate from the numerical simulation results at short production time and/or far from the production well, and show higher temperature variations at the wellbore. Furthermore, the temperature drops caused by the AE effect can increase the radius of investigation of the temperature signal by almost 4

orders of magnitude, which is critical if a monitoring well exists far away from the production well. More importantly, the slope of AE effect on semi-log plot reveals another opportunity to obtain reservoir property, which can be also jointly analyzed with JT effect. The magnitudes of AE increase to more than 0.5 degC in the oil reservoir by higher production rates, which are high enough to be detected. In short, the AE effect in temperature transient is important and useful, which should not be neglected from monitoring temperature transient in the reservoirs.

Table 3. 3. Slope values from the equations in comparison to those for numerical simulation results for the undamaged reservoir.

	Equation	Numerical	Error (%)
Gas reservoir m_1	0.1558	0.1601	2.7
Gas reservoir m_2	0.01129	0.01105	2.2
Oil reservoir m_1	-0.7955	-0.7692	3.4
Oil reservoir m_2	0.05094	0.0479	6.3

3.1.3 Discussions

In discussing our analytical solutions and results, we focus on the significance of the assumptions that have been made for the derivation. The impact of heat loss to over-/under-burden formation, which is ignored in the derivations, is presented with the temperature modeling.

We consider the following assumptions in deriving our analytical solutions: constant production rate, infinite, insulated and confined formation, constant and uniform thermo-physical properties, single-phase flow, and ignoring thermal conduction in all the directions. The assumptions of constant production rate, confined formation, and constant and uniform thermo-physical properties have been presumed here to ensure that the reservoir and fluid properties are constants, as mentioned in section 3.1.1. The infinite formation assumption defines the boundary condition. The fluid flow is set to be single-phase flow to avoid the complexity of the multi-phase flow. Other immobile fluid phases can exist in the reservoir, e.g., connate water. The thermal conduction in the flow direction can be ignored (LaForce, Ennis-King, and Paterson 2014). The convective heat transfer for the high production rates in a high permeability reservoir is much more significant than heat conduction in the flow direction. The heat conduction in the non-flow direction is mainly represented by the heat loss to over-/under-burden formations, which is discussed in the following.

Due to the assumption of slightly compressible fluid in deriving our analytical solutions, the drawdown in the gas reservoir is limited to 10% of the initial reservoir pressure. The production rates are restricted to minimize the fluid property variation induced by the pressure drawdown towards the production well since higher production rates result in higher pressure and temperature perturbations. For the cases presented in this study, analytical solutions are within high accuracies in the conditions of 10% drawdown for the gas reservoir and 30% drawdown for the oil reservoir from the initial reservoir pressure at the production well. We have identified the effect of fluid property variations and addressed it by introducing corrections of fluid properties to this analytical solution in section 5.1. The advantage of higher production rates to temperature monitoring is that the time required obtaining analyzable temperature variations are much shortened from months to hours. In other words, higher rates make it possible to perform TTA in a timely manner.

Heat loss to surroundings can have significant impacts on the temperature response for long-term production/injection from/into the reservoir (LaForce, Ennis-King, and Paterson 2014). The assumption of ignoring the heat conduction in the non-flow direction, which is mainly represented by the heat loss to surroundings, has been made to obtain the analytical solutions. This assumption is made in this study for the relatively high permeability reservoir cases investigated, where the convection dominates over conduction (App and Yoshioka 2013). Numerical studies have been performed on both cases with the heat loss to surroundings to justify this assumption. The mathematical description of the heat loss model is given by Vinsome and Westerveld (1980). The density and heat capacity of the over- and under-burden are set to be the same as the reservoir rock, and the conductivity of the surroundings are set to be 4.31 *W/(m K)* (LaForce, Ennis-King, and Paterson 2014). We have increased the production rates to 986 m^3/day for oil reservoir to observe higher temperature signals, which will induce stronger cooling effect by the thermal conduction.

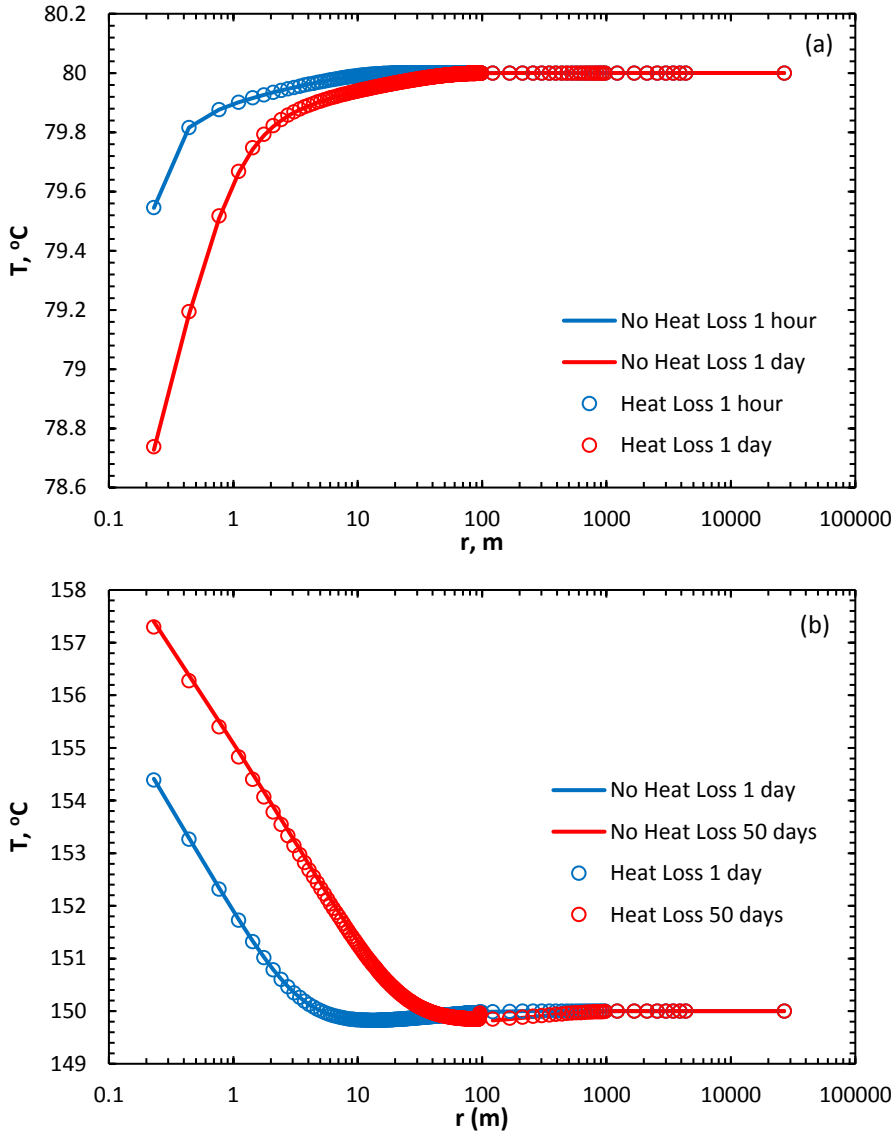

Figure 3. 3. Temperature profiles considering and neglecting the heat loss to surroundings for (a) gas and (b) oil reservoirs with higher production rates.

Figure 3.3 illustrates the comparison of temperature profiles by considering and neglecting heat loss to surroundings for both cases, which are obtained by numerical simulation.

The temperature results considering and neglecting the heat loss to surroundings are almost identical. The increasing temperatures on the bottom-hole location due to the heat loss to surroundings are less than 0.03% after production for one day. Therefore, the effect of heat loss to surroundings on temperature profiles may be safely neglected if TTA is performed in short periods, e.g. days.

3.2 Single Layer Near Wellbore Damaged Reservoir under Transient Flow

In the base of the analytical solution developed in Section 3.1, the near-wellbore damage effect is considered. The governing equation (Equation 3.1) remains the same and the model description includes a near-wellbore damaged zone indicated by the red region in Figure 3.1.

3.2.1 Analytical Solution Derivation

In this section, we derive the temperature transient analytical solution in presence of a near-wellbore damaged zone. Outside of the damaged zone, the temperature profile can be represented by Equation 3.15. Inside the damaged zone, the boundary conditions are different from the case without the damaged zone. To honor temperature continuity, the temperature at the edge of the damaged zone is:

$$T = T_s, r = r_s, t > 0 \tag{3.16}$$

The temperature at the outside boundary of the damaged zone can be calculated by Equation 3.15:

$$T_{sD} = -0.5\ln\left(1+\frac{2t_D}{r_{sD}^2}\right) + C_1\ln\left(1+\frac{2t_D}{r_{sD}^2}\right) + C_1 Ei\left(-\frac{C_2 r_{sD}^2}{4t_D}\right) = \frac{2\pi H k_r k\left(T_s - T_i\right)}{\mu_{JT}\mu q} \tag{3.17}$$

where

$$r_{sD} = \frac{r_s}{r_w} \tag{3.18}$$

To derive an analytical solution from Equation 3.1 with the damaged zone, pressure derivatives with respect to time and space should be evaluated and replaced in Equation 3.1. The transient pressure response for the slightly compressible fluid subject to constant rate production is used to evaluate the pressure derivatives outside of the damaged zone. In the near-wellbore region, the accumulation term in the diffusivity equation vanishes soon after the start of production. Therefore, the steady-state pressure response is sufficient to represent the pressure response in the damaged zone.

$$p_s - p_i = \frac{\mu q}{4\pi H k_r k} Ei\left(\frac{\phi\mu c_t r_s^2}{4kt}\right) \tag{3.19}$$

$$p(r) - p_s = \frac{\mu q}{2\pi H k_r k_s}\ln\left(\frac{r}{r_s}\right) \quad \text{for } r<r_s \tag{3.20}$$

The resulting pressure derivatives are given by:

$$\frac{\partial p}{\partial t} = -\frac{\mu q}{4\pi t H k_r k}\exp\left(-\frac{\phi\mu c_t r_s^2}{4kk_r t}\right) \tag{3.21}$$

$$\frac{\partial p}{\partial r} = \frac{\mu q}{2\pi r H k_r k_s} \tag{3.22}$$

As a result, the energy balance equation and corresponding initial and boundary conditions in the dimensionless form in the damaged region are:

$$\frac{\partial T_D}{\partial t_D}=\frac{1}{r_D}\left[\frac{\partial T_D}{\partial r_D}-\frac{k_{sD}}{r_D}\right]-\frac{C_1}{t_D}\exp\left(-\frac{C_4}{4t_D}\right) \tag{3.23}$$

$$T_D=0, r_D\geq 1, t_D=0 \tag{3.24}$$

$$T_D=T_{sD}, r_D=r_{sD}, t_D>0 \tag{3.25}$$

where

$$C_4=\left\{\frac{\rho_f c_f}{\phi\left[\rho_w c_w S_{wr}+\rho_f c_f\left(1-S_{wr}\right)\right]+\left(1-\phi\right)\rho_s c_s}\right\}\frac{qr_{sD}^2}{2\pi H}\frac{\phi\mu c_t}{kk_r} \tag{3.26}$$

$$k_{sD}=\frac{k}{k_s} \tag{3.27}$$

Applying Laplace transform, implementing the integrating factor, and Laplace inversion gives (the details of the derivation are presented in Appendix B):

$$\begin{aligned}T_D=&-\frac{k_{sD}}{2}\ln\left(1+\frac{2t_D}{r_D^2}\right)+C_1 Ei\left(-\frac{C_4}{4t_D}\right)\\&+\left\{T_{sD}\left(t_D+\frac{r_D^2-r_{sD}^2}{2}\right)+\frac{k_{sD}}{2}\ln\left(\frac{r_D^2+2t_D}{r_{sD}^2}\right)-C_1 Ei\left[\frac{-C_4}{4t_D+2\left(r_D^2-r_{sD}^2\right)}\right]\right\}U'\left(t_D+\frac{r_D^2-r_{sD}^2}{2}\right)\end{aligned} \tag{3.28}$$

By investigating the above solution for the damaged zone, the following can be implied:

i. Based on the derivation process, the temperature signal associated with the JT effect is given by the first term of Equation 3.28. The second term on the RHS of Equation 3.28 represents the temperature changes corresponding to the AE effect. Therefore, the third term on the RHS of Equation 3.28 indicates the temperature continuity at the edge of the damaged zone. It is worthy of notice that the expression of the terms representing the JT and AE effects are different from Equation 3.15. The pressure gradient on distance in the damaged zone is independent of time, and the pressure gradient on time in the damaged zone is independent of distance. These independences remove the additional terms from the JT and AE effects.

ii. Indicated by the Heaviside's unit function in the third term of the solution, the skin effect only appears in the damaged zone and changes the rate of temperature variations towards the production well compared to outside of the damaged zone. Moreover, the time for the temperature propagation front to traverse the damaged zone is also represented by the Heaviside's unit function. The speed to traverse the damaged zone is identical to the speed of JT radius of investigation. Therefore, the temperature profile in the damaged zone is dominated by the slow-moving JT effect, although the AE effect propagates much faster than the JT effect.

iii. For the pressure transient equation, the radius and permeability of the damage zone affect the pressure by a single group referred to as the skin factor. As a result, the pressure cannot be inverted to calculate the radius and permeability of the damaged zone separately. For the temperature transient, however, the radius and permeability of the damaged zone affect the temperature separately. Therefore, from the temperature transient signal, it is possible to characterize the damaged zone more accurately by evaluating its radius and permeability separately.

3.2.2 Results

The analytical solution with the damaged zone is not a function of the similarity variable. Therefore, the temperature profiles with the damaged zone are presented versus reservoir radius in Figures 3.4 and versus production time in the next section. The analytical solutions with damaged zone provide good agreement with the numerical simulation to model the temperature signals. The different rates of the temperature variations (slopes) on two sides of the damaged zone are clearly visible on both analytical solutions and numerical simulations, which helps to identify the radius of the damaged zone. From Equations 3.15 and 3.28, the values of three slopes on far-field temperature profiles which are enlarged in the subplots (m_3), the temperature profiles outside (m_4) and inside the damaged zone (m_5) are $4.606C_1\mu_{JT}\mu q/(2\pi Hkk_r)$, $2.303\mu_{JT}\mu q/(2\pi Hkk_r)$, and $2.303\mu_{JT}\mu q/(2\pi Hk_sk_r)$, respectively. The similar comparisons with numerical simulations are illustrated in Table 3.4, which also indicate acceptable agreement. The procedures to obtain damaged zone properties from radial temperature distributions are introduced in section 4.2.

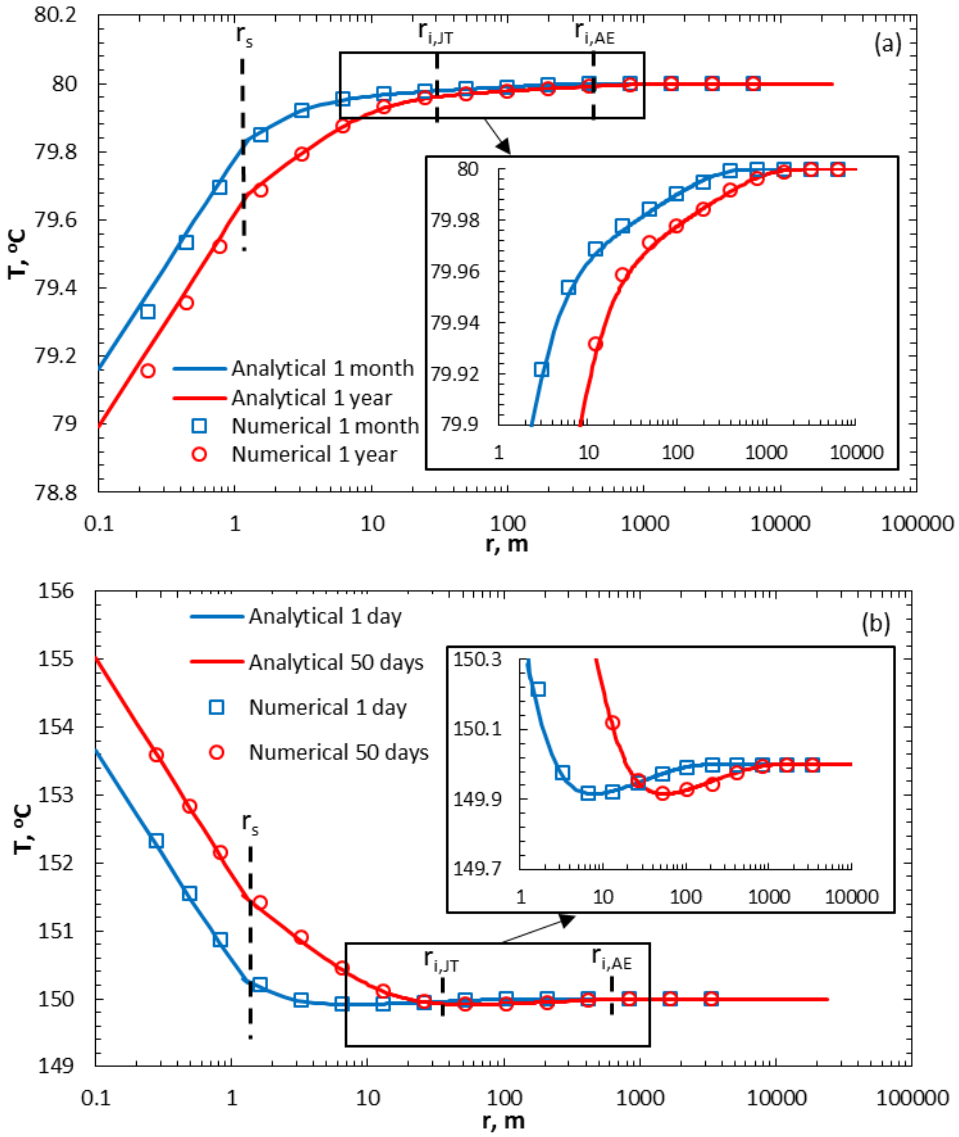

Figure 3. 4. Comparison of temperature profiles between the analytical solution and numerical simulation for damaged (a) gas and (b) oil reservoirs. Left dashed line indicates the radius of the damaged zone.

The most common temperature data are often measured at the production well in practice since the radial measurements of the temperature are rarely available. We analyze the sandface temperature profiles modeled analytically considering the presence and absence of a damaged zone in Figure 3.5, and provide the insights of sandface temperature profile with the damaged zone. Compared with the undamaged cases, the temperature variations considering the presence of a damaged zone are more significant in the near wellbore region. The varying slopes on the temperature profiles after one day of production are due to the Heaviside's unit function in the analytical solution, which indicate the time for the temperature front to traverse the damaged zone (t_s). The damaged zone radius can be determined from the traverse time by the radius of investigation for JT effect, which gives $r_s=(r_w^2+2C_2\eta t_s)^{0.5}$. From Equations 3.15 and 3.28, the two slope values in Figure 3.5 before (m_6) and after (m_7) the traverse time are $-1.152\mu_{JT}\mu q/(2\pi Hk_sk_r)$, and $-1.152\mu_{JT}\mu q/(2\pi Hkk_r)$, respectively. The procedures to obtain damaged zone properties from sandface temperature distributions are introduced in the procedure.

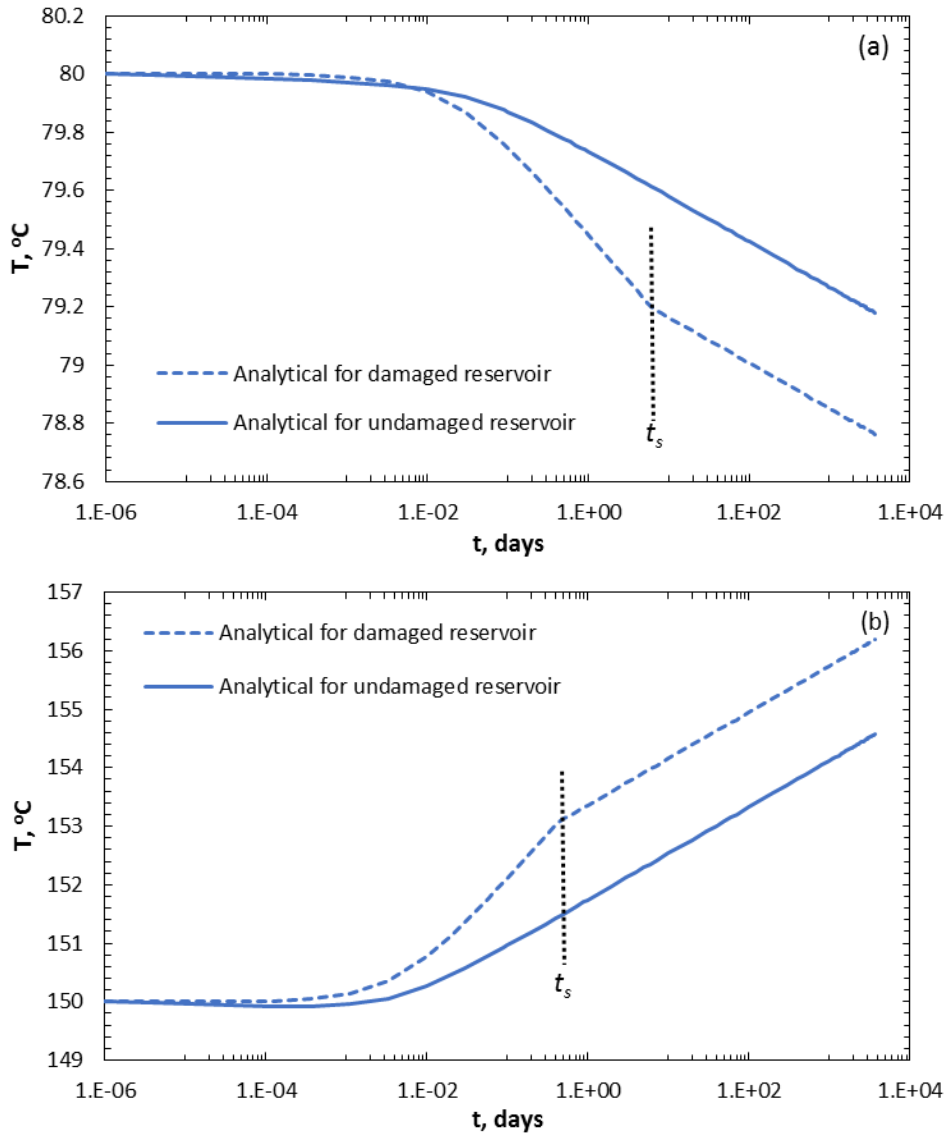

Figure 3. 5. Sandface temperature profiles considering presence and absence of damaged zone for (a) gas reservoir and (b) oil reservoir.

It is worthy of notice that the traverse times for both cases are less than ten days of production, which is not too long for observing temperature signals dominated by the reservoir properties. On the other hand, since the radius of investigation for JT effect travels much slower than that for pressure transient, the damaged zone temperature signals will not be masked by the wellbore storage or other early time effects. Therefore, these distinguishing features of temperature signals make itself perfect candidate to characterize the near wellbore damage.

Table 3. 4. Slope values from the equations in comparison to those for numerical simulation results for the damaged reservoir.

	Equation	Numerical	Error (%)
Gas reservoir m_3	0.02258	0.02027	11.4
Gas reservoir m_4	0.3116	0.2953	5.5
Gas reservoir m_5	0.6231	0.6646	6.7
Oil reservoir m_3	0.1019	0.09212	10.6
Oil reservoir m_4	-1.59	-1.495	6.4
Oil reservoir m_5	-3.18	-3.104	2.4

3.3 Single Layer Reservoir with near Wellbore Non-Darcy Effect under Transient Flow

In this section, we derive an analytical solution to account for the effect of non-Darcy flow in TTA. As detailed in the introduction, current analytical solutions for TTA assumes Darcy flow in the reservoir of slightly compressible fluid (e.g. oil). Despite the non-Darcy flow effect investigated in this section, other near-wellbore effects such as possible damaged zone are considered as a region with different permeability compared to the reservoir permeability. A model schematic is illustrated in Figure 3.1.

3.3.1 Analytical Solution Derivation

Based on this model, we derive the analytical solution for TTA considering the effect of non-Darcy flow effect. The governing equation (Equation 3.1) and boundary conditions (Equations 3.2 and 3.3) for this analytical solution are identical to the existing solutions for TTA. To derive an analytical solution from Equation 3.1, pressure profiles are required in addition to transient temperature boundary conditions. Considering the non-Darcy flow effect, we apply the Forchheimer equation (Forchheimer 1901) to evaluate the pressure derivative with respect to space:

$$\frac{\partial p}{\partial r} = \frac{\mu q}{2\pi r H k_r k} + \beta_{ND}\rho_f \left(\frac{q}{2\pi r H}\right)^2 \tag{3.29}$$

The pressure derivative with respect to time is obtained from transient pressure solution for slightly compressible fluid considering constant rate production (Theis 1935):

$$p(r,t) - p_i = \frac{\mu q}{4\pi H k_r k} Ei\left(-\frac{\phi \mu c_t r^2}{4kt}\right) \tag{3.30}$$

$$\frac{\partial p}{\partial t} = -\frac{\mu q}{4\pi t H k_r k} \exp\left(-\frac{\phi \mu c_t r^2}{4 k k_r t}\right) \tag{3.31}$$

This derivative is appropriate for both Darcy-flow and non-Darcy flow due to the identical time-dependent terms in both transient pressure solutions (Yildiz 1991). As a result, the energy balance equation (Equation 3.1) and the initial and boundary conditions (Equations 3.2 and 3.3) in the dimensionless form are:

$$\frac{\partial T_D}{\partial t_D} = \frac{1}{r_D}\left[\frac{\partial T_D}{\partial r_D} - \frac{1}{r_D} - \frac{Fo}{r_D^2}\right] - \frac{C_1}{t_D}\exp\left(-\frac{C_2 r_D^2}{4 t_D}\right) \tag{3.32}$$

$$T_D = 0, r_D \geq 1, t_D = 0 \tag{3.33}$$

$$T_D = 0, r_D \to \infty, t_D > 0 \tag{3.34}$$

where:

$$Fo = \frac{q \beta_{ND} \rho_f k_r k}{2\pi H \mu r_w} \tag{3.35}$$

The solution for the above partial differential equation (PDE) is obtained by turning the PDE into ordinary differential equation (ODE) using Laplace transform and then solving the ODE using integrating factor, presented in the Appendix. Laplace inversion of the resulting Laplace-domain solution gives (see details in Appendix C):

$$T_D = -0.5\ln\left(1+\frac{2t_D}{r_D^2}\right) + C_1 \ln\left(1+\frac{2t_D}{r_D^2}\right) + C_1 Ei\left(-\frac{C_2 r_D^2}{4 t_D}\right) - Fo\left(\frac{1}{r_D} - \frac{1}{\sqrt{2t_D + r_D^2}}\right) \tag{3.36}$$

Exploring the above solution implies the following:

1. Equation 3.36 indicates the physical causes of transient temperature signals: JT effect, AE effect, and non-Darcy flow effect. The first two effects are extensively discussed in section 3.1, which are represented by the first three terms in Equation 3.36. Therefore, the last term of Equation 3.36 denotes the temperature changes corresponding to the non-Darcy flow effect.
2. The value of the last term in Equation 3.36 infers the effect of non-Darcy flow on transient temperature signals. For the perspective of a given time step, the absolute value of the last term increases with reduced radius and diminishes further into the reservoir. This indicates that the non-Darcy flow impacts the temperature signals only at the near wellbore region, similar to its effect on the pressure signals.
3. Temperature monitoring from production well is mostly applicable sources for TTA. In this case, the value of the last term approaches a constant value of the Forchheimer number (*Fo*) at the late time of production. As a result, the non-Darcy flow effect adds a fixed magnitude of the temperature data in the late time, which does not affect its changing rate (slope in a temporal semi-log plot). The additional heating effect on temperature signals associated with the non-Darcy flow effect is directly proportional to *Fo*. As suggested by Zeng and Grigg (2006), the critical *Fo* for 10% non-Darcy flow effect is 0.11. We will further investigate this criterion for TTA as well as the previous findings in the next section.

We have established a method to account for fluid property variations in existing analytical solutions for TTA in chapter 5. Considering the non-Darcy flow effect, the sandface temperature signals are exaggerated and require the corrections on fluid property variations. For the drawdown test investigated in this section, the fluid property corrections are represented by Equations 5.3 and 5.9. An iterative process to account for fluid property corrections with Equations 5.3 and 5.9 is also provided in chapter 5.

3.3.2 Temperature Modeling and Verification

In this section, we apply the analytical solution considering the non-Darcy flow effect developed in section 3.3.1 as well as the fluid property correction method introduced in chapter 5 to model the transient temperature signals in non-damaged and damaged reservoirs. To verify this analytical solution and the effect of non-Darcy flow in TTA, these analytically modeled results will be compared with those from numerical simulation (CMG-GEM 2015). The verifications are conducted in the same oil reservoir presented by App (2010), the properties of which are illustrated in Table 3.1. The TTA drawdown test procedures include oil productions from a vertical well with the downhole production rate of 986 m^3/day for 5 days. For the non-Darcy flow effect, we use a non-Darcy flow coefficient (β_{ND}) of 10^{12} 1/m reported in Su (2004). The thermophysical properties of the reservoir fluid are estimated by the flash calculations from CMG-WINPROP (2015). We present the fluid properties in three conditions (Table 3.5): the initial reservoir condition, sandface conditions at the end of production period for Darcy flow only ($t_{p,D}$) and considering non-Darcy flow ($t_{p,nD}$).

Table 3. 5. Fluid properties at various pressure and temperature conditions.

	Reservoir initial conditions at t_0	End of production sandface conditions for Darcy flow at $t_{p,D}$	End of production sandface conditions for non-Darcy flow at $t_{p,nD}$	Max variation (%)
Specific heat (J/kg/K)	2202	2340	2433	5.4
Density (kg/m^3)	840	777.5	724.5	13.8
JT coefficient (K/MPa)	-0.445	-0.448	-0.458	2.9
Fluid viscosity (mPa·s)	3.686	1.93	1.633	55.7

The fluid property variations in different conditions are more severe considering the non-Darcy flow effect. Figure 3.6 presents the temperature modeling verification analytically and numerically considering the non-Darcy flow effect. Two sets of temperature modeling are illustrated in this figure: four curves with higher temperature representing the cases considering the non-Darcy flow effect, and the other four curves for Darcy flow only. For both scenarios, the analytical solutions with the corrected fluid properties present good agreements with numerical simulation. If the temperature signals are modeled analytically with the fluid properties in t_0 and t_p conditions, the resulting temperature modeling error at the end of production is higher considering the non-Darcy flow effect (12 compared to 9 degC for Darcy flow only). Along with the fluid property variation values presented in Table 1, the non-Darcy flow effect exaggerates the fluid property variations as well as the temperature modeling errors, which needs to be treated with fluid property correction method. As a result, implementing the fluid property correction method is essential to precisely model the transient temperature behaviors. As suggested in chapter 5, the viscosity is the dominating property on TTA among others. This observation is also tenable with the existence of non-Darcy flow effect, presented in Table 3.5. Therefore, the fluid property correction method can be simplified by applying the correction only on viscosity.

Considering the non-Darcy flow effect significantly increases the sandface temperature signals during production (more than 12 degC after 5 days). This temperature increments are starting at the end of AE effect, going through a transition period with gradually increased

heating, and reaching a relatively constant value at the late time (about 2 hours for this case), which has been predicted in section 3.3.1. The late time slopes in the semi-log plot of Figure 3.6 are identical between the scenarios considering Darcy flow only and non-Darcy flow effect. This finding indicates that the reservoir permeability can be determined from the slope values with the same inversion procedures whether the test is affected by the non-Darcy flow effect or not.

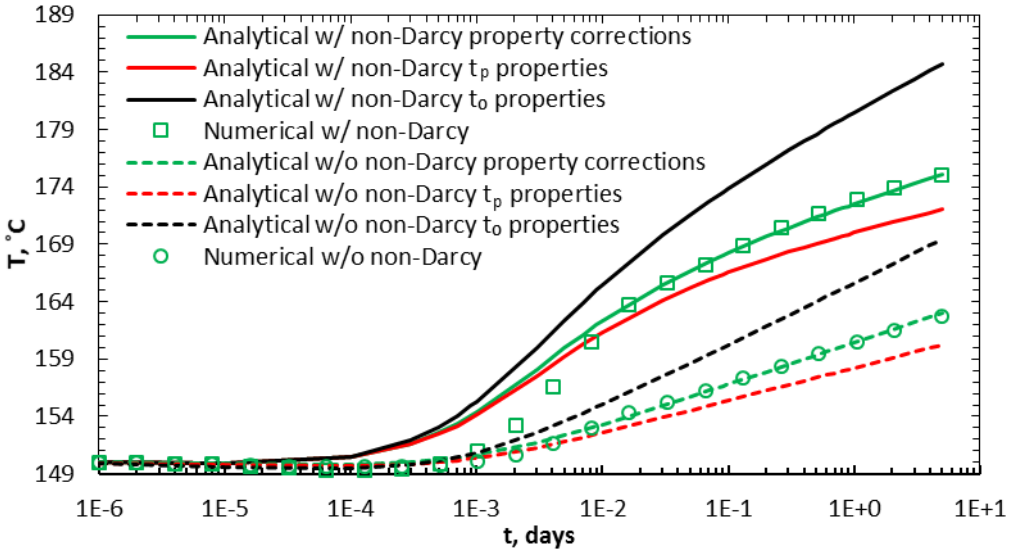

Figure 3. 6. Temperature profiles verifying the analytical solution considering the non-Darcy flow effect against numerical simulation.

We can derive the slope of the late time straight line in the semi-log plot from the analytical solution and relate it to estimate reservoir properties. From the analytical solution, this slope in dimensionless form is:

$$\frac{dT_D}{d\left(\ln t_D\right)} = -0.5 - \frac{t_D Fo}{\left(2t_D + 1\right)^{1.5}} \tag{3.37}$$

Technically, the late time sandface temperature behavior in the semi-log plot is not a straight line. It is approaching a straight line in late time as the last term in Equation 3.37 diminishes and the additional temperature changes due to non-Darcy flow effect are getting close to a constant value. However, the dimensionless time and the Forchheimer number are functions of reservoir and fluid properties. To obtain accurate reservoir properties, we develop the inversion process to estimate the Forchheimer number, and then the reservoir permeability. Basically, starting with the last production time will reduce the complexity since the last term in Equation 3.37 is minimized. In the case presented in Figure 3.6, at the last production time (5 days), the slope in dimensionless form is -0.526 with a Forchheimer number of 4.66. Compare to the case without the non-Darcy flow effect, the error is only 5%, which can be neglected for practical purpose.

With the success of modeling the temperature signals in the non-damaged reservoir, we include the near wellbore damage into the modeling process. As another type of near wellbore effect in TTA, the temperature profiles in a damaged reservoir can be modeled by the analytical solution derived in section 3.2. We have elaborated the impact of the non-Darcy flow effect on temperature modeling (the last term in Equation 3.36) in section 3.3.1, which is independent of JT effect, AE effect as well as the damaged zone effect. Therefore, we can implement this term to the solution presented in section 3.2 to model the temperature profiles in a damaged reservoir. The temperature modeling is conducted on two damaged reservoirs with the same

reservoir properties presented in section 3.2. The damaged zones for these reservoirs have the same permeability of 10 md (half of the reservoir permeability) and radiuses of 0.89 and 2.25 m.

We present the temperature modeling analytically and numerically considering the non-Darcy flow effect in the damaged reservoir in Figure 3.7. The analytical solution derived in section 3.2 and additional term from Equation 3.36 can correctly model the temperature profiles in damaged reservoirs as the analytical and numerical results in Figure 3.7 show acceptable agreements. The reduced permeability in the damaged zone reinforces the JT heating effect in addition to those from non-Darcy flow effect. This raises a challenge to differentiate these two near-wellbore effects. To address this issue, Equation 3.37 is critical for estimation of the reservoir and damaged zone properties, especially for the damaged zone dominated early time temperature profiles. However, if the radius of the damaged zone is too small, the variation in the slope due to the changing permeability between damaged zone and reservoir may be masked by the non-Darcy flow effect (red line in Figure 3.7). In the case of observable slope changes (blue line in Figure 3.7), the time for the changes are represented by the traverse time (Equation 3.38):

$$t_c = \frac{\pi H \left\{\phi\left[\rho_w c_w S_{wr} + \rho_f c_f \left(1 - S_{wr}\right)\right] + \left(1-\phi\right)\rho_s c_s\right\}\left(r_s^2 - r_w^2\right)}{\rho_f c_f q} \tag{3.38}$$

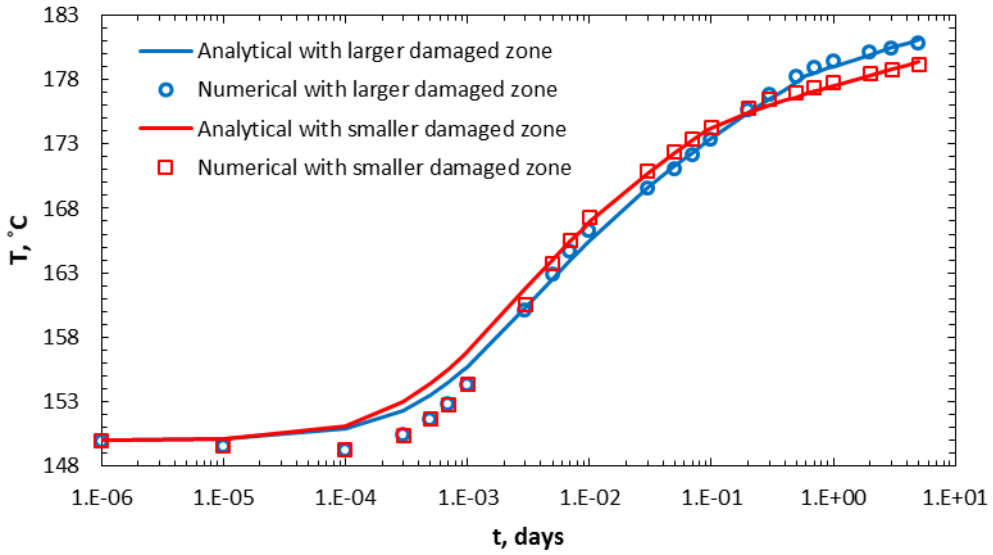

Figure 3. 7. Sandface temperature profiles benchmarking from analytical solution considering non-Darcy flow effect with numerical simulation in the damaged reservoir.

In Figure 3.7, the slopes for the damaged zone are almost identical for both cases since the permeability is the same, so does for the reservoir. The case with larger damaged zone has a longer traverse time compare to that with a smaller damaged zone (0.6 to 0.1 days). The small deviations on the damaged zone temperature modeling between cases are due to the different fluid property variations for these two cases. Better temperature modeling can be achieved by applying the two-time-period fluid property correction method introduced in chapter 5.

It should be noted that to apply this analytical solution for damaged zone modeling, the non-Darcy flow coefficients are assumed to be identical for damaged zone and reservoir. If the coefficients are not identical, there will be another transition period to accommodate this difference after t_c. We understand that this assumption may not be valid for all the cases. As a result, we develop different procedures to evaluate the non-Darcy flow coefficient for the damaged zone and reservoir, which is presented in chapter 4.

3.3.3 Sensitivity Analysis for Non-Darcy Flow Effect

In this section, we conduct sensitivity analyses on various reservoir and production parameters to examine their impacts on the temperature signals considering the non-Darcy flow effect. As suggested by the findings in section 3.1, *Fo* is the critical parameter to determine the magnitude of temperature signals by non-Darcy flow effect as well as the criteria to trigger this effect in TTA. We select two major uncertainties in *Fo* to perform the analyses: production rate and non-Darcy flow coefficient. Based on the results, the criteria for detectable non-Darcy flow effect in TTA is determined.

Figures 3.8 and 3.9 present the sensitivity analyses of temperature modeling considering non-Darcy flow effect under various conditions of production rate and non-Darcy flow coefficient. The reservoir and production parameters are adopted from the case illustrated in section 3.3.2, with the specific parameters variations indicated by the legend of each figure. The ranges of production rate and non-Darcy flow coefficient in these analyses are based on previous studies (App 2010, Su 2004). For all the cases presented in Figures 3.8 and 3.9, the analytically modeled temperature profiles are verified against those from numerical simulations. As expected in section 3.3.1, lower production rate and non-Darcy flow coefficient result in smaller *Fo* as well as weaker non-Darcy flow effect. Compare the temperature profiles in Figures 3.8 and 3.9, the late time slopes in these semi-log plots are related to the production rates, but not with the non-Darcy flow coefficient. This finding proves that the late time slope value for TTA is irrelevant to the non-Darcy flow effect from another perspective.

One goal of these sensitivity analyses is to determine the criteria to detect the non-Darcy flow effect from TTA. We have mentioned the critical *Fo* of 0.11 considering 10% non-Darcy flow effect in section 2.4. As per the discussion for the derived analytical solution, the maximum dimensionless temperature changes due to the non-Darcy flow effect are determined by the value of *Fo*. Therefore, to detect the non-Darcy flow effect from TTA, the additional dimensionless temperature changes due to the non-Darcy flow effect should exceed the critical *Fo* of 0.11:

$$T_{D,nD} = \frac{2\pi H k_r k \Delta T_{nD}}{\mu_{JT} \mu q} \geq Fo_{cri} = 0.11 \tag{3.39}$$

where ΔT_{nD} indicates the additional temperature changes due to the non-Darcy flow effect. Many parameters, which include permeability, thickness, fluid JT coefficient and viscosity depending on the nature of the reservoir, and production constraint of production rates, affect this criterion. The last parameter in Equation 3.39, the temperature changes due to the non-Darcy flow effect, is measured by the downhole temperature monitoring system. Therefore, another criterion is required to ensure the accuracy of the system is capable to detect the small temperature changes. Considering Equations 3.35 and 3.39, this criterion is:

$$\Delta T_{nD} = \left(\frac{2\pi H}{q} \right)^2 \frac{\beta_{ND} \rho_f \mu_{JT}}{r_w} \geq T_{accu} \tag{3.40}$$

where T_{accu} indicates the accuracy of the downhole temperature monitoring system. If both criteria (Equations 3.39 and 3.40) are fulfilled, TTA can be used to detect the non-Darcy flow effect.

We compare the temperature profiles presented in Figures 3.8 and 3.9 with those considering Darcy flow only presented in Figure 3.7 and in chapter 5. For all cases presented in Figures 3.8 and 3.9, the minimum *Fo* is 0.47 and the additional temperature changes due to the non-Darcy flow effect are higher than 1 degC, which is much higher than the accuracy of the current downhole temperature monitoring system. As a result, TTA can detect and evaluate a wide range of non-Darcy flow effect, which is a field-scale asset compared to the traditional method of laboratory experiments. With the progress on the precisions of the downhole

monitoring system (currently 0.1 degC), this criterion can be improved to detect weaker and wider range of non-Darcy flow effect.

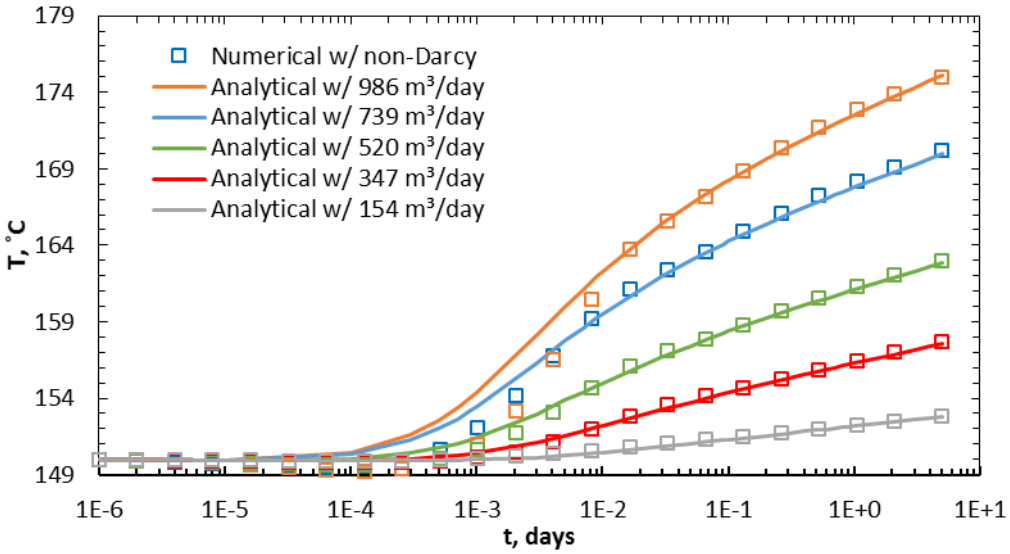

Figure 3. 8. Sensitivity analysis of temperature modeling considering non-Darcy flow effect under various production rates.

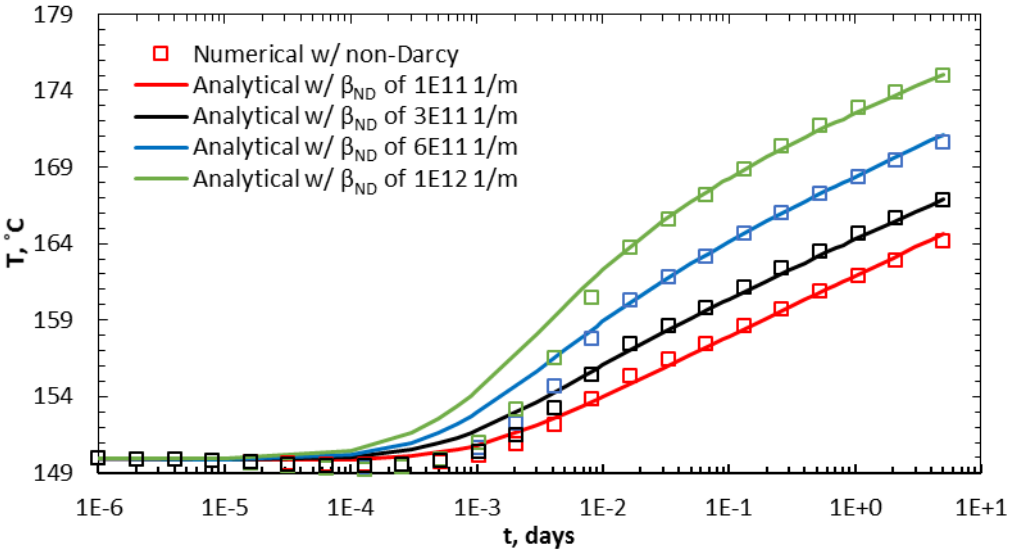

Figure 3. 9. Sensitivity analysis of temperature modeling considering non-Darcy flow effect under various non-Darcy flow coefficient.

3.4 Single Layer Reservoir under Boundary Dominated Flow

Among different flow regimes encountered during the production of a vertical well, the long-lasting BDF is crucial since most of the hydrocarbons of conventional reservoirs are recovered during this period. The production induced temperature response behaves transient for boundary dominated pressure response and can be analyzed for reservoir property estimation. In this section, we derive a novel temperature transient analytical solution to model sandface temperature signal under BDF.

3.4.1 Problem Description and Analytical Solution

In this section, we derive an analytical solution to model the transient temperature signal under radial boundary dominated pressure response. The physical model for this solution contains a fully penetrating production well in a single layer and closed boundary reservoir, where the flow regime is radial before BDF prevails. Also, an observation well is located away from the production well. The reservoir shape is not limited to cylindrical. Temperature modeling results from cubic reservoirs with various ratio of length to width are presented in section 3.4.2. A model schematic is illustrated in Figure 3.10.

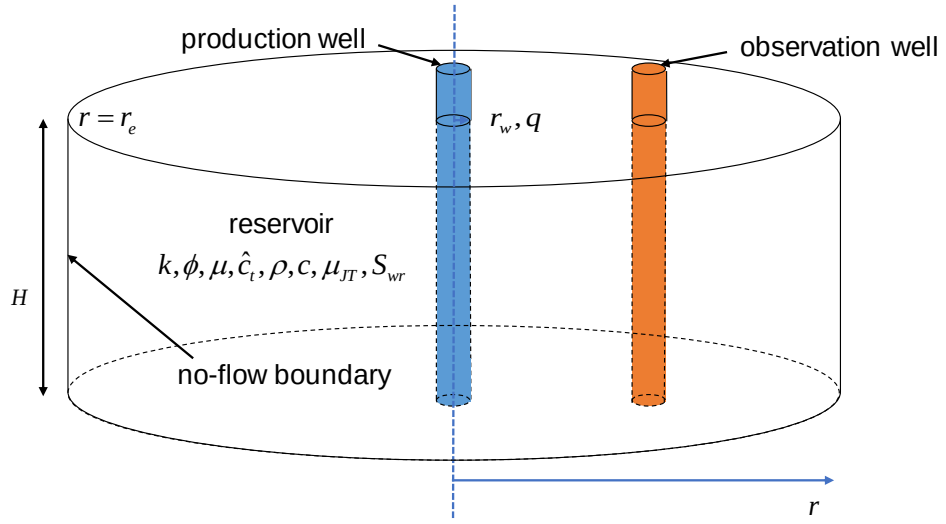

Figure 3. 10. Model description for single layer reservoir under boundary dominated flow.

The governing equation (Equation 3.1) and initial condition (Equation 3.2) to derive this analytical solution are similar to the existing analytical solutions for TTA. The outer boundary condition for TTA under BDF is:

$$\frac{\partial T}{\partial t} \doteq T_i + \frac{\phi\left(\rho_f c_f \mu_{JT} + 1\right)}{\phi\left[\rho_w c_w S_{wr} + \rho_f c_f \left(1 - S_{wr}\right)\right] + \left(1-\phi\right)\rho_s c_s} \frac{\partial p}{\partial t}, r = r_e, t > 0 \tag{3.41}$$

The initial condition is widely used in deriving TTA analytical solution, but may not represent the real conditions for radial BDF. When the BDF is established after the pressure transient period, the radial temperature profile at the beginning of BDF is not uniform at the initial reservoir temperature, especially at the near wellbore region. However, the temperature change from the initial reservoir temperature is negligible over most of the reservoir area. Therefore, for practical purposes, we can assume uniform temperature throughout the reservoir at the beginning of BDF. Equation 3.41 is the expanded version of a simple dimensionless equation. The physical implication of Equation 3.41 is that the temperature behavior at the outer no-flow boundary is dominated by the pressure depletion over time under BDF, which is AE effect. The validity of Equation 3.41 will be examined and illustrated in the remaining of this section as well as in section 3.4.2.

To derive an analytical solution under radial BDF, pseudo-steady state pressure equation is required as input for Equation 3.1 instead of the pressure transient solution for the existing TTA analytical solutions. The pseudo-steady state pressure equation and its derivatives are given by:

$$p(r,t)-p_i=-\frac{qt}{\pi H\phi r_e^2 c_t}-\frac{\mu q}{2\pi H k_r k}\left[\ln\left(\frac{r_e}{r}\right)+\frac{1}{2}\frac{r^2-r_w^2}{r_e^2}-\frac{3}{4}\right] \tag{3.42}$$

$$\frac{\partial p}{\partial r}=\frac{\mu q}{2\pi H k_r k}\left(\frac{1}{r}-\frac{r}{r_e^2}\right) \tag{3.43}$$

$$\frac{\partial p}{\partial t}=-\frac{q}{\pi H\phi r_e^2 \hat{c}_t} \tag{3.44}$$

As a result, the energy balance equation (Equation 3.1) and the corresponding initial and boundary conditions (Equations 3.2 and 3.41) in the dimensionless form are:

$$\frac{\partial T_D}{\partial t_{D1}}=\frac{1}{r_{D1}}\frac{\partial T_D}{\partial r_{D1}}+\frac{1}{r_{D1}^2}+C_3 \tag{3.45}$$

$$T_D=0, t_{D1}=0 \tag{3.46}$$

$$T_D=C_3 t_{D1}, r_{D1}=r_{eD}, t_{D1}>0 \tag{3.47}$$

where

$$r_{D1}=\sqrt{\frac{-k_r k}{\mu_{JT}\mu\rho\rho_f}}\frac{2\pi Hr}{q} \tag{3.48}$$

$$t_{D1}=\frac{-2\pi H k_r k t}{\left\{\phi\left[\rho_w c_w S_{wr}+\rho_f c_f\left(1-S_{wr}\right)\right]+\left(1-\phi\right)\rho_s c_s\right\}\mu_{JT}\mu q} \tag{3.49}$$

$$C_3=\left(\frac{q}{2\pi H}\right)^2\frac{\mu_{JT}\mu c_f\rho_f}{k_r k r_e^2}-\frac{q\left(\rho_f c_f\mu_{JT}+1\right)}{\pi H r_e^2\hat{c}_t} \tag{3.50}$$

$$r_{eD}=\sqrt{\frac{-k_r k}{\mu_{JT}\mu\rho\rho_f}}\frac{2\pi Hr_e}{q} \tag{3.51}$$

Laplace transform is applied here to obtain the solution for Equation 3.45, the details of which are presented in the Appendix D. The analytical solution under BDF is:

$$T_D=0.5\ln\left(1+\frac{2t_{D1}}{r_{D1}^2}\right)+C_3 t_{D1} \tag{3.52}$$

From Equation 3.52, the following can be implied:

1. Compared to the analytical solution in section 3.1, the expression of dimensionless temperature is the same. Although the definitions of dimensionless time and radius (Equations 3.48 and 3.49) are different from Equations 3.11 and 3.12, the ratio of (r_D^2/t_D) is the same. Therefore, the first term in Equation 3.52 represents the same JT effect defined in existing temperature transient analytical solutions. As illustrated in section 3.1, the propagation speed of the JT effect is much slower than the pressure transient. This indicates that temperature transient behavior still exists after pressure transient reaches the boundary. In fact, the JT effect propagates so slow that it rarely reaches the boundary before the depletion. We will further elaborate on this point in section 3.4.2.
2. The second term in Equation 3.52 is associated with the temporal pressure decrease in pseudo-steady state pressure equation (Equations 3.42 and 3.44), which can be referred to as boundary dominated adiabatic expansion (BDAE). This behavior is a whole-field response, inducing equivalent temperature variations. BDAE is similar to the AE effect in existing temperature transient analytical solution, except that it is no longer an early time effect and becomes stronger over time. Therefore, the outer boundary temperature condition can be determined by the second term of Equation 3.52, which was expanded into Equation 3.41.

3. It should be noted that upon the start of BDF, t_{D1} is normally significant. Therefore, BDAE would dominate the temperature response. As a result, the cooling temperature signal will be eventually (and maybe quickly) established during the BDF.
4. BDAE is proportional to C_3. From Equation 3.50, C_3 is a function of multiple reservoir and fluid properties including the reservoir drainage area. We will use this feature to develop the inversion process from this analytical solution, presented in chapter 4.

During the pressure transient period (prior to the establishment of BDF), the analytical solutions to model the temperature transient have been derived in several studies. For the model description presented in Figure 3.10, we use the analytical solution developed in section 3.1 (Equation 3.15). To model the temperature transient in the entire production life cycle, we combine Equations 3.15 and 3.52 to form a composite analytical solution. The identical first terms in Equations 3.15 and 3.52 represent the JT effect, which occurs during both pressure transient and BDF periods. We denote the starting time of pseudo-steady state flow as t_{pss} and apply the Heaviside unit function to other terms in Equations 3.15 and 3.52. As a result, the composite analytical solution for the entire production period is given by:

$$T_D = 0.5\ln\left(1+\frac{2t_D}{r_D^2}\right) - C_1\left[\ln\left(1+\frac{2t_D}{r_D^2}\right) + Ei\left(-\frac{C_2 r_D^2}{4t_D}\right)\right]U\left(t_{D,pss}-t_D\right) + C_3\left(t_D - t_{D,pss}\right)U\left(t_D - t_{D,pss}\right) \tag{3.53}$$

where:

$$t_{D,pss} = \frac{-2\pi H k_r k t_{pss}}{\left\{\phi\left[\rho_w c_w S_{wr} + \rho_f c_f\left(1-S_{wr}\right)\right] + \left(1-\phi\right)\rho_s c_s\right\}\mu_{JT}\mu q} \tag{3.54}$$

This solution includes the JT effect (first term in Equation 3.53), AE effect in the transient period (second term), and BDAE (last term). It should be noted that the different time periods of AE effect results in a slight discontinuity at t_{pss}. This arises from the different analytical solution for AE effect before and after t_{pss}. In practice, AE effect during the transient period is in the order of 0.1-0.2 degC (section 3.1.1), which can be safely neglected given the resolution of temperature monitoring system. Moreover, BDAE evolves stronger over time which quickly masks the AE effect from the pressure transient period after t_{pss}. We will apply and examine this analytical solution in section 3.4.2.

3.4.2 Sandface Temperature Modeling and Verification

In this section, we model and verify the analytical solution against the reservoir temperature profiles obtained from numerical simulation. With the derived analytical solution (Equation 3.53), we can model the temperature transient analytically for the entire life of a production well. First, we will present the sandface temperature modeling results, which is the most common temperature measurement acquired in practice. To verify this analytical solution especially in pseudo-steady state pressure condition, these analytically modeled results are compared with those from numerical simulation (KAPPA-RUBIS 2015). The verifications are conducted for the base case of the same oil reservoir presented by App (2010), the properties of which are presented in Table 3.6.

Figure 3.11 presents the sandface temperature modeling results based on the analytical solution and numerical simulation for the base case. Two plots are compared here, in which the semi-log plot focuses on the temperature signals dominated by the pressure transient behavior, while the Cartesian plot demonstrates those associated with the BDF. In both plots, the analytically and numerically modeled temperature profiles show good agreement.

The semi-log plot in Figure 3.11a has been extensively discussed in section 3.1. The main observation from temporal temperature signals is that the heating JT effect presents a

straight line in this semi-log plot, the slope and intercept of which can estimate reservoir permeability and porosity. As suggested by the analytical solution and confirmed by numerical simulation, the sandface temperature profile under BDF presents a quasi-linear cooling behavior in the temporal Cartesian plot (Figure 3.11b) due to the dominating BDAE, induced by the gradually depleting pressure over time. Based on Equation 3.53, the slope of this straight line is proportional to C_3. As indicated in section 3.4.1, identifying C_3 is a key for the inversion procedure introduced later.

Table 3. 6. Reservoir and fluid properties for the base case and parametric analyses.

	Base case	Parametric analysis cases			
Downhole production rates (m^3/day)	520	154	347	739	986
Thickness (m)	30.48	10	20	30	40
Permeability (md)	20	5	10	100	1000
Drainage area (m^2)	282743	31416	125664	502655	785398
Total compressibility (1/Pa)	9.9×10^{-10}	5.9×10^{-10}	6.9×10^{-10}	1.5×10^{-10}	2.5×10^{-10}
Fluid specific gravity	0.8	0.85	0.9	0.95	1
Fluid specific heat (J/kg/K)	2222	2170	2120	2070	2020
Fluid viscosity (mPa·s)	3.4	1	2	5	10

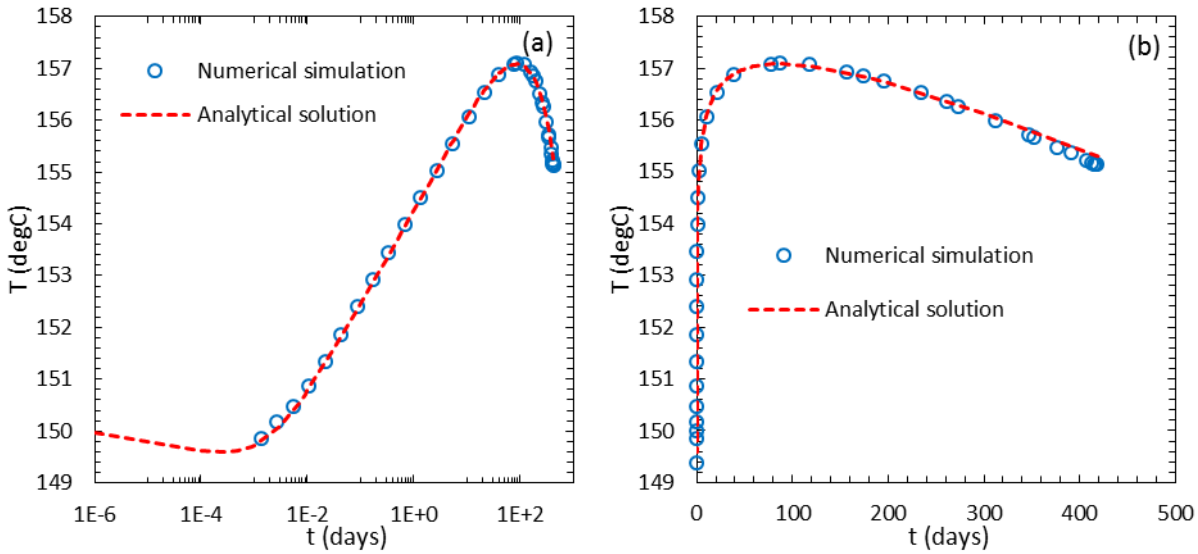

Figure 3. 11. Sandface temperature profiles obtained analytically and numerically in (a) semi-log plot and (b) Cartesian plot.

Between the heating JT effect (Figure 3.11a) and cooling effect during BDF (Figure 3.11b), there is a transition period indicating when the pressure transient reaches the boundary of drainage area (t_{pss}). Similar to PTA, the shape of the closed boundary reservoir controls the start and span of this transition period (Spivey and Lee 2013). Figure 3.12 presents sandface temperature profiles acquired from the numerical simulation for different reservoir shapes with

the same area as the base case. In addition to the radial reservoir presented in Figure 3.11, we include a rectangular reservoir with the ratio of length to width of 1, 2, 5, and 10 to investigate the boundary shape impact on the temperature signal. For reservoirs with higher ratios, the transition period starts earlier and lasts longer (Figure 3.12a). However, when BDF is established after the transition period, the slopes of temperature cooling on the Cartesian plot become identical and independent of shape (Figure 3.12b). This indicates that C_3 is a function of the drainage area of production well, regardless of the reservoir shape. In fact, the shape of the reservoir can be inferred from the end time of transient flow. We calculate the transient period ending time for circular and rectangular shaped (ratios of 5 and 10) reservoirs, which are indicated by vertical lines in Figure 3.12a. These lines are determined by the time for temperature signals to deviate from the straight line in the semi-log plot. We will apply these findings in the inversion process in chapter 4.

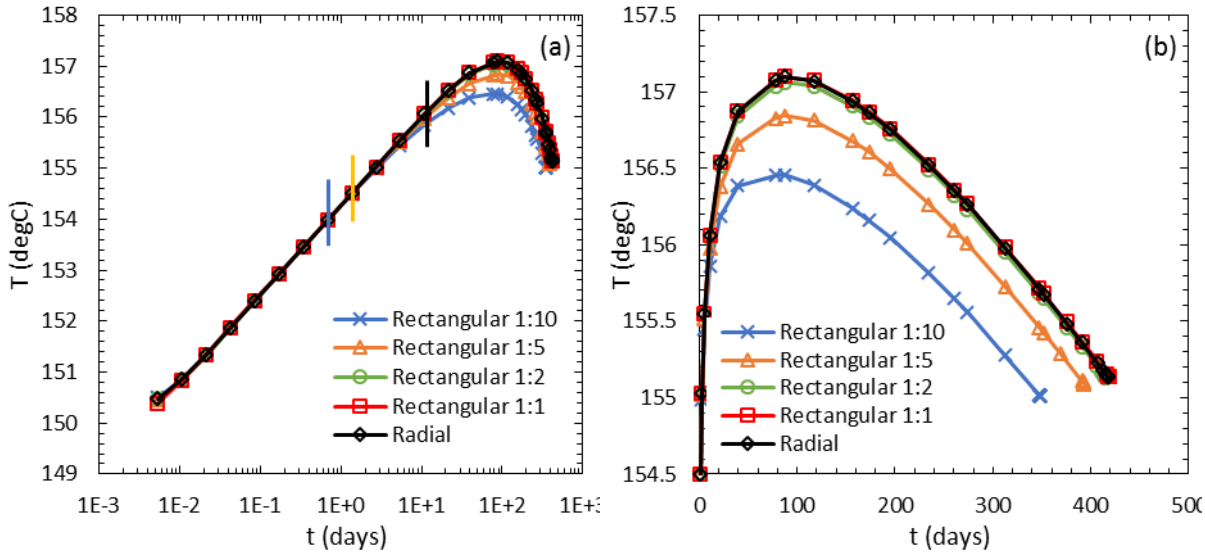

Figure 3. 12. Numerical sandface temperature profiles under different reservoir shapes in (a) a semi-log plot and (b) a Cartesian plot

3.4.3 Parametric Analysis for Reservoir, Production, and Fluid Properties

In this section, we conduct parametric analyses on the various reservoir, production, and fluid parameters to examine their effects on the sandface temperature signals from the production well. With the focus on temperature transient induced by the pseudo-steady state pressure behavior, C_3 is the critical parameter affecting the cooling signal in this period. Therefore, we select eight properties affecting C_3 (Equation 3.50) to perform the analyses, the values of which are presented in Table 3.6.

Figures 3.13 – 3.19 present the parametric analyses of analytically and numerically modeled sandface temperature profiles by varying production rate, reservoir thickness, permeability, drainage area, total compressibility, fluid specific gravity, specific heat, and viscosity, respectively. Several cases are performed over shorter production period because of early depletion. However, all the cases ended with BDF for pressure while being in the transient period for the temperature. Acceptable agreements are achieved between the analytical solution and numerical simulation in all 40 cases presented in the parametric analyses. Based on their impacts on the temperature response, these parameters can be divided into four categories:

1. Effects visible on both (semi-log and Cartesian) plots: downhole production rates and reservoir thickness
2. Effects visible on semi-log plot only: reservoir permeability and fluid viscosity

3. Effects visible on the Cartesian plot only: total compressibility and drainage area
4. Effects non-visible on either plot: fluid specific gravity and specific heat

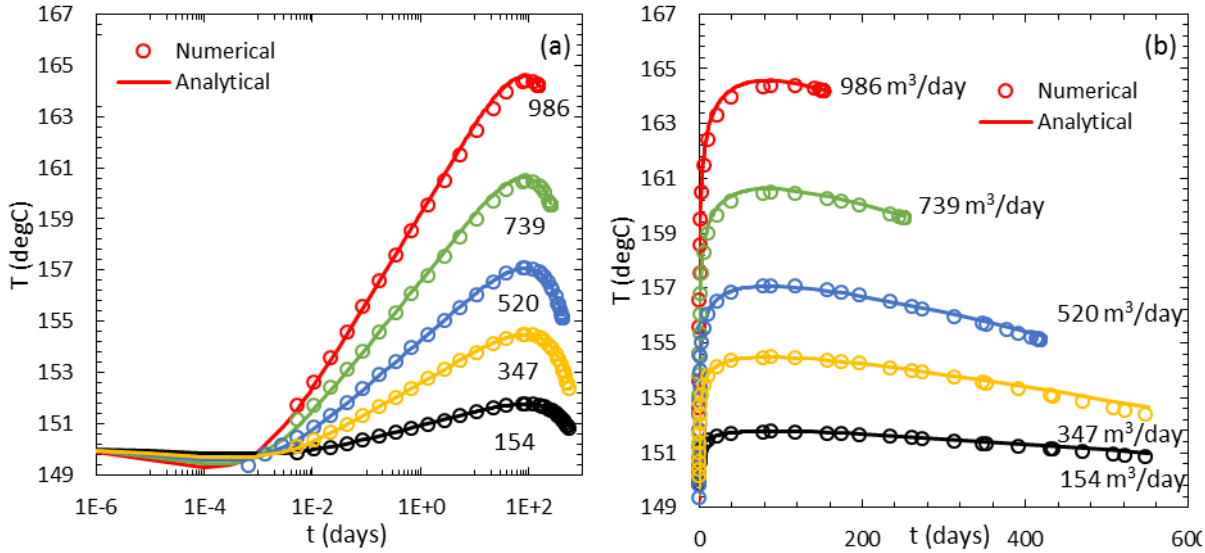

Figure 3. 13. Parametric analysis of sandface temperature modeling for various production rates in (a) a semi-log plot and (b) a Cartesian plot

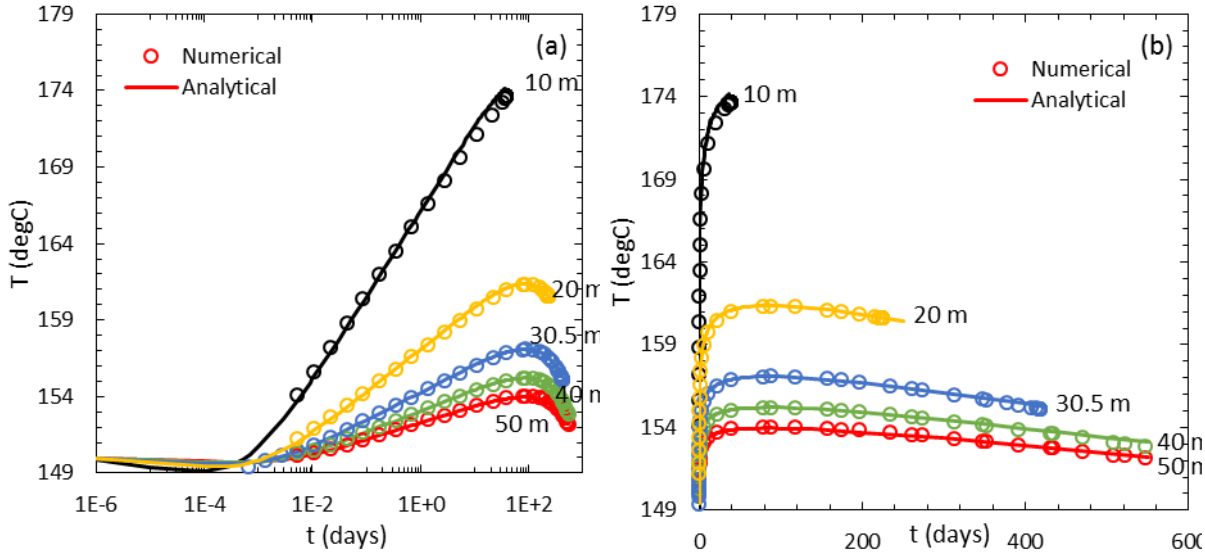

Figure 3. 14. Parametric analysis of sandface temperature modeling for various reservoir thicknesses in (a) a semi-log plot and (b) a Cartesian plot

Correspondingly, the temperature responses in the transient period are sensitive to the parameters in categories 1 and 2, while those associated with BDF are sensitive to the properties in categories 1 and 3. The parameters in categories 1 and 2 are investigated in previous studies, and their impacts on temperature signals before pressure transient reaching boundary are well understood in section 3.1. For the fluid specific gravity and specific heat in category 4, the product of fluid density and specific heat remains relatively constant for various fluid compositions with different API gravities (chapter 5). This leads to the insensitivity of the temperature response to fluid specific gravity and specific heat.

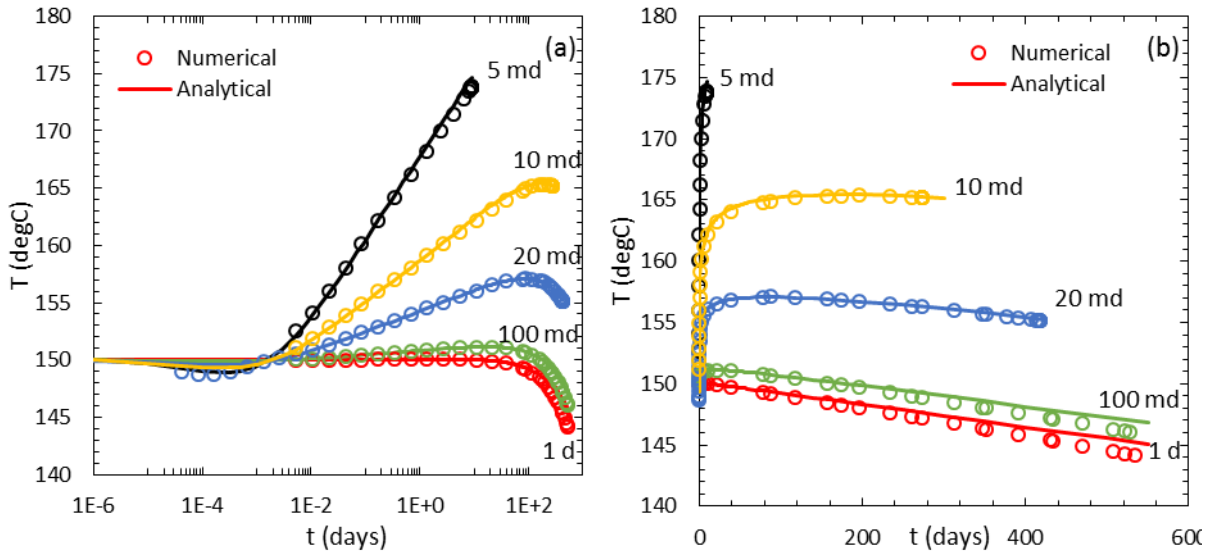

Figure 3. 15. Parametric analysis of sandface temperature modeling for various permeabilities in (a) a semi-log plot and (b) a Cartesian plot

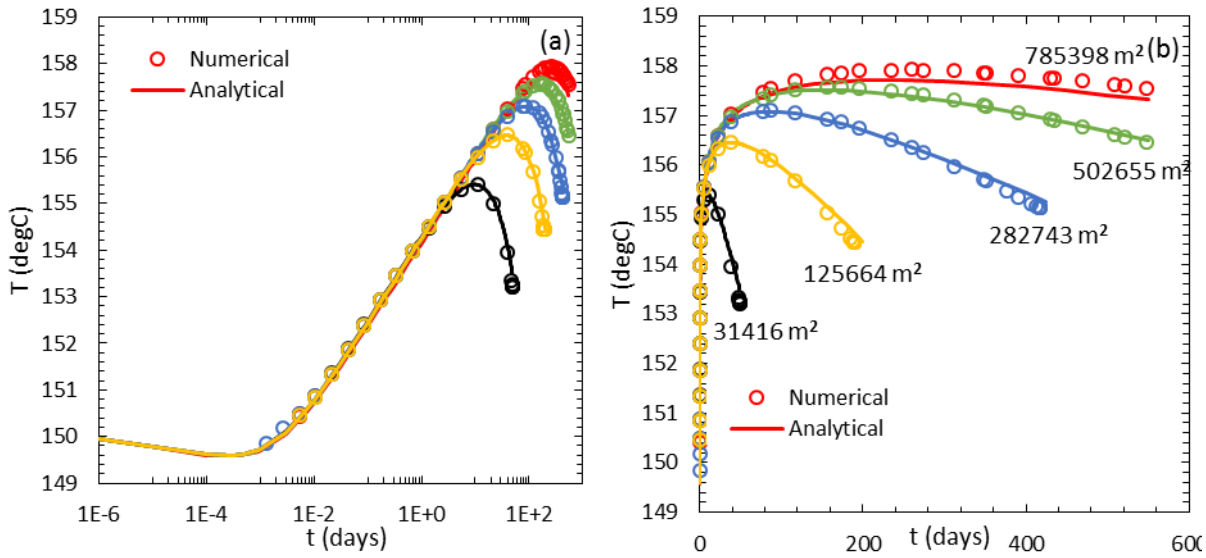

Figure 3. 16. Parametric analysis of sandface temperature modeling for various drainage areas in (a) a semi-log plot and (b) a Cartesian plot

However, the properties in category 2, reservoir permeability and fluid viscosity, are a function of C_3 (Equation 3.50) but do not show strong sensitivity on the temperature modeling results (similar slopes on Figures 3.15b and 3.19b). This is because these two parameters are in the first term in Equation 3.50, which is due to the pressure derivative over radius (Equation 3.43). Compared to the second term in Equation 3.50 associated with the temporal pressure derivative (Equation 3.44), the first term is too small and sometimes negligible. For the base case, the value of the first term in Equation 3.50 is only 0.3% of the C_3 value. In the cases presented in Figures 3.15 and 3.19, the maximum percentage of the first term is 1.2%, significantly smaller than the second term. Therefore, the temperature transient response during BDF is mainly attributed to the pressure depletion process over time. The effects of permeability and viscosity on temperature modeling in this period are negligible.

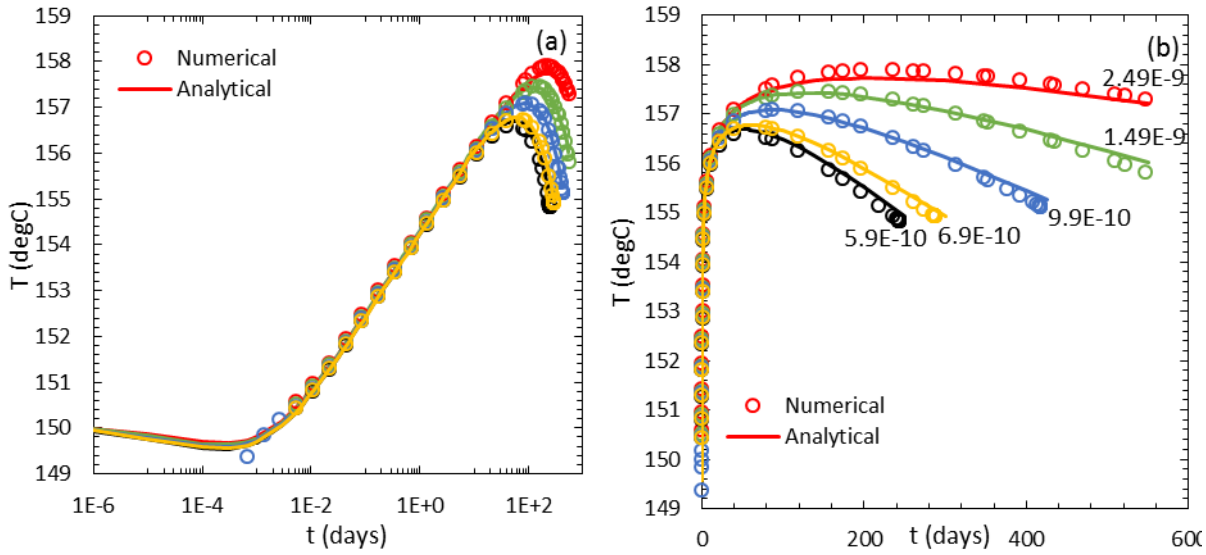

Figure 3. 17. Parametric analysis of sandface temperature modeling for various total compressibilities in (a) a semi-log plot and (b) a Cartesian plot

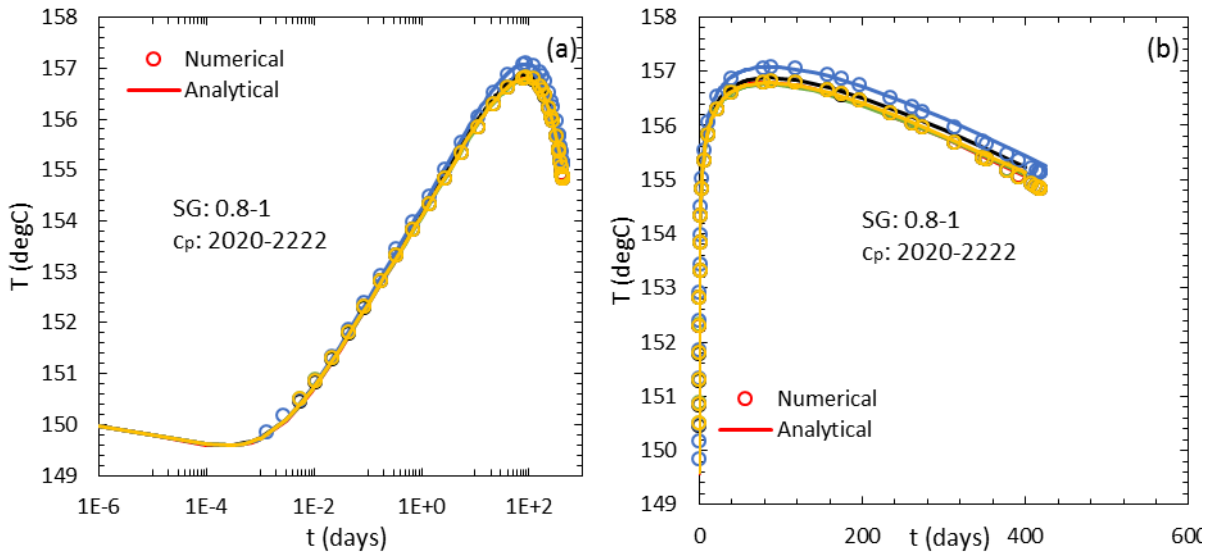

Figure 3. 18. Parametric analysis of sandface temperature modeling for various fluid specific gravities and specific heats in (a) a semi-log plot and (b) a Cartesian plot

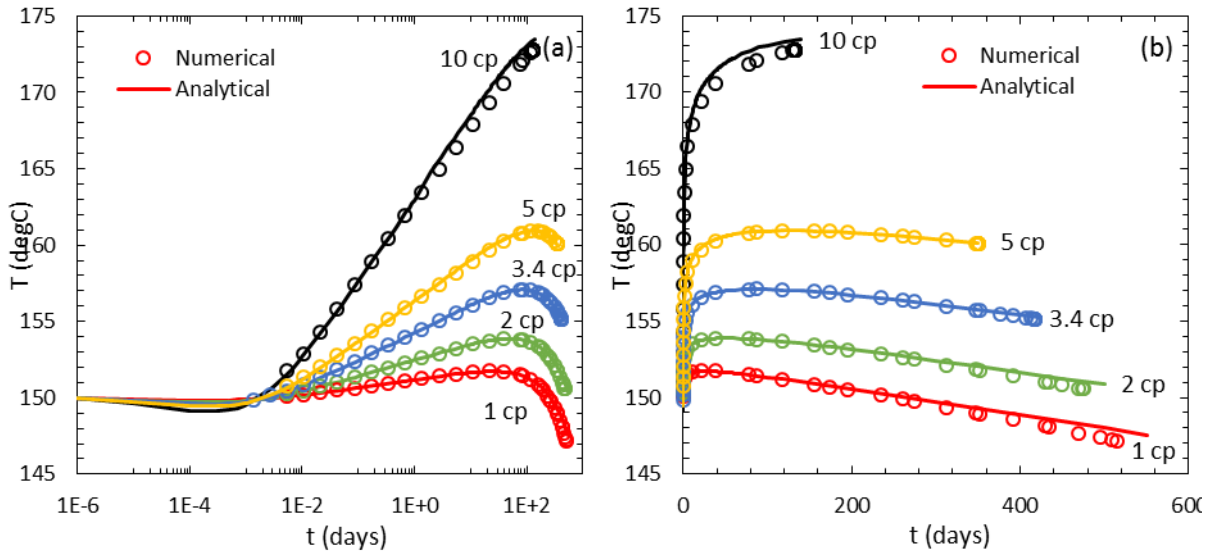

Figure 3. 19. Parametric analysis of sandface temperature modeling for various fluid viscosities in (a) a semi-log plot and (b) a Cartesian plot

3.4.4 Temperature Modeling in Observation Wells

In this section, we explore the potential of TTA at observation wells located away from the production well. During the transient period, TTA at observation wells may not be very useful since the temperature changes are insignificant (normally around 0.1 – 0.2 degC), which are mainly associated with AE effect in this period. However, after pressure transient reaches the no-flow boundary, pressure depletion occurs throughout the entire reservoir. Therefore, a stronger temperature signal is expected in observation wells under BDF.

To investigate the temperature propagation into the reservoir, we present the radial temperature profiles at various production times for the base case in Figure 3.20. Similar to the temporal temperature profiles in previous figures, two plots are presented here for radial temperature modeling. Plotted on a semi-log graph, the temperature signal in the near wellbore region is expanded in Figure 3.20a. In both plots, the analytically and numerically modeled temperature profiles show good agreement.

For the base case, the pressure transient reaches the boundary after 11 days of production. Therefore, all the cases presented in Figure 3.20 are in BDF period. The temporal cooling signals observed in the production well are the sum of JT and BDAE effects. Although the heating JT effect causes a temperature increase of 9-11 degC from the production well into the reservoir, the temperature decreases as the production continues, even in the production well (Figure 3.20a). This observation validates our earlier note from the analytical solution that BDAE outweighs the JT effect during BDF period. In the outer reservoir, BDAE is the only effect to cause cooling (Figure 3.20b). Using the JT effect radius of investigation derived in section 3.1, we can calculate the radius after one year of production as 37 m. Therefore, if the observation wells are located outside of this radius, their recorded temperature signals are only controlled by BDAE.

To compare the sandface temperature signals obtained from the observation wells, we present the temporal profiles in Figure 3.21 with various monitoring locations. The observation wells are located 50 m to 300 m away from the production well, with 50-m spacing. Despite the slight difference in the early time period, the temperature profiles demonstrate an almost identical linear cooling effect of BDAE on the Cartesian plot (Figure 3.21b). It is a clear indication that the temperature changes at the outer boundary can be modeled by BDAE (second term of Equation 3.52, which is expanded in Equation 3.41). In fact, the JT effect is

eliminated from the observation well sandface temperature signals, which is beneficial to the analysis of the thermal perturbation during BDF period presented in chapter 4.

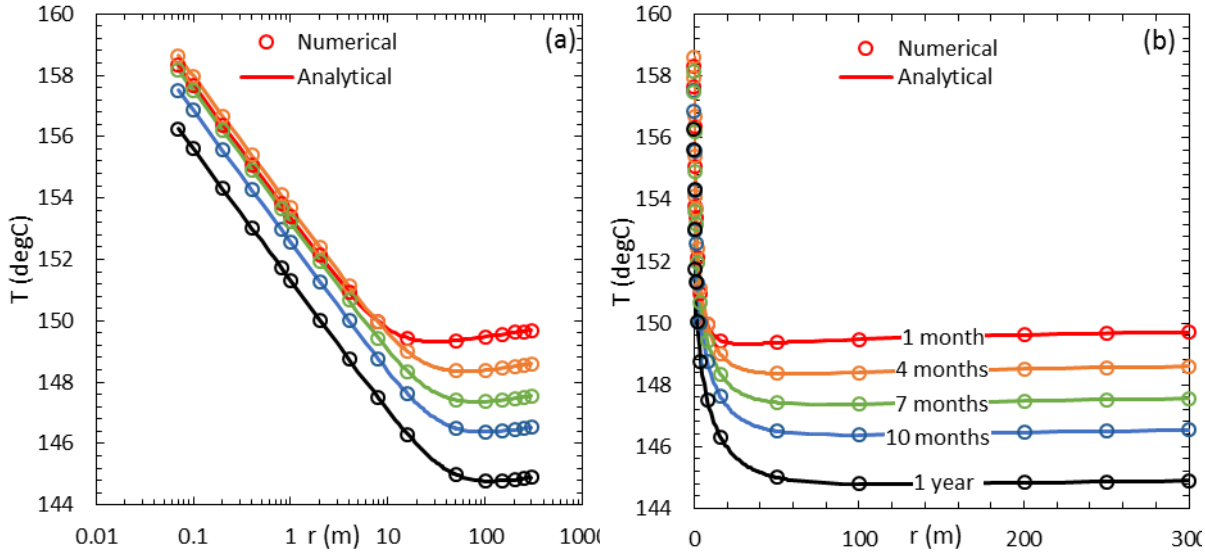

Figure 3. 20. Radial temperature profiles obtained analytically and numerically in (a) a semi-log plot and (b) a Cartesian plot for various production times.

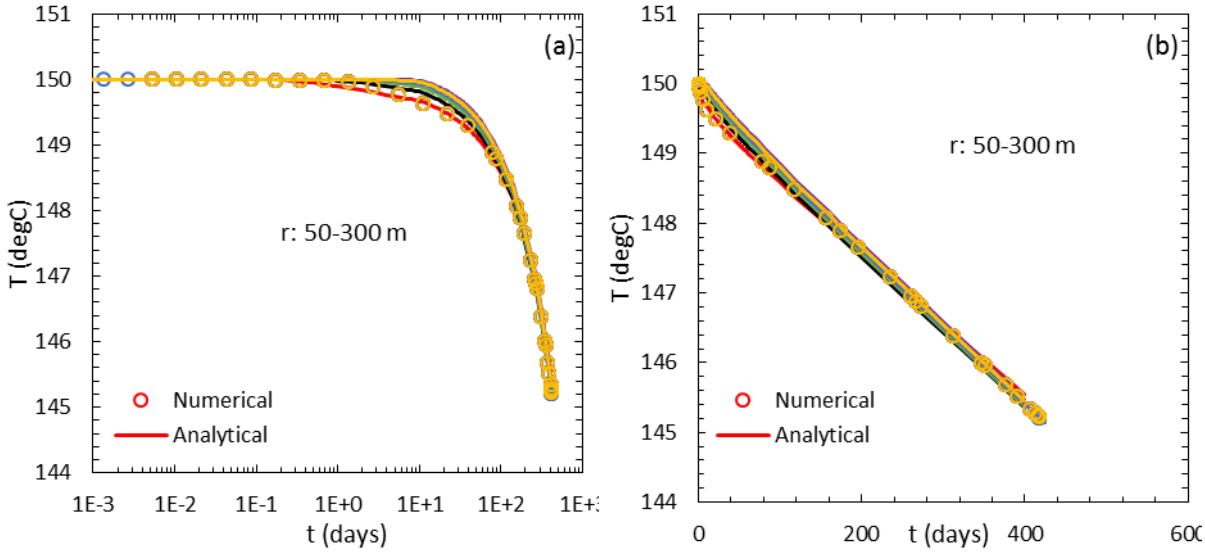

Figure 3. 21. Sandface temperature profiles obtained analytically and numerically in (a) a semi-log plot and (b) a Cartesian plot for observation wells located at different distances from the production well.

3.4.5 Discussions

In this section, two main issues of TTA under BDF will be investigated: (1) the effects of thermal conduction and heat loss to surroundings, and (2) build-up temperature modeling under BDF.

Assumptions made to derive this analytical solution are similar to those associated with existing temperature transient analytical solutions, which have been extensively discussed in section 3.1. One major assumption that may not be valid during the derivation is neglecting thermal conduction and heat loss to upper and/or lower layers. Chevarunotai, Hasan, and Kabir

(2015) pointed out that these effects can be substantial under some circumstances, one of which is a longer production period under BDF. Therefore, we perform numerical simulations to include these two effects in temperature modeling and present the results in Figures 3.22 and 3.23.

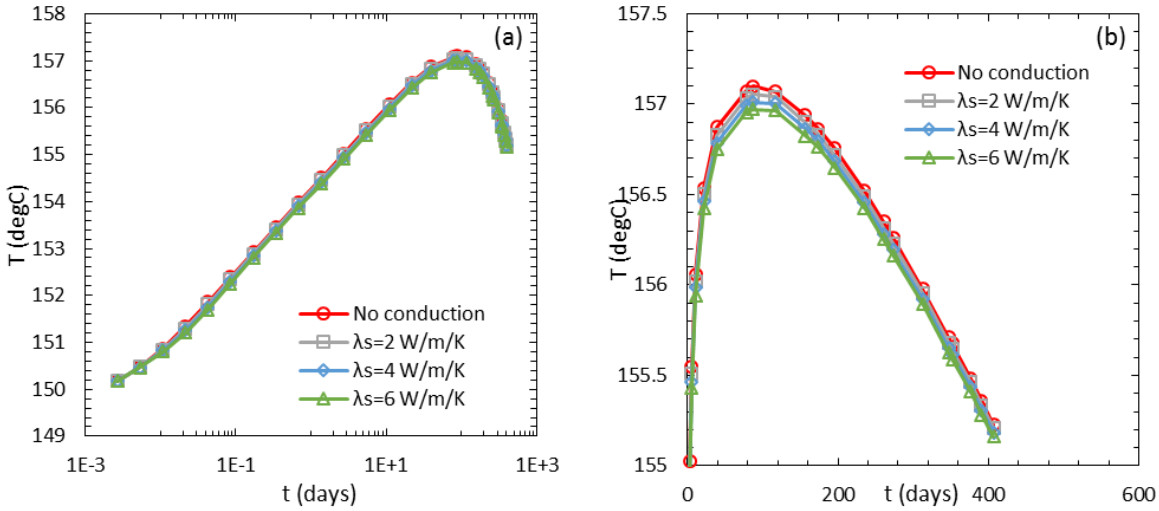

Figure 3. 22. Numerical temperature modeling results for the base case for 0-6 W/m/K rock conductivity in (a) a semi-log plot and (b) a Cartesian plot acquired from the production well.

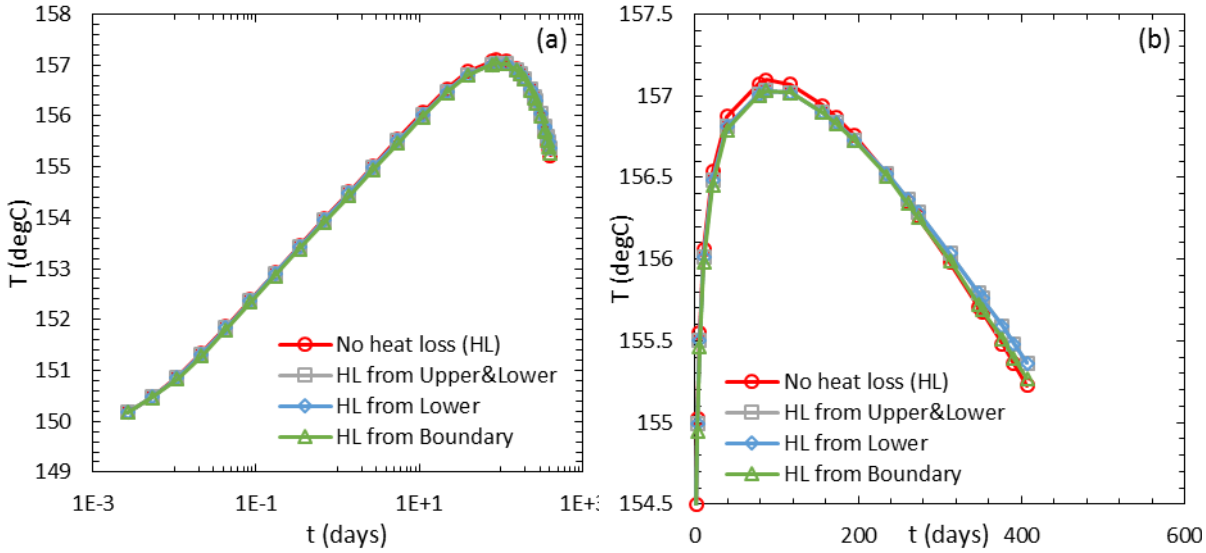

Figure 3. 23. Numerical temperature modeling results for the base case for various types of heat loss to surroundings in (a) a semi-log plot and (b) a Cartesian plot acquired from the production well.

We start investigating the effect of thermal conduction in Figure 3.22, which presents four cases with rock conductivity (λ_s) varied from 0 to 6 W/m/K. This range should cover the majority of reservoir rock encountered in practice. Very similar temperature modeling results presented in both semi-log and Cartesian plots indicate that the effect of thermal conduction is minor even on long-term temperature modeling under BDF. Therefore, we perform the inversion process on the temperature modeling results to investigate the effect of thermal conduction on drainage area estimations. In the most extreme case (λ_s=6 W/m/K), the r_e estimation is 327 m (9% error), slightly higher than the case assuming no conduction. This

observation validates our assumption to ignore the conduction term from the energy balance equation, which results in Equation 3.1 as the governing equation for this analytical solution.

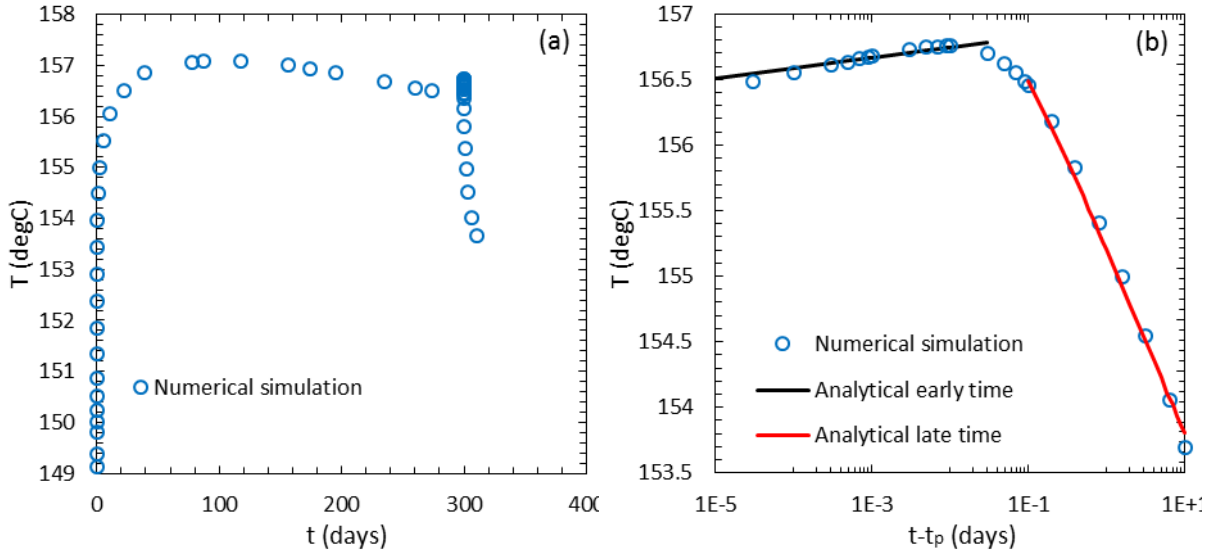

Figure 3. 24. Sandface numerical temperature modeling results (a) for the base case including a shut-in period, which is enlarged and compared with analytical solution results in (b).

On the other hand, we also consider the effect of heat loss to surroundings on the sandface temperature signals from the production well in Figure 3.23. To investigate the effect, we introduce the heat loss to surroundings assuming that the source is from the boundary, lower layer or upper and lower layers. In Figure 3.23a (pressure transient period), the results are very similar. For the extended period under BDF presented in Figure 3.23b, heat loss causes reduced cooling effect especially for those emerging from the lower and/or upper layers, which can be observed in terms of slope changes. After performing the inversion procedures, the r_e estimation increases to 345 m (15% error). Although TTA accuracy is still acceptable considering the heat loss, one may consider applying the approach introduced in Chevarunotai, Hasan, and Kabir (2015) for long-term production under BDF.

Buildup test is generally carried out on data obtained during the shut-in period due to their quality and ease of operation in the field. Monitoring sandface temperature signal over the shut-in period was extended to TTA, the analytical solution of which was derived by Onur and Cinar (2017a). This build-up test thermal analytical solution is based on a shut-in period preceded by a flowing period when the pressure transient does not reach the boundary. Here, we examine if this solution is applicable to the case after the BDF is established.

Figure 3.24a presents the production well sandface temperature modeling results for the base case including a shut-in period of 10 days after producing for 300 days. After shut-in, the heating effect occurs for a couple of hours and follows with a cooling effect. If the shut-in period is long enough, the sandface temperature should approach the initial reservoir temperature. The early-time build-up temperature signal is characterized by a temperature increase due to adiabatic fluid compression from shutting in the well. The late-time signal is governed by heat conduction. Similarly, we have the same two effects controlling the shut-in temperature behaviors with an infinite-acting flowing period. Therefore, we can apply the buildup temperature analytical solution developed in Onur and Cinar (2017a) for the shut-in period. Although this analytical solution was not developed for the condition of BDF, its modeling results still agree with the numerically modeled temperature profile, as shown in Figure 3.24b. The reason for this agreement is that the dominating factors for build-up

temperature profiles are independent of whether the pressure effect reaches the boundary or not. These dominating factors include (1) production rate, permeability, reservoir thickness, fluid viscosity, and JT coefficient for the early-time build-up temperature signals, and (2) thermal conductivity of the reservoir for the late-time build-up temperature signals. Whether the drawdown period is in pressure transient or BDF period, these parameters are identical leading to the same build-up temperature profiles. Therefore, we can apply the same build-up analytical solution developed for the pressure transient period to model those under BDF.

3.5 Multi-Layer Reservoir

Multilayer systems are widely encountered in underground hydrocarbon reservoirs. To obtain accurate multilayer properties and understand the flow behavior in a multilayer system, many testing and analysis procedures have been evolved. In this section, we present an analytical solution to determine the individual layer temperature signal associated with constant rate production of slightly compressible fluid from a fully penetrating vertical well in a multilayer reservoir. The temperature signals are presented at the bottom-hole location and further into the reservoir for two-layered and multi-layered systems, for which each layer may be damaged or undamaged.

3.5.1 Analytical Model

In this section, we develop the analytical solutions to obtain transient temperature profiles for a multilayer oil reservoir produced from a vertical well. A slice of this model schematic is illustrated vertically in Figure 3.25. An *n*-layered reservoir is produced from a vertical well penetrating and perforated all the layers, the constraint of which is constant total production rates q_t from all the layers. The individual layer properties (e.g. permeability, porosity, and damaged zone) are homogenous per each layer. The reservoir fluid is a slightly compressible, single-phase fluid of constant viscosity and thermal expansion coefficient through all the layers. This reservoir is confined by impermeable layers at the top and bottom, and reach infinitely in the radial direction. Cross-flow between layers can occur in adjacent layers to permit fluid communications between layers.

The temperature profiles will be presented for a base case with layer properties varied based on it, which is the same single layer oil reservoir presented by App (2010). The results of the temperature profiles from the analytical solutions are analyzed and compared with the results from numerical simulation. The numerical simulations are performed using a commercial reservoir simulation software (CMG-GEM 2015). Since the fluid composition is not reported by App (2010), we introduce a single component fluid (Cyclohexane) for compositional numerical simulation, the thermo-physical properties of which closely match those from App (2010). An equation of state using the Peng-Robinson technique (Peng and Robinson 1976) is applied at an initial reservoir temperature of 150°C to predict these thermo-physical properties of Cyclohexane over the full range of pressures and temperatures expected to be encountered during the simulation. Slight changes in viscosity coefficients are applied to the flash calculations to mimic the viscosity value from App (2010). Based on the flash test results, the thermo-physical properties of the reservoir fluid at the initial reservoir conditions include specific heat of 2202 J/kg/K, the density of 840 kg/m^3, JT coefficient of -0.41 K/MPa, and viscosity of 3.685 cp. These fluid properties are used only in analytical solutions. Transient temperature signals from the well are associated with the reservoir fluid flow and heat transfer behaviors. Due to the negligible variations in the fluid properties caused by non-isothermal effect, these two processes can be decoupled when analyzing the transient temperature signals (Onur and Çinar 2016). The fluid flow performances of a vertical well produced from a multilayer oil reservoir under layer cross-flow have been investigated by Bourdet (1985),

Ehlig-Economides and Joseph (1987), Park (1989), as mentioned in the introduction. If the well is produced with constant production rate, the ILPRs are different and varying with time. On the other hand, the transient temperature profiles from a vertical well produced from a single layer oil reservoir have been developed in section 3.1. These analytical solutions assumed a constant production rate condition, which is not valid for each layer in a multilayer reservoir. To obtain an analytical solution for the multilayer reservoir, the behaviors of ILPR is required to be analyzed first.

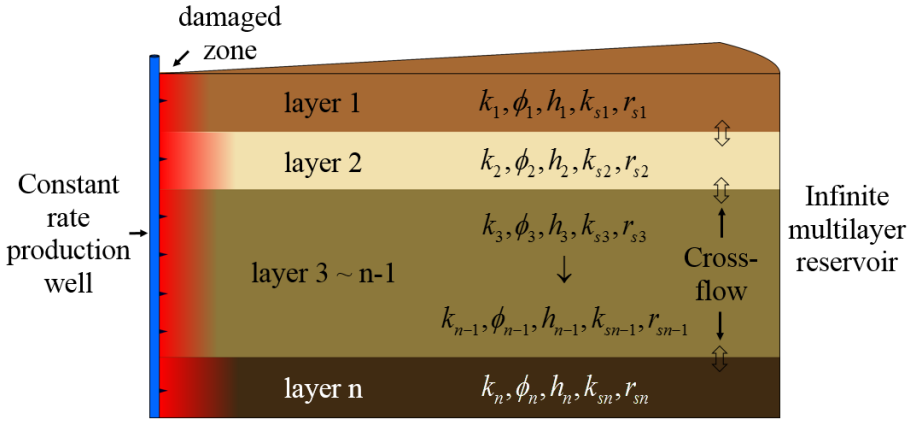

Figure 3. 25. Model description for a multi-layer reservoir.

The ILPR for two-layered multilayer reservoir are simulated and compared with the analytical solution provided from Bourdet (1985) in Figure 3.26a. The ILPRs obtained from analytical solution and numerical simulation are in good agreement and are stabilized shortly after production (less than 0.2 days). With the variance on layer properties of permeability and skin factor, the ILPR for the three-layered reservoir are also approaching constants in less than 1 day after production (Figure 3.26b). Based on these observations, Park (1989) developed the late time ILPR from its analytical solution for the two-layered reservoir and extended it to the multilayer system. These late time ILPR, which are Equation 3.55, are good representations for the layer production rate behaviors after initial fluctuations.

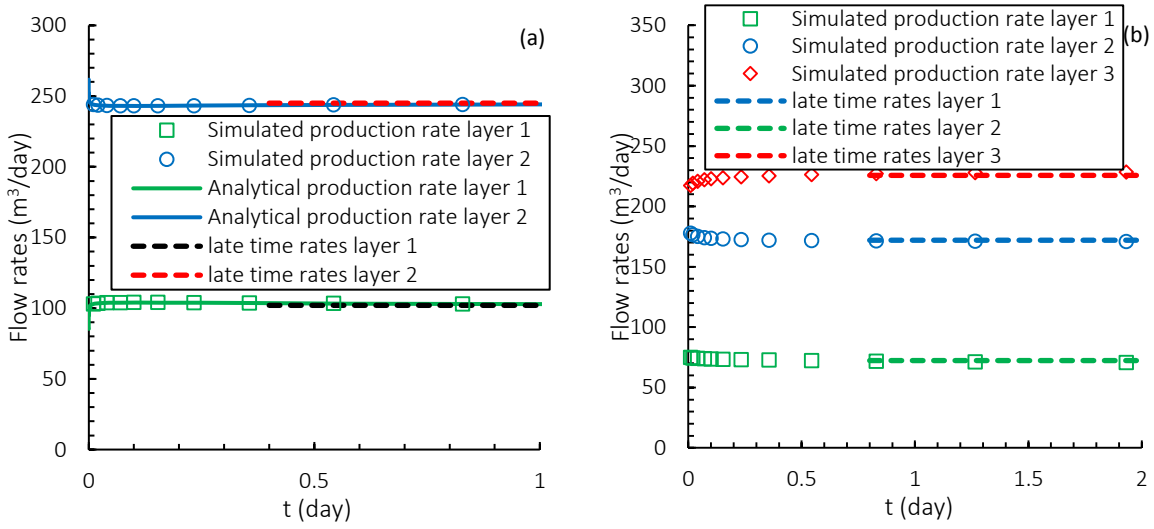

Figure 3. 26. Individual layer production rates for two- (a) and three- (b) layered multilayer reservoir.

$$\left(q_{jD}\right)^{LT} = \kappa_j \left[1 + \sum_{i \neq j} \frac{\kappa_i \left(s_i - s_j \right)}{K_0\left(\sigma_{ij}\right) + \kappa_i s_j + \kappa_j s_i} \right] \tag{3.55}$$

where:

$$q_{jD} = \frac{q_j}{q_t} \tag{3.56}$$

$$\kappa_j = \frac{\left(kh\right)_j}{\left(kh\right)_t} \tag{3.57}$$

where σ is the semi-vertical-permeability between layers (Cheng-Tai and Deans 1983). Subscripts *i* and *j* indicate the layer index, *D* indicates the dimensionless terms, and *t* indicates the summation of the term in all layers. The followings can be implied from inspecting the above solution. Firstly, the late time ILPRs are constant, which are a function of the layer flow capacity (*kh*), vertical permeability and skin factor in each layer. Secondly, if skin factors are identical for all layers, the late time ILPR of a given layer is proportional to the flow capacity ratio of the layer to the sum of flow capacities of all layers. Thirdly, if skin factors are different for each layer, the layer with smaller skin factor produces more than the flow capacity percentage in all the layers. This indicates that cross-flow direction is towards the lower skin layer, from the higher skin layer. These physical insights of ILPR will be further analyzed in section 3.5.2.

With the input of late time ILPR, we can use the single layer analytical solutions to represent the temperature profiles in each layer. We select the analytical solutions from Equation 3.28 since it can be used to perform the damaged zone characterization as well. In section 3.5.2, we will present the temperature profiles for the multilayer reservoir, and examine the validity of this assumption.

3.5.2 Solution Verification

In this section, we obtain the temperature profile from our derived analytical solution and compare the results to those from numerical simulations to validate the analytical solution. The individual layer temperature profiles are presented for two- and three-layered systems based on the properties given in Table 3.7.

Table 3. 7. Individual layer properties for Figures 3.26-3.31.

	Two-layered system		Three-layered system		
	Layer 1	*Layer 2*	*Layer 1*	*Layer 2*	*Layer 3*
Downhole production rates (m^3/day)	347		470		
Permeability (md) (Figures 3.26-3.29 and 3.31)	20	40	10	20	40
Damaged zone permeability (md) (Figures 3.27, 3.28, 3.31)	10	24	5	12	16
Damaged zone radius (m) (Figures 3.27, 3.28, 3.31)	2.08	0.98	2.08	0.98	3.08
Skin factor (Figures 3.27, 3.28, 3.31)	3.3	1.7	3.3	1.7	5.55
Porosity (-) (Figures 3.30 only)	0.1	0.3	0.1	0.2	0.3

The temperature profiles calculated by the analytical solutions are benchmarked with the results from numerical simulation to validate the analytical solutions. Figures 3.27a and 3.27b present the comparison of radial temperature distributions from the analytical solution

and numerical simulation for the two-layered system after producing for 1 and 50 days. The analytical solutions provide a decent agreement with the numerical simulation to predict the temperature signals for both layers. This agreement stands for the three-layered system as well, presented in Figure 3.28. The physical behaviors of the individual layer temperature signals are determined by the damaged zone properties, JT effect, and AE effect, from the near wellbore region further into the reservoir. The characterization methods to acquire the individual layer and damaged zone are very similar to those for single layer reservoir, which are extensively discussed in section 3.1. However, since the radial temperature distributions are rarely measured, the characterization techniques will be applied to the regularly deployed temperature measurements, which are obtained at the bottom-hole location.

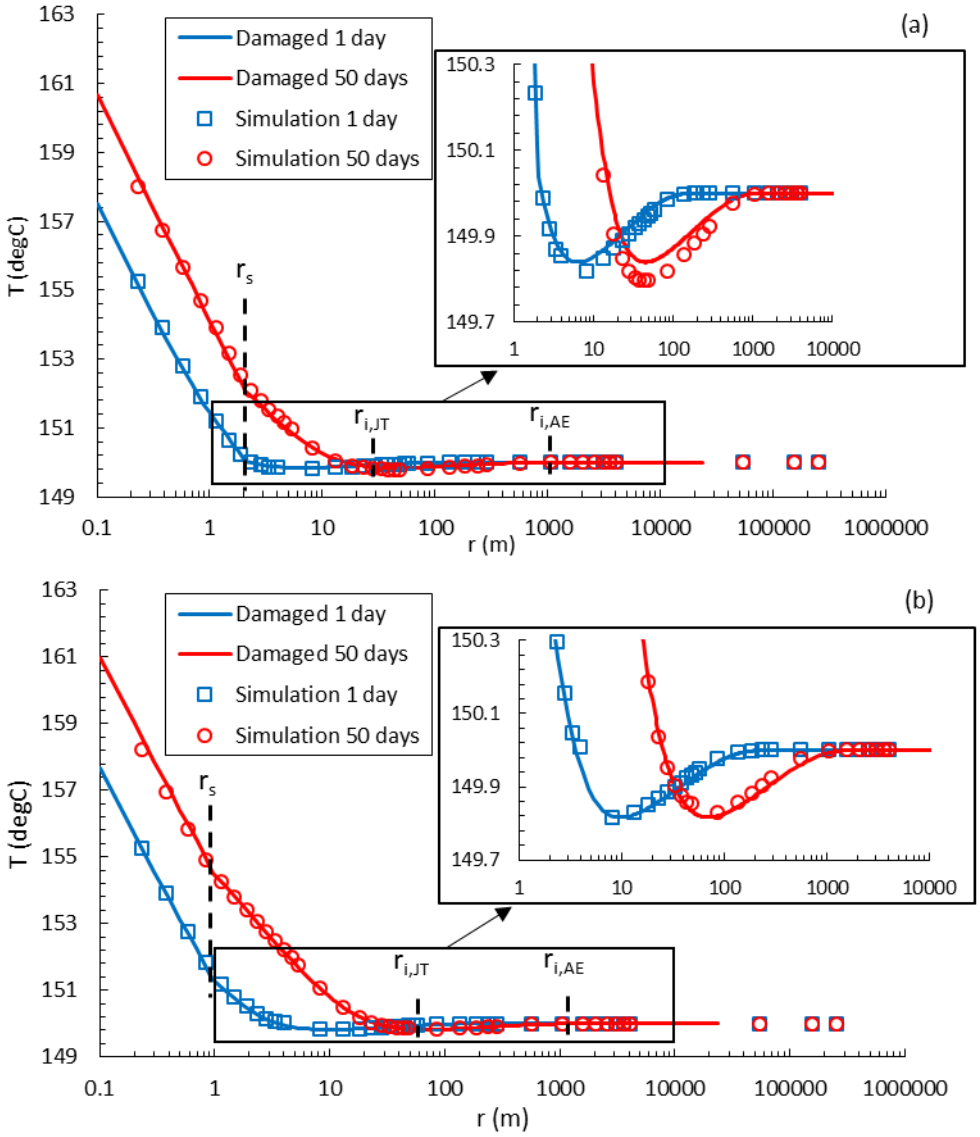

Figure 3. 27. Comparison of temperature profiles between the analytical solution and numerical simulation in (a) layer 1 and (b) layer 2 for the two-layered system. The squares and circles indicate the results from numerical simulation and solid lines indicate the results from analytical solutions. The dotted lines indicate the radius of investigations for JT and AE effects. Sections of the temperature profiles dominated by AE effect are enlarged in the subplots.

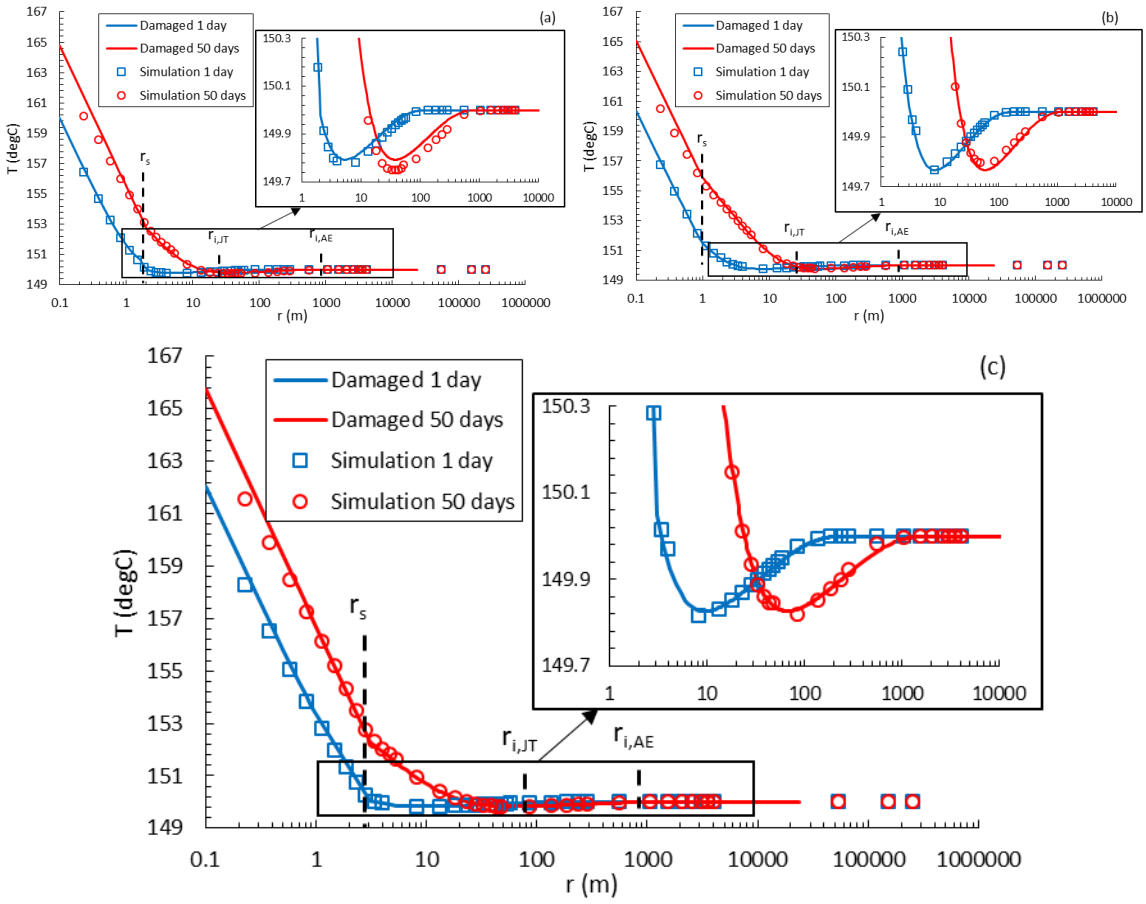

Figure 3. 28. Comparison of temperature profiles between the analytical solution and numerical simulation in (a) layer 1, (b) layer 3, and (c) layer 3 for the three-layered system.

3.5.3 Individual Layer Temperature Profiles

The temperature profiles for an individual layer in a multilayer reservoir are a function of the similarity variable (r^2/t) and are primarily affected by the reservoir properties of permeability and porosity (section 3.1). In this section, the individual layer temperature profiles are presented versus the similarity variable. Based on the temperature signals and analytical solution, the impacts of permeability and porosity variations on the temperature signals are investigated, and the procedures to perform individual layer property characterization are procured.

First, we analyze the individual layer temperature profiles of the undamaged reservoir with layer permeability variations in Figures 3.29. The temperature profiles in Figures 3.29 are calculated by the analytical solution, the layer properties of which are based on Table 3.7. For both two- and three-layered systems, the magnitude of JT and AE effect on temperature signals are identical under different layer permeabilities. This can be explained by the expressions of the slopes for these two effects obtained from the analytical solution. The slope of JT effect is a function of k_ih_i/q_i. In section 3.5.1, we have analyzed the ILPR behavior that it is proportional to layer flow capacity for the undamaged reservoir. Therefore, the slope of the JT effect is irrelevant to layer permeability. However, the permeability affects the radius of investigation of JT and AE effects. With higher layer permeability, the temperature fronts propagate faster, which resulting further radius of investigation for JT and AE effects.

Secondly, the individual layer temperature profiles of the undamaged reservoir with layer porosity variations are presented in Figures 3.30, calculated from the analytical solution with the layer properties defined in Table 3.7. Similar to the previous case, the temperature

signals for two- and three-layered systems are analogous. The porosity variation from one layer to another does not affect the magnitude of the JT effect, as well as the radius of investigation of the JT and AE effects. The layer temperatures differ only on the magnitude of the AE effect when experiencing porosity variation between layers. Under higher layer porosity saturated with oil and irreducible water, more oil can expand upon pressure release to result in higher temperature variation. However, the AE effect is generally an early time thermal behavior observed from bottom-hole. Therefore it can be easily masked by the thermal wellbore storage and may not be observed. If the AE effect can be monitored, the characterization of layer porosity can be performed.

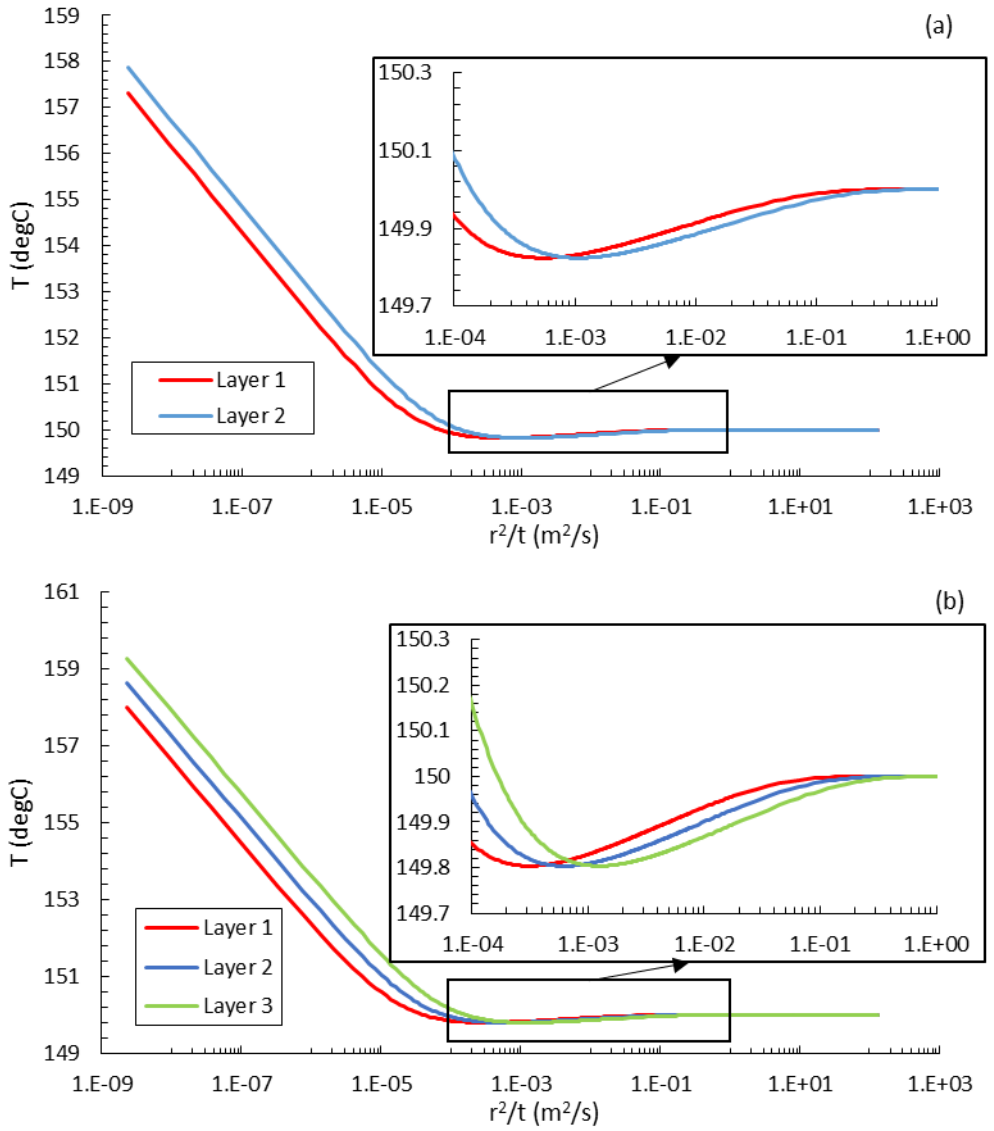

Figure 3. 29. Individual layer temperature profiles of the undamaged reservoir with layer permeability variations for (a) two- and (b) three-layered system.

The transient temperature analytical solution for a damaged single layer reservoir is a function of radius and time separately, as indicated by Equation 3.56. We have demonstrated the temperature profiles versus radius in section 3.5.2. In this section, the individual layer temperature profiles are presented versus time at bottom-hole location, which are the common temperature measurements encountered in the field. We vary the layer permeability, damaged zone permeability and radius to illustrate their impact on the temperature signals. From the

expressions of the analytical solution, the procedures to perform damaged zone characterization are obtained.

The individual layer bottom-hole temperature profiles of the damaged reservoir with layer permeability and skin variations are presented in Figures 3.31. The temperature signals are calculated by the analytical solution with the damaged zone (Equation 3.28), the layer properties of which are based on Table 3.7. For two- and three-layered systems, bottom-hole temperature profiles for each layer have a slope change that separates the damaged zone temperature behavior in early time and the reservoir temperature behavior in late time. The time at the slope change is when the temperature front traverses the damaged zone, which indicates its potential to calculate the damaged zone radius. The traverse time ranges from 2 hours to 2 days in Figures 3.31 and could be long enough to survive the thermal wellbore storage. The speed of the temperature propagation is proportional to the ILPR. Therefore, the traverse time is determined by the damaged zone radius over ILPR.

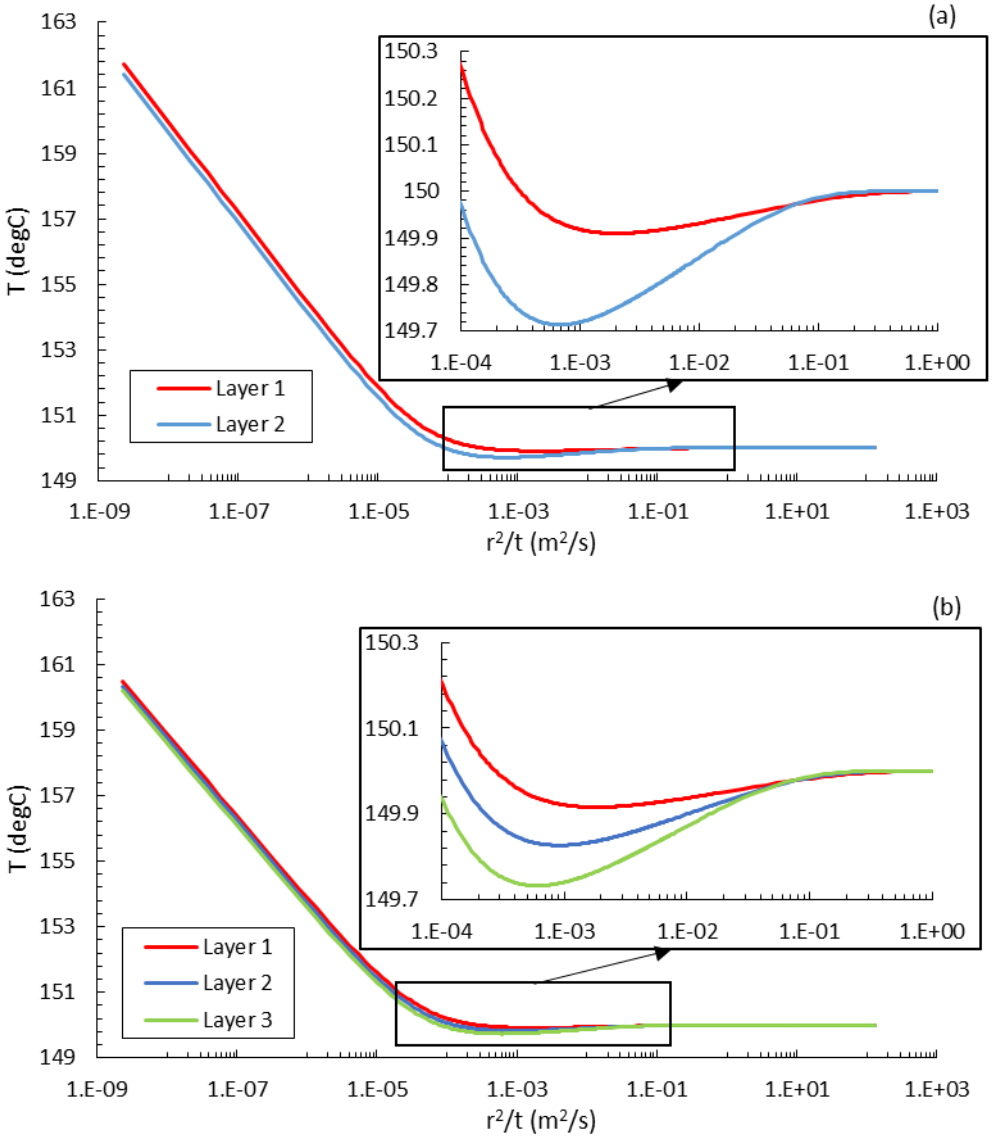

Figure 3. 30. Individual layer temperature profiles of the undamaged reservoir with layer porosity variations for (a) two- and (b) three-layered system.

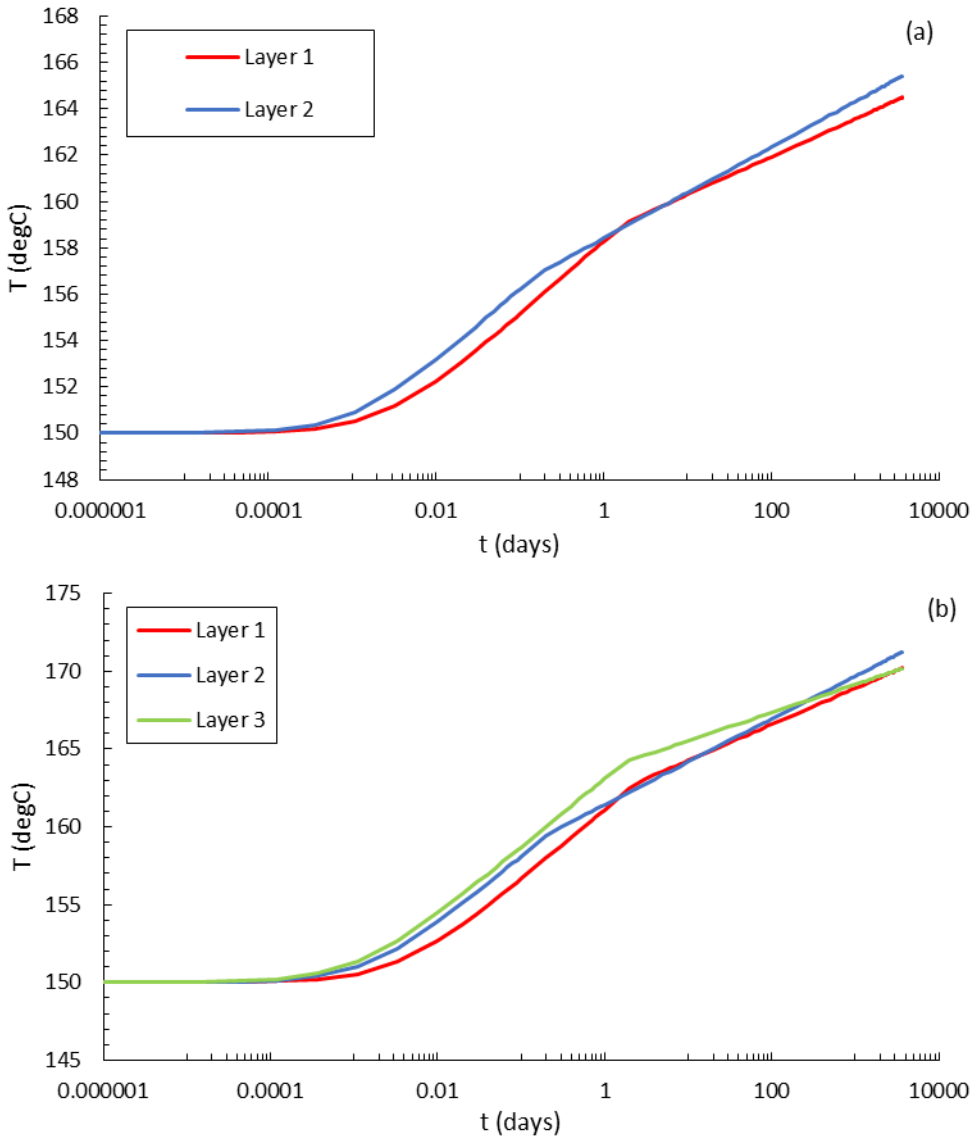

Figure 3. 31. Individual layer bottom-hole temperature profiles of the damaged reservoir with layer permeability and skin variations for (a) two- and (b) three-layered system.

3.5.4 Discussions

In discussing our proposed TTA technique, we first explore the effect of layers communication on the temperature profiles. Then, we discuss the assumptions made in the derivation of the analytical solution and their implications for the limitations of the interpretation procedures.

Layers communication (cross-flow) plays an important role in constructing analytical solutions to obtain multilayer reservoir temperature profiles. Firstly, the existence of the cross-flow stabilizes the late time ILPR. Secondly, the cross-flow brings the fluids from other layers, the temperature profiles of which can perform differently from this layer. In this section, we investigate the effect of vertical permeability on the individual layer temperature profiles.

In the above cases, we assign 1 md as the vertical permeability between layers. In general, the vertical permeability is not likely to be higher than the lateral permeability (10-40 md). Therefore, we assume the temperature profiles for a two-layered system under 0.1 (1% of the lateral permeability) and 40 md vertical permeability to represent low and high vertical permeability cases in Figures 3.32, the other properties of which are presented in Table 3.7. In

both layers, the results under different permeabilities reach a good agreement, indicating that the magnitude of the cross-flow has a negligible effect on the temperature behaviors. On the other hand, from the analysis of Equation 3.55 in section 3.5.1, we discovered that the late time ILPR are irrelevant to vertical permeability for the undamaged reservoir, but relevant for the damaged reservoir. Therefore, the effect of vertical permeability on layer temperature profiles for the undamaged reservoir is even less. In short, the effect of layers communication on layer temperature profiles is negligible.

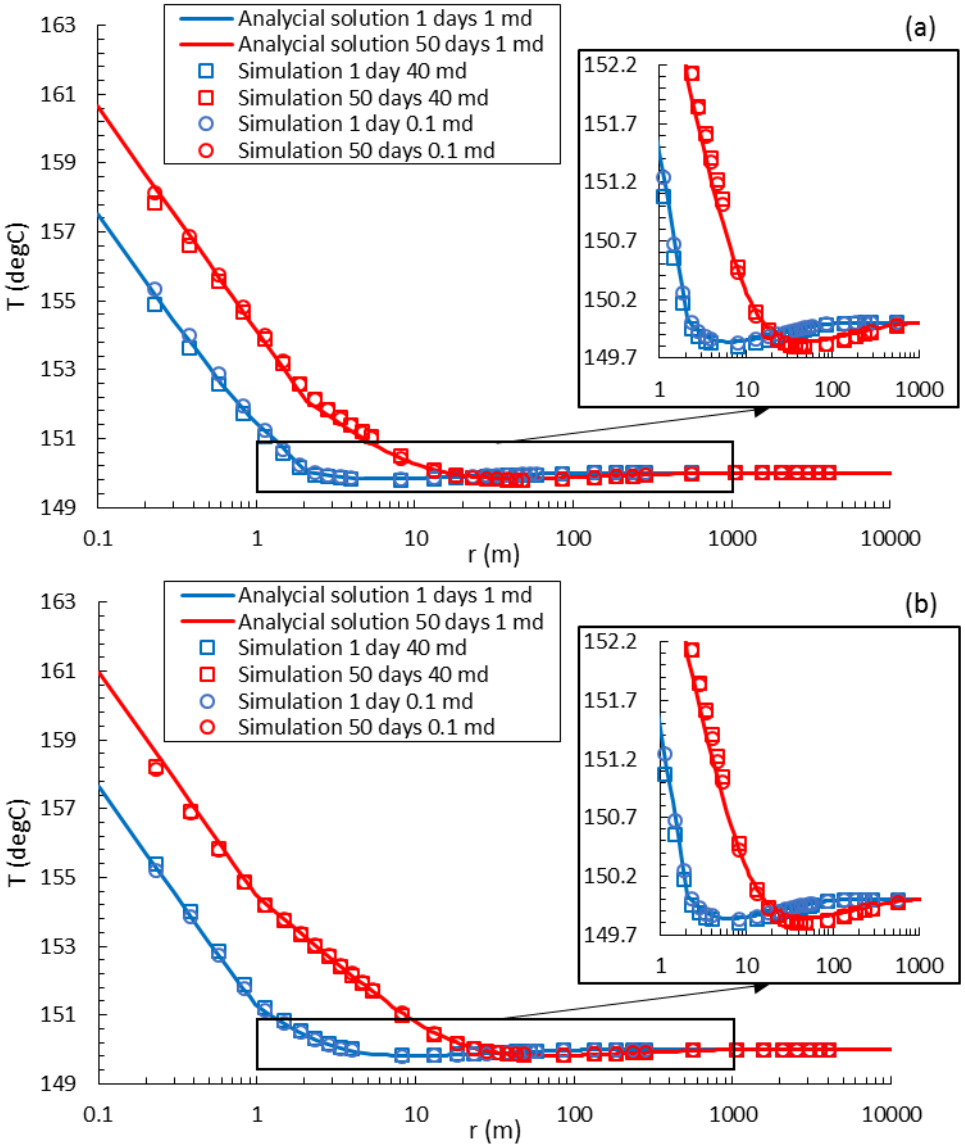

Figure 3. 32. Comparison of temperature profiles between analytical solution (vertical permeability of 1 md) and numerical simulation (vertical permeability of 0.1 and 40 md) in (a) layer 1 and (b) layer 2 for the damaged two-layered system.

As mentioned in section 3.5.1, this analytical solution to predict the individual layer temperature profiles associated with the production from a multilayer reservoir is constructed with two steps, which include identifying the ILPR for each layer and applying single layer analytical solution with ILPR. The assumptions and limitations of this analytical solution are discussed based on these two steps.

To discover the ILPR for each layer, the model assumes homogeneous and horizontal layers with different layer properties from each other. The reservoir fluid is a slightly

compressible, single-phase fluid of constant viscosity, and produced at a constant rate from the production well penetrating all the layers. These conditions are commonly assumed in transient pressure analysis to predict the pressure and rate behaviors of the produced reservoir. The only assumption that may not be valid in some circumstances is the identical fluid in all the layers. If different fluids exist in the layer of interest with no communication with other layers, numerical simulation is required to predict the temperature signals. In a thick reservoir with different properties of thin layers, assuming single-phase fluid is quite valid, which is the main focus of this research.

The known ILPR can be applied to any single layer transient temperature analytical solution to predict the individual layer temperature behaviors. Each of these solutions requires certain assumptions to obtain. One of the main controversies for the solutions to date raises from the assumption of constant viscosity and JT coefficient. These properties alter under various pressure and temperature conditions, especially in near wellbore region. However, this argument does not affect the integrity of this analytical solution. We have developed a method to account for the fluid property variations in TTA, which have not published. With this method, the analytical solution in this section can be simply revised to minimize the errors associated with this assumption.

Chapter 4. Inverse Modeling in Conventional Reservoir

After presenting the forward temperature modeling results, we develop reservoir characterization procedures from the analytical solutions. In this chapter, temperature interpretation techniques are provided based on semi-log and Cartesian plot analysis using the synthetic temperature data obtained from production and monitoring wells. For each scenario mentioned in chapter 3, specific outputs are produced from the procedures, which include permeability, porosity, damaged zone properties, Non-Darcy flow coefficient, reservoir drainage area, and reservoir shape. Decent accuracies of the estimations are achieved in this thesis.

4.1 Single Layer Homogeneous Reservoir under Transient Flow

In chapter 3, the insight of reservoir and damaged zone properties on temperature distributions have been briefly investigated by finding the slope values of temperature distributions affected by JT, AE effects. In this section, the detailed recommended procedures to apply semi-log temperature interpretations techniques to characterize the reservoir properties are presented. Reservoir and fluid properties required in order to apply this interpretation include production rates, densities and specific heats for rock and fluids, fluid properties of JT coefficient and viscosity, and reservoir properties of formation thickness and irreducible water saturation. These properties are routinely acquired from core analysis and log interpretation (Tiab and Donaldson 2012), except for specific heat capacity and JT coefficient, which are also obtainable from laboratory tests (Francis, McGlashan, and Wormald 1969, Waples and Waples 2004). Even with inadequate data for these properties, grouped reservoir properties can be acquired based on the following procedures.

1. Graph the temperature data, T, vs. the similarity variable, r^2/t, on a semi-log scale (similar to Figure 3.2).
2. Identify the JT and AE in the temperature data (indicated by the dotted lines in Figure 3.2).
3. Draw two straight lines through the temperature data affected by JT and AE effects, and find the slopes m_1 and m_2.
4. Calculate the permeability k, and parameter C_1 from the slopes using Equations 4.1 and 4.2:

$$k = \frac{1.152\mu_{JT}\mu q m_1}{2\pi H k_r} \tag{4.1}$$

$$C_1 = \frac{2\pi H k k_r m_2}{2.303\mu_{JT}\mu q} \tag{4.2}$$

5. Calculate the porosity ϕ from the parameter C_1 using Equation 4.3:

$$\phi = \frac{2\mu_{JT}C_1\rho_s c_s}{\rho_f c_f \mu_{JT} + 1 - 2\mu_{JT}C_1\left[\rho_w c_w S_{wr} + \rho_f c_f \left(1 - S_{wr}\right) - \rho_s c_s\right]} \tag{4.3}$$

4.2 Single Layer Near Wellbore Damaged Reservoir under Transient Flow

The AE effect may not be observable in the bottom-hole location with the damaged zone. Therefore, porosity needs to be independently estimated from other sources of data (e.g. well logging) to obtain reservoir and damaged zone properties from sandface temperature distribution.

1. Graph the sandface temperature data, T, vs. the production time, t, on a semi-log scale (similar to Figure 3.4).
2. Identify the time to traverse the damaged zone in the temperature data (indicated by the dotted lines in Figure 3.4).
3. Draw two straight lines before and after the traverse time, and find the slopes m_6, and m_7.
4. Calculate the permeability k from the slope m_7, using Equation 4.4:

$$k = -\frac{1.152\mu_{JT}\mu q}{2\pi m_7 H k_r} \tag{4.4}$$

5. Calculate the damaged zone permeability k_s from the slope m_6, and m_7 using Equation 4.5:

$$k_s = \frac{k m_7}{m_6} \tag{4.5}$$

6. Calculate the damaged zone radius using Equation 4.6:

$$r_s = \sqrt{r_w^2 + \frac{\rho_f c_f q t_s}{\pi H\left\{\phi\left[\rho_w c_w S_{wr} + \rho_f c_f\left(1 - S_{wr}\right)\right] + \left(1-\phi\right)\rho_s c_s\right\}}} \tag{4.6}$$

In an event where the radial temperature profile at a specific time is given, the following procedure can be used for temperature data interpretation:

1. Graph the temperature data, T, vs. the radius, r, on a semi-log scale (similar to Figure 3.3).
2. Identify the JT and AE effects, and the damaged zone radius in the temperature data (indicated by the dotted lines in Figure 3.3).
3. Draw three straight lines through the temperature data affected by JT, AE effects and damaged zone, and find the slope m_3, m_4, and m_5.
4. Calculate the permeability k, and parameter C_1 from the slopes m_3, and m_4 using Equations. 4.7 and 4.8:

$$k = \frac{2.303\mu_{JT}\mu q m_3}{2\pi H k_r} \tag{4.7}$$

$$C_1 = \frac{2\pi H k k_r m_4}{4.606\mu_{JT}\mu q} \tag{4.8}$$

5. Calculate the porosity ϕ from the parameter C_1 using Equation 4.3.
6. Calculate the damaged zone permeability k_s from the slopes m_4, and m_5 using Equation 4.9:

$$k_s = \frac{k m_4}{m_5} \tag{4.9}$$

4.3 Single Layer Reservoir with near Wellbore Non-Darcy Effect under Transient Flow

With the accurate temperature modeling introduced in section 3.3, the inversion procedures can be developed to complete the TTA process considering the non-Darcy flow effect. Based on the procedures introduced in sections 4.1 and 4.2, we first present the modified procedures for non-damaged reservoir characterization considering the non-Darcy flow effect. The synthetic data presented in Figures 4.1 and 4.2 correspond to the temperature signals obtained by numerical simulation to represent the field measurements in the same condition for Figures 3.6 and 3.7.

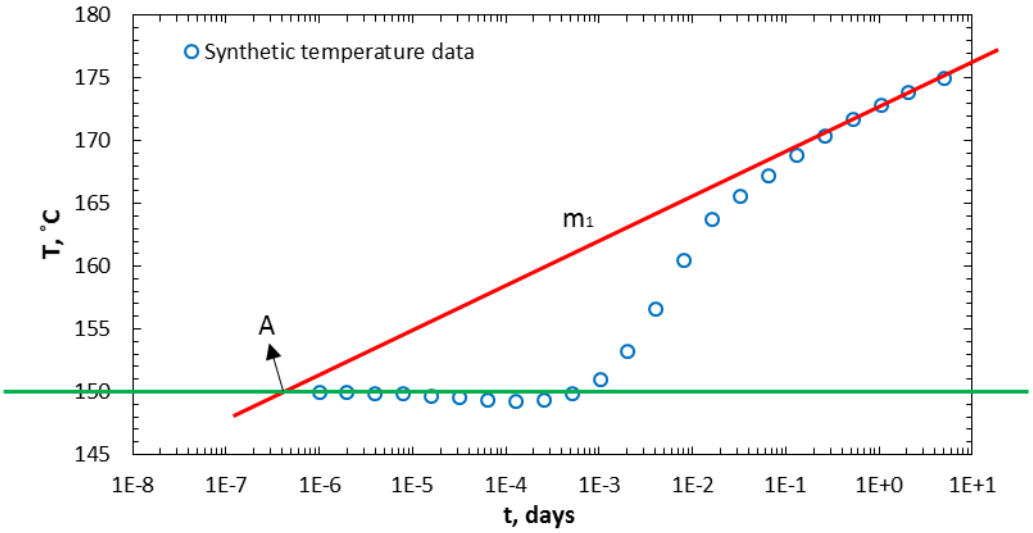

Figure 4. 1. Sandface synthetic temperature signals for a non-damaged reservoir.

The modified characterization procedures considering the non-Darcy flow effect are:

1. Graph the temperature data, T, vs. the production time, t, on a semi-log plot (Figure 4.1).
2. Identify the late time effect in the temperature data (indicated by the red line in Figure 4.1), draw a straight line through the last production time, and find the slope m_1 for it.
3. Calculate the averaged fluid properties of ρ_f, c_f, μ, μ_{JT} from the fluid property correction method introduced in chapter 5.
4. Identify the initial reservoir temperature in the temperature data (indicated by the green line in Figure 4.1), draw straight line through it, and find the intersection of the red line and green line to obtain t_A.
5. Calculate non-Darcy flow coefficient β_{ND} from the t_A and m_1 using Equation 4.10:

$$\beta_{ND} = \frac{4\pi^2 H^2 r_w m_1}{\mu_{JT} q^2 \rho_f} \log\left\{ \frac{\left\{\phi\left[\rho_w c_w S_{wr} + \rho_f c_f \left(1 - S_{wr}\right)\right] + \left(1-\phi\right)\rho_s c_s\right\}\pi H r_w^2}{86400 q \rho_f c_f t_A} \right\} \tag{4.10}$$

6. Calculate the permeability k using Equation 4.11 considering the non-Darcy flow effect:

$$k = \left| \frac{2.303\left(0.5 + \dfrac{t_{p,D} Fo}{\left(2t_{p,D}+1\right)^{1.5}}\right)\mu_{JT}\mu q}{2\pi H k_r m_1} \right| \tag{4.11}$$

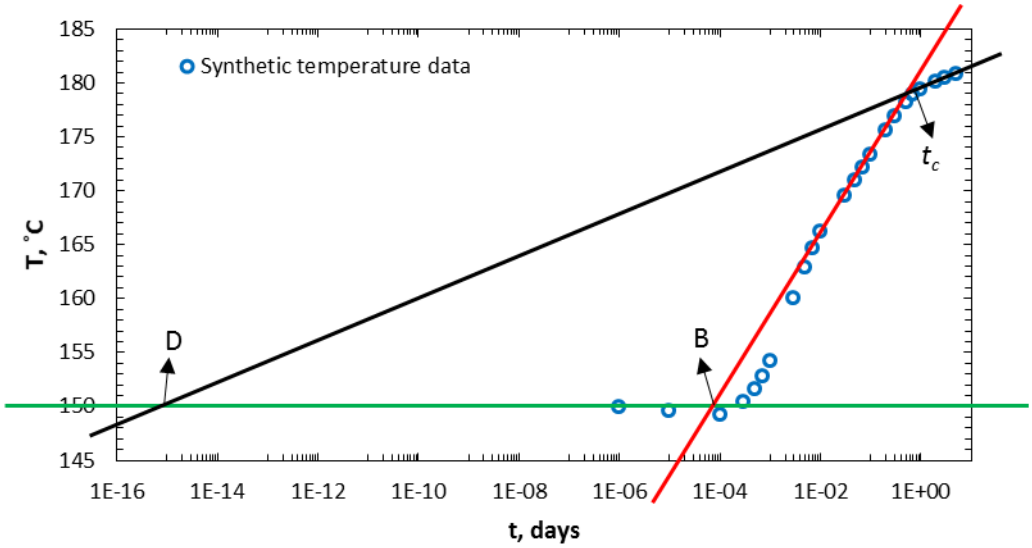

Figure 4. 2. Sandface synthetic temperature signals for a damaged reservoir.

Similar to the inversion process for the non-damaged reservoir, the slopes of the early time and late time sandface temperature behaviors in a semi-log plot can reveal the permeabilities of the damaged zone and the reservoir. Considering the non-Darcy flow effect, the early time straight line may be masked by the non-Darcy flow transition period, which has been extensively discussed in section 3.3. To accommodate the features of the non-Darcy flow effect in TTA, we modified the current characterization procedures for the damaged reservoir as below:

1. Graph the temperature data, T, vs. the production time, t, on a semi-log plot (Figure 4.2).
2. Identify the initial layer temperature (indicated by the green line in Figure 4.2) and draw a straight line through it.
3. Identify the temperature responses corresponding to the reservoir properties (indicated by the black line in Figure 4.2); draw straight lines through the last production time, and find the slope m_3.
4. Calculate the average fluid properties of ρ_f, c_f, μ, μ_{JT} from the fluid property correction method introduced in chapter 5.
5. Find the time step for the early time temperature signals deviated from the black line, which is traverse time t_c. If a straight line is observed before t_c, continue to step 6, otherwise jump to step 10.
6. Identify the temperature responses corresponding to the damaged zone properties (indicated by the red line in Figure 4.2); draw a straight line through t_c, and find the slope m_2. The intercept of the red and black lines is traverse time t_c.
7. Identify the intersection of the red line and green line to obtain t_B.
8. Calculate non-Darcy flow coefficient β_s for the damaged zone from the t_B and m_2 using Equation 4.12:

$$\beta_s = \frac{4\pi^2 H^2 r_w m_2}{\mu_{JT} q^2 \rho_f} \log\left\{ \frac{\left\{\phi\left[\rho_w c_w S_{wr} + \rho_f c_f \left(1 - S_{wr}\right)\right] + \left(1-\phi\right)\rho_s c_s\right\}\pi H r_w^2}{86400 q \rho_f c_f t_B} \right\} \tag{4.12}$$

9. Calculate the damaged zone permeability k_s from the m_2 using Equation 4.13:

$$k_s = \left| \frac{2.303\left(0.5 + \frac{t_{c,D}Fo}{\left(2t_{c,D}+1\right)^{1.5}}\right)\mu_{JT}\mu q}{2\pi H k_r m_2} \right| \tag{4.13}$$

10. Calculate the damaged zone radius using Equation 4.14:

$$r_s = \sqrt{r_w^2 + \frac{86400\rho_f c_f q t_c}{\pi H\left\{\phi\left[\rho_w c_w S_{wr} + \rho_f c_f\left(1-S_{wr}\right)\right] + \left(1-\phi\right)\rho_s c_s\right\}}} \tag{4.14}$$

11. Identify the intersection of the black line and green line to obtain t_D.
12. Calculate non-Darcy flow coefficient β_{ND} for the reservoir using Equation 4.15:

$$\beta_{ND} = \frac{4\pi^2 H^2 r_w m_3}{\mu_{JT} q^2 \rho_f} \log\left\{\frac{t_c r_w^2}{\left(r_s^2 - r_w^2\right)t_D}\right\} \tag{4.15}$$

13. Calculate the reservoir permeability k from the m_3 using Equation 4.16:

$$k = \left| \frac{2.303\left(0.5 + \frac{t_{p,D}Fo}{\left(2t_{p,D}+1\right)^{1.5}}\right)\mu_{JT}\mu q}{2\pi H k_r m_3} \right| \tag{4.16}$$

Table 4. 1. Permeability and non-Darcy flow coefficient estimates for non-damaged and damaged reservoirs.

Non-damaged reservoir	Reference	Figure 4.1	Errors (%)
Permeability (mD)	20	20.5 (Equation 4.11)	3
Non-Darcy flow coefficient (1/m)	10^{12}	1.22×10^{12} (Equation 4.10)	22
Damaged reservoir	**Reference**	**Figure 4.2**	**Errors (%)**
Reservoir permeability (mD)	20	26.6 (Equation 4.16)	33
Damaged zone permeability (mD)	10	8.7 (Equation 4.13)	13
Damaged zone radius (m)	2.2	2.34 (Equation 4.14)	6.4
Non-Darcy flow coefficient (1/m)	10^{12}	1.12×10^{12} (Equation 4.12)	12
		1.11×10^{12} (Equation 4.15)	11

The above-mentioned reservoir and damaged zone characterization procedures are applied to the synthetic data presented in Figures 4.1 and 4.2 represented the field cases for non-damaged and damaged reservoirs. We compare the properties estimations from the inversion process with those from the settings to produce the synthetic data in Table 4.1. In general, the reservoir and damaged zone characterization results show acceptable accuracies against the true values (less than 30% errors for all the cases). The estimations are exceptional

for permeability estimation of the non-damaged reservoir and damaged zone radius estimation of the damaged reservoir (less than 7% errors). The damaged zone and reservoir permeability estimations can be improved by applying multiple property corrections on the different time period, as suggested in section 5.1. The results of non-Darcy flow coefficient characterizations are in the same order of magnitude and very close to the reference values, which validate the opportunity for TTA to identify and estimate the non-Darcy flow effect. Since the evaluations of non-Darcy flow coefficient are often conducted at laboratory scale or field scale with complex multi-rate test currently, we recommend implementing TTA into the procedures to identify non-Darcy flow behaviors in the industry.

4.4 Single Layer Reservoir under Boundary Dominated Flow

The inversion process to characterize the reservoir is the ultimate goal of TTA. The validated analytical solution developed in section 3.4 can assist in achieving this goal under BDF. The procedures introduced in sections 4.1-4.3 characterize the reservoir and possible damaged zone by estimating reservoir permeability, porosity, and damaged zone properties. In this section, we will introduce the inversion procedures for TTA under BDF as an extension of previous procedures. Field measurements are represented by synthetic temperature data obtained through numerical simulation. The transient period interpretation procedures are herein extended for BDF by introducing the Cartesian plot interpretation method. The procedure is as follows:

1. Graph the temperature data, *T*, vs. the production time, *t*, on a Cartesian plot (Figure 4.3).
2. Identify the late time effect under BDF in the temperature data (indicated by the red line in Figure 4.3). Line fit the late time period data, and find the slope *m*.
3. Calculate the drainage area *A* using Equation 4.19:

$$m = \frac{86400\left[\left(\frac{q}{2\pi H}\right)^2 \frac{\mu_{JT}\mu c_f \rho_f}{k_r k r_e^2} - \frac{q\left(\rho_f c_f \mu_{JT} + 1\right)}{\pi H \hat{c}_t r_e^2}\right]}{\phi\left[\rho_w c_w S_{wr} + \rho_f c_f \left(1 - S_{wr}\right)\right] + \left(1-\phi\right)\rho_s c_s} \tag{4.17}$$

$$r_e = \sqrt{\frac{86400\left[\left(\frac{q}{2\pi H}\right)^2 \frac{\mu_{JT}\mu c_f \rho_f}{k_r k} - \frac{q\left(\rho_f c_f \mu_{JT} + 1\right)}{\pi H \hat{c}_t}\right]}{m\left\{\phi\left[\rho_w c_w S_{wr} + \rho_f c_f \left(1 - S_{wr}\right)\right] + \left(1-\phi\right)\rho_s c_s\right\}}} \tag{4.18}$$

$$A = \pi r_e^2 \tag{4.19}$$

For sandface temperature signal acquired from the production well only, the distance to the closest boundary can be identified from the traditional semi-log plot:

1. Graph the temperature data, *T*, vs. the production time, *t*, on a semi-log plot (Figure 4.4).
2. Identify the JT effect in the temperature data (indicated by the red line in Figure 4.4), draw straight line through this period, and find the first deviation point *b* from it.
3. Calculate the distance to the closest boundary *L* using Equation 4.21:

$$t_b = \sqrt{\frac{L^2}{345600\phi\mu\hat{c}_t t_b^2 k k_r}} \tag{4.20}$$

$$L = \sqrt{345600 \frac{\phi \mu \hat{c}_t t_b^2}{k k_r}} \tag{4.21}$$

Applying Equation 4.19 on the field data simulated in Figure 4.3, the drainage area can be precisely estimated. As mentioned in the parametric analysis, the first term in C_3 (Equation 3.50) is negligible. As a result, a simplified equation to estimate the drainage area is:

$$r_e = \sqrt{\frac{-86400q\left(\rho_f c_f \mu_{JT} + 1\right)}{m\pi H \hat{c}_t \left\{\phi\left[\rho_w c_w S_{wr} + \rho_f c_f \left(1 - S_{wr}\right)\right] + \left(1-\phi\right)\rho_s c_s\right\}}} \tag{4.22}$$

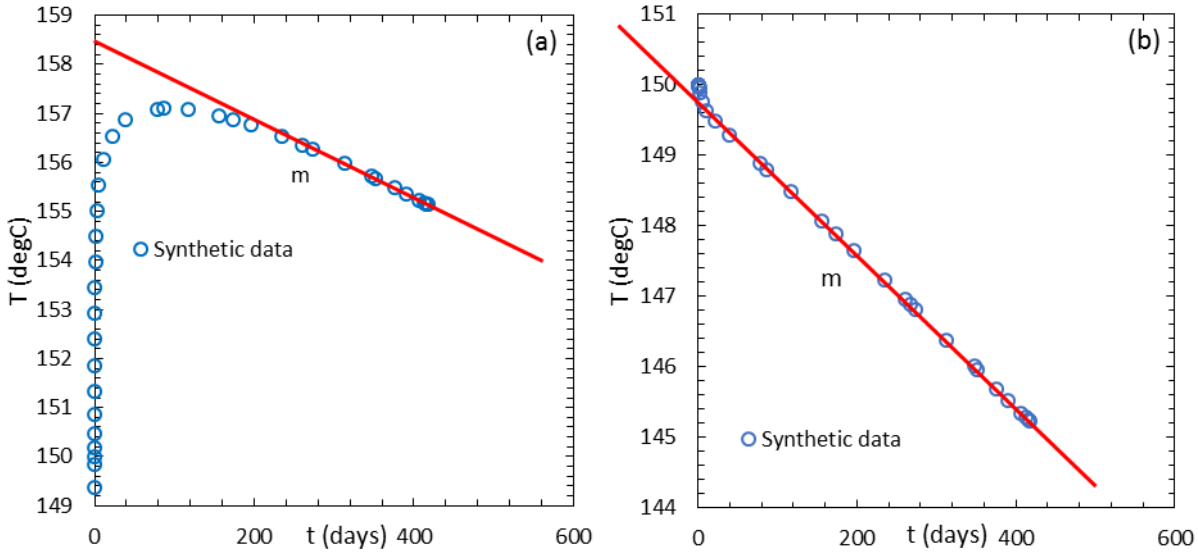

Figure 4. 3. Synthetic temperature data for the base case acquired from (a) production well and (b) observation well located 150 m from the production well.

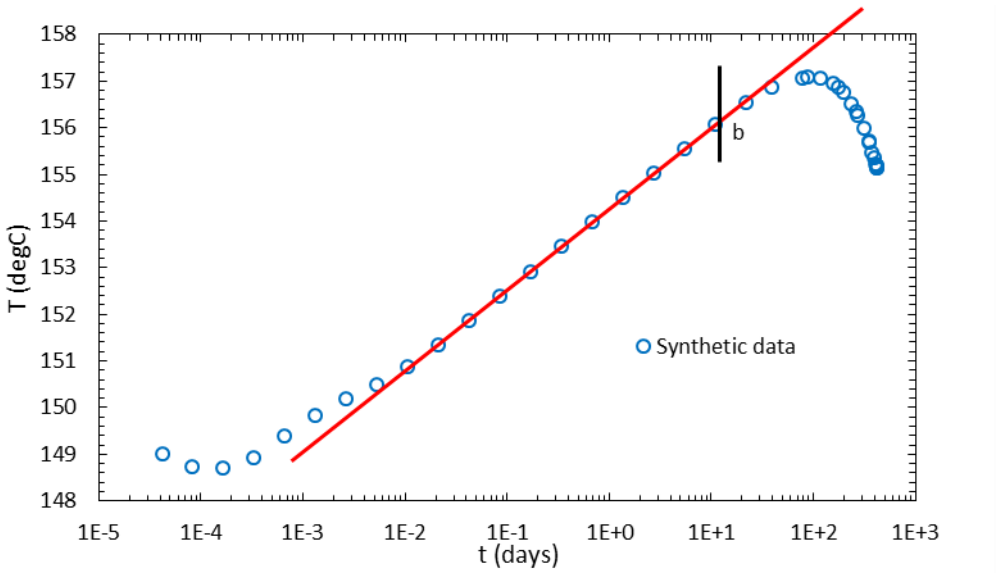

Figure 4. 4. Synthetic temperature data for the base case acquired from the production well plotted in the semi-log plot.

The estimation results for both production and observation wells are presented in Table 4.2. In both scenarios, the drainage area estimations from Equation 4.22 are very close to those from Equation 4.18, indicating that the simplification does not render too much accuracy. On

the other hand, the estimations from observation well are more accurate compared to those from the production well. This is expected since the cooling signal in observation well is purely attributed to BDAE (unless the observation is reached by JT effect front), which allows for the derivation of Equation 4.18. JT effect is the main source of the inaccurate production well temperature analysis, which does not influence the observation well measurements. Therefore, TTA from observation wells under BDF may be more reliable compared to TTA from the production well under the same conditions.

The estimation of the distance to the closest boundary from Equation 4.20 is also in very good agreement with the reference value. In practice, if this estimation is similar to the results from Equation 4.18 or 4.22, the reservoir shape should be close to a circular reservoir. Otherwise, the estimation suggests a higher aspect ratio (ratio of length to width) of the target reservoir. In short, comparing the estimations of drainage area and distance to the closest boundary may help to identify the reservoir shape from TTA.

Table 4. 2. Drainage area and distance to the closest boundary estimations from Figures 4.3 and 4.4.

Production well	Reference	Figures 4.3 and 4.4	Errors (%)
r_e estimation from Equation 4.18 (m)	300	318.3	6.1
r_e estimation from Equation 4.22 (m)	300	318.8	6.3
L estimation from Equation 4.21 (m)	300	287.2	4.3
Observation well	Reference	Figure 4.3	Errors (%)
r_e estimation from Equation 4.18 (m)	300	299.4	0.2
r_e estimation from Equation 4.22 (m)	300	299.9	0.03

4.5 Multi-Layer Reservoir

Detailed reservoir characterization procedures based on temperature transient for a single layer reservoir has been presented in sections 4.1-4.4. Additional procedures are required for a multilayer reservoir since the ILPR is not identified and is related to individual layer properties. Therefore, two unknowns (layer permeability and ILPR) need to be identified from the JT effect of the temperature signals, which requires two values determined from the JT effect of the temperature signals. We select the slopes (indicated by the black lines in Figure 4.5) of the temperature signals and the intercepts (indicated by A_i in Figure 4.5) between temperature signals and initial layer temperature (indicated by the green line in Figure 4.5) as these two values obtained from the temperature signals. The temperature signals associated with the JT effect are presented by the first term in Equation 3.15. Therefore, the slopes of the temperature signals in the near wellbore region in a semi-log plot (T vs r^2/t) are $1.152\mu_{JT}\mu q_i/(2\pi h_i k_i k_r)$. If we neglect the minor effect of AE effect on the intercepts, which can be calculated by JT effect only as:

$$\left[\frac{r^2}{t}\right]_{A_i} = \frac{\rho_f c_f q_i}{\left\{\phi_i\left[\rho_w c_w S_{wri} + \rho_f c_f\left(1-S_{wri}\right)\right] + \left(1-\phi_i\right)\rho_s c_s\right\}\pi h_i} \tag{4.23}$$

If the AE effect is observable, additional reservoir properties can be revealed from the slope of AE effect (indicated by the red line in Figure 4.5), which is represented by the second

and third terms in Equation 3.15. As a result, the slopes of the temperature signals associated with AE effect are $2.303C_{1i}\mu_{JT}\mu q_i/(2\pi h_i k_i k_r)$.

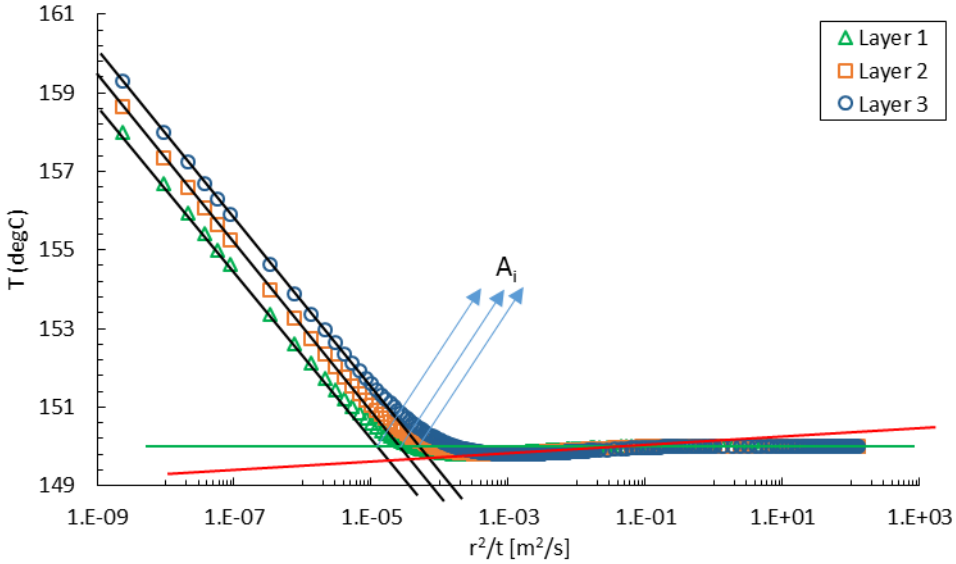

Figure 4. 5. Synthetic temperature signals for a three-layered system in an undamaged multilayer reservoir.

A procedure to characterize the individual layer properties of an undamaged multilayer reservoir is introduced below. The synthetic data are the temperature signals for a three-layered model and generated by numerical simulation to represent the field measurements.

1. Graph the temperature data from each layer, T, vs. the similarity variable, r^2/t, on a semi-log scale (Figure 4.5).
2. Identify the JT effect and initial layer temperature in the temperature data (indicated by the black and green lines in Figure 4.5), draw straight lines through them, and find the slope m_{1i} for black lines.
3. Identify the intersection of black lines with the green line to obtain A_i.
4. Calculate the ILPR q_i from the A_i using Equation 4.24:

$$q_i = \frac{\left\{\phi_i\left[\rho_w c_w S_{wri} + \rho_f c_f\left(1-S_{wri}\right)\right]+\left(1-\phi_i\right)\rho_s c_s\right\}\pi h_i\left[\frac{r^2}{t}\right]_{A_i}}{\rho_f c_f} \tag{4.24}$$

5. Calculate the layer permeability k_i from m_{1i} using Equation 4.25:

$$k_i = \frac{1.152\mu_{JT}\mu q_i m_{1i}}{2\pi h_i k_r} \tag{4.25}$$

6. If the AE is visible, draw straight lines through them (indicated by the red lines in Figure 4.5), and find the slope m_{2i} for red lines.
7. Calculate parameter C_{1i} from the m_{2i} using Equation 4.26:

$$C_{1i} = \frac{2\pi h_i k_i k_r m_{2i}}{2.303\mu_{JT}\mu q_i} \tag{4.26}$$

8. Calculate the porosity ϕ_i from the parameter C_{1i} using Equation 4.27:

$$\phi_i = \frac{2\mu_{JT}C_{1i}\rho_s c_s}{\rho_f c_f \mu_{JT} + 1 - 2\mu_{JT}C_{1i}\left[\rho_w c_w S_{wr} + \rho_f c_f\left(1-S_{wri}\right) - \rho_s c_s\right]} \tag{4.27}$$

It was mentioned above that the AE effect may be masked by the thermal wellbore storage. In that case, characterization procedures can be implemented from steps 1-5 to obtain ILPR and permeability only.

These methods to characterize layer permeability and ILPR can be executed based on the prior knowledge of multiple layer properties, which include densities and specific heat capacities for fluid and rock, layer thickness, porosity and irreducible water saturation, and fluid JT coefficient and viscosity. If these properties are not available or imprecise, the layer permeability and ILPR cannot be accurately determined. In this case, instead of acquiring permeability and production rates for each layer, we propose to obtain the permeability and production rates ratio between layers, which are less dependent on those indefinite properties. These ratios can be easily derived from Equations 4.24 and 4.25 assuming identical densities and specific heat capacities for fluid and rock, layer porosity, and irreducible water saturation between layers:

$$\frac{q_i}{q_j} = \frac{h_i \left[\frac{r^2}{t}\right]_{A_i}}{h_j \left[\frac{r^2}{t}\right]_{A_j}} \tag{4.28}$$

$$\frac{k_i}{k_j} = \frac{m_{1i} \left[\frac{r^2}{t}\right]_{A_i}}{m_{1j} \left[\frac{r^2}{t}\right]_{A_j}} \tag{4.29}$$

Indicated by Equations 4.28 and 4.29, the ratio of ILPR is the product of layer thickness and the intercepts, and the ratio of layer permeability is the product of slopes and intercepts. Therefore, the ratio of layer permeability can be determined from the temperature signals without the knowledge of other properties.

Similar to the above procedures, the slopes of the damaged zone and layer temperature behaviors can be used to evaluate the permeabilities of the damaged zone and the layer. And the intercept between temperature signals in the damaged zone and the initial layer temperature can be used to obtain the ILPR. From Equation 3.28, the values of two slopes on temperature profiles before (m_3) and after (m_4) the traverse time are $2.303\mu_{JT}\mu q_i/(2\pi h_i k_i k_r)$, and $2.303\mu_{JT}\mu q_i/(2\pi h_i k_{si} k_r)$, respectively. The traverse time can be related to the radius of the damaged zone from the last term in Equation 3.28 (Heaviside's unit function), while the intercepts remain the same as Equation 4.23 with r_w instead of r.

Based on the above theory, the characterization methods to obtain the damaged zone and layer properties of a multilayer reservoir are presented below.

1. Graph the temperature data from each layer, T, vs. the production time, t, on a semi-log scale (Figure 4.6).
2. Identify the damaged zone and reservoir temperature behaviors in the temperature data (indicated by the black and red lines in Figure 4.6), draw straight lines through them, and find the slope m_{3i} for black lines and m_{4i} for red lines.
3. Identify the initial layer temperature (indicated by the green line in Figure 4.6) and draw straight lines through them.
4. Identify the intersection of black lines and green line to obtain B_i.
5. Calculate the ILPR q_i from the B_i using Equation 4.30:

$$q_i = \frac{\left\{\phi_i\left[\rho_w c_w S_{wri} + \rho_f c_f \left(1 - S_{wri}\right)\right] + \left(1-\phi_i\right)\rho_s c_s\right\}\pi h_i r_w^2}{\rho_f c_f t_{B_i}} \tag{4.30}$$

6. Calculate the layer permeability k_i from the m_{4i} using Equation 4.31:

$$k_i = -\frac{1.152\mu_{JT}\mu q_i}{2\pi h_i k_r m_{4i}} \tag{4.31}$$

7. Calculate the damaged zone permeability k_{si} from the m_{3i} using Equation 4.32:

$$k_{si} = \frac{k_i m_{4i}}{m_{3i}} \tag{4.32}$$

8. Calculate the damaged zone radius using Equation 4.33:

$$r_{si} = \sqrt{r_w^2 + \frac{\rho_f c_f q_i t_{si}}{\pi h_i \left\{\phi_i \left[\rho_w c_w S_{wri} + \rho_f c_f \left(1 - S_{wri}\right)\right] + \left(1-\phi_i\right)\rho_s c_s\right\}}} \tag{4.33}$$

As mentioned in section 3.5, the uncertainties of applying this characterization method still exist due to the possibility of missing or inaccurate reservoir and fluid properties. For the damaged layers, we propose similar simplified procedures to obtain the permeability and production rates ratio between layers, as well as the ratio of damaged zone permeability between layers, derived from Equations 4.30 to 4.32:

$$\frac{q_i}{q_j} = \frac{h_i t_{B_j}}{h_j t_{B_i}} \tag{4.34}$$

$$\frac{k_i}{k_j} = \frac{m_{4j} t_{B_j}}{m_{4i} t_{B_i}} \tag{4.35}$$

$$\frac{k_{si}}{k_{sj}} = \frac{m_{3j} t_{B_j}}{m_{3i} t_{B_i}} \tag{4.36}$$

Similar to the ratio of layer permeability, the ratio of damaged zone permeability can be acquired from the temperature signals without the knowledge of other properties.

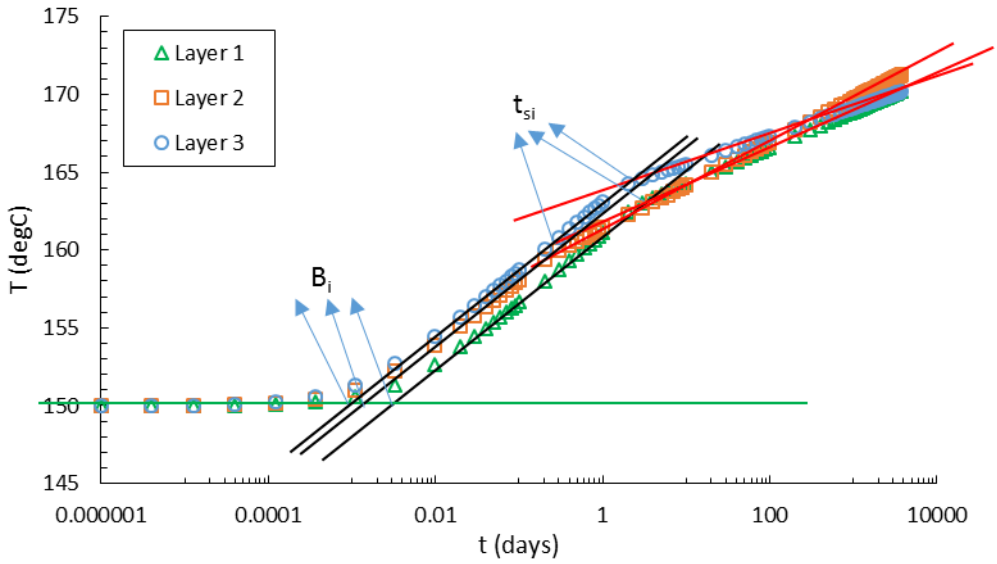

Figure 4. 6. Synthetic temperature signals for a three-layered system in a damaged multilayer reservoir.

Due to the limited availability of the inflow temperature field data from multilayer reservoir, we are not able to explore the temperature field data from multilayer pays. However, single layer inflowing temperature field data for a multilayer reservoir is accessible from

Ramazanov et al. (2010). In this section, we perform the interpretation techniques presented in section 3.5.2 to analyze the data of Figure 4.4 from Ramazanov et al. (2010). Based on the required information defined in section 3.5.2, this field case provides the layer thickness of 5 m, volumetric heat capacity ratio of fluid to saturated matrix of 1.2, m_3 of 0.5315, m_4 of 0.361, t_B of 0.002273 days, t_s of 0.0261 days, casing inner diameter of 0.065 m, and fluid JT coefficient of -0.22 K/MPa. With the validated ILPR estimation from the field data to the analytical solution, these interpretation techniques can be extended from this single-layer to a multilayer reservoir.

We first calculate the ILPR for this layer. The wellbore radius is represented by the monitoring location positioned at the inner casing, which assumes to be 0.06 m (less than 0.065 m). From Equation 4.28, the estimated ILPR from field data is 20.7 m^3/day. Secondly, the layer mobility (k/μ) and the damaged/undamaged permeability ratio can be calculated from Equations 4.29 and 4.30, which are 4.86 mD/cp and 1.47. Finally, the skin factor is evaluated from the estimated radius of the damaged zone, which is obtained from Equation 4.31 to be 0.212 m. As a result, the skin factor is 0.593. A summary of comparison between the estimated values from interpretation techniques in this section and the counterparts obtained by field measurements and estimation from Ramazanov et al. (2010) is illustrated in Table 4.3. All the estimated values are very close to those from the reference, suggested that the interpretation techniques are feasible to perform characterization on TTA from field data.

Table 4. 3. Comparison of estimated values in this section and those from Ramazanov et al. (2010).

	This section	Ramazanov et al. (2010)	Error (%)
Layer mobility (mD/cp)	5.35	4.9	9.2
Undamaged/damaged permeability ratio	1.47	1.47	-
Radius of the damaged zone (m)	0.212	0.25	15.2
Skin factor	0.593	0.6	1.2

Chapter 5. Effect of Fluid Property and Production Rate Variations on Temperature Transient Analysis in Conventional Reservoir

In chapters 3 and 4, we performed the forward and inverse modeling using newly developed analytical solutions. Although it is convenient to apply the analytical solutions, their scopes are limited to the assumptions made for the derivation. In this chapter, we address two main assumptions of constant fluid property and production rates, which can be invalid in field cases with high drawdown and complex production history.

5.1 Accounting for Fluid Property Variation in Temperature Transient Analysis

Significant fluid property variation can be induced due to pressure and temperature dynamics in the reservoir associated with oil production. The existing analytical solutions for TTA generally assume constant fluid properties, which can be invalid especially for cases of high drawdown and strong temperature signals. In this section, we present a method to account for the fluid property variations in TTA. The corrections are performed on four identified fluid properties in an iterative manner which can be easily implemented in available temperature analysis procedures. Through application to example problems, we show that using fluid property correction method presented herein can improve the permeability estimations by 60% for the conditions considered in this section. With these improvements, the applicability of TTA using analytical solutions can be extended from cases with limited sandface temperature signals of a few degC to stronger signals of 20-30 degC.

5.1.1 Problem Description and Methodology

In this section, we develop a method to account for the fluid property variations in TTA. To examine the extent and scope of this effect, we compare the transient temperature signals modeled analytically in section 3.1 (drawdown test) and by Palabiyik et al. (2016) (buildup test), and using numerical simulation. The temperature profiles are modeled in the same oil reservoir presented by App (2010). The numerical simulations are performed using a commercial reservoir simulation software (CMG-GEM 2015). The reservoir fluid is produced from a vertical well with the downhole production rate of 986 m^3/day for 5 days drawdown period (t_p) followed by 15 days shut-in period (t_s), same as those settings in Palabiyik et al. (2016). It is worthy of notice that the numerical simulation is tailored to satisfy the assumptions made to derive the analytical solutions, which include radial flow with no vertical cross-flow, neglecting the geothermal gradient, and homogeneous reservoir. Therefore, this numerical model is a single-layer radial model. If a thick reservoir with significant geothermal gradient is encountered, vertical refinement can be used to make multilayer system with different T_i for each layer. For the damaged reservoir introduced later in section 5.1.2, a different permeability zone is added outside the production well with a constant radius to represent the near wellbore damage (Figure 3.1).

Based on the flash calculations from CMG-WINPROP (2015), the thermo-physical properties of the reservoir fluid at the initial reservoir condition and sandface conditions at the end of production period (t_p) and end of buildup period (t_s) are presented in Table 5.1 and used as references in analytical modeling.

Figure 5.1 presents the comparison between the analytical solution and numerical simulation for transient drawdown and buildup temperature profiles. The analytical solutions are presented considering fluid properties in two endpoint conditions. For the drawdown period, the two endpoints are the sandface pressure and temperature at initial reservoir conditions (at t_0) and those at end of the production period (at t_p). Same conditions for the buildup test occur

at end of production (at t_p) and at end of buildup period (at t_s). The analytically modeled drawdown and buildup temperature profiles at the two endpoint conditions diverge from the numerical simulation results (especially at the late time) in which variation of fluid properties are considered. These modeling errors are most significant for the drawdown test, which results in more than 9 degC temperature differential at t_p (70% of the total sandface temperature signal observed). The errors for buildup period are slightly better (more than 6 degC temperature differentials at t_s) due to the stabilized pressure and temperature profiles with minimized fluid dynamics on the shut-in period. The simulated temperature signals, which consider the fluid property variations in the reservoir, do not agree with either temperature profiles modeled analytically. Therefore, the fluid property variations must be taken into account in the analytical solution.

Table 5. 1. Fluid properties at various pressure and temperature conditions.

	Initial reservoir conditions at t_0	End-of-drawdown sandface conditions at t_p	End-of-buildup sandface conditions at t_s	Max variation (%)
Specific heat (J/kg/K)	2202	2340	2230	6.3
Density (kg/m^3)	840	777.5	837.2	7.4
JT coefficient (K/MPa)	-0.445	-0.448	-0.439	2
Fluid viscosity (mPa·s)	3.686	2.323	3.577	37
Pressure (MPa)	144.8	79.9	143.3	44.8
Temperature (degC)	150	163	156	9.3

The simulated transient temperature signals in Figure 5.1 present nearly straight lines (quasi-linear behaviors) in these semi-log plots. This indicates the potential to average each fluid property to account for the effects of fluid property variations in modeling the transient temperature signals. The temperature discrepancies in Figure 5.1, which are dominated by the JT effect of drawdown test and thermal conduction for buildup test, occur at the late time. Therefore, the proposed method to address the fluid property variation should be applied to the region affected by the JT effect and thermal conduction for drawdown and buildup tests respectively. The drawdown transient temperature signal induced by JT effect can be modeled by (first term in Equation 3.15):

$$\frac{4\pi Hk_r k}{\mu\mu_{JT}}\boxed{\frac{\left(T_{sf}-T_i\right)}{q}}=-\ln\left(1+\left\{\frac{\rho_f c_f}{\phi\left[\rho_w c_w S_{wr}+\rho_f c_f\left(1-S_{wr}\right)\right]+\left(1-\phi\right)\rho_s c_s}\right\}\frac{\boxed{tq}}{\pi r_{sf}^2 H}\right) \tag{5.1}$$

And the asymptotic solution to model late-time temperature profiles for buildup is (Palabiyik et al. 2016):

$$\frac{4\pi Hk_r k\left(T_{sf}-T_{p,sf}\right)}{\mu\mu_{JT}q}=-Ei\left(\frac{K_m r_{sf}^2}{4\left\{\phi\left[\rho_w c_w S_{wr}+\rho_f c_f\left(1-S_{wr}\right)\right]+\left(1-\phi\right)\rho_s c_s\right\}\left(t-t_p\right)}\right) \tag{5.2}$$

We use the late-time approximate analytical solutions (Equations 5.1 and 5.2) since the fluid property variations are most significant in this time period. Therefore, the early-time

differences between analytically and numerically modeled temperature profiles are expected since they are dominated by the AE effect.

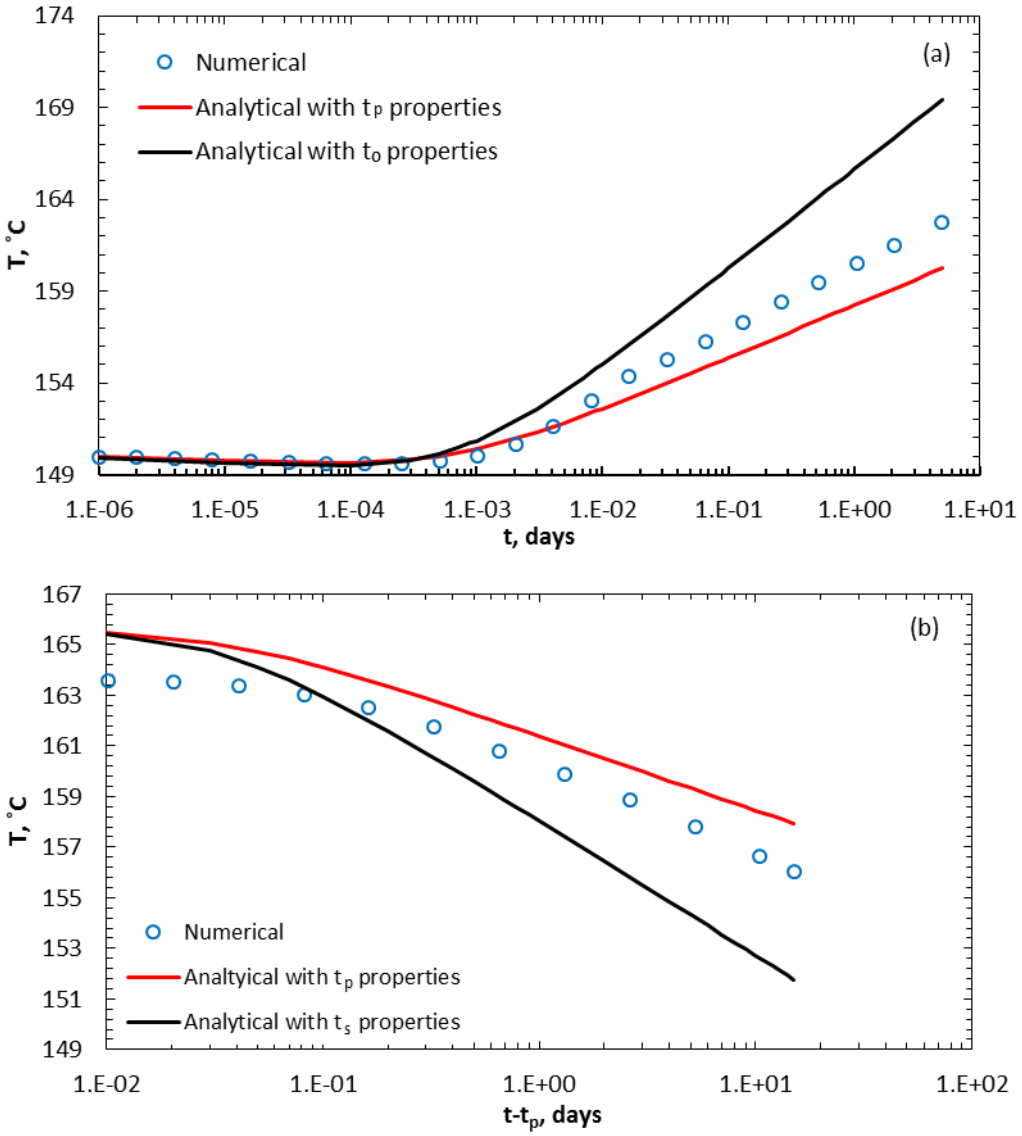

Figure 5. 1. Comparison of transient temperature profiles for (a) drawdown and (b) buildup between the analytical solution and numerical simulation.

From Equations 5.1 and 5.2, the fluid properties affecting the temperature response are JT coefficient, viscosity, density, and specific heat. The transient temperature is a function of the production time for drawdown or shut-in time for buildup, where the four fluid properties differently affect this functionality. The density and specific heat of the producing fluid are directly multiplied by time, and as a group, muted by the logarithmic function. To account for the variations of these two, the density and specific heat of fluid requires arithmetic average over time when the JT effect dominates for drawdown or conduction controls for buildup. Similar techniques have been applied and validated in Vilarrasa et al. (2010). To be specific, the fluid property correction methods for density and specific heat are (Equation 5.3 for drawdown and Equation 5.4 for buildup):

$$\overline{\rho c} = \frac{1}{t_p - t_{JT}} \int_{t_{JT}}^{t_p} \rho c\left(p, T\right) dt \tag{5.3}$$

$$\overline{\rho c} = \frac{1}{t_s - t_p}\int_{t_p}^{t_s} \rho c\left(p,T\right)dt \tag{5.4}$$

where t_{JT} is the time at the start of JT effect. t_{JT} can be calculated from the radius of investigation of the JT effect (section 3.1). For practical purposes, it can be estimated from the time at which the temperature exceeds the initial reservoir temperature. The AE effect preceding the JT effect causes a slight cooling effect.

On the contrary to the functionalities of density and specific heat, JT coefficient and viscosity affect the transient temperature signals in another way. For the drawdown temperature profile calculated from Equation 5.1, the late-time JT effect presents a quasi-linear behavior on the semi-log plot (Figure 5.1a), the slope of which is directly proportional to JT coefficient and viscosity. Here, we derive a method to account for these two fluid properties from the constant slope value of the quasi-linear behavior. To develop this averaging method, we start with taking derivative of Equation 5.1considering the input from Equation 5.3:

$$\frac{4\pi Hk_r k}{\mu\mu_{JT} q}dT_{sf} = -\frac{\dfrac{\overline{\rho_f c_f}}{\phi\left[\rho_w c_w S_{wr} + \overline{\rho_f c_f}\left(1-S_{wr}\right)\right] + \left(1-\phi\right)\rho_s c_s}\dfrac{q}{\pi r_{sf}^2 H}}{1+\left\{\dfrac{\overline{\rho_f c_f}}{\phi\left[\rho_w c_w S_{wr} + \overline{\rho_f c_f}\left(1-S_{wr}\right)\right] + \left(1-\phi\right)\rho_s c_s}\right\}\dfrac{tq}{\pi r_{sf}^2 H}}dt \tag{5.5}$$

During the late-time JT effect, the RHS denominator of Equation 5.5 is controlled by the second term. As a result, Equation 5.5 becomes:

$$\frac{4\pi Hk_r k}{\mu\mu_{JT} q}dT_{sf} = -\frac{dt}{t} \tag{5.6}$$

Integrating Equation 5.6 from t_{JT} to t_p provides:

$$\frac{4\pi Hk_r k}{q}\int_{t_{JT}}^{t_p} dT_{sf} = -\int_{t_{JT}}^{t_p} \mu\mu_{JT}\frac{dt}{t} \tag{5.7}$$

As a result, the slope of the late-time temperature profile in a semi-log plot is:

$$\frac{T_{sf,p} - T_{sf,JT}}{\ln\left(\dfrac{t_p}{t_{JT}}\right)} = -\frac{q}{4\pi Hk_r k}\frac{\displaystyle\int_{t_{JT}}^{t_p} \mu\mu_{JT}\frac{dt}{t}}{\ln\left(\dfrac{t_p}{t_{JT}}\right)} \tag{5.8}$$

The quasi-linear behavior of JT effect dictates that this slope value should be close to a constant. Therefore, we use the last term of Equation 5.8 as the average value of JT coefficient and viscosity product, which is a nearly constant value:

$$\overline{\mu\mu_{JT}} = \frac{\displaystyle\int_{t_{JT}}^{t_p} \mu\mu_{JT}\left(p,T\right)\frac{dt}{t}}{\ln\left(\dfrac{t_p}{t_{JT}}\right)} \tag{5.9}$$

The averaging technique applied in Equation 5.9 is a harmonic mean, which makes the minimum of the arguments dominant. Comparable methods of applying both arithmetic and harmonic means under different scenarios successfully address the permeability upscaling by heterogeneity index (Tiab and Donaldson 2015).

The effects of viscosity and JT coefficient variations on buildup do not come from the shut-in period since the dominating thermal conduction is irrelevant to these two properties. Instead, these effects are due to the initial condition of the temperature profile at t_p mainly

dominated by the JT effect during the drawdown period. Therefore, the property correction method of viscosity and JT coefficient for buildup test should be based on its drawdown period, which is also represented by Equation 5.9.

The dependences of these four fluid properties under pressure and temperature conditions are generally non-linear. In this study, we use CMG-WINPROP (2015) to simulate these fluid properties under various pressure and temperature conditions. We present two types of temperature modeling in this section: (1) forward modeling to predict the temporal temperature profiles for known fluid and reservoir properties and, (2) inverse modeling to estimate reservoir properties from temperature data. For the inversion process, the field measurements of pressure and temperature are available and can be applied to calculate the required fluid property values in the correction method. With the given reservoir properties and production parameters in the forward modeling approach, the transient temperature profiles can be represented by Equation 3.15, and the pressure distribution can be estimated from the transient pressure solution for slightly compressible fluid (Theis 1935), given by Equation 5.10 for drawdown and Equation 5.11 for buildup:

$$\boxed{\frac{\left(p_{sf}-p_i\right)}{q}}=\frac{\mu}{kh}Ei\left(-\frac{\phi\mu\hat{c}_t r_w^2}{k\boxed{t}}\right) \tag{5.10}$$

$$p(r_{sf},t)-p_i=-\frac{\mu q}{4\pi Hk_r k}\ln\left(\frac{t}{t-t_p}\right) \tag{5.11}$$

The pressure profiles obtained from Equations 5.10 and 5.11 are also affected by the fluid property variations, to be specific, the viscosity and compressibility variations. Precise estimations of pressure profiles are critical to the forward modeling of temperature transient since the fluid properties are calculated based on pressure and temperature conditions. Therefore, we develop similar averaging techniques to account for the viscosity and compressibility variations for transient pressure estimations:

$$\overline{\mu}=\frac{\int_{t_o}^{t_p}\mu\left(p,T\right)\frac{dt}{t}}{\ln\left(\frac{t_p}{t_o}\right)} \tag{5.12}$$

$$\overline{c_t}=c_r+\frac{1}{t_p-t_0}\int_{t_0}^{t_p}c_o\left(p,T\right)dt \tag{5.13}$$

And for the buildup test:

$$\overline{\mu}=\frac{\int_{t_p}^{t_s}\mu\left(p,T\right)\frac{dt}{t}}{\ln\left(\frac{t_s}{t_p}\right)} \tag{5.14}$$

An iterative algorithm is introduced to resolve the non-linearity of the fluid properties dependence on pressure and temperature. As these four properties vary moderately with pressure and temperature, the approximations can be achieved quickly within several iterations. The detailed procedure of this algorithm is:

1. Determine initial estimates of the fluid density, specific heat, viscosity, and JT coefficient (e.g. under initial reservoir pressure and temperature condition).

2. Obtain the temperature and pressure data or calculate the temperature and pressure profiles within the time period of interest using Equations 5.1 and 5.10 for drawdown and 5.2 and 5.11 for buildup.
3. Calculate the temporal distributions of the four fluid properties.
4. Calculate the average fluid properties within the time period of interest using Equations 5.3, 5.9, 5.12, and 5.13 for drawdown and 5.4, 5.9, and 5.14 for buildup.
5. Check if the average fluid properties and the estimations before this step of iteration are within the predetermined convergence criteria. Repeat steps 2-5 until the convergence criteria are fulfilled. The fluid property corrections for temperature transient estimations are obtained from Equations 5.3, 5.4, and 5.9, while those to calculate pressure profiles are acquired from Equations 5.12-5.14. All these averaged values are required to pass the convergence criteria, or otherwise are subject to another round of the iterative process.

A flow chart to demonstrate this procedure is presented in Figure 5.2.

The above procedures are suitable for a non-damaged reservoir where the late-time temporal temperature profiles behave quasi-linearly on a semi-log plot. However, for a damaged reservoir, two quasi-linear behaviors can be observed due to different permeabilities in the damaged zone and undamaged zone. For this case, the fluid property corrections are performed separately based on whether the time period is dominated by the damaged zone properties. We will perform this two-time-period approach in a damaged reservoir in the next section.

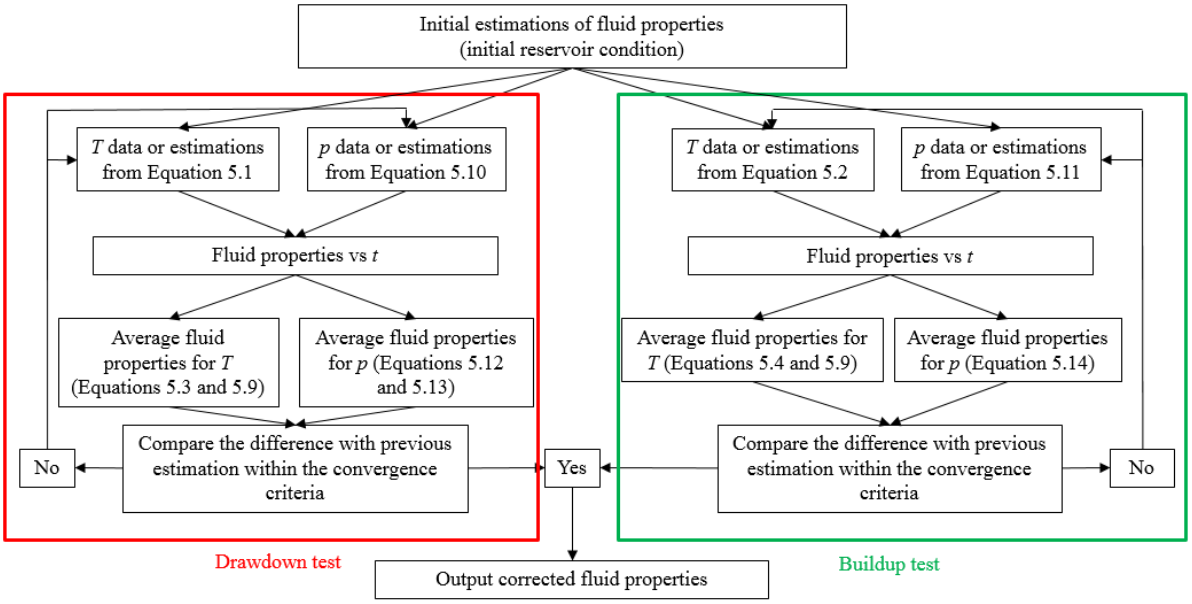

Figure 5. 2. Flowchart of the iterative algorithm to obtain corrected fluid properties.

5.1.2 Sensitivity Analysis of Fluid Properties

In this section, we perform a sensitivity analysis to identify the contribution of each fluid property on the transient temperature signals. Based on Equations 5.1 and 5.2, we have identified the variations of four fluid properties due to dynamic pressure and temperature conditions, which are density, specific heat, viscosity and JT coefficient. The functionalities of these fluid properties on the temperature profile are different, which is briefly discussed while developing the averaging algorithm. On the other hand, the pressure and temperature dependencies of these fluid properties are distinct. This section provides a sensitivity analysis to identify the primary fluid properties affecting the transient temperature signals.

We compare the fluid properties in three conditions in Table 5.1. The viscosity shows the highest variation among the four, which suggests that the viscosity is most sensitive to the dynamic pressure and temperature conditions. Furthermore, the effects of fluid property variations on the temperature profiles are investigated and presented in Figure 5.3. Two red curves display the temperature profiles with all the fluid properties at t_0 and t_p for drawdown, t_p and t_s for buildup. For the drawdown test, the curves for each fluid property represent the temperature profile obtained with the specific fluid property at t_p while the other fluid properties remain at t_0. For the buildup test, the fluid properties vary from t_p to t_s condition.

Among the four fluid properties, changing the specific heat, density and JT coefficient cause negligible changes in the temperature profile. Viscosity appears to play a major role in shifting the temperature profile to closely match the profile when all the fluid properties are evaluated at t_p for drawdown test. This finding, along with the property percent change comparisons presented in Table 5.1, demonstrates that the viscosity is the dominating property on the transient temperature response among four fluid properties. Therefore, the fluid property correction method can be simplified by applying the correction only on viscosity. This simplified method will be examined in the next section.

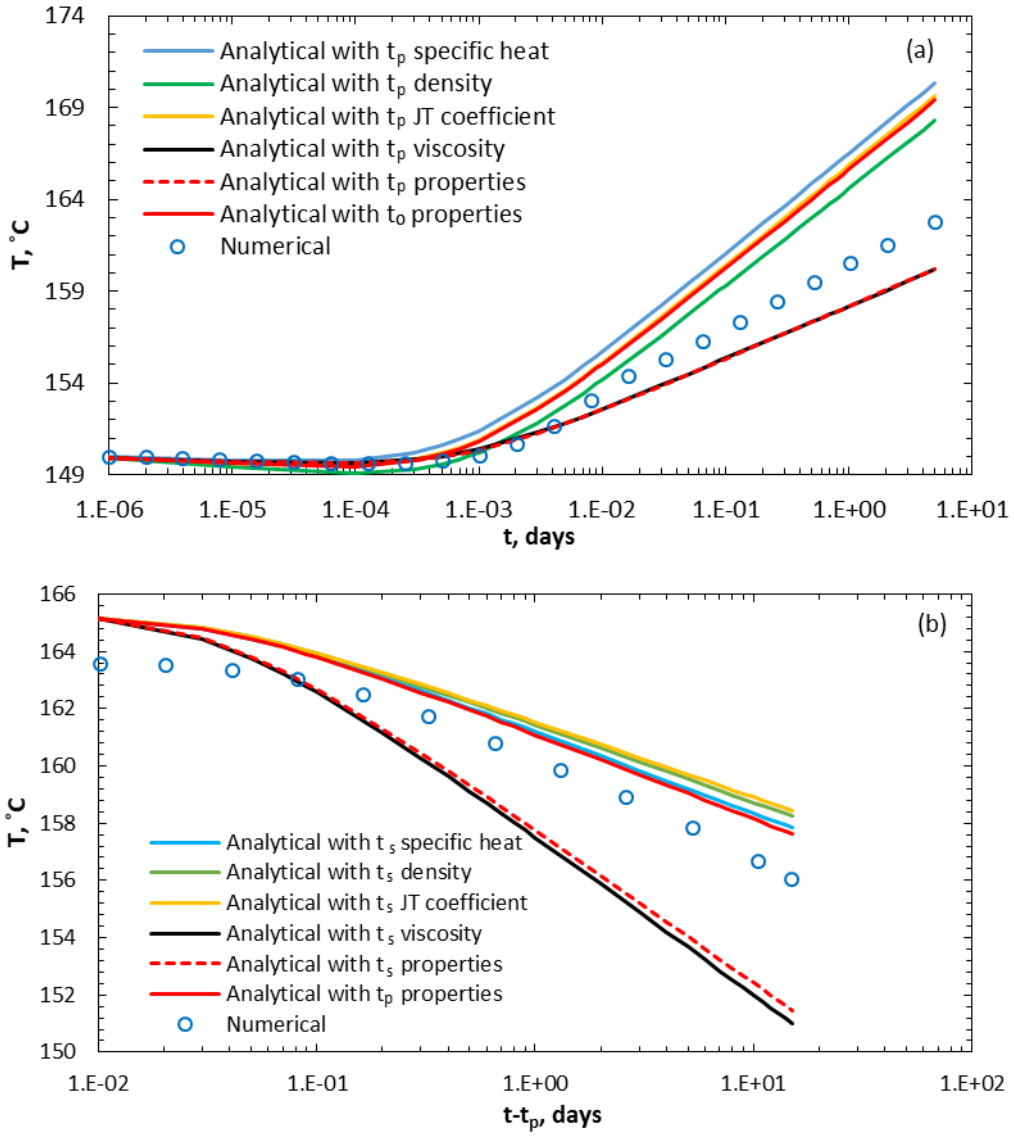

Figure 5. 3. Sensitivity analysis of fluid property variations in temperature profiles for (a) drawdown and (b) buildup.

5.1.3 Temperature Modeling Results

In this section, we apply the iterative algorithm developed in section 5.1.1 to obtain the corrected fluid properties and use these properties as input for the analytical solution for drawdown and buildup tests. These analytically modeled results will be compared with those from numerical simulation to verify the developed fluid property correction method.

We start with the validation of temperature profiles in a non-damaged reservoir under various production rates and with different reservoir fluid components, which are presented in Figure 5.4. The solid curves represent the analytical solution with the fluid property correction method under five production rates over the range of 154-986 m^3/day. The original reservoir fluid is Cyclohexane which is changed to Decane for one case to verify the results for the different fluid component. These profiles are modeled with the input of corrected fluid properties iteratively calculated based on Equations 5.3, 5.4, and 5.9. Good agreement between analytical (solid curves) and numerical (dotted curves) solutions is observed for all cases over the late-time period. The early-time mismatch is observable which was expected and addressed below.

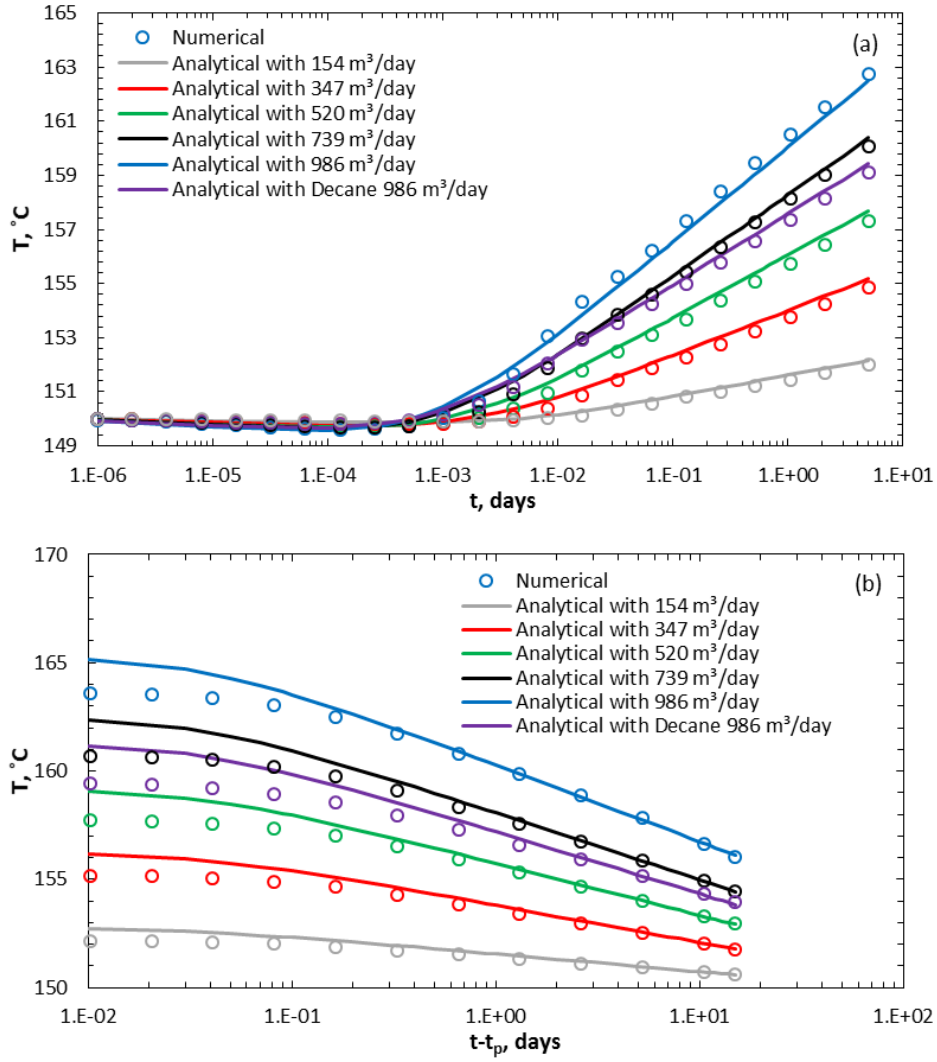

Figure 5. 4. Temperature profiles comparing analytical solution with fluid property correction method and numerical simulation for (a) drawdown and (b) buildup periods in a non-damaged reservoir.

The effects of fluid property variations on the temperature signal are most significant for high drawdown condition. The developed method holds up nicely against this condition, especially compared to analytical solution results under the assumption of constant fluid property illustrated by Figure 5.5.

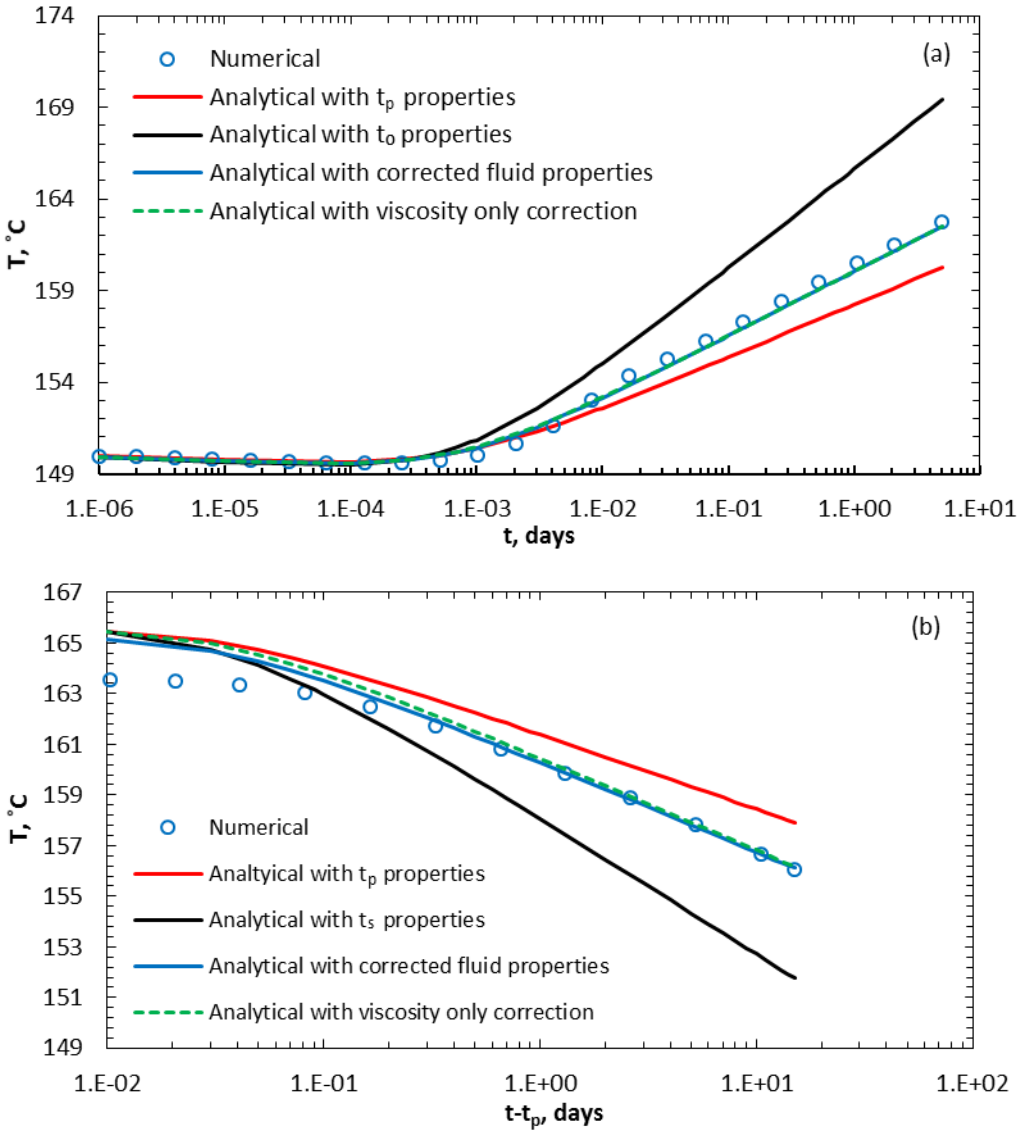

Figure 5. 5. Temperature profiles verifying the analytical solution with correcting all fluid properties versus viscosity only correction against numerical simulation for 986 m^3/day production rate during (a) drawdown and (b) buildup periods.

Three conditions at t_0, t_p, and corrected fluid properties, are considered for analytical temperature modeling of the drawdown test (Figure 5.5a). The JT heating effects in the late time are overestimated by the fluid property values at t_0 and underestimated at t_p condition. Also, endpoint conditions corresponding to buildup test over- and under-estimate the sandface temperature signals (Figure 5.5b). The temperature profiles for both tests using corrected fluid properties precisely predict the temperature signals, which are validated against the numerical simulation results. The averaging technique is most reliable at the late time which corresponds to most field data for practical purposes.

In the early production period (less than 20 minutes for drawdown and 1 day for buildup), the analytical temperature modeling deviates from the numerical simulation, where

the AE effect occurs. This is because the corrected properties are based on the proceeding JT effect and thermal conduction, which may not be accurate for AE effect. Since the AE effect causes only minor cooling or heating on the temperature profile and may be masked by the wellbore storage effect, considering only the late-time effect should be valid in both forward modeling and inversion processes.

Another form of the fluid property correction method is to correct for the viscosity only. The temperature signals modeled with this approach (shown by the green dashed line in Figure 5.5) are very close to the ones with corrections for all the four fluid properties. This simplified correction method can be used to reduce the computational cost of property corrections.

With the success of modeling the temperature signals in the non-damaged reservoir, we include the near wellbore damage into the modeling process. The damage zone has a permeability of 10 md (half of the reservoir permeability) and a radius of 2.25 m. The same iterative process developed in section 5.1.1 is applicable to the transient temperature analytical solution for damaged reservoir derived in the appendix. Since the buildup analytical solution does not include the near wellbore damage, we only present the modeling results for the drawdown test.

The fluid property correction method is applied to the damaged reservoir, the results of which are shown in Figure 5.6. Acceptable agreements between analytical and numerical results are observed. The temperature response in a damaged reservoir behaves similarly to that in a non-damaged reservoir. The damaged zone permeability in the near wellbore region strengthens the heating JT effect, which causes the non-linearity on the slopes of the semi-log plot. The fluid properties are corrected as a whole in the time period dominated by JT effect, which does not account for the changing slope. This induces a minor discrepancy on modeling the different temperature changes in damaged and non-damaged zones.

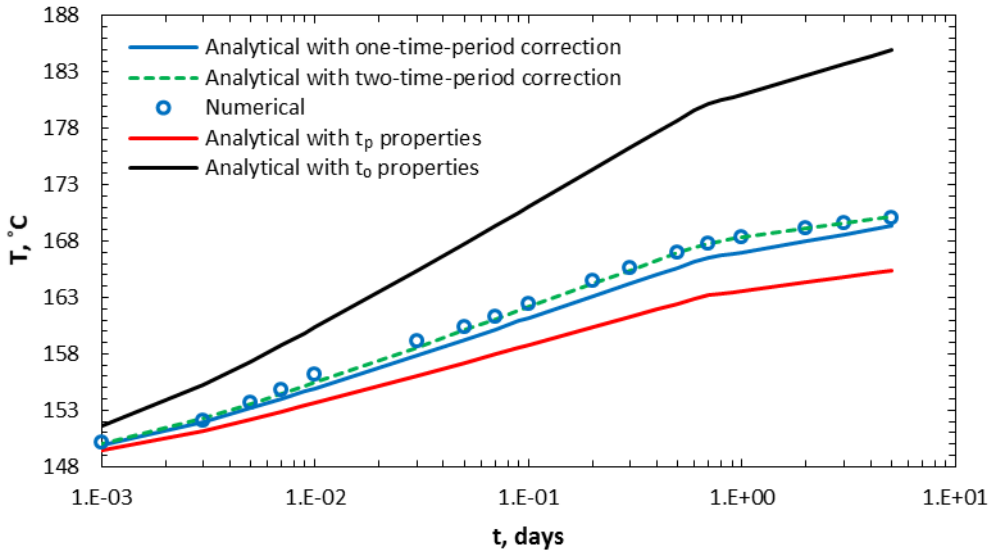

Figure 5. 6. Sandface drawdown temperature profiles benchmarking from analytical solution with fluid property correction method with numerical simulation in the damaged reservoir.

We introduce a two-time-period fluid property correction method specifically for the damaged reservoir in section 5.1.1. The temperature modeling based on this two-time-period fluid property correction method is presented as the green dashed curve in Figure 5.6. Compare to the original method (blue curve), this approach reduces the discrepancies in both time periods, and achieve a better match. We will apply both methods shortly to obtain reservoir and damaged zone properties from the temperature data, and examine the results accordingly.

5.1.4 Pressure Modeling Results

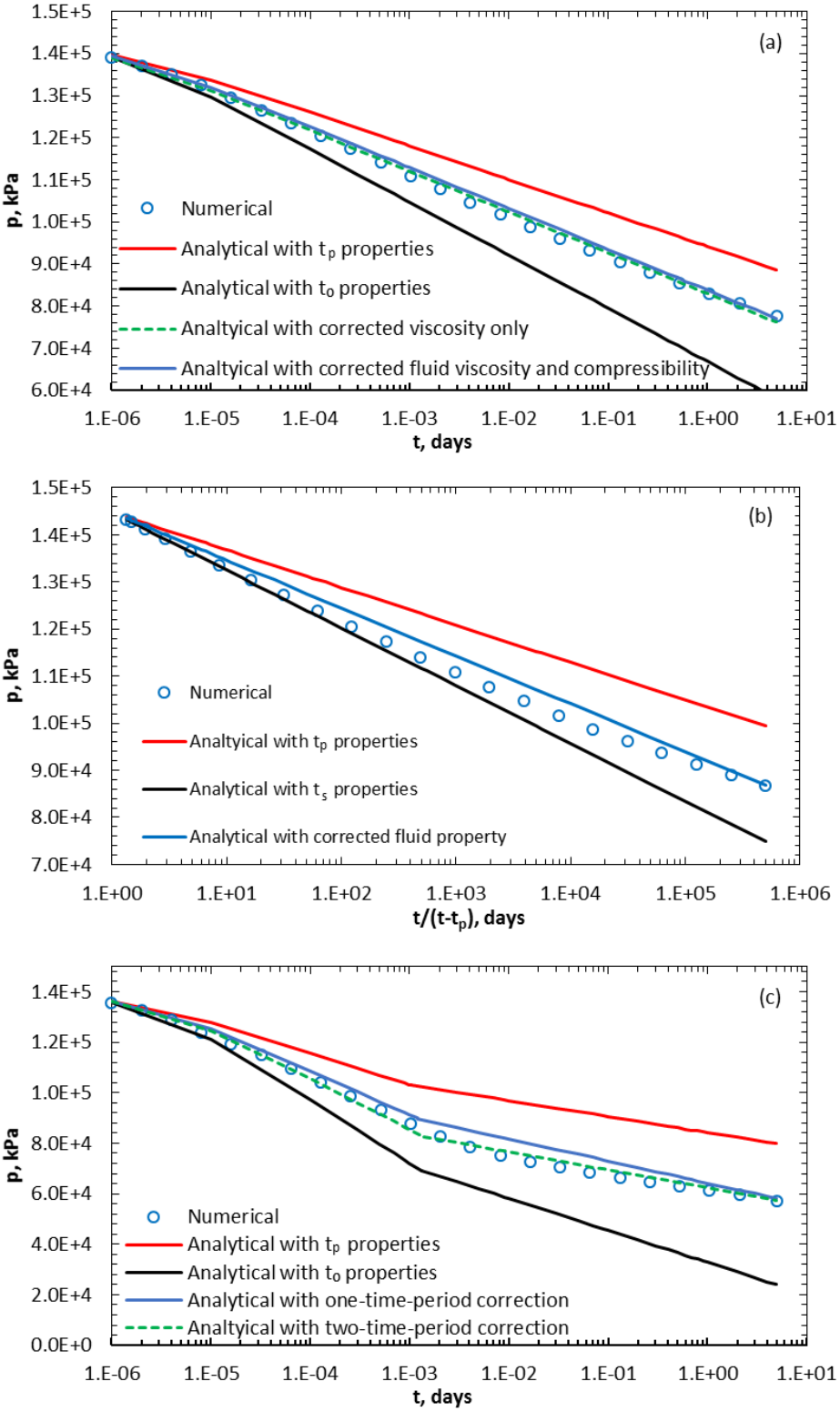

Figure 5. 7. Pressure profiles from the analytical solution with fluid property correction method against numerical simulation for a non-damaged reservoir during (a) drawdown and (b) buildup periods. The drawdown results for the damaged reservoir are shown in (c).

The application of fluid property correction method for the temperature modeling results was presented in sections 5.1.1-5.1.3. However, the validity of this method to model pressure, which is another variable affecting fluid property variation, is not yet illustrated. We developed a similar averaging method to correctly predict temporal pressure profiles for the forward modeling iterative process. In this way, accurate temporal fluid property profiles are established with the input of modeled pressure and temperature.

The analytical and numerical results are presented in Figure 5.7 (for the same cases as Figures 5.5 and 5.6) to validate the pressure modeling results. The analytical modeling results are obtained from fluid properties under three corresponding conditions for both drawdown and buildup tests. The fluid property correction method for the drawdown test accounts for viscosity only or both viscosity and compressibility, which is calculated from Equations 5.12 and 5.13. The compressibility is irrelevant for buildup pressure modeling (Equation 5.11); hence viscosity is the only fluid property to be considered (Equation 5.14). In the semi-log plots, we observe satisfying compliance between numerical and analytical pressure results with the input of corrected fluid properties. This agreement is maintained for viscosity only correction in drawdown test (Figure 5.7a) and improved by two-time-period correction for the damaged reservoir (Figure 5.7c). The fluid property values at t_p condition cause under-estimation of pressure drop (14 MPa and 79% of the simulated pressure drop), while those at other conditions over-estimate the pressure drop (18 MPa and 127% of simulated pressure drop). These modeling results confirm that accurate pressure modeling can be achieved with the fluid property correction method. And with that, accurate temporal fluid property profiles can be calculated from the correct temperature and pressure estimations.

5.1.5 Modified Characterization Procedures and Results

The ultimate goal of TTA is to obtain reservoir properties from modeling temperature signals. Accurately modeling temperature signals is the premise to achieve this goal, which has been enhanced by the fluid property correction method. Therefore, it is required to modify the existing characterization procedures, introduced in chapter 4, to account for the fluid properties variation. Below, we first present the modified procedures for non-damaged reservoir characterization while applying to synthetic data. The synthetic data presented in Figure 5.8 correspond to the drawdown and buildup temperature signals in high drawdown conditions (production rate of 985 m^3/day) obtained by numerical simulation to represent the field measurements.

The modified characterization procedure using the fluid property correction method is:

1. Graph the temperature data, T, vs. the production time, t, on a semi-log plot (Figure 5.8).
2. Identify the late-time effect in the temperature data (indicated by the red line in Figure 5.8), draw straight line through it, and find the slope m_1 for it.
3. Calculate the average fluid properties of ρ_f, c_f, μ, μ_{JT} from the fluid property correction method (Equations 5.3, 5.4, and 5.9 along with the iterative algorithm). If the effect of viscosity is dominating for all fluid properties, simplified procedures can be applied to average viscosity only.
4. Calculate the permeability k from m_1 using Equation 5.15, which can be derived from Equation 5.8:

$$k = -\frac{1.152\mu_{JT}\mu q}{2\pi H k_r m_1} \tag{5.15}$$

And for the drawdown test only:

5. Identify the initial reservoir temperature in the temperature data (indicated by the green line in Figure 5.8), draw straight line through it, and find the intersection of the red line and green line to obtain t_A.
6. Calculate porosity ϕ from the t_A using Equation 5.16, which can be derived from section 3.1:

$$\phi = \frac{\dfrac{86400 q \rho_f c_f t_A}{\pi H r_w^2} - \rho_s c_s}{\rho_w c_w S_{wr} + \rho_f c_f (1 - S_{wr}) - \rho_s c_s} \tag{5.16}$$

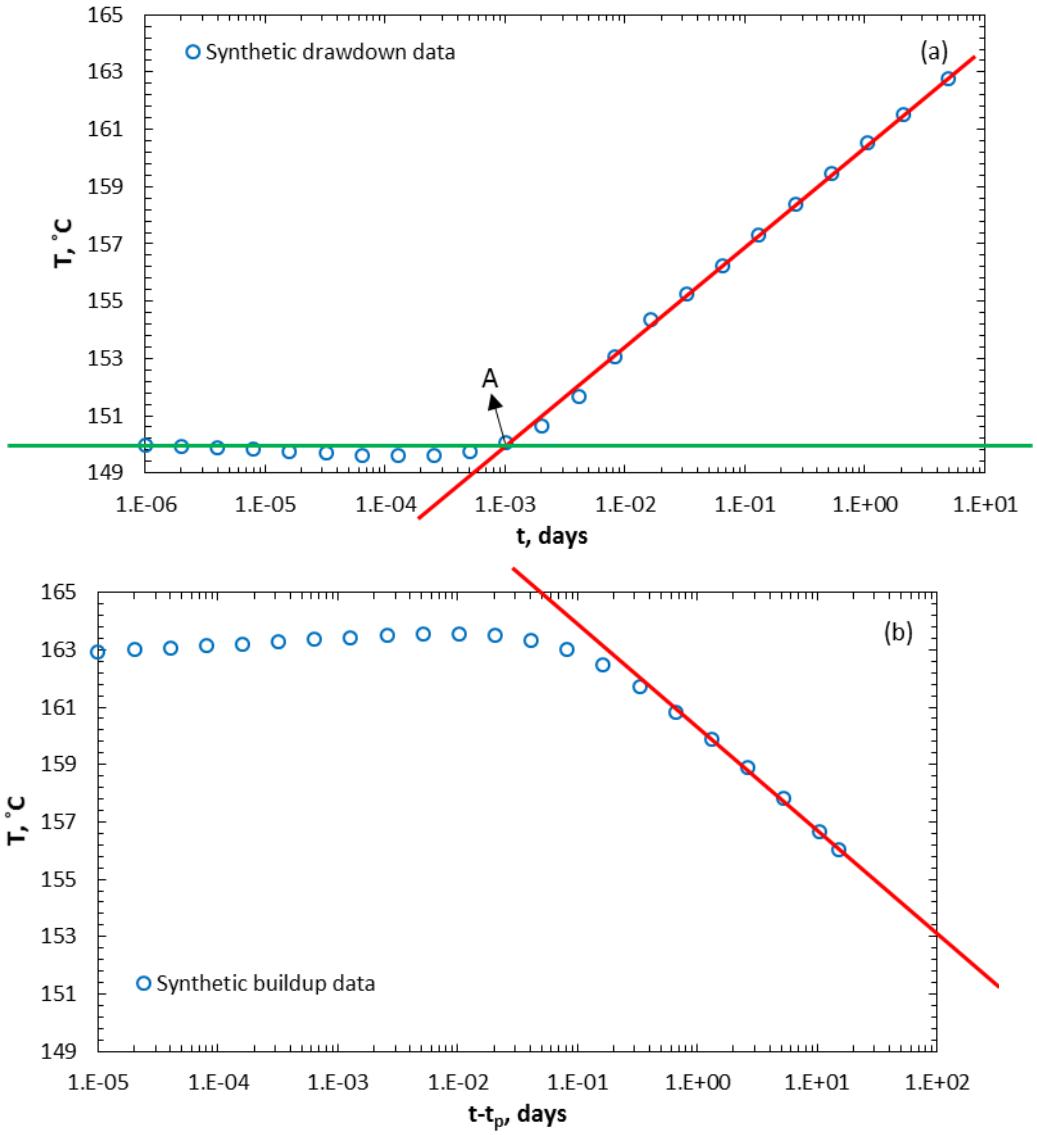

Figure 5. 8. Sandface synthetic temperature signals for an oil reservoir of (a) drawdown, and (b) buildup tests.

The calculations of porosity and permeability require the input of fluid properties. The developed fluid property correction method should be applied before step 4, and the corrected fluid property values should be used in Equations 5.15 and 5.16 for permeability and porosity estimations. Meanwhile, t_A identified from the temperature measurements can be used to represent t_{JT} in Equations 5.3 and 5.9. As a result, a new step to implement the fluid property correction method is inserted as step 3 in the characterization procedures.

This revised characterization procedure is applied to the data in Figure 5.8 and the results are compared with those from original procedures assuming the fluid properties at two other conditions in Table 5.2. Applying the fluid property correction method significantly improves the accuracy of reservoir characterization from TTA, especially for permeability estimation. In the extreme case, the fluid property correction method enhances the accuracy of permeability estimation by almost 60% compared to those assuming the fluid properties at initial reservoir condition. For the porosity estimation, the characterization accuracy is improved by more than 20%. In short, the developed fluid property correction method can be applied on the sandface temperature field data for a non-damaged reservoir with significant improvements on the precisions of reservoir property estimations without further complication of the characterization procedure.

Table 5. 2. Permeability and porosity estimates for the oil reservoir.

Drawdown estimation	Reference	Fluid property corrections	t_o condition	t_p condition	Max improvements (%)
Permeability (mD)	20	21.3	32.6	17.4	56.5
Porosity	0.25	0.242	0.24	0.188	21.6
Buildup estimation	Reference	Fluid property corrections	t_p condition	t_s condition	Max improvements (%)
Permeability (mD)	20	19.4	16.2	29.4	44

Similar to the characterization procedures for the non-damaged reservoir, the slopes of the damaged zone and reservoir temperature behavior can reveal the permeabilities of the damaged zone and the reservoir. Including the fluid property correction method, the characterization procedures to obtain the damaged zone and reservoir properties of a damaged reservoir are presented below.

1. Graph the temperature data, T, vs. the production time, t, on a semi-log plot (Figure 5.9).
2. Identify the temperature responses corresponding to damaged zone and reservoir (indicated by the red and black lines respectively in Figure 5.9); draw straight lines through them, and find the slope m_2 for red lines and m_3 for black lines. The intersection of these two lines is traverse time t_c.
3. Identify the initial layer temperature (indicated by the green line in Figure 5.9) and draw a straight line through them.
4. Identify the intersection of the red line and green line to obtain t_B.
5. Calculate the average fluid properties of ρ_f, c_f, μ, μ_{JT} from the fluid property correction method (Equations 5.3, 5.4, and 5.9 along with the iterative algorithm). Two average values are required for each property, one for the damaged zone time period (t_B-t_c), one for reservoir time period (t_c-t_p).
6. Calculate the porosity ϕ from the t_B using Equation 5.17:

$$t_B = \frac{\left\{\phi\left[\rho_w c_w S_{wr} + \rho_f c_f \left(1 - S_{wr}\right)\right] + \left(1-\phi\right)\rho_s c_s\right\}\pi H r_w^2}{86400\rho_f c_f q} \tag{5.17}$$

7. Calculate the reservoir permeability k from the m_3 using Equation 5.18:

$$k = -\frac{1.152\mu_{JT}\mu q}{2\pi H k_r m_3} \tag{5.18}$$

8. Calculate the damaged zone permeability k_s from the m_2 using Equation 5.19:

$$k_s = -\frac{1.152\mu_{JT}\mu q}{2\pi H k_r m_2} \tag{5.19}$$

9. Calculate the damaged zone radius using Equation 5.20:

$$r_s = \sqrt{r_w^2 + \frac{86400\rho_f c_f q t_c}{\pi H\left\{\phi\left[\rho_w c_w S_{wr} + \rho_f c_f\left(1-S_{wr}\right)\right] + \left(1-\phi\right)\rho_s c_s\right\}}} \tag{5.20}$$

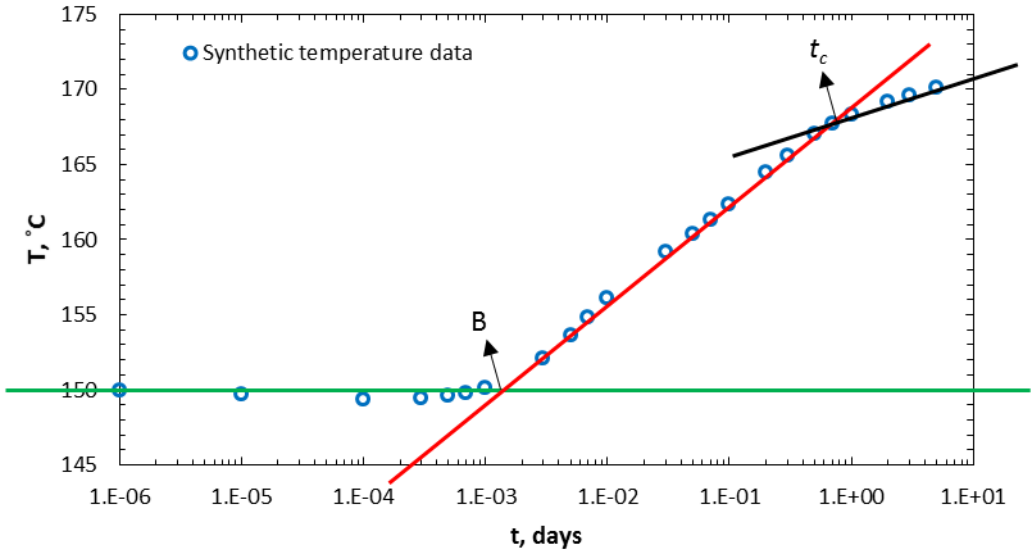

Figure 5. 9. Sandface synthetic temperature signals for a damaged reservoir.

Step 5 is added to the original characterization procedure to implement the fluid property correction method. Compared to the procedures for the non-damaged reservoir, the two-time-period correction method is required here since it can model the temperature signals more precisely. The improvement in the forward modeling leads to better accuracy for the damaged zone and reservoir permeability estimations for a damaged reservoir presented in Table 3. Compared to the estimations made with the input of one-time-period fluid property correction, the characterization results with the inputs of fluid properties corrected before and after the traverse time deliver higher accuracy (3.8% better on damaged zone permeability estimation and 20% better on reservoir permeability estimation).

Table 5. 3. Permeability and porosity estimates for the oil reservoir.

Estimations	Reference	One-time-period	Two-time-period	Further improvements (%)	t_o condition	t_p condition
Damaged zone permeability (mD)	10	9.58	10.2	3.8	16	7.7
Reservoir permeability (mD)	20	24.7	19.3	20	42.2	19.9

5.2 Dynamic Temperature Analysis under Variable Rate and Pressure Conditions for Transient and Boundary Dominated Flow

Current analytical approaches for TTA heavily rely on the assumption of constant rate production, which is often invalid for the extended period of production. This section addressed this issue by introducing novel analytical approaches to model temperature signals under dynamic rate and pressure conditions. The specific methods share underlying theories of the superposition principle and production rate normalization from PTA and include a newly derived analytical solution when these theories are not applicable. With adapting these methods, cases with complex production history are modeled using analog cases producing at a constant rate.

5.2.1 Problem Description and Methodology

In this section, several approaches to analyze the transient temperature signals associated with variable rate and pressure productions are developed, which is the main subject of this section. The physical model for these analyses can be represented by Figure 3.10. For the majority of the production wells under extended periods of production, the pressure transient will reach the reservoir outer boundary. This arrival time divides the production into early pressure transient flow period and late BDF period. As shown in section 3.4, the temperature transient (mainly JT effect) travels so slow that, in both periods, the temperature signal remain transient. On the other hand, variable rate production can be classified as step-rate production (continuous pressure variation), and constant pressure production (continuous rate variation). Both production strategies are likely to be applied in either/both transient and BDF periods. Therefore, to cover the majority of production strategies applied in the field, we consider the following four production scenarios:

1. Step-rate production during early pressure transient flow period
2. Constant pressure production during early pressure transient flow period
3. Step-rate production during late BDF period
4. Constant pressure production during late BDF period

For each of the scenarios listed above, we develop suitable approaches to account for production rate variation in TTA. For the first three scenarios, comparable methods have been developed to incorporate production rate variation in PTA and decline curve analysis. These approaches include the superposition principle and material balance time concept for transient and BDF periods. We apply the principles underlying these methods to TTA and develop the following novel approaches: superposition cumulative production approach for scenario 1, simplified superposition approach for scenario 2, and modified material balance time approach for scenario 3. For scenario 4, we develop a novel analytical solution to model the temperature transient profiles under constant pressure production during BDF period. The details of these approaches are presented below.

5.2.1.1 Step-rate production during early pressure transient flow period

To extend its application to variable rate production, PTA uses the principle of superposition. Similar to the governing diffusivity equation (Equation 5.21) for PTA, the energy balance equation (Equation 3.1) for TTA can also benefit from the principle of superposition due to its linearity. The principle of superposition is capable of simplifying complex boundary conditions with linear combinations of solutions for simple boundary conditions and modeling multiple well productions with total contributions from each well.

$$\frac{1}{r}\frac{\partial}{\partial r}\left(r\frac{\partial p}{\partial r}\right)=\frac{\phi\mu\hat{c}_t}{k}\frac{\partial p}{\partial t} \tag{5.21}$$

To model the pressure and temperature signals associated with variable rate production condition, the principle of superposition is applied to the solutions of Equations 3.1 and 5.21. For constant rate production during the pressure transient flow period, these solutions are Equations 5.10 and 5.1. The variables in Equations 5.10 and 5.1 are generalized in the boxes, which are very similar for both equations except for the RHS. For the constant production rate condition, *qt* is equal to the cumulative production *Q*. Therefore, the following analogy is valid: $(p-p_i)/q$ and *t* from PTA are equivalent to $(T-T_i)/q$ and *Q*, respectively in TTA.

To analyze the pressure signals for a production period with *n* rate changes, Bourdet, Ayoub, and Pirard (1989) introduced the superposition time function and rate-normalized pressure change. Using these two variables instead of *p* and *t*, the pressure signals during variable production rate condition can be analyzed in the same way as those during constant production rate condition. Following the same approach, we propose the superposition cumulative production function (Equation 5.22) and rate-normalized temperature changes (Equation 5.23) to perform variable rate TTA.

$$\log Q_e=\log\left(Q-Q_{n-1}\right)+\sum_{j=1}^{n-1}\left(\frac{q_j-q_{j-1}}{q_n-q_{n-1}}\right)\log\left(\frac{Q-Q_{j-1}}{Q_{n-1}-Q_{j-1}}\right) \tag{5.22}$$

$$\frac{T\left(t_{n-1}\right)-T\left(t\right)}{q_n-q_{n-1}} \tag{5.23}$$

5.2.1.2 Constant pressure production during early pressure transient flow period

Theoretically, the superposition cumulative production approach developed in section 5.2.1.1 is valid for any type of production during pressure transient flow period, including constant pressure production. However, in practice, applying this approach to constant pressure production can be very challenging and sometimes impossible. Since production rates are continuously changing for constant pressure production, superposition procedure requires numerous steps for both PTA and TTA, which results in infinite calculations for extended production period. To analyze data corresponding to constant pressure production, Hurst (1934) showed that the same production data can be analyzed by plotting $(p-p_i)/q$ vs *log(t)*. As noted in section 5.2.1.1, $(p-p_i)/q$ and *t* in PTA are equivalent to $(T-T_i)/q$ and *Q*, respectively in TTA. Therefore, by plotting temperature data in terms of $(T-T_i)/q$ vs *log(Q)*, same straight line behavior (as that for constant rate production response) is expected on a semi-log plot. The validity of this approach will be examined in section 5.2.2 for temperature signals from constant pressure production during pressure transient flow period.

5.2.1.3 Step-rate production during late boundary dominated flow period

In section 3.4, we derived a temperature transient analytical solution during BDF period and extensively discussed the thermal behavior in this period. The main contributor for this period is boundary dominated adiabatic expansion (BDAE) instead of JT effect for pressure transient flow period. However, for each production rate variation, a new pressure transient is initiated associated with significant JT effect, which may mask the AE effect. Thus, we choose to derive a novel temperature transient analytical solution for constant pressure production during BDF period. For step-rate production, BDAE can be well established for each production rate. Therefore, we start the analysis with the equation of BDAE (section 3.4):

$$\frac{\partial T}{q\partial t}=\frac{-\left(\rho_f c_f \mu_{JT}+1\right)}{\pi H\hat{c}_t r_e^2\left\{\phi\left[\rho_w c_w S_{wr}+\rho_f c_f\left(1-S_{wr}\right)\right]+\left(1-\phi\right)\rho_s c_s\right\}} \tag{5.24}$$

For each constant rate period in step-rate production, q is a constant. Therefore, the left hand side (LHS) of Equation 5.24 is equivalent to $\partial T/\partial Q$. The RHS of Equation 5.24 is a function of various reservoir and fluid properties, the values of which remain constants for each of the constant rate periods in the test. As a results, by plotting temperature signals on a Cartesian plot of T-T_i (temperature changes in this constant rate period) vs Q-Q_{n-1} (cumulative production variations in this constant rate period), temperature data for each of the constant rate periods are expected to behave as a straight line with the same slope given by the RHS of Equation 5.24. A similar technique of plotting pressure changes versus cumulative production is proved to be useful in PTA, known as material balance time concept. Herein, we apply this approach to address the temperature signals for step-rate production during late BDF period.

5.2.1.4 Constant pressure production during late boundary dominated flow period

The governing equation (Equation 3.1) and initial condition (Equation 3.3) to derive this analytical solution are the same for those in section 3.4. The last term in Equation 5.21 is assumed to be insignificant and ignored since the production well is under constant pressure. The production rate decline is proved to exponentially decline for constant pressure production during BDF period (Fetkovich 1980). Therefore, we introduce the exponential decline production rate (Equation 5.25) to governing equation:

$$q=q_i\exp\left(-Dt\right) \tag{5.25}$$

$$\begin{aligned}&\left\{\phi\left[\rho_w c_w S_{wr}+\rho_f c_f\left(1-S_{wr}\right)\right]+\left(1-\phi\right)\rho_s c_s\right\}\frac{\partial T}{\partial t}\\&=\frac{q_i\rho_f c_f\exp\left(-Dt\right)}{2\pi rH}\left[\frac{\partial T}{\partial r}+\frac{q_i\mu\mu_{JT}\exp\left(-Dt\right)}{2\pi rHk}\right]\end{aligned} \tag{5.26}$$

To simplify the derivation process, we transform the governing equation (Equation 5.26) and the corresponding initial condition (Equation 3.3) into dimensionless forms:

$$C_5\frac{\partial T_D}{\partial t_{D2}}=\frac{\exp\left(-t_{D2}\right)}{r_D}\frac{\partial T_D}{\partial r_D}-\frac{\exp\left(-2t_{D2}\right)}{r_D^2} \tag{5.27}$$

$$T_D=0, t_D=0 \tag{5.28}$$

where

$$t_{D2}=Dt \tag{5.29}$$

$$C_5=\frac{2\pi Hr_w^2 D\left\{\phi\left[\rho_w c_w S_{wr}+\rho_f c_f\left(1-S_{wr}\right)\right]+\left(1-\phi\right)\rho_s c_s\right\}}{\rho_f c_f q_i} \tag{5.30}$$

We apply the Method of Characteristics to obtain the solution for Equation 5.27, the details of which are presented in the Appendix E. The analytical solution for constant pressure production during BDF period is:

$$T_D=\frac{\exp\left(-t_{D2}\right)-1}{2}+\frac{C_5 r_D^2-2\exp\left(-t_{D2}\right)}{4}\ln\left[\frac{C_5 r_D^2+2-2\exp\left(-t_{D2}\right)}{C_5 r_D^2}\right] \tag{5.31}$$

Similar to the superposition principle for early pressure transient flow period, the material balance time concept is useful for analysis in late BDF period, including constant pressure production. Therefore, we transform Equation 5.31 in term of cumulative production using the cumulative production definition of exponential decline (Equation 5.32), which can be derived from Equation 5.25:

$$Q = \int_0^t q dt' = \frac{q_i}{D}\left[1 - \exp\left(-Dt\right)\right] \tag{5.32}$$

$$T_D = -\frac{DQ}{2q_i} + \frac{C_5 r_D^2 - 2}{4}\ln\left(1 + \frac{2DQ}{C_1 r_D^2 q_i}\right) + \frac{DQ}{2q_i}\ln\left(C_5 r_D^2 + \frac{2DQ}{q_i}\right) - \frac{DQ}{2q_i}\ln\left(C_5 r_D^2\right) \tag{5.33}$$

As cumulative production increases, the second and third terms on the RHS of Equation 5.33 diminish. As a result, the temperature signals for constant pressure production during late BDF period are proportional to cumulative production as suggested by Equation 5.34:

$$\frac{\partial T_D}{\partial Q} = -\frac{D}{2q_i}\left[\ln\left(C_5 r_D^2\right) + 1\right] \tag{5.34}$$

Similar to Equation 5.24, Equation 5.34 implies that the temperature data can be plotted on a Cartesian plot versus the cumulative production Q. If temperature signals are acquired at the same location, the dimensionless radius remains a constant as well as other parameters on the RHS of Equation 5.34. Therefore, the temperature data on this Cartesian plot is expected to behave quasi-linearly for constant pressure production during late BDF period.

5.2.1.5 Summary

Table 5. 4. Temperature transient analysis approaches for variable rate and constant pressure production.

Production strategy	Step-rate	Constant pressure	Step-rate	Constant pressure
Flow regime	Early pressure transient flow period		Late BDF period	
Method	Superposition cumulative production	Simplified superposition	Material balance time	Novel analytical solution
Coordinates	Equation 5.22 vs. Equation 5.23	$(T-T_i)/q$ vs. Q	$T-T_i$ vs. $Q-Q_{n-1}$	Equation 5.34
Plotting	Semi-log		Cartesian	

In short, we develop suitable approaches to account for production rate variation in TTA for each scenario. Table 5.4 summarizes the approaches and we will apply and examine these methods in the following section.

5.2.2 Results

We present TTA results under step-rate and constant pressure production in this section. We examine the proposed approaches for each scenario with a base case. With the successful validation of the methods, detailed TTA characterization procedures are provided for each scenario.

To verify the proposed approaches, we numerically simulate the temperature signals for variable rate and constant pressure productions in the base case. We use CMG-GEM (2015), KAPPA-RUBIS (2015) to perform the simulation. The base case is the same oil reservoir presented by App (2010).

5.2.2.1 Step-rate production during early pressure transient flow period

We begin with verification of TTA on step-rate production during early pressure transient flow period. Two production strategies are proposed here for the base case: a sequence of increased flow rate and a sequence of decreased flow rates (Table 5.5). Figure 5.10 presents the sandface temperature signals obtained from the production well using numerical simulation for the base case with increased and decreased flow rate sequences. A heating effect is observed on every flow period with a rate increase and vice versa. The magnitude of temperature increase or decrease is proportional to the rate change for the specific flow period. This indicates that the most recent flow period has the greatest impact on the current flow period compared to previous flow periods.

Table 5. 5. Flow sequence for step-rate production during early pressure transient flow period.

Flow period	Duration (day)	Increased flow rates (m^3/day)	Decreased flow rates (m^3/day)
1	1	40	270
2	1	60	120
3	1	120	60
4	2	270	40

We apply the superposition cumulative production method developed in section 5.2.1.1 on the temperature data. The detailed procedure to apply this method is:

1. Graph the temperature, *T*, vs. the production time, *t* (Figure 5.10).
2. Identify each flow period with constant production rate in the temperature data (4 flow periods in Figure 5.10).
3. Calculate the rate normalized temperature changes (Equation 5.23) and superposition cumulative production function (Equation 5.22) for every time step in each flow period.
4. Plot the rate normalized temperature changes vs. the superposition cumulative production, on a semi-log plot (Figure 5.10).

Following this procedure, the interpretation results of superposition cumulative production approach are illustrated in Figure 5.11. Temperature data for various flow periods are overlapped (>0.97 R-squared values) given the same reservoir and fluid properties responsible for the temperature profiles. Similar to the temperature profiles associated with constant rate production, we can observe the early AE effect and late JT effect on the temperature data. Therefore, the superposition cumulative production approach reduces the step-rate to the constant rate production, and the reservoir characterization procedure for TTA under constant rate production can be modified and applied to step-rate production considering this approach:

1. Identify the late-time effect in the treated temperature data (indicated by the red lines in Figure 5.11), draw straight line through it, and find the slope m_1 for it.
2. Calculate the permeability k from m_1 using Equation 5.35, which can be derived from Equation 5.1:

$$k = -\frac{1.152\mu_{JT}\mu}{172800\pi H k_r m_1} \tag{5.35}$$

3. Identify the initial reservoir temperature in the treated temperature data (indicated by the black lines in Figure 5.11), draw straight line through it, and find the intersection of the red line and black line to obtain Q_A.
4. Calculate porosity ϕ from the Q_A using Equation 5.36, which can be derived from Equation 5.1:

$$Q_A = \frac{\left\{\phi\left[\rho_w c_w S_{wr} + \rho_f c_f \left(1 - S_{wr}\right)\right] + \left(1-\phi\right)\rho_s c_s\right\}\pi H r_w^2}{\rho_f c_f} \tag{5.36}$$

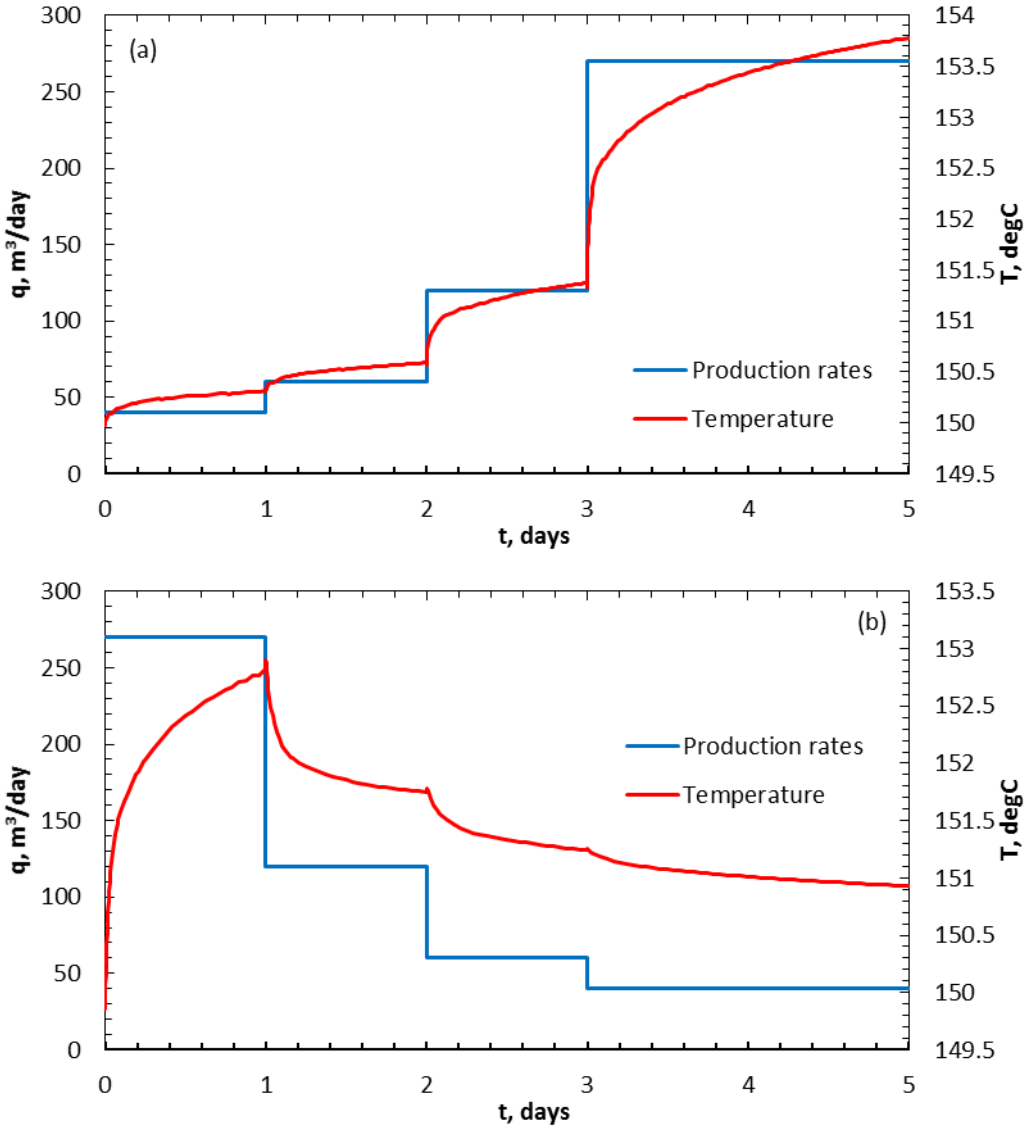

Figure 5. 10. Sandface temperature profiles obtained from the production well using numerical simulation for the base case with increased (a) and decreased (b) flow rate sequences in pressure transient flow period.

Table 5.6 presents TTA characterization results using the above procedure on the temperature data in Figure 5.11. Red lines are the logarithmic trend lines from the synthetic temperature data, the slope and intercept of which are calculated based on the trend line equation in Figure 5.11. The estimations are compared with the reference settings in the numerical simulation, and the agreements are obtained for all estimations. Permeability estimation, as the primary target for TTA reservoir characterization, achieves more than 90%

accuracy in both cases. Compared to the estimation accuracy for cases with constant rate production (section 3.1), the results are equivalent.

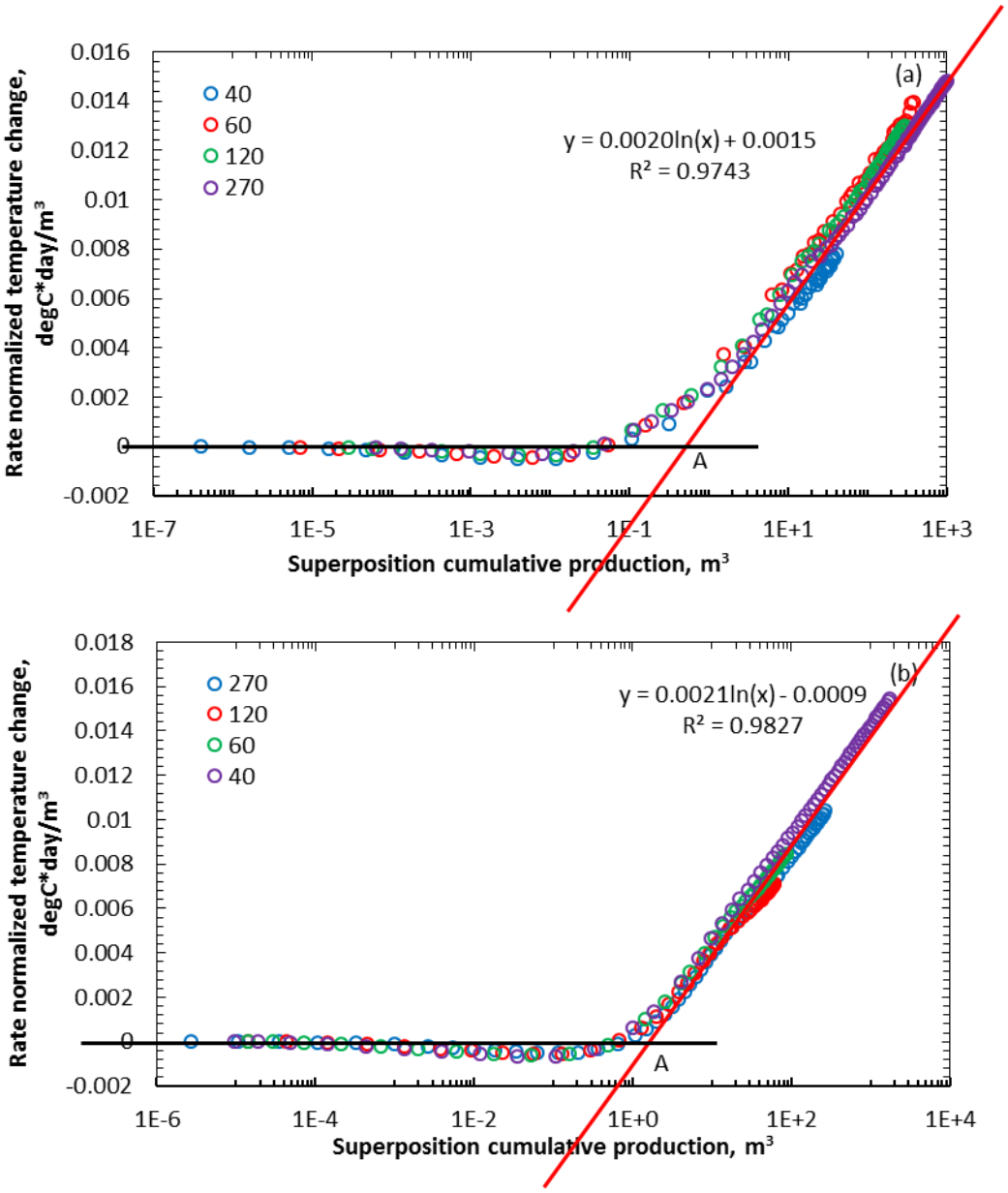

Figure 5. 11. Interpretation results of superposition cumulative production on temperature data with increased (a) and decreased (b) flow rate sequences.

Table 5. 6. TTA characterization results for step-rate production during early pressure transient flow period.

	Estimation (Figure 5.11a)	Estimation (Figure 5.11b)	Reference	Error (Figure 5.11a)	Error (Figure 5.11b)
Slope (red line)	0.0046	0.00483	0.0049	6%	1.4%
Permeability (md)	21.3	20.3	20	6.5%	0.2%
Intercept	0.7	1.1	0.81	14%	36%

5.2.2.2 Constant pressure production during early pressure transient flow period

In this section, the proposed approach of simplified superposition is examined to analyze the temperature signals associated with constant pressure production during early pressure transient flow period. We simulate the temperature data for the base case under three bottom-hole pressures (BHPs): 120 MPa (83% of initial reservoir pressure), 100 MPa (70%), and 80 MPa (56%). Figure 5.12a presents the sandface temperature signals with constant pressure production. We observe similar heating effects, which are significantly affected by the flow rate variation associated with constant pressure production. In the most extreme case (80 MPa BHP), the quasi-linear behavior of the JT effect does not exist in this semi-log plot. Therefore, the simplified superposition approach is definitely required to account for the flow rate variation.

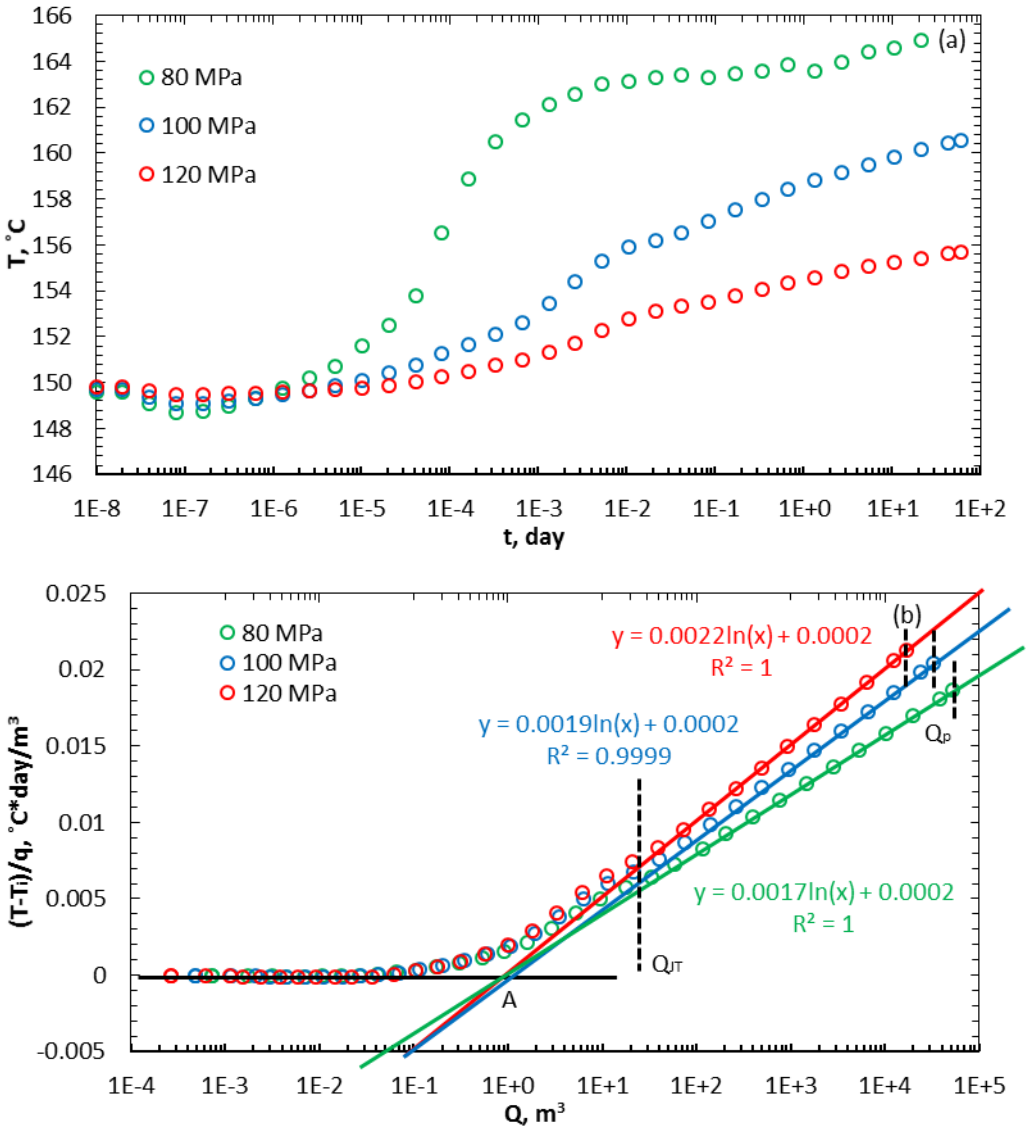

Figure 5. 12. Sandface temperature profiles obtained from the production well using numerical simulation for the base case with constant pressure production, (a) before implementing and (b) after implementing the simplified superposition approach.

To perform the simplified superposition approach, the rate normalized temperature change, $(T-T_i)/q$, is plotted vs. the cumulative production, Q, on a semi-log plot (Figure 5.12b).

After applying the simplified superposition approach, the quasi-linear behaviors of the JT effect on the semi-log plot can be observed for all three cases. Meanwhile, the magnitudes of the early AE effect are correctly justified for production rate variation, resulting in an agreement between cases with different BHP. The slopes of JT effect are slightly varied between cases due to the effect of fluid property variations (mainly from the viscosity variation). We will apply a procedure similar to those introduced in section 5.1 to account for it, and perform reservoir characterization for constant pressure production during early pressure transient flow period:

1. Identify the late-time effect in the temperature data (indicated by the red, blue, and green lines in Figure 5.12b), draw straight lines through it, and find the slope m_1.
2. Calculate the average fluid viscosity from below correction method (Equation 5.37). Q_{JT} and Q_p are the start and end of the quasi-linear behavior associated with the JT effect:

$$\bar{\mu} = \frac{\int_{Q_{JT}}^{Q_p} \mu(p,T)\frac{dQ}{Q}}{\ln\left(\frac{Q_p}{Q_{JT}}\right)} \tag{5.37}$$

3. Calculate the permeability k from m_1 using Equation 5.38, which can be derived from Equation 5.1:

$$k = -\frac{1.152\mu_{JT}\bar{\mu}}{172800\pi H k_r m_1} \tag{5.38}$$

4. Identify the initial reservoir temperature in the temperature data (indicated by the black lines in Figure 5.12b), draw straight line through it, and find the intersection of the red line and black line to obtain Q_A.

Table 5. 7. TTA characterization results for constant pressure production during early pressure transient flow period.

	80 MPa	100 MPa	120 MPa
Slope estimation	0.0039	0.0045	0.0051
Reference (md)		0.0049	
Corrected viscosity (cp)	2.38	2.8	3.2
Reference (cp)		3.2	
Permeability estimation (md)	18.6	19	19.6
Reference (md)		20	
Error (%)	7	5	2
Q_A estimation	0.8	0.9	1
Reference (md)		0.81	
Error (%)	1	11	23

5. Calculate porosity ϕ from the Q_A using Equation 5.36, which can be derived from Equation 5.1.

Table 5.7 presents TTA characterization results using the above procedure on the temperature data in Figure 5.12a. The agreements for all estimations further validate the approach of simplified superposition in term of estimation accuracy. To be specific, the fluid property correction method (section 5.1) precisely assess the average fluid viscosity for three cases of different BHP. Along with the JT effect slope estimations, all cases provide very accurate permeability estimations, which are verified against the simulation setting. Therefore, the approach of simplified superposition is successfully performed and addressed the production rate variation for constant pressure production during early pressure transient flow period.

5.2.2.3 Step-rate production during late boundary dominated flow period

After demonstrating the analysis results for the early pressure transient flow period, we now present and examine TTA results on step-rate production during late BDF period. Similar increased and decreased flow sequence are proposed as the production strategies for the base case (Table 5.8). Compared to those for early pressure transient flow period (Table 5.5), the duration of each flow period is significantly extended to maximize the visibility of temperature profile during BDF period. As presented in Figure 5.13, the temperature signals from the production well in each flow period start with a substantial temperature jump or drop associated with the pressure transient flow period for less than 100 days. When the pressure transient reaches the boundary, the temperature begins to drop due to BDAE. In section 3.4, we showed that the temperature signals from the monitoring well is merely related to BDAE and can eliminate the JT effect. Therefore, we also present the temperature data from a monitoring well in Figure 5.13, which is located 200 m from the production well. The rates of decreasing BDAE temperature signals from both wells seem to be directly proportional to the production rate. This finding brings up the approach of material balance time to address TTA for step-rate production during late BDF period.

The main step to perform the material balance time approach on temperature data is to break down each flow period and plot the temperature changes versus cumulative production in a Cartesian plot. In details, the procedure is:

1. Graph the temperature data, T, vs. the production time, t (Figure 5.13).
2. Identify each flow period with constant production rate in the temperature data (4 flow periods in Figure 5.13).
3. Calculate the temperature changes, $T\text{-}T_i$, and cumulative production, $Q\text{-}Q_{n\text{-}1}$, for every time step in each flow period.
4. Plot the temperature changes, vs. the cumulative production, on a Cartesian plot (Figures 5.14 and 5.15).

Figures 5.14 and 5.15 illustrate the interpretation results of material balance time approach on temperature data for the production and monitoring wells respectively. The temperature data for each flow period present similar cooling signal of BDAE and nearly identical slope on this Cartesian plot. Between the temperature data from different wells, those from the monitoring well demonstrate more uniform slope values, which is due to the exclusion of JT effect at the monitoring well. To further validate the slope value of BDAE, we perform the following procedure on Figures 5.14 and 5.15 to estimate the reservoir drainage area:

5. Identify the BDF period in the temperature data (Figures 5.14 and 5.15), draw straight line through it, and find the slope m_2 for it.
6. Calculate the drainage area A from m_2 using Equation 5.39, which can be derived from Equation 5.24:

$$A = \frac{-\left(\rho_f c_f \mu_{JT} + 1\right)}{m_2 H \hat{c}_t \left\{\phi\left[\rho_w c_w S_{wr} + \rho_f c_f \left(1 - S_{wr}\right)\right] + \left(1-\phi\right)\rho_s c_s\right\}} \tag{5.39}$$

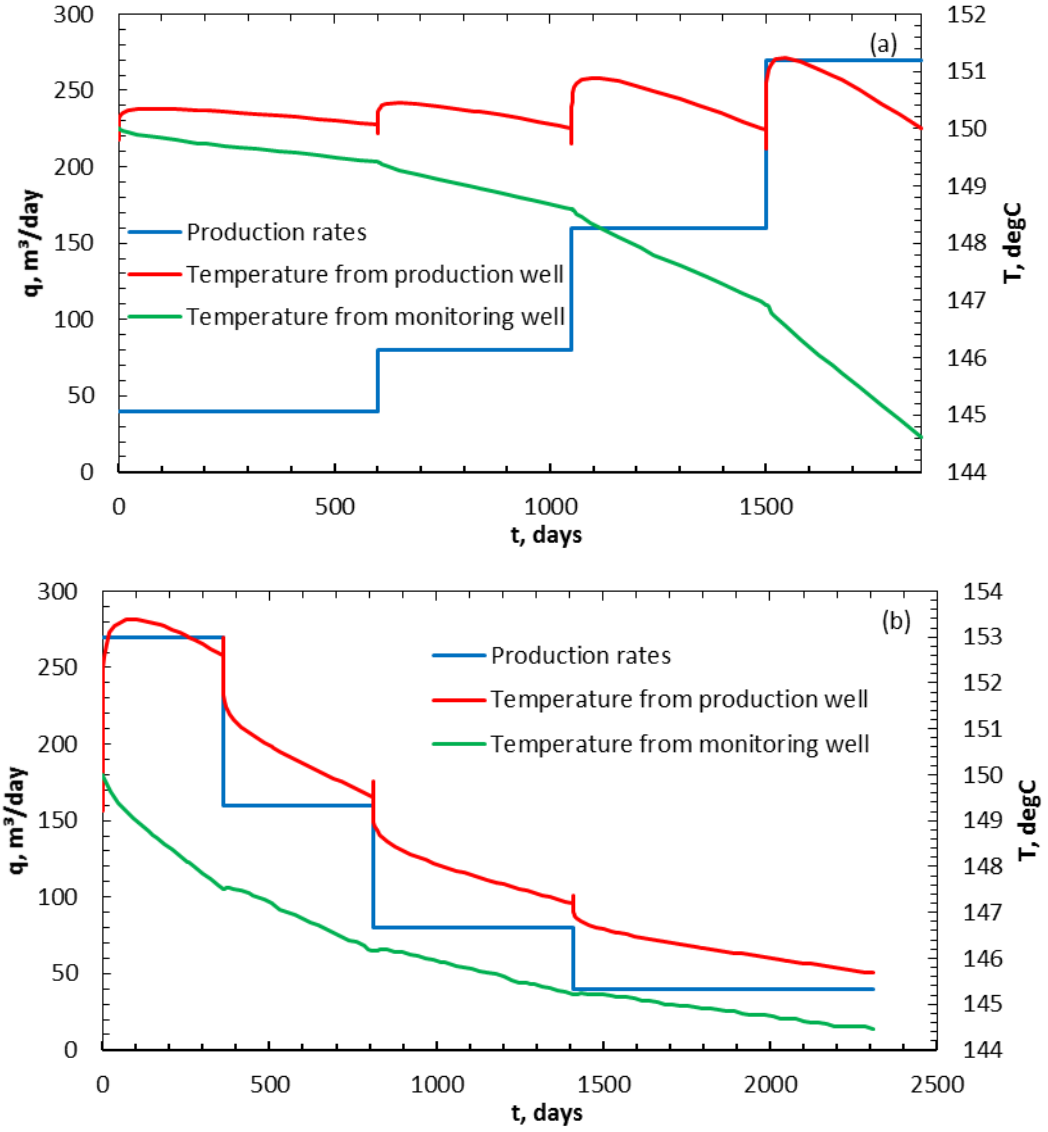

Figure 5. 13. Sandface temperature profiles obtained from the production and monitoring wells using numerical simulation for the base case with increased (a) and decreased (b) flow rate sequences in BDF period.

Performing the above procedure, the drainage area using temperature data from Figures 5.14 and 5.15 are estimated and summarized in Table 5.9. The average error is below 20% for the worst case. As expected, the temperature data in monitoring well are much better compare to those from the production well. The accuracy of the monitoring well TTA outperforms those from the production well by more than 10% suggesting that TTA for BDF using monitoring well(s) temperature data can be very useful.

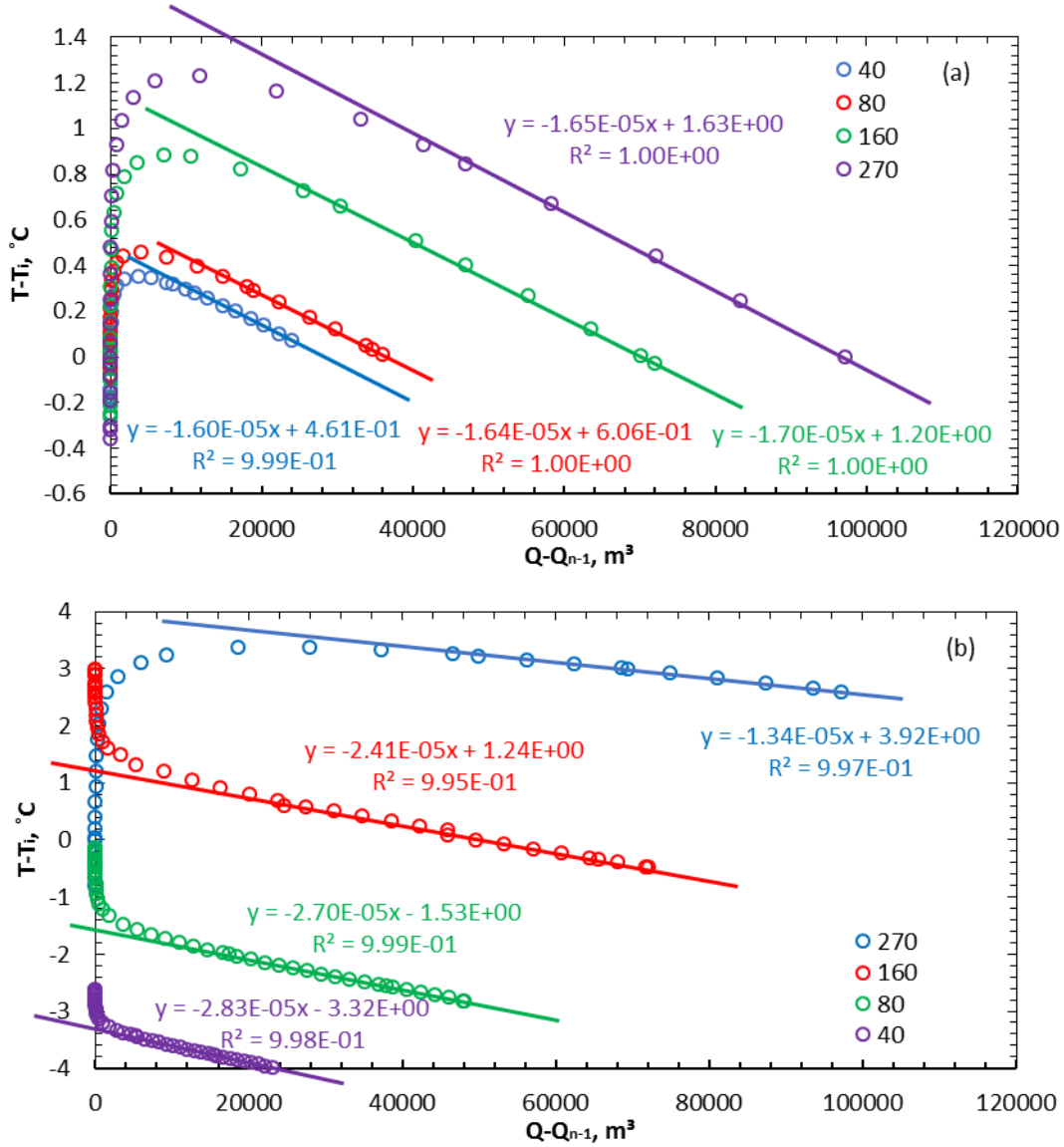

Figure 5. 14. Interpretation results of material balance time approach on temperature data from the production well with increased (a) and decreased (b) flow rate sequences.

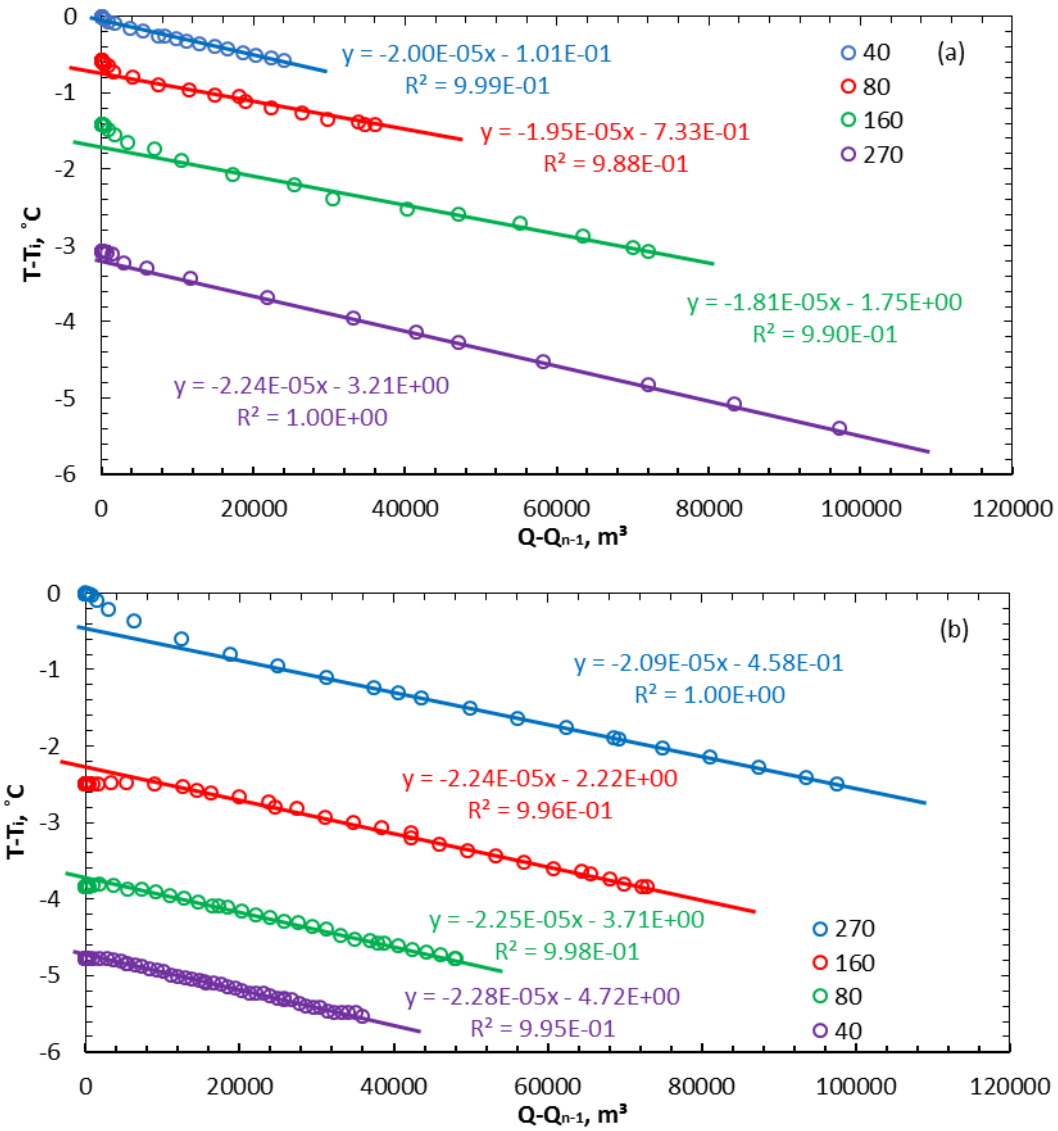

Figure 5. 15. Interpretation results of material balance time approach on temperature data from monitoring well with increased (a) and decreased (b) flow rate sequences.

Table 5. 8. Flow sequence for step-rate production during late boundary dominated flow period.

Flow period	Increased flow rates (m^3/day)	Decreased flow rates (m^3/day)
1	40 for 600 days	270 for 360 days
2	80 for 450 days	160 for 450 days
3	160 for 450 days	80 for 600 days
4	270 for 360 days	40 for 900 days

Table 5. 9. TTA characterization results for step-rate production during late boundary dominated flow period.

	Estimates (m^3, flow periods 1-4)	Average estimate (m^3)	Reference (m^3)	Error (flow periods 1-4)	Average error
A from Figure 5.14a	236843/228282 /228282/228282	230432	282743	16%/19% /19%/19%	18%
A from Figure 5.14b	182626/334071 /365251/391341	318322		35%/18% /29%/38%	12%
A from Figure 5.15a	316083/249035 /260894/311294	284326		11%/12% /8%/10%	1%
A from Figure 5.15b	285353/311294 /311294/326117	308514		1%/10% /10%/15%	9%

5.2.2.4 Constant pressure production during late boundary dominated flow period

With the derived analytical solution (Equation 5.31), we can model the temperature transient analytically for constant pressure production during late BDF period. To verify this solution, analytically modeled results are compared with simulated temperature data and illustrated in Figure 5.16. The verifications are conducted under similar settings initiated in section 5.2.2.2, the flow parameters of which are presented in Table 5.10. The analytically and numerically modeled temperature profiles show good agreement.

Table 5. 10. Flow parameters for the exponential decline of production rate.

BHP (MPa)	q_i (m^3/day)	D (day^{-1})
60	945.8	0.0059
80	674.5	
100	408.8	

As suggested by the analytical solution and confirmed by numerical simulation, the sandface temperature profile under BDF presents quasi-linear cooling behavior for all three cases in the Cartesian plot (Figure 5.16b) graphed versus the cumulative production. The BDAE under exponential decline of production rate, induced by the gradually depleting reservoir average pressure over time, is accounted for to observe this quasi-linear behavior. Almost identical slopes of the quasi-linear behavior for all the cases indicate that these slopes are strong functions of reservoir and fluid properties. We can perform the reservoir characterization analysis based on the slope calculation from Equation 5.34, using the following procedure:

1. Identify the late-time effect on the temperature data (indicated by the black lines in Figure 5.16b), draw straight lines through it, and find the slope m_3.
2. Estimate reservoir permeability k from m_3 using Equation 5.40, which can be derived from Equation 5.34:

$$k = \frac{\mu_{JT}\mu D\left(1+\ln C_1\right)}{4\pi H m_3} \tag{5.40}$$

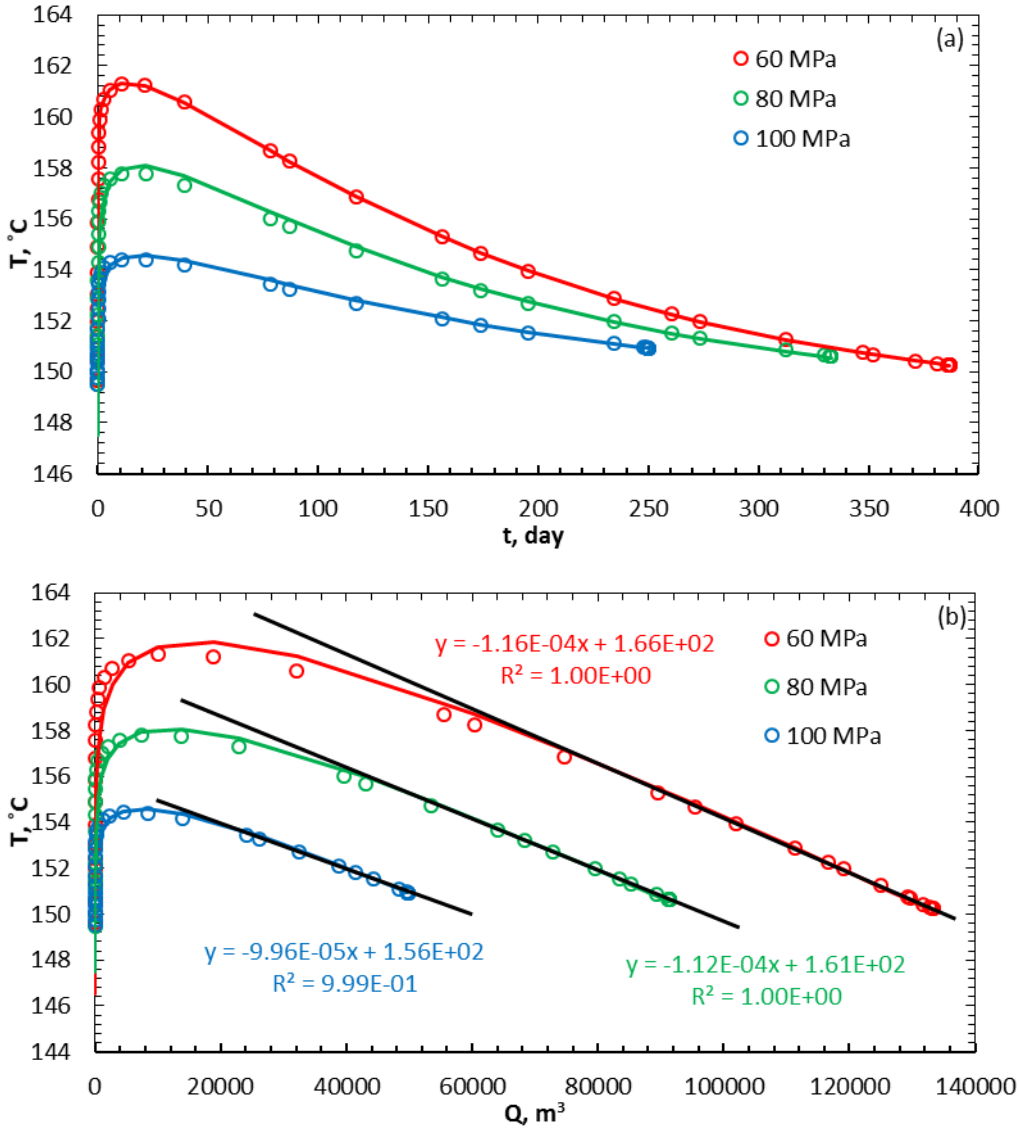

Figure 5. 16. Sandface temperature profiles obtained from the production well using numerical simulation (dotted lines) for the base case with constant pressure production. (Solid lines represent analytical results.)

Table 5.11 illustrates the TTA characterization results using the above procedure on the temperature data in Figure 5.16b. The agreements for all estimations further validate the newly derived analytical solution (Equation 5.31) in terms of modeling accuracy. Along with the slope estimations, all cases provide very accurate permeability estimations (less than 5% error), which are verified with the simulation setting. In addition, since the JT effect is taken into consideration in deriving the analytical solution along with the exponential decline of production rates, monitoring well surveillance is not required to improve the estimation accuracy during BDF period for constant pressure production. The estimations from the production well alone fulfill the reservoir characterization objective and our analytical solution works well for this scenario.

Table 5. 11. TTA characterization results for constant pressure production during late BDF period.

	Slope estimation	Permeability estimation (md)	Error
60 MPa	1.14×10^{-4}	19.5	2.4%
80 MPa	1.08×10^{-4}	19.9	0.4%
100 MPa	9.82×10^{-5}	20.9	4.5%
Reference	1.08×10^{-4}	20	-

5.2.3 Case Studies

In section 5.2.2, we presented and investigated our proposed methods with numerical simulation results. To further demonstrate the applicability of our proposed approaches, we apply them to two case studies published in the literature (Ramazanov et al. 2010, Onur and Cinar 2017b). These two cases are step-rate and constant pressure production during the early pressure transient period. In these cases, TTA was performed in a short period of time while BDF is not yet established. We have yet located published temperature data during late BDF period.

5.2.3.1 Temperature data for step-rate production

Onur and Cinar (2017b) reported series of temperature data associated with a step- rate TTA, which consists of 5 production and 2 buildup periods. We select a portion of this test (production periods 2-5) with a sequence of increased production rate to perform the analysis. Figure 5.17 presents the temperature data and production rates for this test, which is conducted on three cases (1 for an undamaged reservoir, 2 for a stimulated reservoir, and 3 for a damaged reservoir). The stimulated reservoir tends to have smaller temperature signal since the stimulated permeability results in a smaller pressure drop for the same production rate. The estimation of damaged zone parameters in TTA has been developed for constant production rate condition (section 3.2). Therefore, with the approach of superposition cumulative production, it can be also estimated for variable rate production scenario.

Following the procedure introduced in section 5.2.2.1, the results of applying the superposition cumulative production approach are illustrated in Figure 5.18. The proposed method is applicable to all three cases since the agreement between production periods for each case is acceptable. Flow periods with higher production rate present the best results due to stronger temperature changes observed. Long production period is critical to detect the contrast between the reservoir and the stimulated/damaged zone since temperature signals for shorter production period may not propagate far into the reservoir (Figures 5.18b and 5.18c). The effect of the stimulated/damaged zone is noted by the green line, the smaller slope of which indicates the stimulated zone (Figure 5.17b, case 2), and vice versa (Figure 5.18c, case 3). The stimulated/damaged zone permeability and radius can be characterized similarly to those for the reservoir:

1. Identify the stimulated/damaged zone effect in the temperature data (indicated by the green lines in Figure 5.18), draw straight line through it, and find the slope m_4 for it.
2. Calculate the stimulated/damaged zone permeability k_s from m_4 using Equation 5.41, which is similar to Equation 5.35:

$$k_s = -\frac{1.152\mu_{JT}\mu}{2\pi H m_4} \tag{5.41}$$

3. Identify the initial reservoir temperature in the temperature data (indicated by the black lines in Figure 5.18), draw straight line through it, and find the intersection of the green line and black line to obtain Q_s.
4. Calculate the stimulated/damaged zone radius r_s from the Q_s using Equation 5.42, which is similar to Equation 5.36:

$$Q_s = \frac{\left\{\phi\left[\rho_w c_w S_{wr} + \rho_f c_f \left(1 - S_{wr}\right)\right] + \left(1-\phi\right)\rho_s c_s\right\}\pi H r_s^2}{\rho_f c_f} \tag{5.42}$$

5. Calculate the skin factor:

$$S = \left(\frac{k}{k_s} - 1\right)\ln\left(\frac{r_s}{r_w}\right) \tag{5.43}$$

Table 5.12 presents TTA characterization results on the temperature data in Figure 5.18. Compare with the results in Table 5.5, the estimation errors are slightly higher in some cases due to the data quality. Overall, the estimations are fairly decent. This case study extends the applicability of the superposition cumulative production approach from theoretical analysis of simulated temperature data to field case implementation.

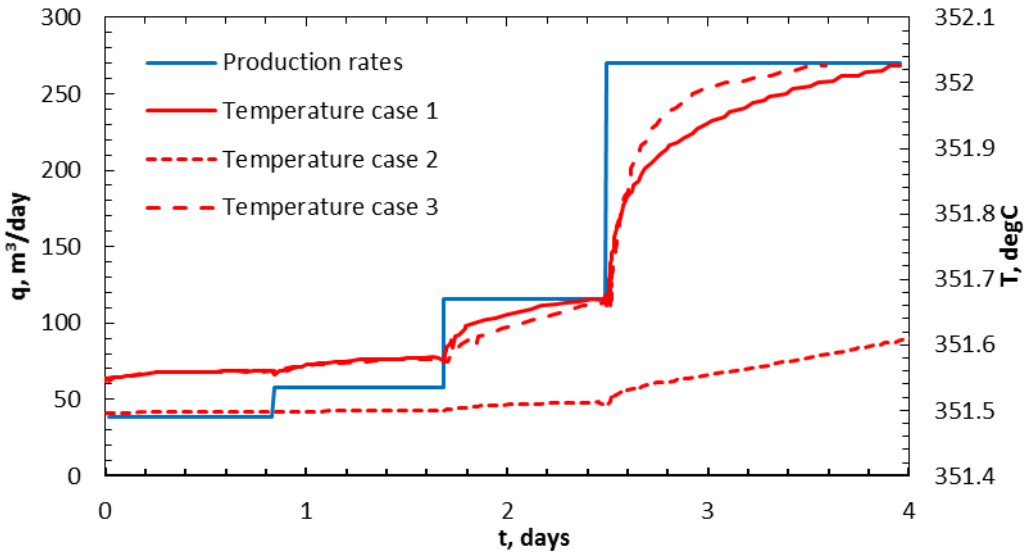

Figure 5. 17. Temperature and production rate data reported in Onur and Cinar (2017b) for production periods 2-5.

Table 5. 12. TTA characterization results on temperature data in Figure 5.18.

	Case 1 (Figure 5.18a)	Case 2 (Figure 5.18b)	Case 3 (Figure 5.18c)
Reservoir permeability (md)	109	139	71.4
Reference (md)		105.6	
Error (%)	3.2	31.6	32.4
Stimulated/damaged zone radius (m)	-	1.5617	2.0162
Reference (m)	-	1.4591	1.3635
Error (%)	-	7	47.9
Stimulated/damaged zone permeability (md)	-	719	32.4
Reference (md)	-	567.5	34.15
Error (%)	-	26.7	5.1
Skin factor	-	-2.038	3.343
Reference	-	-2	5
Error (%)	-	1.9	33.1

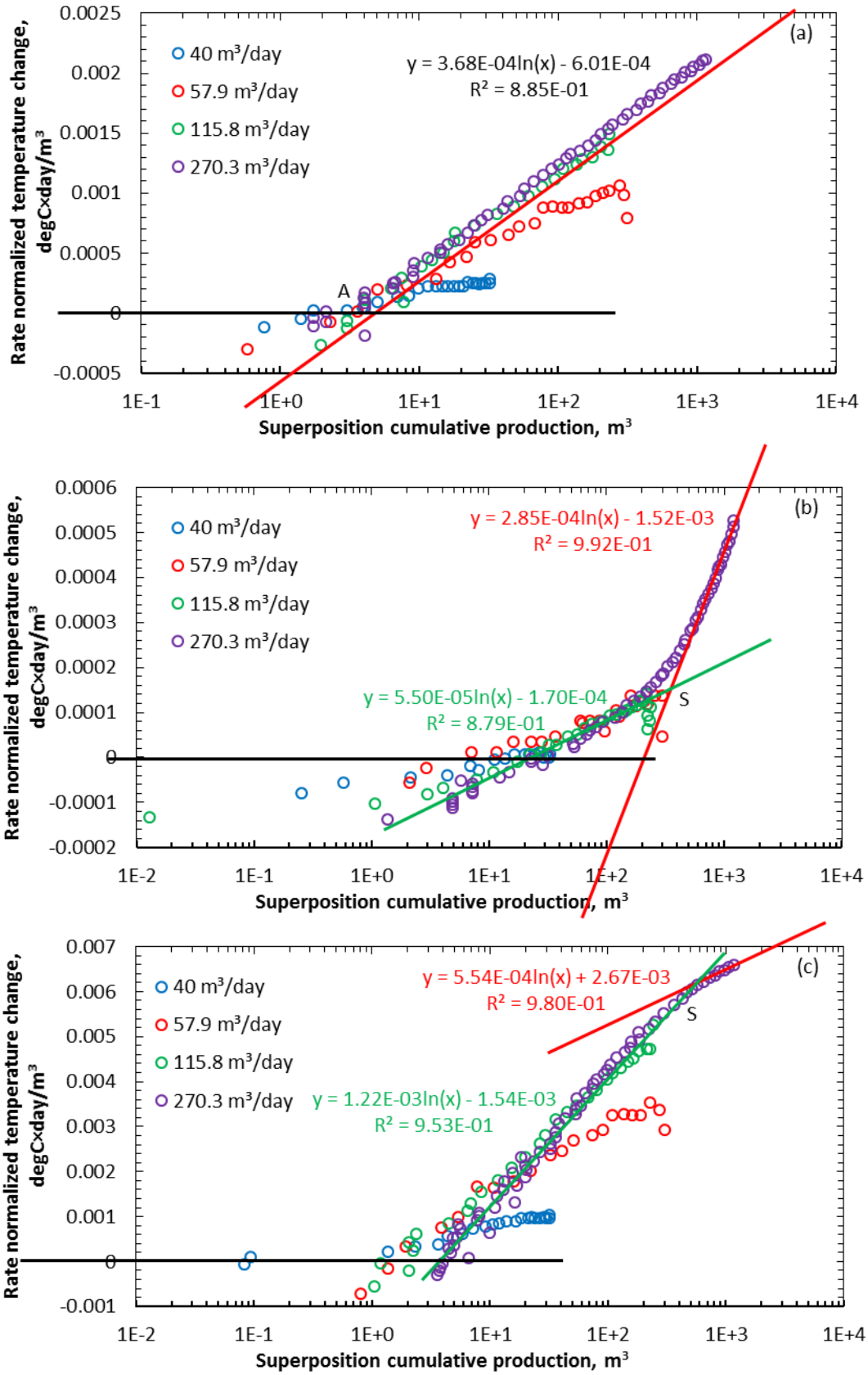

Figure 5. 18. Interpretation results of superposition cumulative production on temperature data in Figure 5.17 for (a) case 1, (b) case 2, and (c) case 3.

5.2.3.2 Temperature data for constant pressure production

Ramazanov et al. (2010) documented a set of temperature data associated with constant drawdown production of an oil well, the pressure of which are 5 atm, 25 atm, and 100 atm for the initial reservoir pressure of 200 atm. Since they did not report the production rate histories for this three drawdown conditions, we simulate the rates and present them along with the temperature data in Figure 5.19a. The production rate and magnitude of temperature changes are significantly higher for high drawdown cases. And the temperature signals are much smoother compared to our simulation cases in section 5.2.2.2. However, in Ramazanov et al. (2010), the authors pointed out that their analytical solution did not match with the temperature signals, especially for the high drawdown case. Therefore, we apply our procedure in section 5.2.2.2 to check the validity of the simplified superposition approach.

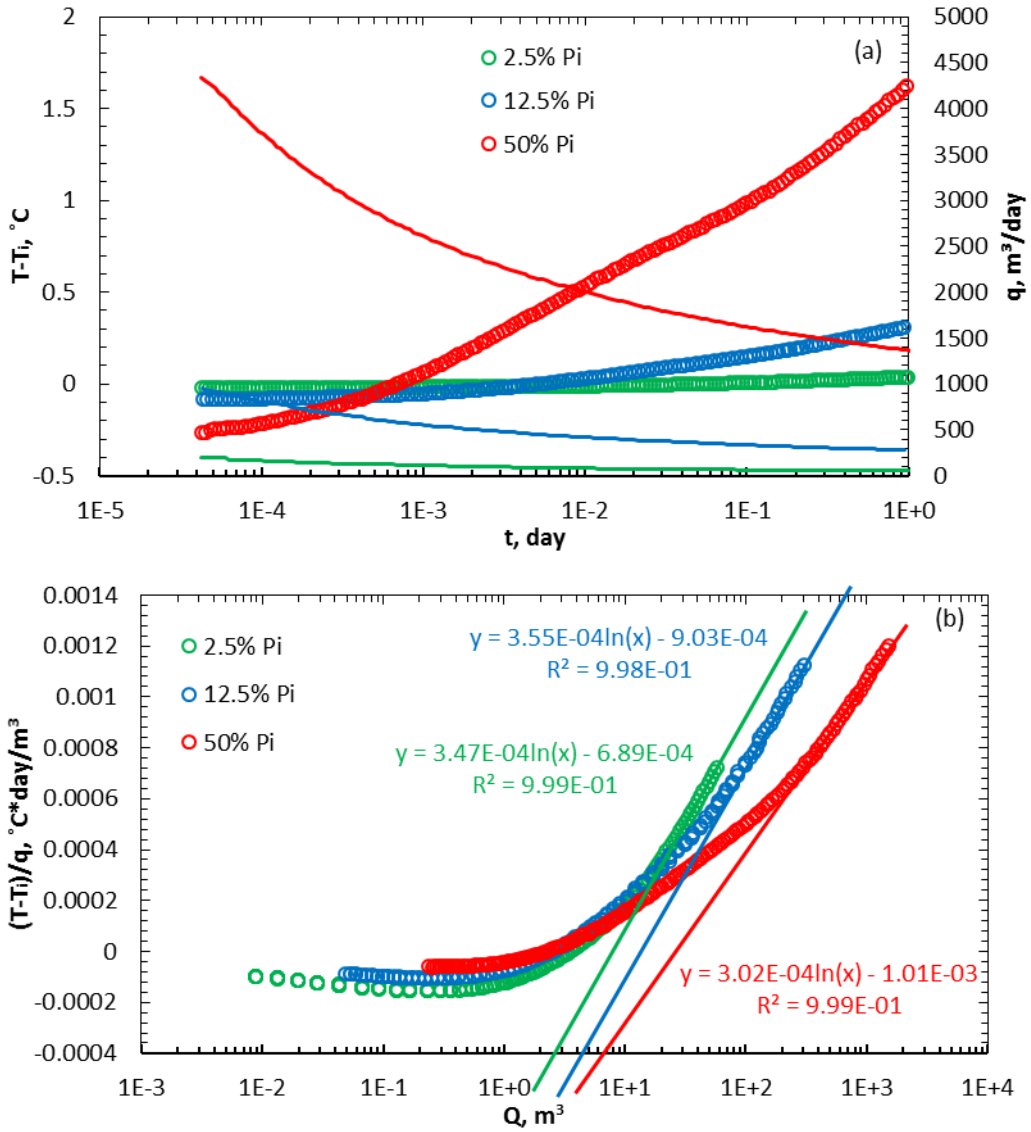

Figure 5. 19. Case study on temperature data (Ramazanov et al. 2010) from constant pressure production, (a) data, and (b) interpretation results. (Dotted lines for temperature, solid lines for production rates)

Figure 5.19b illustrates the results of implementing the simplified superposition approach on the temperature data of Figure 5.19a. The almost identical slopes on three different

drawdown cases validate the simplified superposition approach on this case study. Further reservoir characterization results are presented in Table 5.13. Very precise results are achieved for all three cases on permeability estimations. Slightly more errors are observed for higher drawdown case, which is only 5% maximum. In short, the simplified superposition approach successfully addresses this case study.

Table 5. 13. TTA characterization results on temperature data in Figure 5.19.

	5 atm	25 atm	100 atm
Slope estimation	0.00083	0.00083	0.00076
Permeability estimation (md)	26.7	25.8	28.8
Reference (md)		25	
Error (%)	6.8	3.2	15.2

Chapter 6. Application of Temperature Transient Analysis in Unconventional Reservoir

Implementation of temperature downhole monitoring system has contributed to the unconventional reservoir characterization and fracture diagnostic in the past decade. Thermal modeling research in this area has often focused on the temperature profiling along the horizontal wellbores. In this chapter, we apply analytical and numerical approaches used in previous chapters to analyze production temperature data in the unconventional reservoir. Two cases are presented here: a numerical model to simulate thermal signals from producing multi-stage hydraulic fractured horizontal well (MFHW) and an analytical model to analyze flow-back temperature data.

6.1 Forward Numerical Modeling in Producing Unconventional Reservoir

In this section, we develop a new forward model to simulate the temporal temperature signals along a producing unconventional well with hydraulic fractures.

6.1.1 Model Description

To simplify the modeling process, we first consider a single fracture model to perform the forward prediction analysis. Figure 6.1 presents the model of the single fracture model. Because of the model symmetry, this model contains only half of the fracture (the blue plane in Figure 6.1) with the surrounding stimulated zone (green to orange areas) and the homogeneous-formation of shale gas reservoir (red areas). The entire model geometry is $400\times150\times80$ m^3 for the base case. We select the fracture geometry of this model to be comparable with previously published fracture models (Yoshida, Zhu, and Hill 2014) (Cui, Zhu, and Jin 2015) (Sun, Yu, and Sepehrnoori 2017). The dimensionless fracture conductivity (F_{CD}) is set to 50 while other parameters can vary in the range of values in the bracket in Table 6.1. Other model properties include fracture height of 80 m, fracture porosity of 0.32, fracture width of 0.1 m, reservoir porosity of 0.08, reservoir initial temperature of 140 degC, rock conductivity of 3.17 W/mK, and reservoir initial pressure of 10 MPa. The reservoir fluid is single phase methane and is produced with a constant bottom-hole pressure of 8 MPa, the fluid property of which is computed through CMG-WINPROP (2015).

We perform the simulations in (CMG-GEM 2015) thermal model using Cartesian gridding. In the vertical direction, the total grid number is 19, and the grid sizes linearly decrease towards the horizontal well. In the two horizontal directions, the total grid number is 25 for each direction. The grid refinement is linear for y-direction and logarithmic for x-direction, both of which are decreased towards the perforation.

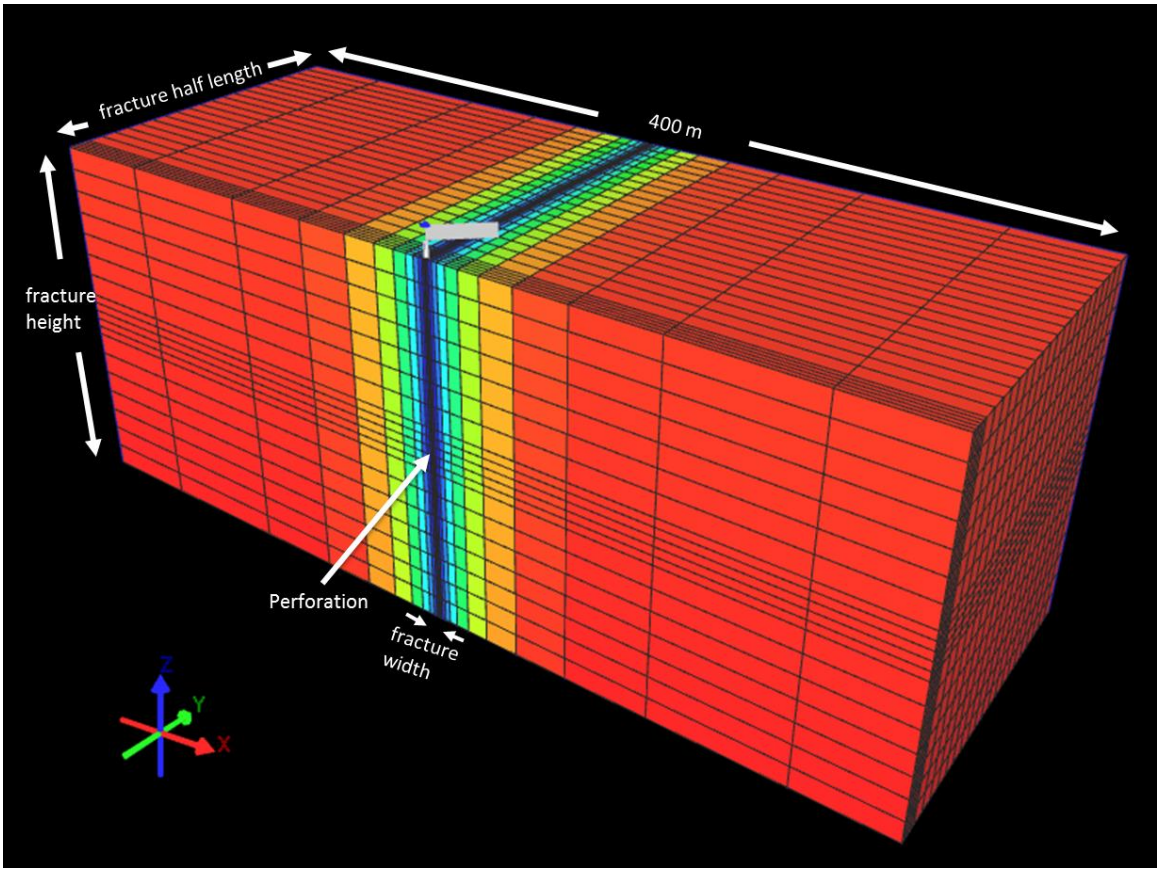

Figure 6. 1. Model schematic and griding system for the single fracture model.

Table 6. 1. Model parameters for unconventional reservoir.

	Fracture permeability k_f (mD)	Fracture width w_f (Crafton)	Stimulated zone permeability k (mD)	Fracture half-length X_f (Crafton)	Dimensionless fracture conductivity F_{CD}
Yoshida, Zhu, and Hill (2014)	40 (10-100) mD×ft		0.006	150 (62-198)	44.4
Cui, Zhu, and Jin (2015)	900	0.23	0.000583	500	710.1
Sun, Yu, and Sepehrnoori (2017)	2000 (800-5000)	0.002 (0.001-0.004)	0.1	365 (20-250)	1.1
This model	450 (30-300)	0.33	0.006	492 (32.8-492)	50

6.1.2 Physical Insight of the Temperature Signal

We simulate the base case to obtain the temporal temperature signal at the perforation. The temperature signal at the perforation is referred to as arriving temperature, which can be measured from DTS implemented behind the casing. We consider this type of temperature signal for our analysis since it is independent of the wellbore thermal effect and directly impacted by the fracture and reservoir properties.

Figure 6.2 presents the arriving temperature signal after 60 days of production for the base case. The temperature signal at the perforation drops significantly at the early time and is followed by the warming process for at least 60 days. To investigate the early cooling effect, we plot the temperature signal in a semi-log plot (Figure 6.2b). Forward thermal modeling in the conventional reservoir (chapter 3) revealed the main baro-thermal effects associated with hydrocarbon production: AE effect and JT effect. Those effects are also visible in Figure 6.2, in which the JT effect is a cooling effect due to the positive value of gas JT coefficient.

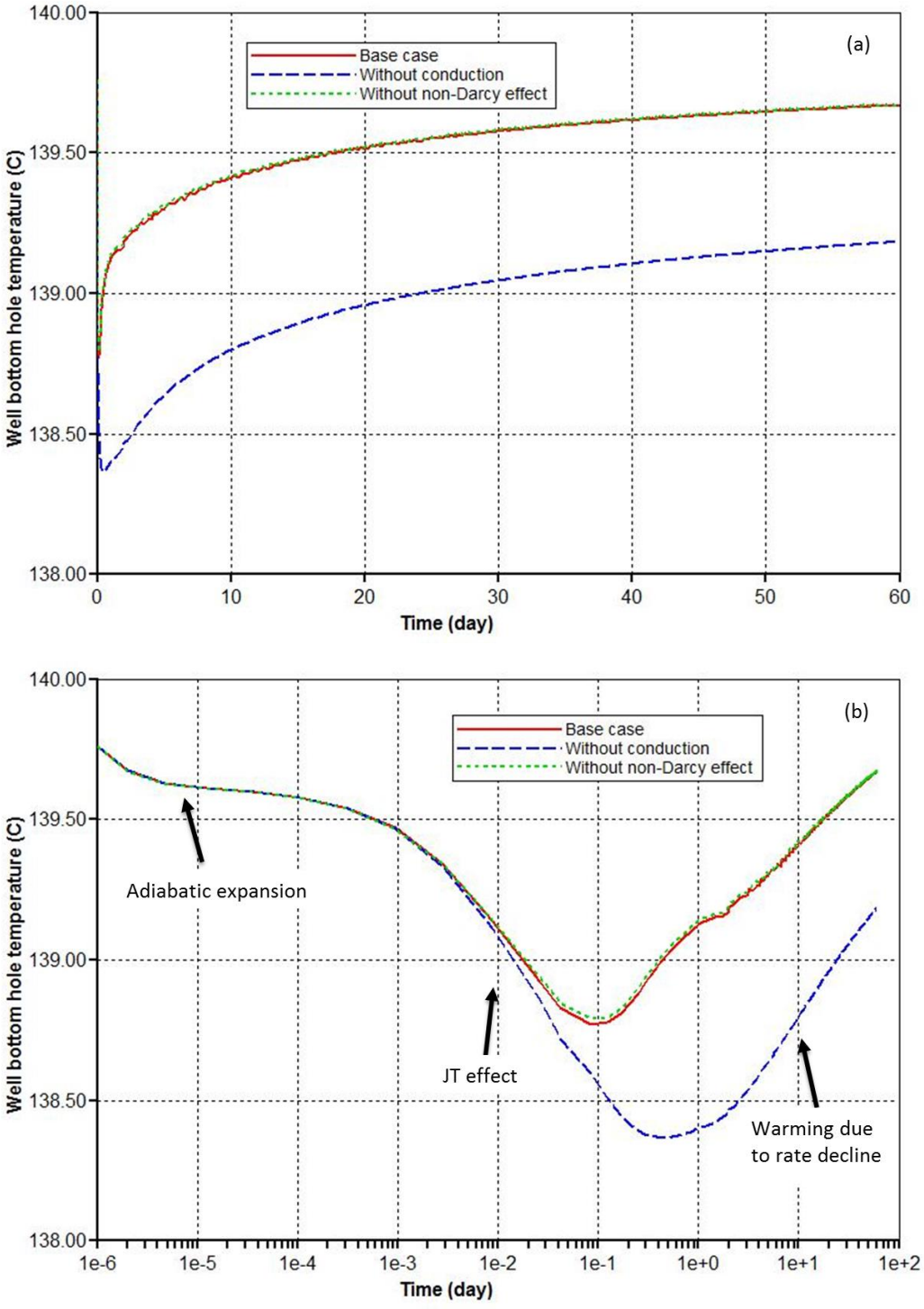

Figure 6. 2. Temporal arriving temperature profiles obtained from numerical simulation in (a) Cartesian and (b) semi-log plots for the base case.

Heating effect encountered during production can be related to heat conduction with surrounding formations. To determine if that is the case for the heating effect in Figure 6.2, we simulate the base case with zero thermal conductivity as the blue dashed line. Compared with the base case considering the heat conduction, the maximum cooling for zero thermal conductivity case is increased, but the trend of heating effect remains almost identical although the magnitude of the temperature signals is different. This finding suggests that even without the heat conduction, the heating effect still occurs. The heating effect is the result of production rate decline for a constant drawdown production. We observed a similar trend in Figures 5.12 and 5.16 for constant pressure production, although the temperature reverse is limited in the conventional reservoir due to the abundant flow to the wellbore.

Despite the effect of thermal conductivity, we also include the non-Darcy flow effect in the numerical modeling. The temperature profile excluding the non-Darcy flow effect illustrates very similar behavior with the one considering the effect. We consider the thermal conduction and non-Darcy flow effects for the following analysis.

6.1.3 Effect of Fracture Conductivity

As stated in the literature review (chapter 2), temperature signal sensitivity analysis on fracture and reservoir properties has been reported in several publications (Yoshida, Zhu, and Hill 2014, Cui, Zhu, and Jin 2015, Sun, Yu, and Sepehrnoori 2017). The effect of fracture conductivity is the most controversial factor among all the properties analyzed previously. Figure 6.3 presents the sensitivity analysis on fracture conductivity from Yoshida, Zhu, and Hill (2014), Cui, Zhu, and Jin (2015), Sun, Yu, and Sepehrnoori (2017). Yoshida, Zhu, and Hill (2014) and Cui, Zhu, and Jin (2015) showed that high conductivity fracture resulted in weaker cooling effect, but Sun, Yu, and Sepehrnoori (2017) reported the opposite observations. To investigate the reason behind this inconsistency, numerical simulation is performed on the base case with fracture conductivity variation illustrated in Table 6.1.

Figure 6.4 illustrates the sensitivity analysis of arriving temperature temporal profiles on fracture conductivity. All the temperature profiles follow the same trend for the base case (Figure 6.2). The maximum cooling effect is observed around 0.1 days, while higher fracture conductivity results in stronger cooling signals from the start of production to about 1 day. However, after the heating effect starts dominating (about 5 days), the effect of fracture conductivity is reversed. Higher fracture conductivity produces a stronger heating effect, therefore smears the cooling temperature signals more significantly. This observation explains the controversy from previous publications. Depending on the time of interest (0.01-0.5 day for Sun, Yu, and Sepehrnoori (2017), and 1-300 days for Yoshida, Zhu, and Hill (2014) and Cui, Zhu, and Jin (2015)), the effect of fracture conductivity on the temperature signals are different.

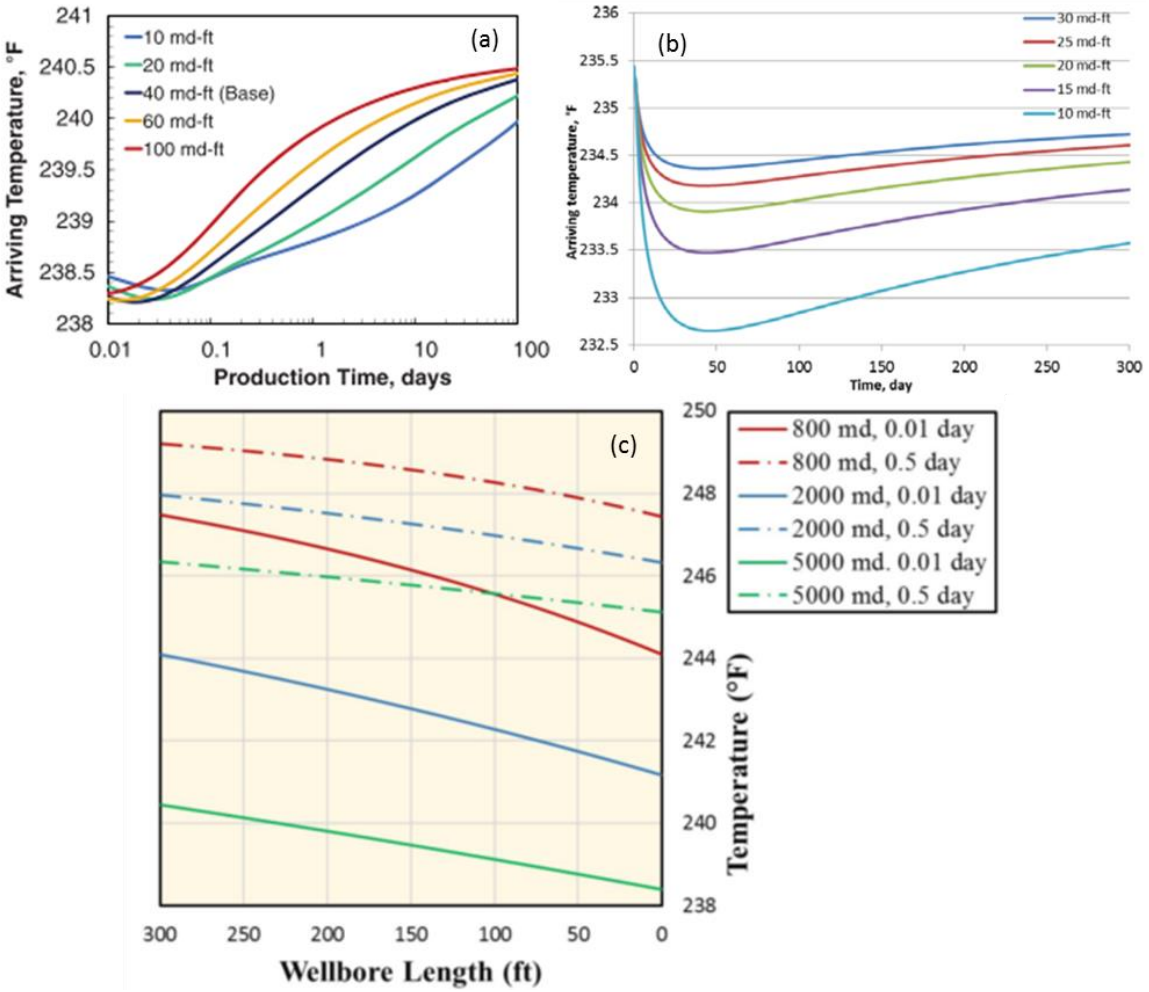

Figure 6. 3. Temperature signal sensitivity analysis on fracture conductivity reported in Yoshida, Zhu, and Hill (2014), Cui, Zhu, and Jin (2015), Sun, Yu, and Sepehrnoori (2017) (c).

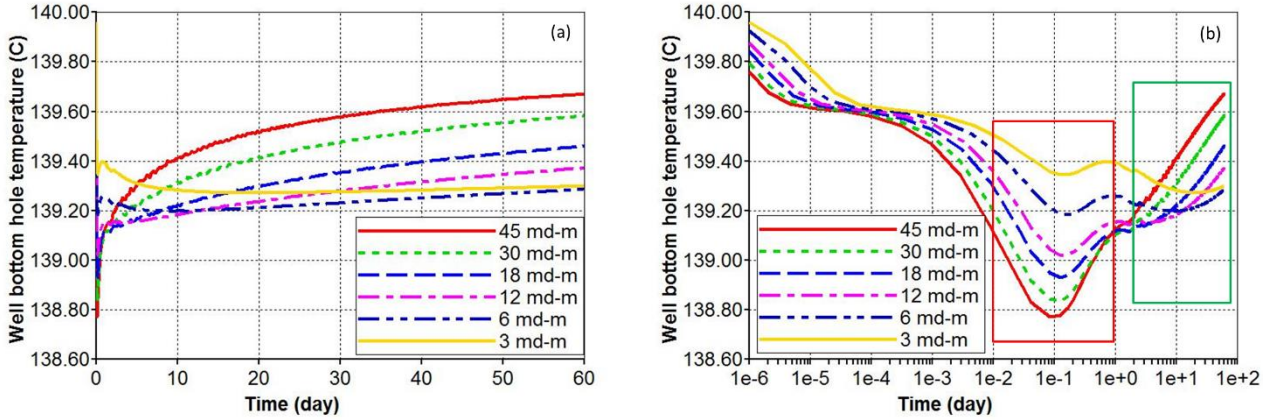

Figure 6. 4. Arriving temperature temporal profiles with various fracture conductivities in (a) Cartesian and (b) semi-log plots.

6.1.4 Effect of Fracture Half-Length under Constant Dimensionless Fracture Conductivity

Rate transient analysis has been widely applied to characterize hydraulic fracture and unconventional reservoir. For finite conductivity fracture evaluation, the production rate decline is sensitive to the dimensionless fracture conductivity (F_{CD}, defined in Equation 6.1) in the transient flow period. However, the production rate data is not sensitive to the individual

properties in Equation 6.1 unless F_{CD} changes. Therefore, in this section, we investigate the effect of fracture half-length along with fracture conductivity while keeping the dimensionless fracture conductivity constant (F_{CD}=50, property variations illustrated in Table 6.1).

$$F_{CD} = \frac{k_f w}{k x_f} \tag{6.1}$$

Figure 6.5 illustrates this sensitivity analysis with arriving temperature temporal profiles. Compared to Figure 6.4, the temperature signals before the maximum cooling are almost identical, indicating that the variations of fracture half-length impose a minimum effect on the temperature profiles. After 1 day of production, the reverse effect in Figure 6.4 is compensated by the variations of fracture half-length. As a result, the case with higher fracture conductivity and half-length presents a stronger cooling effect. Under constant F_{CD}, the temperature signals are sensitive to the individual properties in Equation 6.1. To be specific, the cooling effect is a strong function of fracture conductivity, and the proceeding heating effect is the combined effect of fracture conductivity and half-length.

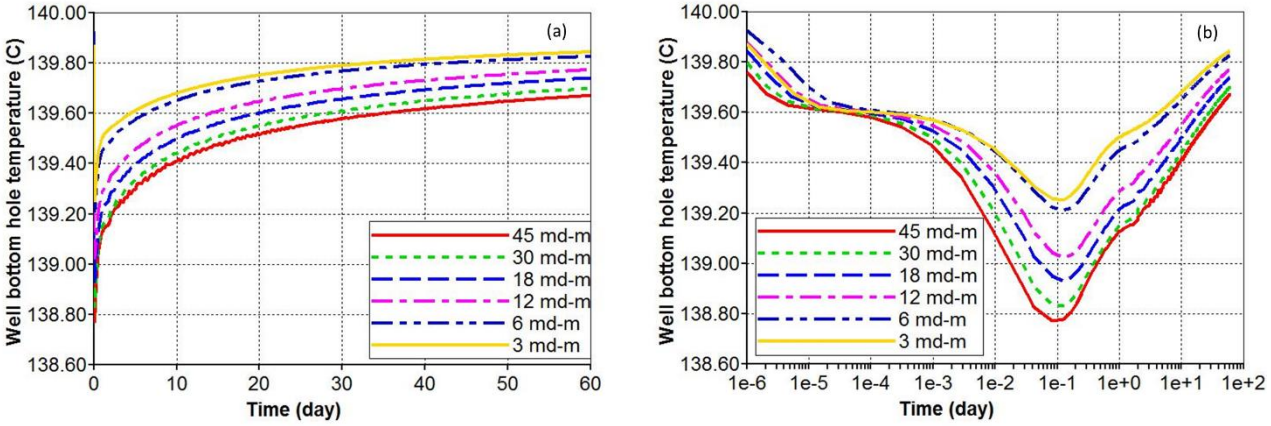

Figure 6. 5. Arriving temperature temporal profiles with various fracture half-lengths and conductivities in (a) Cartesian and (b) semi-log plots.

6.2 Fracture Diagnostic during Stimulation Fluid Flow-back

In this section, we investigate the temperature signals obtained during stimulation fluid flow-back to perform fracture diagnostics. First, we perform numerical simulations to identify the inflow fluid temperature signals from each fracture in the flow-back period. An analytical solution is then derived to estimate the fluid temperature profile of a shut-in test during stimulation fluid flow-back subject to after-flow. With the development of the analytical solution, the forward modeling results are validated against those from the numerical simulation. Several properties of wellbore and temperature are selected to perform sensitivity analyses on the temperature profile. In the end, we introduce and apply inversion procedures to estimate the inflow temperature profile and after-flow rate of each fracture from temperature data.

6.2.1 Problem Description and Objectives

As mentioned in section 2.7, successful thermal modeling for fracture diagnostic relies on accurate estimation of inflow temperature from each fracture during production and flow-back period. To investigate the nature of the inflow temperature during the flow-back period and identify the relevant assumptions and challenges in its modelling, we first perform numerical simulations. Figure 1 presents the model schematic for the wellbore-fracture thermal

model of the flow-back period, which is very similar to Figure 6.1 with the additional horizontal wellbore to simulate the inflow temperature inside the wellbore. The setting of the fracture system is identical to Figure 6.1. For the base case, the horizontal wellbore has a diameter of 0.11 m and is surrounded with a low conductivity (0.9 W/mK) 0.1-m thick cement layer.

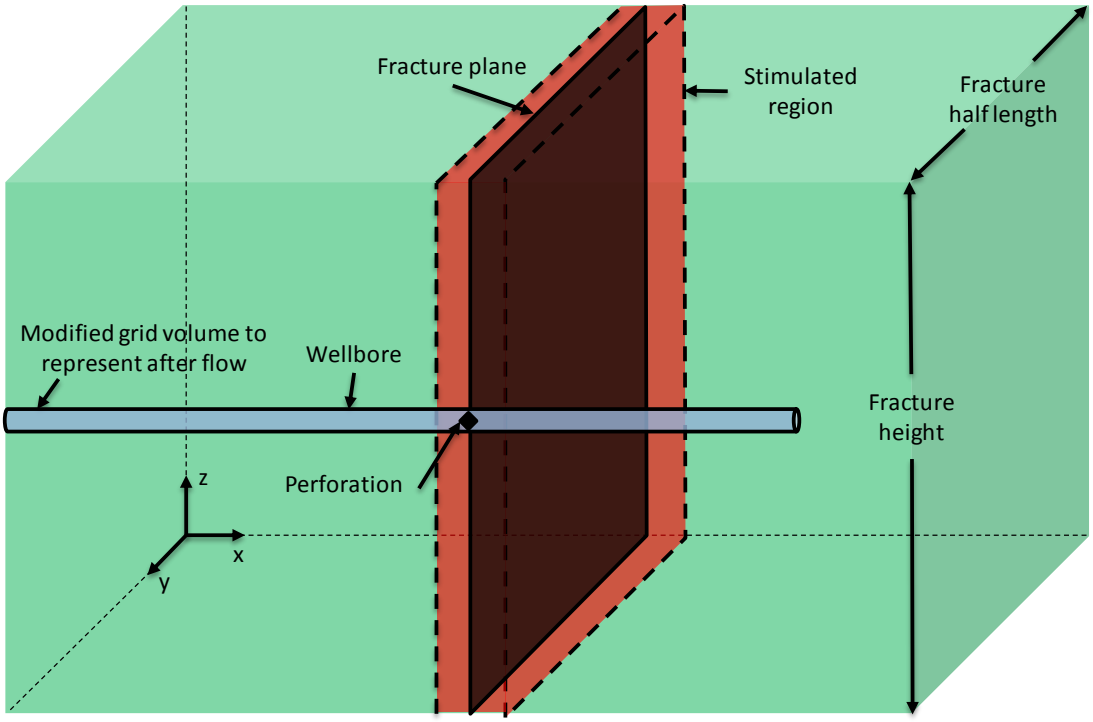

Figure 6. 6. Model schematic for the single fracture model.

To simulate the hydraulic fracturing process for single fracture stage, 112 m^3 of stimulated fluid at 49 degC is injected for 1.5 hours into the fracture through the horizontal wellbore. The well is shut-in for 10 days (warm-back) before starting to produce (flow-back). Figure 6.7 shows the temperature field around the perforation after 2 days of the flow-back period. The inflow temperature is 75.6 degC, which is cooler than 77 degC of geothermal temperature. This suggests that the effect of hydraulic fracturing can still dominate the thermal behavior of the flow-back period, since the JT effect of oil produced for this case is a heating effect. Moreover, a region near the perforation (roughly 5×1×10 m^3) shows a very similar temperature to the inflow temperature. This observation indicates that if one can estimate the temperature at the perforation surrounding region, the inflow temperature can be obtained.

For thermal modeling of conventional reservoir production, surrounding region temperature can be obtained from build-up temperature signals of the shut-in test (Izgec et al. 2009, Nojabaei, Hasan, and Kabir 2014, Wu, Xu, and Ling 2015). Therefore, we added a shut-in period (2 days) after 5 days of flow-back in the base case. Figure 6.8 demonstrates the temperature field around the perforation after 8 hours of a shut-in. Away from the fracture, the wellbore temperature heats up towards the surrounding region temperature (geothermal) as expected. However, near the fractured zone, the wellbore temperature also heats up, which makes it higher than the surrounding region temperature. From the temperature field, it seems the warmer fluid from upstream intrudes into the fractured zone after shut-in resulting in the warmer temperature signals. This observation is confirmed from the velocity field of Figure 6.8.

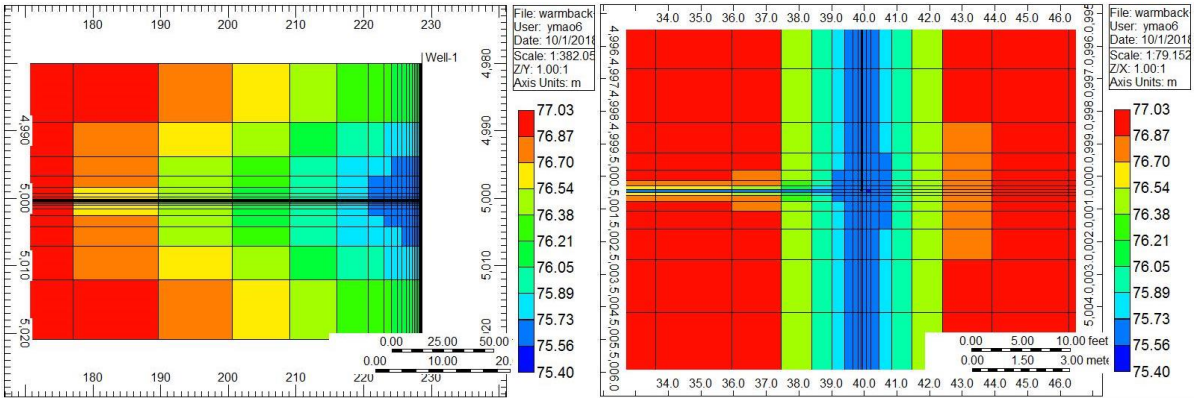

Figure 6. 7. Temperature field around the perforation in a fracture plane view (left) and wellbore vertical view (right).

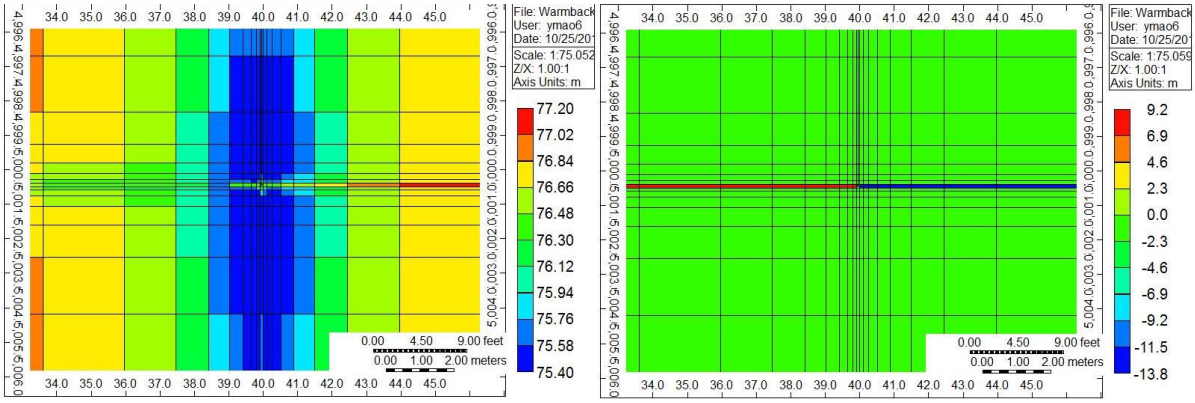

Figure 6. 8. Temperature (left) and velocity (right) field around the perforation in a wellbore vertical view.

In short, the objective of section 6.2 is to perform fracture diagnostic with flow-back temperature signals. The main objective is identifying inflow temperature from each of the fractures, which is critical as an input for PLT analysis. From preliminary simulation studies above, we found out that the inflow temperature is identical to the surrounding fractured region temperature, which is masked by the heating effect introduced from wellbore fluid flow after the shut-in test (after-flow). Therefore, we propose to analyze this heating effect with analytical and numerical models, which will be explained in the next section. With the quantified heating effect, we can obtain the inflow temperature for each fracture.

6.2.2 Analytical and Numerical Model Descriptions

To investigate the heating effect associated with after-flow, we introduce analytical and numerical approaches to model the temperature signal. Figure 6.9 presents the model description and temperature field, which contains half of the wellbore distance between fractures. The boundary condition at the casing wall is no flow and given temperature distribution, obtained based on multiple cases simulated by CMG-STARS (2015) for the flow-back period (Figure 6.10). The wellbore fluid movement is represented by the inflow away from the perforation and the condition of thermal insulation is used at the inflow. The fluid temperature at the center of the conduit represents the measured shut-in temperature signals from DTS or PLT.

With model description presented in Figure 6.9, we develop an analytical solution of the fluid temperature. The governing equation of this model is an energy balance over the wellbore and fluid provided by Hasan, Kabir, and Lin (2005):

$$(1+C_T)\frac{\partial T_f}{\partial t}+v\frac{\partial T_f}{\partial x}=vL_R\left[T_{ei}(x)-T_f\right]+v\left(\phi'-\frac{g\sin\theta}{c_f Jg_c}\right)$$
$$\phi'=\mu_{JT}\frac{dp}{dx}-\frac{v}{c_f Jg_c}\frac{dv}{dx} \tag{6.2}$$

where ϕ' is a lumped parameter, C_T is the dimensionless thermal-storage parameter of the wellbore system, T_{ei} is the boundary condition (casing wall temperature illustrated in Figure 6.9), θ is well inclination from horizontal, and Jg_c is the conversion factor.

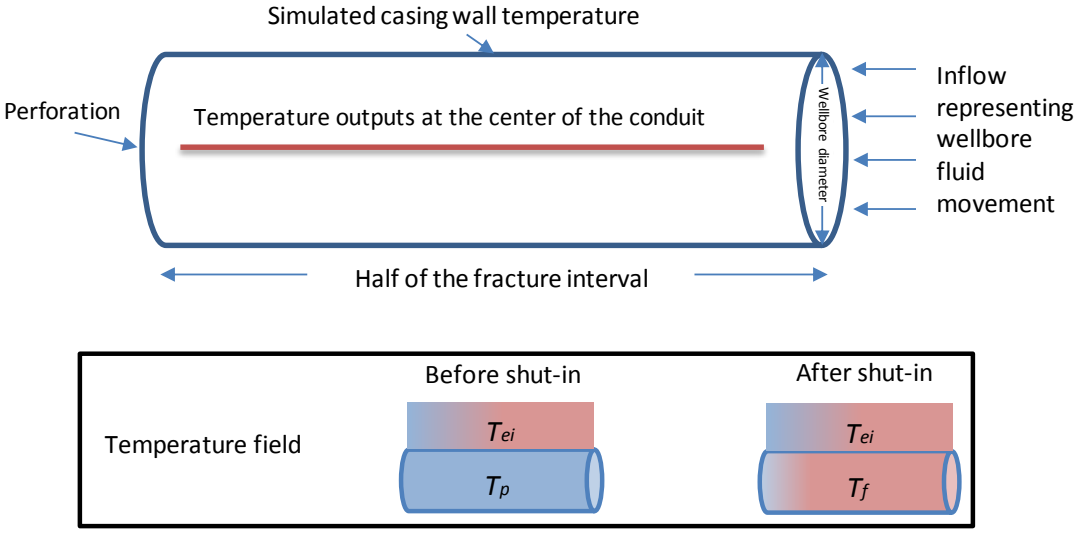

Figure 6. 9. Model schematic and temperature field to investigate the heating effect associated with after-flow.

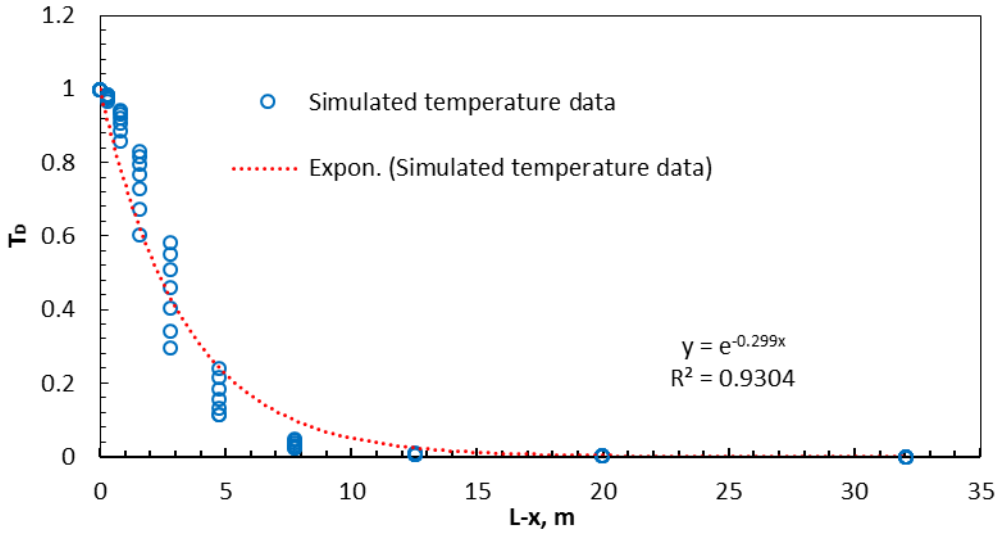

Figure 6. 10. Correlation on casing wall temperature boundary condition for T_{ei}.

Izgec et al. (2009) developed an approximate analytical solution of fluid-temperature subject to Equation 6.2 for buildup with after-flow effect and Spindler (2011) rigorously derived this solution with the Method of Characteristics and Laplace Transform. However, the boundary condition of their solution (T_{ei}) assumes homogeneous geothermal temperature near

the wellbore, which is not valid for this case. Instead, we use the correlation from Figure 6.10 to represent the boundary condition:

$$T_{ei}(x) = T_D \exp\left(-\frac{L-x}{a}\right) = T_i + \left(T_{\text{inflow}} - T_i\right)\exp\left(-\frac{L-x}{a}\right) \tag{6.3}$$

We set x direction the same as the after-flow direction (Figure 6.9) to comply with Equation 6.2. Therefore, L in equation 6.3 represents half of the fracture interval length (Figure 6.9). Before proceeding to the derivation, further assumptions are made to simplify Equation 6.2. Since we model the horizontal wellbore fluid temperature during the shut-in period, θ is equal to zero and pressure and velocity derivatives on space can be ignored. As a result, the last term in Equation 6.2 can be neglected, and the final governing equation for this study is:

$$\left(1+C_T\right)\frac{\partial T_f}{\partial t} + v\frac{\partial T_f}{\partial x} = vL_R\left[T_{ei}(x) - T_f\right] \tag{6.4}$$

The initial condition of Equation 6.4 is a constant producing wellbore fluid temperature before shut-in (T_p):

$$T_f\big|_{t=0} = T_p \tag{6.5}$$

We apply the Method of Characteristics to obtain the solution for Equation 6.4, the details of which are presented in the Appendix F. The analytical solution for wellbore fluid temperature during the flow-back period associated with after-flow is:

$$\begin{aligned} T_f &= T_i + \left(T_p - T_i\right)\exp\left(-\frac{vL_R t}{1+C_T}\right) \\ &+ \frac{aL_R\left(T_{\text{inflow}} - T_i\right)}{aL_R + 1}\exp\left(\frac{x-L}{a}\right)\left[1 - \exp\left(-\frac{vL_R t}{1+C_T} - \frac{vt}{\left(1+C_T\right)a}\right)\right] \end{aligned} \tag{6.6}$$

From inspecting Equation 6.6, the followings can be implied:

i. The derivation process relies on the assumption of constant velocity (v), which may not be the case for after-flow. While after-flow rates from communications between fractures can be considered as relatively constant, velocities in cases like wellbore-storage (WBS) are certainly declined over time. It is difficult to develop rigorous solution if time-dependent velocity is considered. We will show that the replacement of constant velocity by variable velocity in Equation 6.6 can provide satisfactory results for the variable velocity problem in the next section.

ii. The first and second terms on the RHS of Equation 6.6 are identical to those in Izgec et al. (2009), Nojabaei, Hasan, and Kabir (2014), which represents the warm-back process from T_p to T_i. The last term diminishes away from the fracture and indicates the heating effect associated with after-flow near the fracture. This observation provides different modeling equation for the fractured and non-fractured region: in the non-fractured region, one can model the wellbore fluid temperature with first and second terms on RHS of Equation 6.6; and in the fractured region, all the terms are required.

iii. C_T and vL_R are wellbore system parameters given in Hasan, Kabir, and Lin (2005), Izgec et al. (2009), Nojabaei, Hasan, and Kabir (2014). For this study, we focus on exploring other parameters including v, a, and T_{inflow}.

With the derived analytical solution (Equation 6.6), the wellbore fluid temperature can be modeled. To verify the analytically modeled results, we develop a comparable numerical model (same schematic in Figure 6.9) as a validation set. This numerical simulation is performed on non-isothermal flow module from COMSOL (2015), which includes sub-modules of laminar flow and heat transfer. The initial and boundary conditions in the sub-modules are set according to Figure 6.9 and the physics-controlled mesh type is used for this

finite element model. In section 6.2.3, the results from analytical and numerical models are presented.

6.2.3 Analytical Solution Verification on the base case

In this section, we model and verify the analytical solution against the wellbore fluid temperature profiles obtained from numerical simulation. With the derived analytical solution (Equation 6.6), we can model the wellbore fluid temperature analytically associated with after-flow during the flow-back period. First, we present the temporal temperature modeling results at various locations from the perforation. To verify this analytical solution, these analytically modeled results are compared with those from numerical simulation COMSOL (2015). Table 6.2 presents the properties of the base case for the verification.

Table 6. 2. Wellbore model setting for the base case and parametric analyses.

	Base case	Parametric analysis	
After-flow velocity (m/day)	20	10	30
Wellbore radius (m)	0.06	0.08	0.1
a (boundary condition coefficient) (m)	3	2	1
T_p (degC)	73	72	74
T_i (degC)	77		
T_{inflow} (degC)	73		
Fracture interval ($2L$) (m)	30		

Figure 6.11 presents the wellbore temperature modeling results obtained from the analytical solution and numerical simulation for the base case. The temporal temperature variations at different distances from the perforation show good agreement between analytical solutions (solid curves) and numerical simulations (dotted curves) for all the cases. As expected from the first and second terms of Equation 6.6, the wellbore fluid temperature starts increasing after shut-in towards the casing wall temperature (boundary condition of Equation 6.3). Away from the perforation (e.g. 10 m), the temperature can increase up to almost T_i of 77 degC. At the perforation, the temperature should remain at T_f of 73 degC if there is no after-flow. The heating effect of wellbore fluid temperature at the perforation is due to the warmer fluid away from the perforation moving in, which is mathematically represented by the last term in Equation 6.6. Therefore, as we mentioned in section 6.2.2, different modeling equations can be applied for fractured and non-fractured regions. The inversion procedures based on this approach will be introduced in section 6.2.5.

Shortly after the shut-in (0.2 days for the base case), the wellbore steady state temperature is reached, which indicates the thermal balance between convection due to after-flow and heat transfer to surrounding rock. After the validation of the analytical solution for the base case, we incorporate the variable velocity scenario into Equation 6.6 to illustrate the wellbore fluid temperature profile. The velocity profile is calculated by Equation 6.7 (Spivey and Lee 2013) from pressure transient analysis data simulated by (KAPPA-RUBIS 2015) in a buildup test of MFHW.

$$q_{sf} = \frac{C}{B}\frac{\partial p_s}{\partial t} \tag{6.7}$$

where q_{sf} is the volumetric after-flow rate, C is the wellbore storage coefficient, B is the formation volume factor, and p_s is the bottom-hole shut-in pressure during the test. The results of the velocity profile are presented in Figure 6.12 at two monitoring locations.

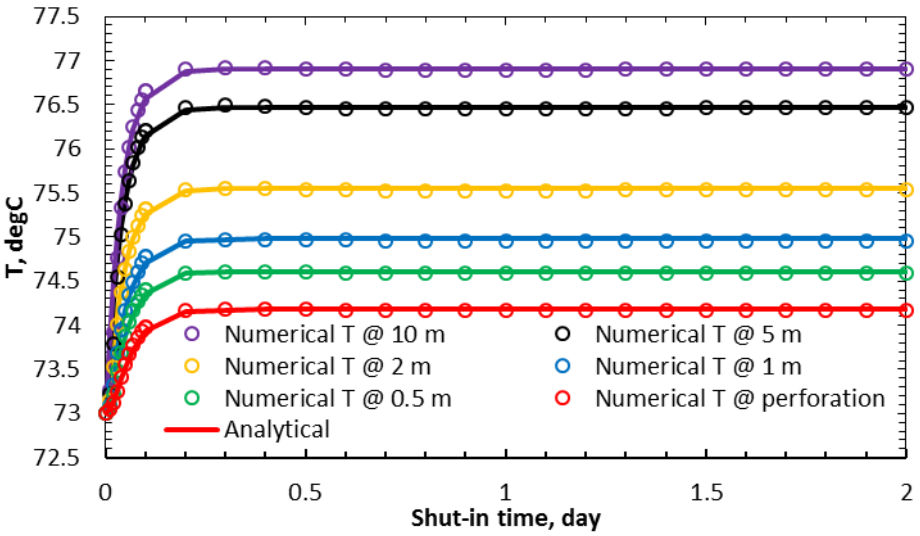

Figure 6. 11. Wellbore temperature profiles obtained analytically and numerically for the base case.

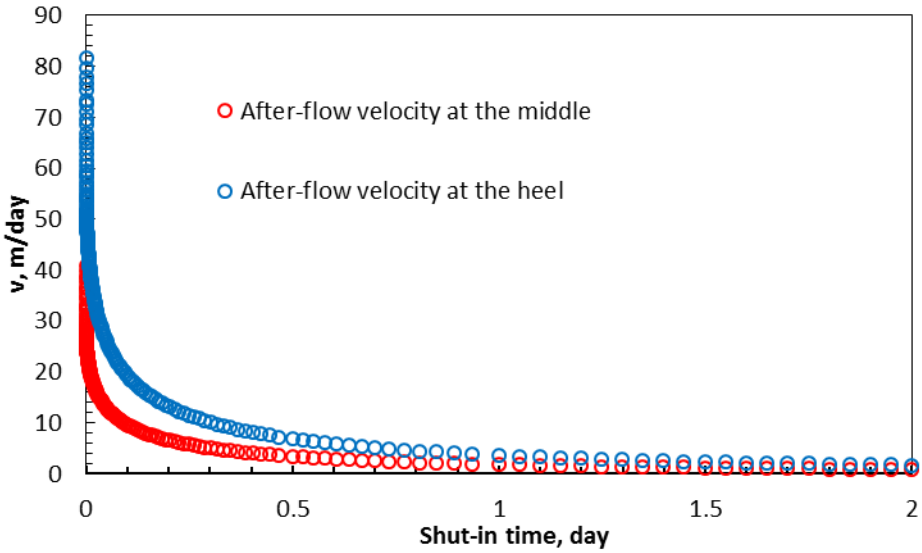

Figure 6. 12. After-flow velocity data used to model wellbore temperature profile.

The wellbore temperature modeling results obtained from the analytical solution and numerical simulation for the variable after-flow velocity case monitored at the toe are illustrated in Figure 6.13. Again, good agreements are achieved between analytical solutions (solid curves) and numerical simulations (dotted curves) for all the cases. Validation of the analytical solution on variable velocity indicates that the convolution effect of velocity variation on temperature modeling can be captured by replacement of constant velocity with variable velocity in the equation derived assuming constant velocity.

Despite similarities between Figures 6.11 and 6.13, the steady-state temperature at a late time is not established for the variable velocity case. As after-flow velocity declines over time, less amount of warm fluid is brought into the fractured region, which results in a continuously dropping temperature profile after initial heating. Mathematically, L_R is changing with variable velocity since vL_R is a constant (Hasan, Kabir, and Lin 2005, Izgec et al. 2009, Nojabaei, Hasan, and Kabir 2014). The variation in L_R affects the value of the last term in Equation 6.6, which determines the temperature after the initial heating. Temperature signals obtained at the perforation indicates that it will eventually reach the surrounding region temperature (inflow temperature at the perforation), which depends on how fast the after-flow velocity declines and how long the shut-in test lasts. We will use these observations to develop inversion procedures to analyze temperature signals associated with variable after-flow velocity.

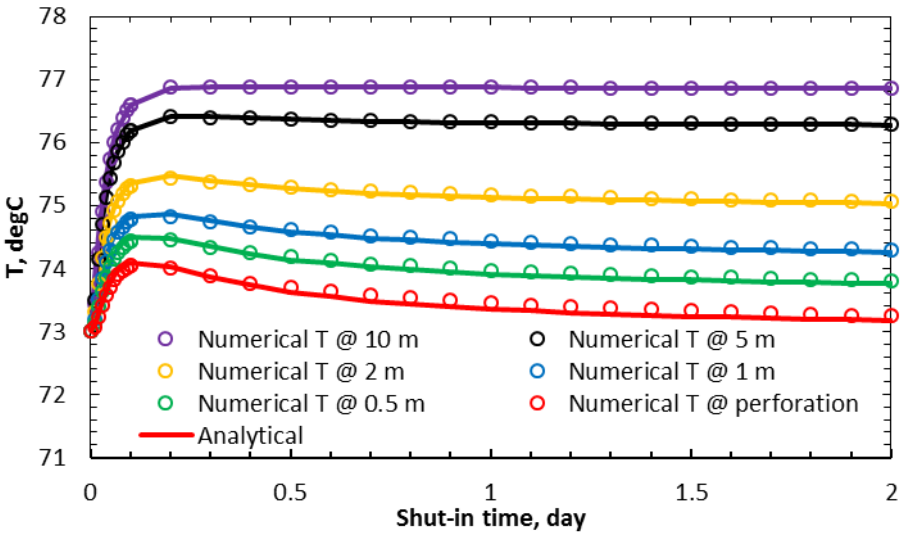

Figure 6. 13. Wellbore temperature profiles obtained analytically and numerically for the variable after-flow velocity case monitored at the heel.

6.2.4 Parametric Analysis

In this section, several parametric analyses are performed to identify the effects of different properties on the temperature profile. We select four properties to perform the analyses on constant velocity cases, the values of which are presented in Table 6.2. These analyses are presented in terms of the spatial steady state wellbore fluid temperature profiles.

Figures 6.14 – 6.17 present the parametric analyses of analytically and numerically modeled temperature profiles by varying after-flow velocity, wellbore radius, boundary condition coefficient (a), and flowing temperature (T_p), respectively. Acceptable agreements are achieved between the analytical solution and numerical simulation in all 12 cases presented in the parametric analyses. For various conditions of production fluid temperature before the shut-in (Figure 6.17), the steady-state wellbore fluid temperature after the shut-in test remains unchanged. As the initial condition, flowing temperature does not affect the steady-state wellbore fluid temperature profile as long as other properties remain the same. The effect of flowing temperature is mainly presented during the initial heating effect.

For properties sensitive to the temperature profile, the effects of after-flow velocity and wellbore radius illustrate similar behavior. Higher velocity and larger wellbore radius result in further heating effect near the fracture during the shut-in period. This is due to more thermal energy brought into the fractured region from the higher after-flow mass rate. Therefore, the

after-flow mass rate is one critical factor for evaluating the heating effect, which mathematically given by the last term of Equation 6.6.

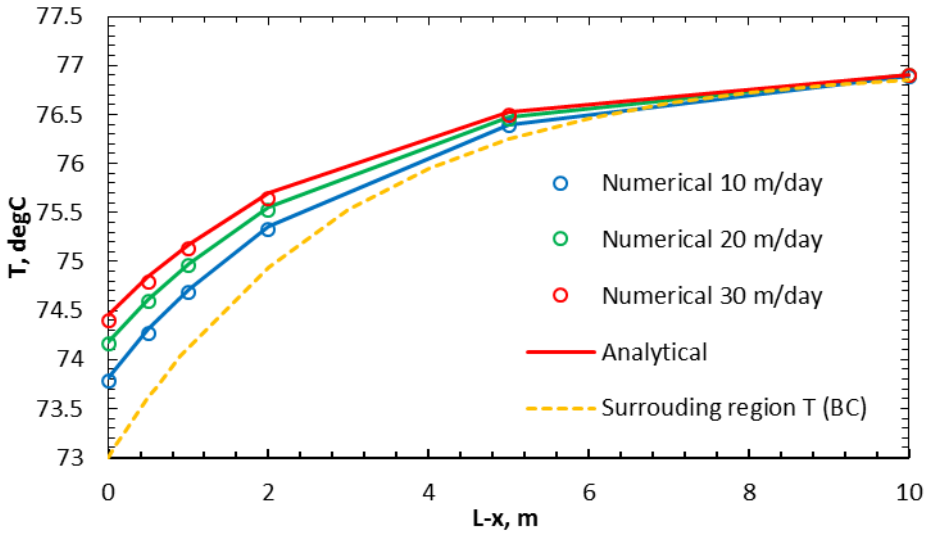

Figure 6. 14. Parametric analysis of steady-state wellbore fluid temperature modeling for various after-flow velocities

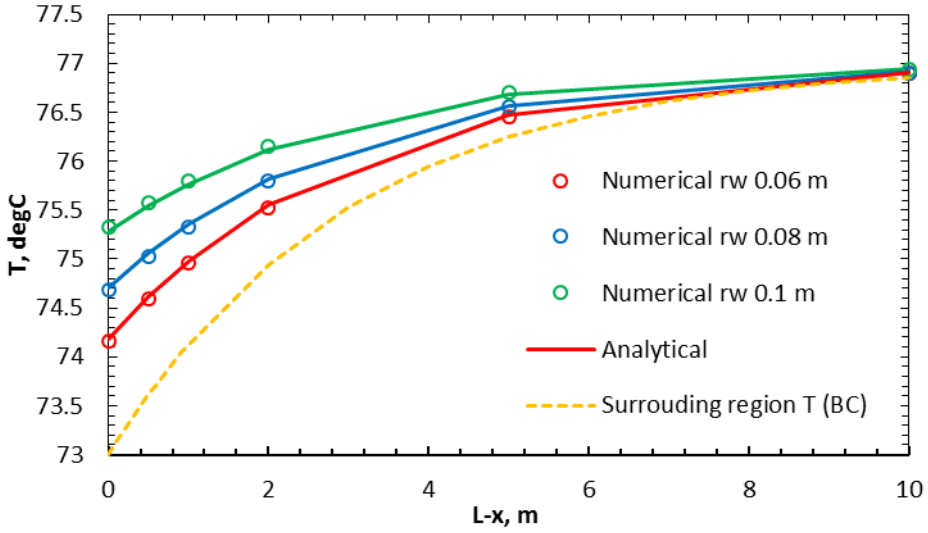

Figure 6. 15. Parametric analysis of steady-state wellbore fluid temperature modeling for various wellbore radii

The last case in this parametric study is associated with the boundary condition coefficient (a). A smaller value of a indicates a smaller fractured region and a stronger heating effect. This observation can be attributed to the variation on the boundary condition. Wellbore fluid temperature raises quicker for a narrower cool area near the perforation subject to the same hotter fluid moving in. The same can be applied to varying other properties that affect the boundary condition (e.g. T_i and T_{inflow}). It should be noted that the last term of Equation 6.6 contains those parameters as well. These effects can be jointly analyzed in section 6.2.5 for the inversion process.

After the parametric analyses on constant velocity cases, we analyze the variable velocity cases. For this analyses, another set of after-flow velocity profile (monitored at the middle in Figure 6.12) is used to model the wellbore fluid temperature profile. Since steady-state wellbore fluid

temperature profile cannot be achieved for variable velocity cases, we present the temperature similar to Figure 6.13 in Figure 6.18. Compared to Figure 6.13, the initial heating effect is smaller and the temperature declines faster in Figure 6.18. Therefore, the temperature profile is sensitive to the magnitude and decline behavior of after-flow velocity.

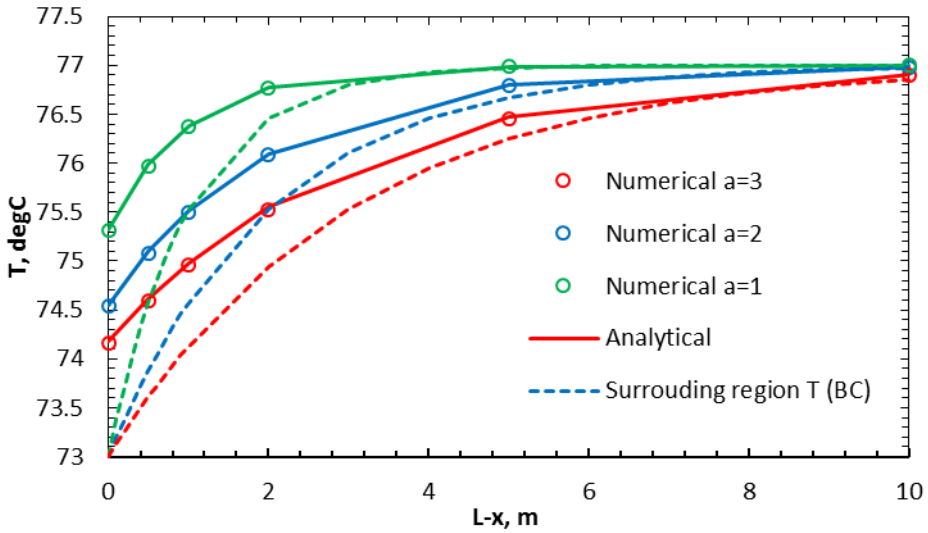

Figure 6. 16. Parametric analysis of steady state wellbore fluid temperature modeling for various boundary condition coefficient

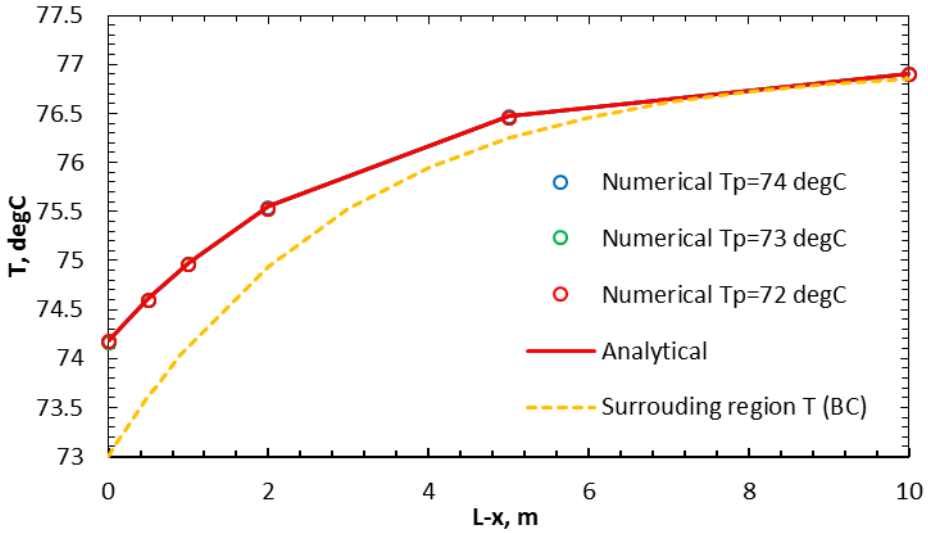

Figure 6. 17. Parametric analysis of steady-state wellbore fluid temperature modeling for various flowing temperature (T_p)

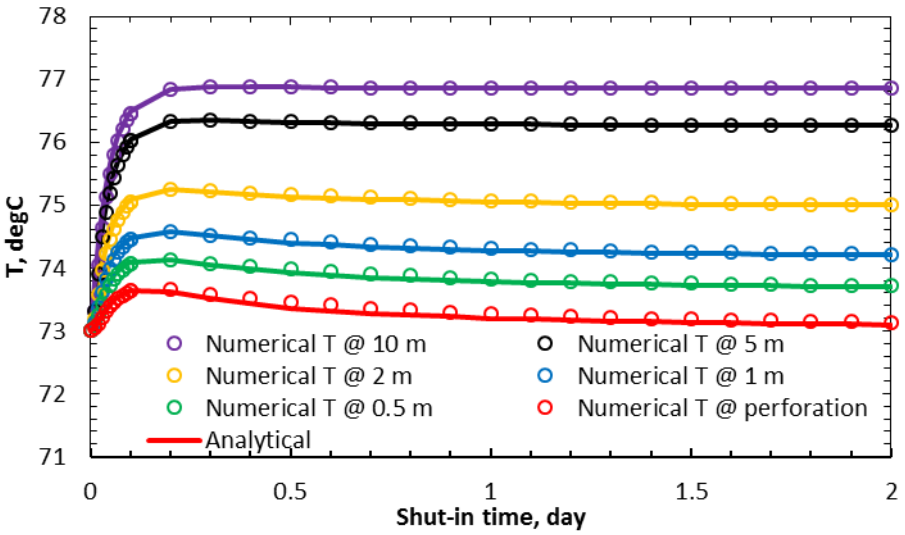

Figure 6. 18. Wellbore temperature profiles obtained analytically and numerically for the variable after-flow velocity case monitored at the middle.

6.2.5 Inversion Procedures

After presenting the forward temperature modeling results, we develop inflow temperature and after-flow velocity characterization procedures from the analytical solutions. In this section, temperature interpretation techniques are provided in terms of a semi-log plot analysis applied to synthetic temperature data obtained from numerical simulation.

Wellbore property and temperature condition required in order to apply this interpretation include C_T (estimation provided by Hasan, Kabir, and Lin (2005), Izgec et al. (2009), Nojabaei, Hasan, and Kabir (2014)) and flowing temperature (T_p) (recorded by temperature monitoring system before shut-in). Even with inadequate data for these properties, grouped properties can be acquired based on the following procedures.

1. Identify the non-fractured region (in Figure 6.11, L-x>10 m) and fractured region (in Figure 6.11, L-x<5 m) temperature profiles.
2. Graph the temperature data from the non-fractured region, T_{nf}, vs. the shut-in time, on a semi-log scale (similar to Figure 6.19a).
3. Identify the initial reservoir temperature (T_i) from the steady state temperature data (indicated by the black line in Figure 6.19a).
4. Perform exponential regression analysis on the initial heating temperature data (indicated by the red line in Figure 6.19a), and estimate the exponential fitting coefficient b_{nf} (25.97 in Figure 6.19a). From Equation 6.6:

$$b_{nf} = \frac{vL_R}{1+C_T} \tag{6.8}$$

As discussed when the analytical solution (Equation 6.6) was presented, the wellbore fluid temperature during a shut-in test is governed by different terms in Equation 6.6 depending on the monitoring locations. Steps 1-4 are based on the fact that in the non-fractured region, one can model the wellbore fluid temperature with only first and second terms on RHS of Equation 6.6. In the fractured region, all the terms are required for modeling. Therefore, the last term in Equation 6.6 represents the temperature difference between non-fractured and fractured regions. Based on this observations, the following inversion procedure is developed:

5. Graph the temperature difference between non-fractured and fractured regions, ΔT=T-T_{nf}, vs. the shut-in time, on a semi-log scale (similar to Figures 6.19b and c).

6. Identify ΔT_j and ΔT_k from the steady state temperature data (indicated by the black lines in Figures 6.19b and c). From Equation 6.6:

$$\Delta T_j = \frac{aL_R\left(T_{\text{inflow}} - T_i\right)}{aL_R + 1}\exp\left(\frac{x-L}{a}\right)_j \tag{6.9}$$

7. Calculate boundary condition coefficient (a) from Equation 6.9:

$$a = \frac{\left(x-L\right)_j - \left(x-L\right)_k}{\ln\left|\Delta T_j\right| - \ln\left|\Delta T_k\right|} \tag{6.10}$$

For multiple temperature measurements in the fractured region, this calculation can be performed multiple times for further accuracy.

8. Perform exponential regression analysis on the early-time temperature data (indicated by the red lines in Figures 6.19b and c), and estimate the exponential fitting coefficient $b_{f,j}$ and $b_{f,k}$ (38.13 in Figure 6.19b and 38.77 in Figure 6.19c). From Equation 6.6:

$$b_f = \frac{vL_R}{1+C_T} + \frac{v}{\left(1+C_T\right)a} = \frac{vL_R}{1+C_T}\left(1+\frac{1}{aL_R}\right) \tag{6.11}$$

9. Calculate aL_R and L_R from Equations 6.8, 6.10, and 6.11:

$$aL_R = \left[\frac{b_f}{b_{nf}} - 1\right]^{-1} \tag{6.12}$$

$$L_R = \frac{aL_R}{a} \tag{6.13}$$

10. Calculate v and T_{inflow} from Equations 6.8, 6.9, 6.12, and 6.13:

$$v = \frac{b_{nf}\left(1+C_T\right)}{L_R} \tag{6.14}$$

$$T_{\text{inflow}} = T_i + \Delta T_j\left(1+\frac{1}{aL_R}\right)\exp\left(\frac{L-x}{a}\right)_j \tag{6.15}$$

The above-mentioned characterization procedures are applied to the synthetic data presented in Figure 6.19. We compare the property estimations from the inversion process with those from the settings to produce the synthetic data in Table 6.3. In general, the characterization results show good accuracies against the true values (less than 15% errors for all the cases). The estimations are exceptional for inflow temperature and boundary condition coefficient estimation of the fractured region (less than 3% errors). With this accurate estimation, one can obtain the inflow temperature profile to conduct PLT analysis for each of the fractures during the flow-back period of MFHW.

Table 6. 3. Property estimations for constant velocity case from Figure 6.19.

Property	Reference	Estimation	Errors (%)
T_i (degC)	77	76.9	0.1
T_{inflow} (degC)	73	72.96	0.1
a (boundary condition coefficient)	3	2.92	2.7
v (m/day)	20	22.4	12

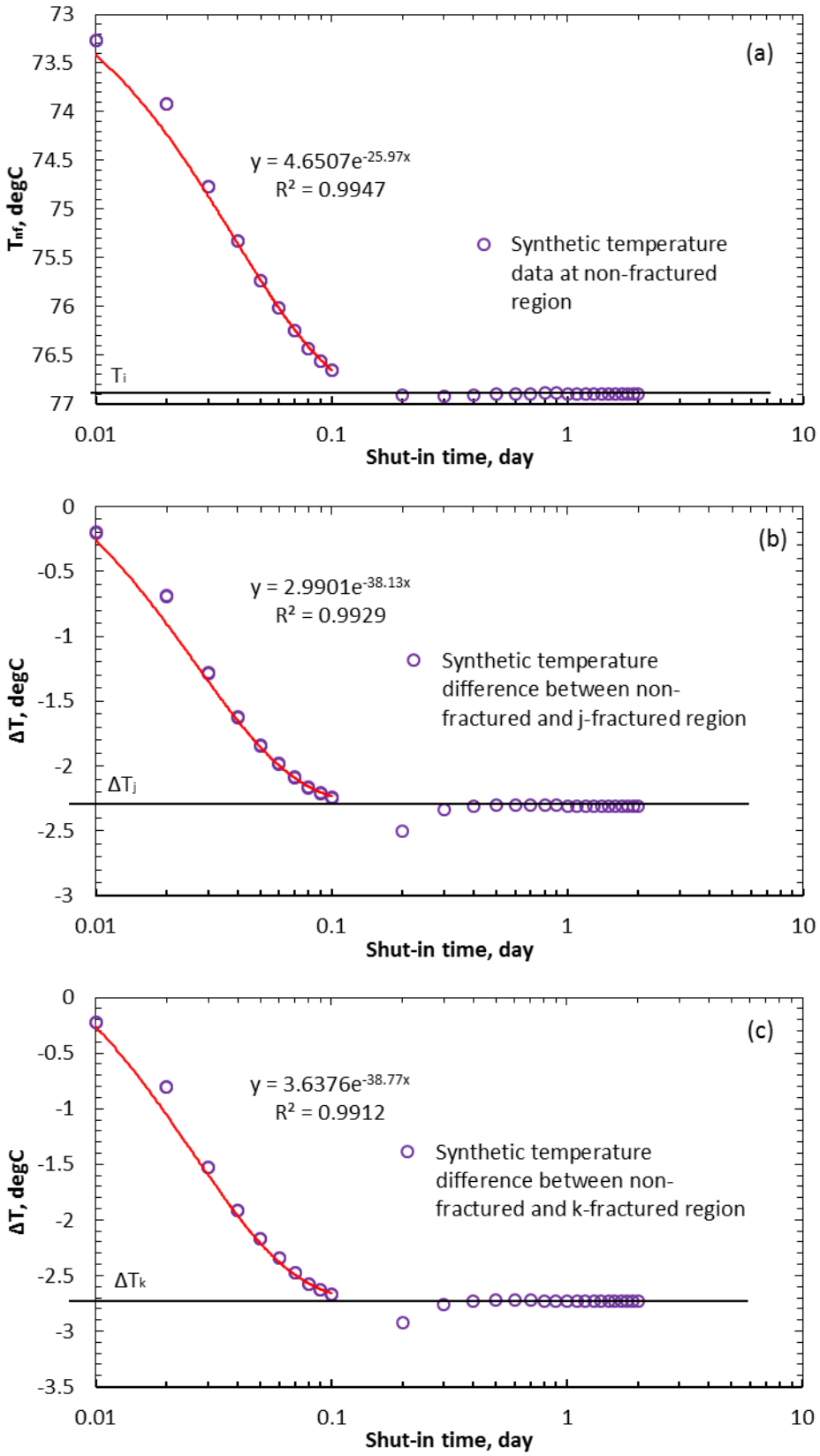

Figure 6. 19. Inversion procedures performed on the synthetic data of the constant velocity base case for (a) non-fractured region, (b) fractured region (L-x=0.5 m), and (c) fractured region (L-x=0 m).

The inversion procedure presented above assumed constant flow velocity which may not be the case for after-flow during well shut-in. Steps 1-5 of the inversion procedure above are valid to estimate b_{nf} and T_i when flow velocity is variable. The steps to estimate boundary condition coefficient (a) can be modified to:

6. From Equation 6.6, ΔT follows Equation 6.16:

$$\Delta T = \frac{aL_R\left(T_{\text{inflow}} - T_i\right)}{aL_R + 1}\exp\left(\frac{x-L}{a}\right)\left[1-\exp\left(-\frac{vL_R t}{1+C_T} - \frac{vt}{\left(1+C_T\right)a}\right)\right] \tag{6.16}$$

   where L_R and v are a function of time for variable after-flow cases.

7. Since we have multiple temperature data in the fractured region, one can calculate the boundary condition coefficient (a) from Equation 6.17:

$$a = \frac{\left(x-L\right)_j - \left(x-L\right)_k}{\ln\left|\frac{\left(\Delta T\right)_j}{\left(\Delta T\right)_k}\right|} \tag{6.17}$$

Table 6.4 illustrates the property estimation results from performing above inversion processes to data in Figure 6.20. The estimations of T_i and a present decent accuracy compared with numerical settings again. Further estimations on variable velocity and inflow temperature can be performed rigorously with curve fitting on multiple temperature data in Figure 6.13. The complexity of variable velocity prevents simple analytical approach to extract this information comparable to the constant velocity case. One may roughly estimate the inflow temperature from the endpoint fluid temperature at the perforation during a long shut-in test, but this estimation highly relies on assuming negligible after-flow velocity at the end of the test.

Table 6. 4. Property estimations for variable velocity case from Figure 6.20.

Property	Reference	Estimation	Errors (%)
T_i (degC)	77	76.87	0.2
a (boundary condition coefficient)	3	3.03	1

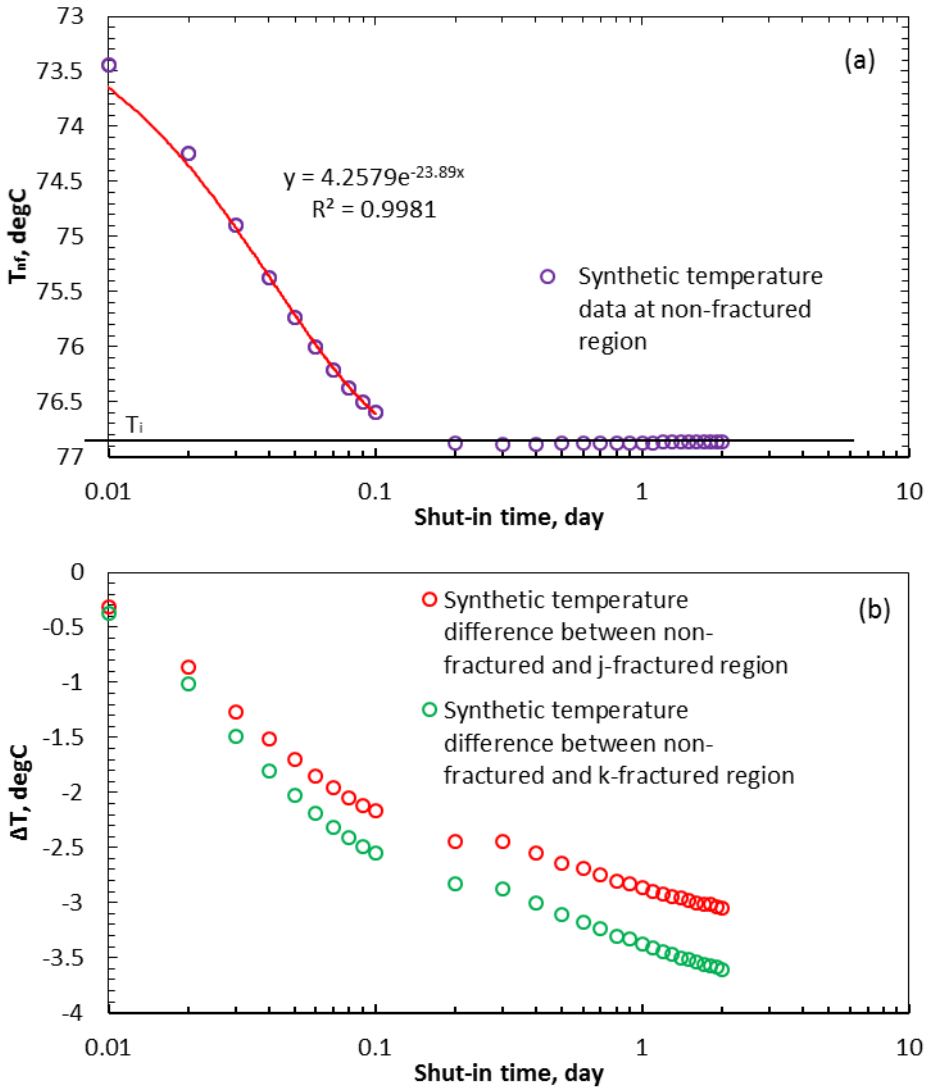

Figure 6. 20. Inversion procedures performed on the synthetic data of the variable velocity case for (a) non-fractured region and (b) fractured region (L-x=0 and 0.5 m).

Chapter 7. Application of Temperature Transient Analysis in CO_2 Storage Leakage Detection and Characterization

Temperature can be used to detect the leakage of fluids from the CO_2 storage zone. These thermal signals arise from expansion of the leaking CO_2 associated with the pressure drop across the leak, known as the Joule-Thomson effect, which has the potential to reveal the nature of leakage and determine the wellbore leakage rate of CO_2. In this chapter, we investigate the strength of the temperature signals for two scenarios in which leakage occurs either through a leaky well or a leaky fault. In addition, we identify and analyze the major mechanisms contributing to the temperature signal. In the end, we investigate the strength of the temperature signal as a function of leakage rate and develop a control volume analysis to relate these two in the complex two-phase leakage conditions. This analytical thermal model for CO_2 leakage enables quick analysis with sufficient accuracy to estimate the leakage rate.

7.1 Effect of Leakage Pathway Flow Properties on Thermal Signal Associated with the Leakage from CO_2 Storage Zone

In this section, we start numerical simulations with single-porosity models to investigate the thermal signal in the AZ. We investigate the thermal responses of leakage for both leaky wells and leaky faults. Moreover, we study the thermal effects by extending a base case problem defined in an earlier work (Zeidouni, Nicot, and Hovorka 2014b) to a range of IZ depths and caprock thickness. Thus, the thermal signal investigations are conducted with various initial pressure and temperature conditions for the IZ and AZ. Furthermore, we analyze the effect of capillary pressure on the temperature signals from the leakage with the shallowest depth of the IZ and AZ. After the single-porosity models, we investigate the effect of treating the leakage pathways as fractured media using dual-porosity/dual-permeability modeling approach. Finally, by sequentially considering IZ and AZ as naturally fractured reservoirs, we study their corresponding thermal signals.

7.1.1 Single-Porosity Models

In this section, we analyze the effects of depth and capillary pressure on the strength and trend of the thermal signal by sequentially considering non-fractured media. For the base case, whose properties are adopted from Zeidouni, Nicot, and Hovorka (2014b), we consider CO_2 injection at a bottom-hole pressure of 13 MPa (equivalent to 195 kton/year (270,000 m^3/day)) into a 55-m thick brine aquifer for two years. We carefully control the bottom-hole pressure to ensure the integrity of the caprock by limiting the maximum pressure in the IZ to be less than 90% of the fracture pressure for IZ, which is calculated from Heller and Taber (1986). A 20-m thick impermeable cap-rock separates the IZ from a 10-m thick AZ. Both IZ and AZ have identical flow properties (Table 7.1). The depth at the top of IZ is 1000 m. The IZ and AZ are connected by either (a) a leaky well, or (b) a leaky fault. The leaky well and leaky fault properties are presented in Table 1. The schematics of these models are illustrated in Figure 7.1.

We consider the same relative permeability curves (Table 7.2) for all the fluid flow media of the system. The equation of state for fluid components in the simulation are Peng-Robinson models, where brine and CO_2 are the only two fluid components in the system. The injected CO_2 temperature is 41.7°*C*, identical to the initial reservoir temperature, and the geothermal gradient is 0.03°*C*/*m*. The rock density and heat capacity are 2,650 kg/m^3 and 1,000 *J*/(*kg*.*K*), respectively. The total thermal conductivity is 2.51 *W*/(*m*.*K*). We perform the simulations in CMG-GEM (2015) thermal model using Cartesian gridding. In the vertical

direction, the total grid number is 24, which includes 5 for the AZ, 10 for the caprock, and 9 for the IZ. In the two horizontal directions, the total grid number is 91 for each direction, and the grid sizes decrease towards the injection well accordingly. Because of the symmetry of the injection well, only a quadrant of the system with the injection well at the corner of the model is simulated to reduce the computational cost. Therefore, the injection rate and drainage area are one-fourth of the values listed above.

Table 7. 1. Description of the base case problem.

Porosity (fraction)	0.3	Leaky pathway lateral permeability (m^2)	10^{-13}
Lateral permeability (m^2)	10^{-13}	Leaky pathway vertical permeability (m^2)	10^{-14}
Vertical permeability (m^2)	10^{-14}	Leaky pathway porosity (fraction)	0.3
Reservoir radial extent (km)	24	Leak-injector distance (m)	100
Brine salinity (wt%)	15	Leaky-well radius (m)	0.3
Rock compressibility (1/MPa)	5e-4	Leaky fault width (m)	1
		Initial pressure at 1000-m depth (MPa)	8.03

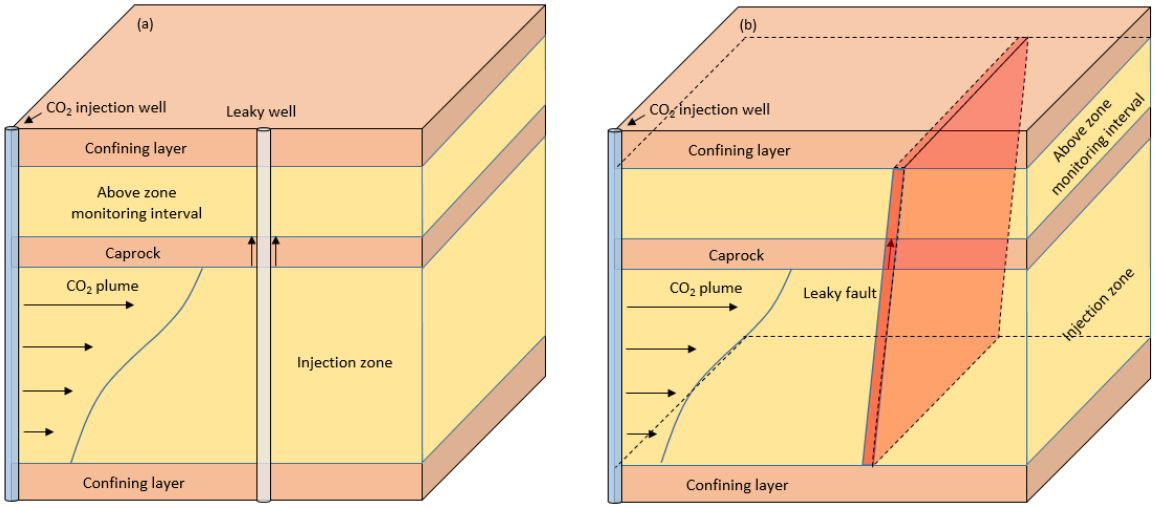

Figure 7. 1. Model descriptions for (a) leaky well and (b) leaky fault base cases. (The proposed temperature measurements are along the leaky well in the AZ and along a horizontal well intercept with a leaky fault in the AZ.)

Table 7. 2. Relative-permeability of CO_2-rich phase (Corey 1954).

$k_{rg} = \left(1-\hat{S}\right)^n \left(1-\hat{S}^2\right)$	where:	$\hat{S} = \dfrac{S_a - S_{wirr}}{1 - S_{wirr} - S_{gc}}$, n=2, Sgc=0.05

Before presenting the results to the variation of depth and caprock thickness, we present the theoretical background to understand the thermal signature of leakage from a CO_2 storage site.

7.1.1.1 Physical insight of the leakage thermal signal

To gain a physical insight into the leakage thermal signal, we start with the governing equation for the temperature variation in porous media (Equation 1.13). The physical meanings of each term in Equation 1.13 are informative, which are represented by the equilibrium between the heat transfer process and the baro-thermal effects. In the LHS of Equation 1.13, the heat transfer process are divided into three terms: heat capacity, convective and conductive heat transfer terms from left to right. The terms on the RHS of Equation 1.13 involving pressure derivatives represent two effects: the adiabatic expansion and the JT effects. The adiabatic expansion effect is related to the pressure derivative with respect to time and the thermal expansion coefficient, which represents the temperature changes associated with the rate of fluid expansion or compression in a given location. The JT effect is associated with the temperature variation caused by the pressure gradient, where the JT coefficient is evaluated at constant enthalpy conditions.

Among the four heat transfer effects mentioned above, the effects of the adiabatic expansion may be negligible for this study. The adiabatic expansion effect is significant only if there are quick and/or abrupt changes in the pressure. The temperature changes caused by adiabatic expansion effect is illustrated at the end of this section.

Simple calculations can be used to represent the JT effect and adiabatic expansion across the leak, which is adapted from Ramazanov et al. (2010):

$$T\left(x_1,t\right)-T\left(x_1,t_0\right)=\mu_{JT}\left[p\left(x_1,t\right)-p\left(x_2,t\right)\right]+T\left(x_2,t\right)-T\left(x_2,t_0\right) \tag{7.1}$$

$$T\left(x,t_1\right)-T\left(x,t_0\right)=\eta_a\phi\left[p\left(x,t_1\right)-p\left(x,t_2\right)\right]+T\left(x,t_2\right)-T\left(x,t_0\right) \tag{7.2}$$

Equation 7.1 indicates that the temperature difference across the leak is the product of the JT coefficient, and the pressure difference across the leak, where x_1 and x_2 respectively denote the lowermost layer of AZ and the topmost layer of IZ at the location of the leak, and t_0 is the initial time. Equation 7.2 presents that the temperature variation in AZ is the product of the adiabatic expansion coefficient, porosity, and pressure variation in AZ. We use Equations 7.1 and 7.2 to calculate the temperature changes in the lowermost layer of AZ at the location of the leak due to the JT and adiabatic expansion effects (Figures 7.1 and 7.2). The coefficients of the JT and adiabatic expansion are computed by applying the averaging method to the CO_2-brine mixture (Ramazanov and Parshin 2006, Alves, Alhanati, and Shoham 1992). The value of CO_2-brine mixture JT coefficient in various IZ conditions depends on the value of the CO_2 JT coefficient, while the brine JT coefficient slightly varies with pressure and temperature status. The values of the CO_2 JT coefficient under various pressure and temperature circumstances are presented in Figure 7.2. In order to fairly represent the temperature signals associated with the leaks, the IZ conditions (34-40 degC, 8-13 MPa) result in a moderate JT coefficient value for CO_2 (1-8 K/MPa).

Figure 7.3 shows the temperature changes in the lowermost layer of AZ at the location of the leak for both leaky fault and leaky well. The temperature variations in the lowermost layer of AZ at the leaks can be described by identifying three periods based on the time for a CO_2 breakthrough at the leak. Before the CO_2 breakthrough, the leaking fluid is brine. For this period, the temperatures slightly increase for the leaky well and leaky fault. Upon the CO_2 breakthrough, the temperature changes drop significantly, which shows cooling across the leakage pathway for both leaky well and leaky fault. After injection for 10 months, the temperature variations reach a plateau for the leaky well. However, for the leaky fault, the temperature starts to elevate in AZ to approaching the initial temperature.

Similarly, the leakage thermal signal due to the JT effect can be divided into three periods: the brine leakage, the CO_2 breakthrough, and after the CO_2 breakthrough. The temperature slightly increases during the brine leakage because the water phase has a small

negative value of the JT coefficient. With the increasing magnitude of the pressure difference across the leak, the temperature slightly rises. During the CO_2 breakthrough, the CO_2 flux through the leaks suddenly escalates which alters the value of the JT coefficient to a positive value. In the meantime, the magnitude of the pressure difference across the leaks reaches the maximum. Therefore, the temperature drops significantly right after the CO_2 breakthrough. The behaviors of the thermal signals for a leaky well and leaky fault after the CO_2 breakthrough are mainly due to the variation in the pressure differences across the leaks. For a leaky well, the pressure differences remain relatively constant. With a higher value of the JT coefficient for CO_2 brine mixture due to the increasing CO_2 flux through the leaks, the temperature variations after the CO_2 breakthrough slightly decrease (Figure 7.3a). For a leaky fault, the pressure difference reduces quickly, which brings the temperature change back to a higher level (Figure 7.3b).

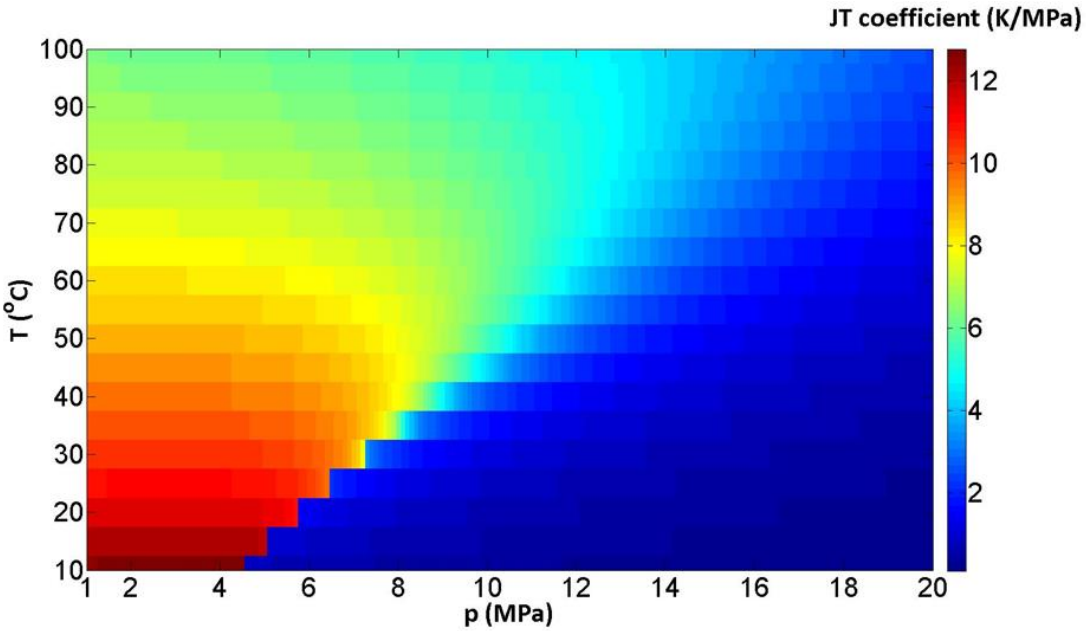

Figure 7. 2. JT coefficient for CO_2 under various pressure and temperature conditions.

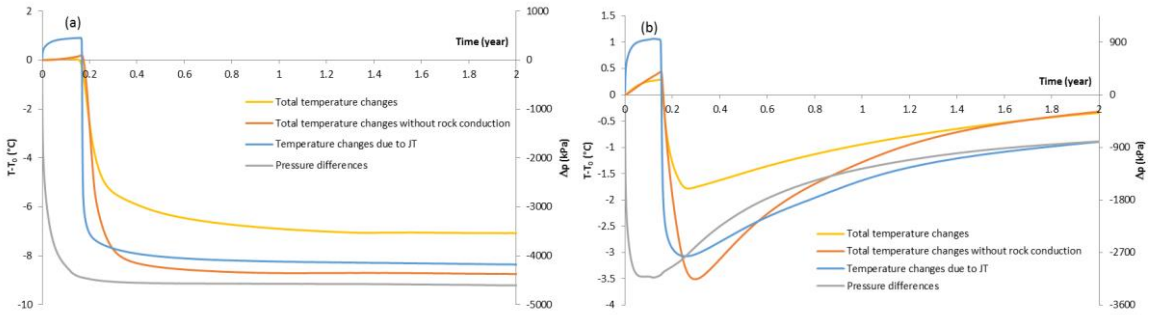

Figure 7. 3. Temperature changes in the lowermost layer of AZ at the location of a leak of 1000-m-IZ for (a) leaky well and (b) leaky fault base cases.

The magnitudes of pressure differences across the leaks reach the maximum at the CO_2 breakthrough, which are ~4600 kPa for the leaky well and ~3100 kPa for the leaky fault. The pressure difference across the leaky well is higher because of the lower pressure increase in AZ (Figure 7.4a) due to the limited leakage flux. After CO_2 breakthrough, the magnitude of the pressure difference between IZ and AZ decreases by a small amount. The behavior of pressure difference across the leak is mainly controlled by the compressibility and mobility of

the leaking fluid. The high CO_2 compressibility and mobility cause higher pressure variations in AZ. At the same time, the pressure in IZ also increases but at a lower rate. Therefore, a lower pressure differential across the leak is observed after the CO_2 breakthrough.

After analyzing the JT effects in Figure 7.3 separately, we will connect the JT effect to the temperature changes in AZ. The trends of the total temperature changes for both cases are analogous to those of the temperature changes due to the JT effect. The total temperature changes for both cases tend to minimize the temperature variations caused by the JT effect from the initial monitoring temperature, which is most obvious during the CO_2 breakthrough. In the condition of neglecting the heat conduction in the rock, the differences between the total temperature changes in AZ and those due to the JT effect become smaller. For the leaky well (Figure 7.1a), the temperature changes in AZ closely follow those from the JT effect. For the leaky fault (Figure 7.1b), the agreement can be observed upon the CO_2 breakthrough. These results demonstrate that among the four heat transfer mechanisms (heat conduction, heat convection, JT effect and adiabatic expansion effect), the JT effect and heat conduction are the dominant mechanisms.

Figure 7.4 shows the temperature changes due to the adiabatic expansion in AZ for both leaky fault and leaky well. The temperature changes due to the adiabatic expansion in the leaky well case are small compared to those due to the JT effect because of relatively negligible pressure change in AZ. These small temperature changes can be explained based on the pressure derivative with respect to time for a single-phase flow in a porous medium as it is inversely proportional to time and vanishes for a long time. In the leaky fault case, the temperature changes are relatively higher due to the significant pressure build-up in AZ. The temperature variations caused by the adiabatic expansion effect increase with gas/water ratio at the leaks to reach 0.5 degC after injection for 2 years. This effect can be the main cause for the temperature changes neglecting the heat conduction deviating from the JT effect in Figure 7.3b, while the adiabatic expansion increases the temperature gradually after the CO_2 breakthrough. This effect is in the same order of magnitude but less significant compared to the temperature drop caused by the JT effect. Therefore, the temperature changes due to the adiabatic expansion are negligible in the leaky well case, but may not be negligible in the leaky fault case.

Based on the above observations, the temperature signals associated with CO_2 leakage can be used as a complementary measurement with the pressure signals, or as an indicator of CO_2 leakage when pressure measurements are not available. The thermal signals can distinguish the phase changes across the leak because of the varying JT coefficient. The CO_2 leakage is clearly represented by sudden drops on the temperature profiles (presented by Figure 7.3). On the other hand, the pressure variations in AZ increase with injection time (presented by Figure 7.4). The CO_2 leakage is indicated by the variations in the increasing speed of the pressure signal, which is hard to be identified, especially for the leaky fault.

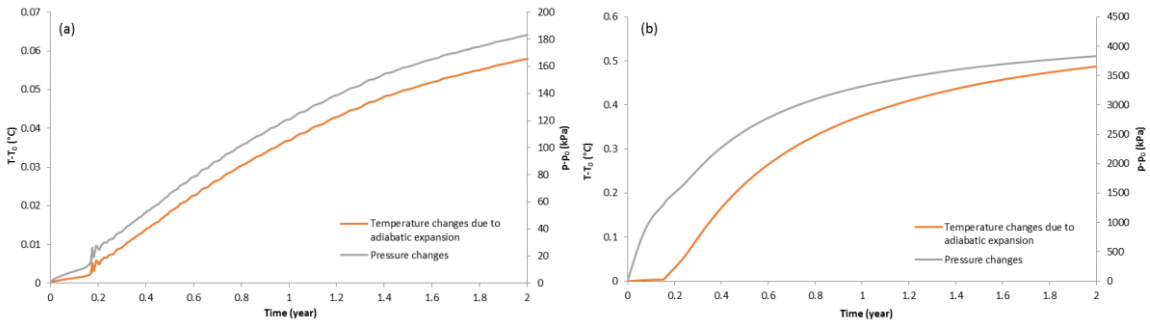

Figure 7. 4. Temperature changes due to adiabatic expansion in the AZ of a leak of 1000-m-IZ for (a) leaky well and (b) leaky fault base cases.

7.1.1.2 Effect of depth and caprock thickness on the leakage thermal signal

We investigate the three IZ-Seal-AZ systems with various depths and caprock thickness, and demonstrate their temperature signals in AZ. The depths at the top of IZ (seal base) for the three systems are 1000 m, 1500 m, and 2000 m. The initial temperature of IZ for each system is varied based on the same temperature gradient of 0.03°C/m. As a result, the temperatures at the bases of 1500-m-IZ and 2000-m-IZ are 56.7°C and 71.7°C respectively. Also, the injection temperature is considered to be the same as the base of IZ. All other properties of the system and the injection temperature are kept constant. The 2-year injection history for different depth is set to be the same with the base cases since the bottom-hole pressure constraints are not equivalent for different depth.

At larger depths, both temperature and pressure are higher. The CO_2 density decreases as a function of temperature increment, and it increases as a function of pressure augmentation. The net effect highly depends on the temperature gradient (Ennis-King and Paterson 2001, Bachu 2003). For the conditions used in this study, the density increases with depth. The higher density means that the injected CO_2 takes less volume upon injection, and consequently, the breakthrough time for CO_2 at the leak will increase with the depth. The CO_2 viscosity also increases with density (Fenghour, Wakeham, and Vesovic 1998). Therefore, it takes longer to sense the cooling (caused by the JT effect upon the CO_2 leakage) when the depth increases. Figure 7.5 illustrates that the breakthrough time varies from 0.17, 0.18, to 0.2 years for 1000-, 1500-, and 2000-m-IZ for the leaky well case. The breakthrough times for the leaky fault case are slightly shorter due to a higher leakage rate through the fault (compared to the well case) which reduces the resistance to flow.

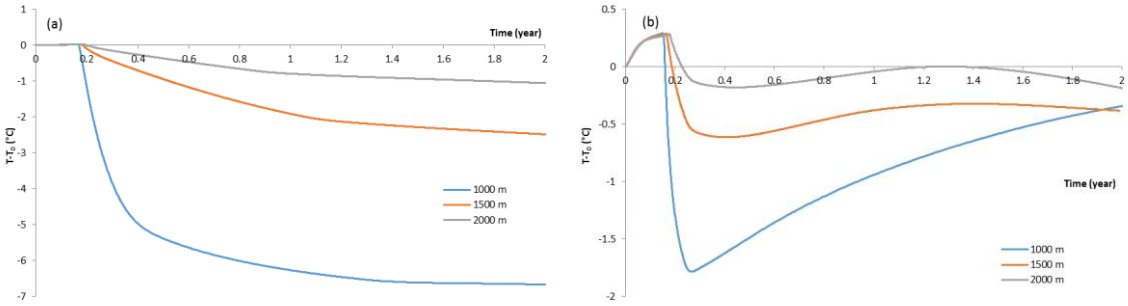

Figure 7. 5. Temperature changes in the lowermost layer of AZ at the location of the leak for (a) leaky well and (b) leaky fault varied depth cases.

For both cases, the temperature signals after CO_2 breakthrough will be driven by the JT effect. The larger pressure gradient at shallower depths implies larger temperature signal. On the other hand, the JT coefficient at the CO_2 breakthrough varies from 1.46, 0.73, to 0.43 K/MPa for 1000-, 1500-, and 2000-m-IZ leaky well cases. The net effect is that the strength of the cooling signal in AZ for leaky well after 2 years reduces from 6.6°C in the 1000-m case to 2.5 and 1°C in the 1500- and 2000-m-IZ cases, respectively. The temperature signals for leaky fault are similar to those for leaky well, but with smaller magnitude. This implies more difficulties when detecting the leaky faults with IZ depths more than 2000 m. To investigate the sensitivity of temperature signals on various caprock thickness, the caprock thickness at the 1000-m-IZ for the three systems are 20 m, 50 m, and 100 m. At larger caprock thickness, the leakage pathway is longer and consequently, the breakthrough time for CO_2 at the leak will increase with the caprock thickness. Figure 7.6 illustrates that the breakthrough time varies from 0.17, 0.32, to 0.76 years for 20, 50, and 100 m caprock thickness for the leaky well case. On the other hand, longer leakage pathway results in longer cooling effect associated with the CO_2 breakthrough

when the caprock increases, which is most significant for the leaky well cases. The magnitude of temperature cooling effect for both leaky well (plateau after CO_2 breakthrough) and fault (upon CO_2 breakthrough) cases are almost identical under various caprock thickness. This is due to the equivalent pressure drop between IZ and AZ, and the JT coefficient at the CO_2 breakthrough at different caprock thickness. In short, the effect of caprock thickness on temperature signals is most significant on the CO_2 breakthrough time, as well as the speed of the cooling effect.

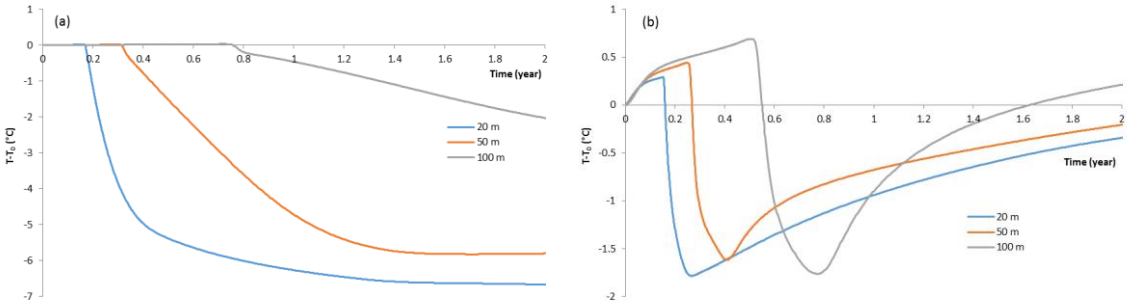

Figure 7. 6. Temperature changes in the lowermost layer of AZ at the location of the leak for (a) leaky well and (b) leaky fault varied depth cases.

7.1.1.3 Effect of the capillary pressure on the leakage thermal signal

If the leak permeability is less than 10 md, the pressure analysis may not be useful to detect the leaks (Gasda et al. 2013), whilst the temperature signal can still be useful. The capillary pressure can affect the temperature signal associated with CO_2 leakage no matter what the leak type is. However, it is most significant in less permeable leaks. The capillary pressure in the leakage pathways can delay the CO_2 leakage breakthrough because the CO_2 cannot leak unless the capillary entry pressure is overcome. On the other hand, the capillary pressure in the leaks will impact the pressure profile, water/gas flux through the leaks, as well as the temperature variations. In this section, we incorporate the effect of the capillary pressure in the leaks and investigate the changes in the leakage thermal signals. The input function for the capillary pressure to the numerical simulation is listed in Table 7.3.

Table 7. 3. Simulated function for capillary pressure (Van Genuchten 1980).

$P_c = -P_0\left(\left[S^*\right]^{-1/m} - 1\right)^{1-m}$	where:	$S^* = \frac{S_a - S_{wirr}}{1 - S_{wirr}}$, P_0=20 kPa, m=0.457

By considering the capillary pressure in the lowermost layer of AZ at the location of the leaky well for 1000-m-IZ, we obtain the changes of the temperature and gas flux (Figure 7.7a). The CO_2 arrival time at the leak remains the same because the capillary pressure in the leaks will not affect the CO_2 front in IZ. However, the arrived CO_2 barely leaks through the well because of the existence of capillary entry pressure. In the presence of the capillary pressure, the CO_2 breakthrough time is postponed to 1.3 years after injection, and the temperature starts to decrease after the CO_2 breakthrough. This results in delayed and weaker temperature signals in AZ. We also obtain the temperature variations and gas flux at the leak for the leaky fault (Figure 7.7b). In presence of the capillary pressure, the CO_2 arrival time remains the same with higher breakthrough CO_2 flux for the fault. The effect of the capillary pressure after the CO_2 breakthrough is to restrict the CO_2 flux at the leak, and as a result, restrain the pressure build-up in AZ. This phenomenon is clearly visible in Figure 7.7b. After 0.7 years, the effect of the capillary entry pressure is overcome, and the CO_2 flux at the leak

increases to a maximum. Therefore, we observed two cooling stages associated with CO_2 arrival and the end of resistance from capillary entry pressure. As a result, the temperature in the AZ decreases less significantly but increases more slowly compared to the case neglecting the capillary pressure, mainly due to the reduced CO_2 flux and pressure differences across the leak after the CO_2 breakthrough with the presence of capillary pressure. It is harder to detect the temperature signal in the leaky fault case with the presence of capillary pressure since the temperature variation at the CO_2 breakthrough is lower due to less gas flux through the leaks.

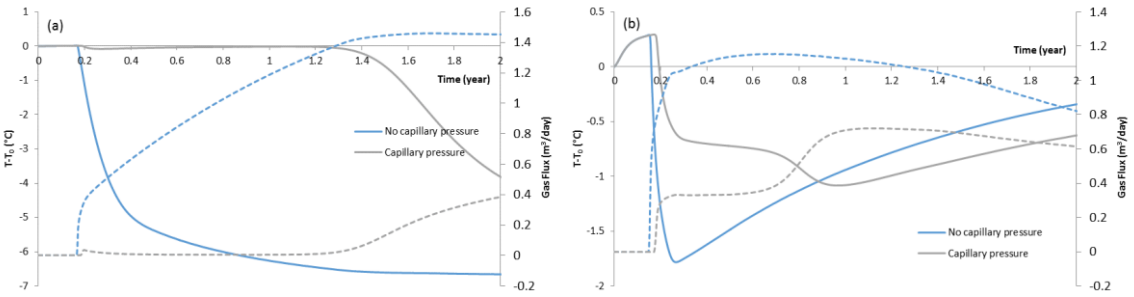

Figure 7. 7. Temperature variations (solid) and gas flux (dashed) considering the capillary pressure in the lowermost layer of AZ at the location of the leak for (a) leaky well and (b) leaky fault cases.

7.1.2 Dual-Porosity/Dual-Permeability Models

The leakage pathway is likely to have different pore structure system compared to the IZ and AZ media. The porosity of the leakage pathway can be secondary porosity initiated from different processes such as fracturing and/or dissolution whereas that of IZ and AZ might be intergranular primary porosity (especially for clastic reservoirs). In this section, we investigate the effect of such a difference on the thermal signal.

We consider the leakage pathway as a fractured medium and simulate the flow within using the dual-porosity/dual-permeability models. Based on the dual-porosity/dual-permeability models, a fracture cell is assigned for every matrix grid block within the leak. Therefore, to make these cases comparable to the single-porosity problem, the porosity and permeability of the dual-porosity system should be equal to that of the single-porosity problem (30%, 100 md lateral and 10 md vertical respectively). The permeability of the dual-porosity/dual-permeability model can be calculated by:

$$k = \frac{k_m (S - w) + k_f w}{S} \tag{7.3}$$

where w is the fracture width in micrometer, and S is the fracture spacing in micrometer. A realistic fracture dimension is chosen from the Madison Formation (Choi, Cheema, and Islam 1997), where the fracture width is 1 mm, and average fracture spacing is 7 cm. To emphasize the effect of the fracture system, we assume a small permeability (1 md vertical and 10 md lateral) for the matrix system. As a result, the permeability of the fracture system calculated from equation 4 is 860 md vertically and 8.6 D laterally. The porosity of the fractures can be calculated by:

$$\phi = \frac{w}{S} \tag{7.4}$$

As a result, the porosity of the fracture is 1.43%, and the porosity of the matrix is 8.57% for the dual-porosity/dual-permeability models. It is worthwhile to note that the underground fractures are unlikely to be fully open. The permeability of the fracture is a function of the fracture dimensions, as well as the rock structures in the fractures.

In this section, we investigate the physical insight of the leakage thermal signal with dual-porosity structure. Next, we incorporate the effects of the leakage pathway flow properties: fracture permeability, fracture spacing, and porosity. However, we found that the temperature signals are almost insensitive to fracture spacing and porosity. Therefore, these results are not presented here. Finally, we investigate the temperature signals from the leaks in the naturally fractured reservoirs.

7.1.2.1 Physical insight of the leakage thermal signal for fractured leakage pathway

Figure 7.8 shows the temperature changes in the lowermost layer of AZ at the dual-porosity leaks for the both leaky fault and leaky well. The same three time regions and trends in Figure 7.3 can be observed in Figure 7.8. Meanwhile, the JT effect and heat conduction are still the dominant heat transfer mechanisms in AZ. The pressure rises at the leaks for the dual-porosity models remain identical to those for the single-porosity model, which indicates the equivalent permeability for the two models.

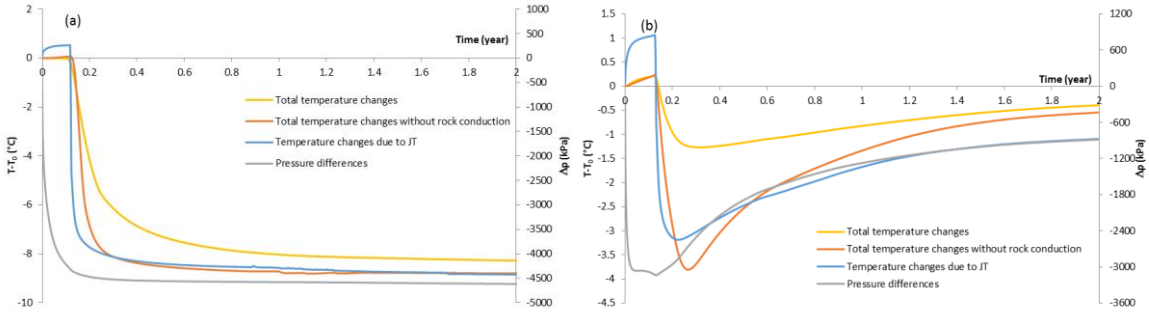

Figure 7. 8. Temperature changes in the lowermost layer of AZ at the dual-porosity leak of 1000-m-IZ for (a) leaky well and (b) leaky fault cases.

Figure 7.9a shows the temperature variations at the base of AZ for the leaky well. We observe higher temperature changes after the CO_2 breakthrough, which can be explained by a larger JT effect stemming from a higher CO_2 flux across the leaks. The CO_2 breakthrough occurs earlier due to reduced resistance to additional flow through the fractures. The temperature signals obtained from dual-porosity/dual-permeability models are similar, which indicate that the fluid flows between matrix blocks are minimal.

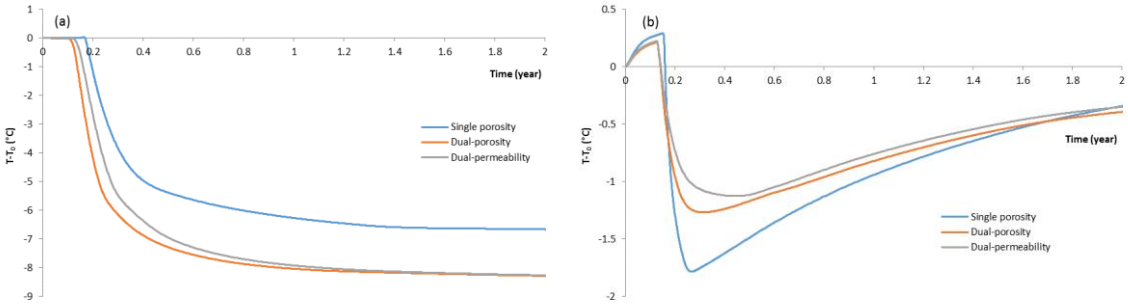

Figure 7. 9. Temperature changes in the lowermost layer of AZ at the location of the leak for (a) leaky well and (b) leaky fault cases.

We obtain the results before and after the CO_2 breakthrough for the leaky fault (Figure 7.9b). The temperature change after the CO_2 breakthrough is less significant for the dual-porosity/dual-permeability models compared to the single-porosity case due to more significant heat conduction at the CO_2 breakthrough. The temperature increases one month later due to the

reduced pressure change (initiated from the increased leakage rate). Similar to those for the leaky well case, the difference between temperature variations from the dual-porosity model and those from the dual-permeability model are small.

7.1.2.2 Effect of leakage pathway flow properties: fracture permeability

The permeability of the fracture system can be either high in open fractures, or low in fractures filled with fine grains. The variation of the fracture permeability poses a huge impact on the pressure profile, as well as the temperature changes. We have selected three cases with different fracture permeabilities to demonstrate its impact on the temperature signals, while the values of fracture permeability are within the range of commonly occurred leakage in CO_2 storage project (Gasda et al. 2013). Figure 7.10a presents temperature variations under different fracture permeability in the lowermost layer of AZ at the location of the leaky well for 1000-m-IZ. The CO_2 breakthrough occurs earlier under higher fracture permeability, which allows the CO_2 front to propagate faster through the fractures. Under lower fracture permeability, the temperature changes at the CO_2 breakthrough are less and last longer due to a smaller JT effect caused by less magnitude and gradually increasing CO_2 flux. For the cases with fracture permeability less than 10 md, the temperature signals in AZ do not reach the plateau after two years of injection. These results indicate that the temperature signals are large enough to be detected for the leaky well.

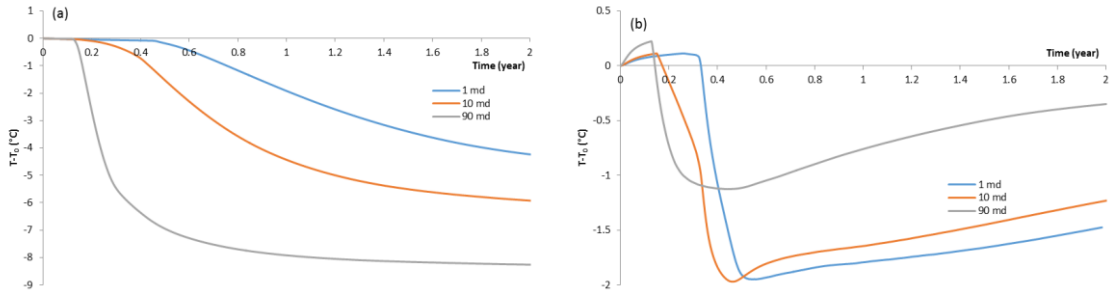

Figure 7. 10. Temperature changes of various fracture permeability in the lowermost layer of AZ at the location of the leak for 1000-m-IZ of (a) leaky well case and (b) leaky fault case.

We also obtain the temperature changes for the leaky fault (Figure 7.10b). The CO_2 breakthrough time is similar to what is presented in Figure 7.10a. However, the temperature profiles are mainly controlled by the pressure rises across the leaks. Under low fracture permeability, the AZ pressure increases slowly, which maintains the pressure rises across the leaks to a higher level, and increases the temperature signals in AZ at the CO_2 breakthrough. In the three cases presented in Figure 7.10b, the temperature signals in AZ are strong enough to be detected by the downhole temperature monitoring system.

7.1.2.3 Effect of naturally fractured injection zone and above zone

Naturally fractured reservoirs increase the CO_2 storage capacity, as well as CO_2 injectivity. The presence of the natural fractures in IZ and AZ significantly impacts the temperature signals in AZ. Figure 7.11a exhibits the temperature variations in the lowermost layer of AZ at the location of the leaky well for 1000-m-IZ when the natural fractures are considered for IZ and AZ. The CO_2 breakthrough occurs much earlier if the IZ is naturally fractured. Therefore, the fracture system in the IZ improves the fluid flow capacity in the IZ tremendously, which also shortens the time to reach the maximum temperature change after the CO_2 breakthrough. With the natural fractures in the AZ, the temperature changes after the

CO_2 breakthrough decrease compared to the case without the natural fractures in AZ. This observation indicates that the presence of the fracture system in AZ reduces the pressure drops across the leaky well after the CO_2 breakthrough, therefore reduces the temperature cooling effect.

We procure the temperature changes for the leaky fault (Figure 7.11b). The CO_2 breakthrough occurs similarly to what is presented in Fig. 11a. However, the temperature change is smaller with the existence of the fracture system in IZ and AZ. The higher amount of fluid flow in the leaky fault cases are intensified by the existence of the fracture system in the IZ and AZ. The aggravations on the fluid flow behavior result in the reduced pressure drop across the leaky fault. It is worthwhile to note that the temperature profile with the fracture system in IZ and AZ for 0.2 years is similar to that without the fracture system in IZ and AZ for 2 years. This demonstrates how the systems in IZ and AZ improve the fluid flow behavior.

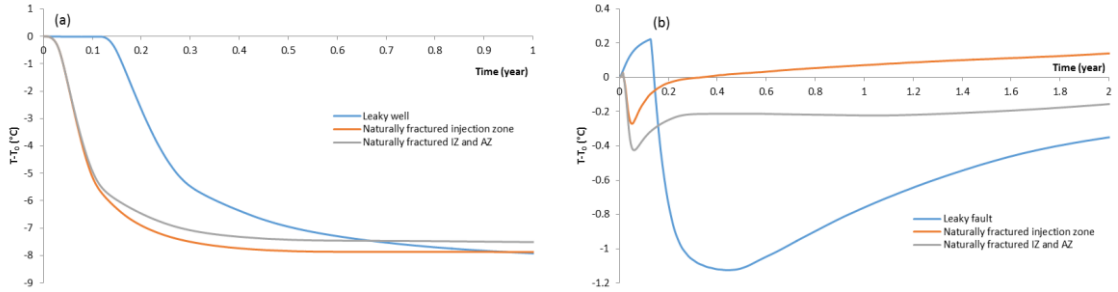

Figure 7. 11. Temperature variations in the lowermost layer of AZ at the location of the leak for 1000-m-IZ of (a) leaky well case and (b) leaky fault case considering the presences of the natural fractures in IZ and AZ.

7.2 Temperature Analysis for Early Detection and Rate Estimation of CO_2 Wellbore Leakage

In this section, we start with the development of the leakage thermal model to estimate the leakage rate from thermal signals. The steady-state results of leakage rate estimation obtained from the leakage thermal model are compared and validated with the synthetic data from the IZ-leak-AZ model constructed in section 7.1. Thus, the accuracies of integrated and discretized leakage thermal model are determined and predicted by a thermal effect ratio and the corresponding dimensionless number. Moreover, we extend the estimation to the preceding transient period by considering the major thermal contribution from the leaking CO_2. Despite the results of leakage rate estimation, we explore additional applications of the leakage thermal model to include predicting leakage transmissibility from rate estimation. Finally, a procedure to perform the leakage rate and transmissibility estimations is presented followed by further discussions on several remaining issues of the approach.

7.2.1 Model Description

In this section, we derive an analytical solution for wellbore leakage rate estimation through thermal control volume analysis. A physical model description is first introduced for the target leaky well, for which the mathematical formulation is developed to derive an analytical solution.

7.2.1.1 Physical model description

The physical problem to be modeled in this study is a cemented leaky well penetrating IZ and AZ separated by an impermeable caprock layer with a thickness of *H* (Figure 7.12 a,b). The well was initially perforated in the IZ which was cement-plugged upon abandonment to ensure integrity. Wellbore leakage can occur through: (1) the cement behind the casing and (2) cement plug inside the casing. The well is equipped with DTS or FBG behind casing imager to capture temperature signals in all directions as well as temperature logging or PDG measurements inside the casing. Therefore, temperature anomalies due to the CO_2 leakage inside or outside the casing can be captured.

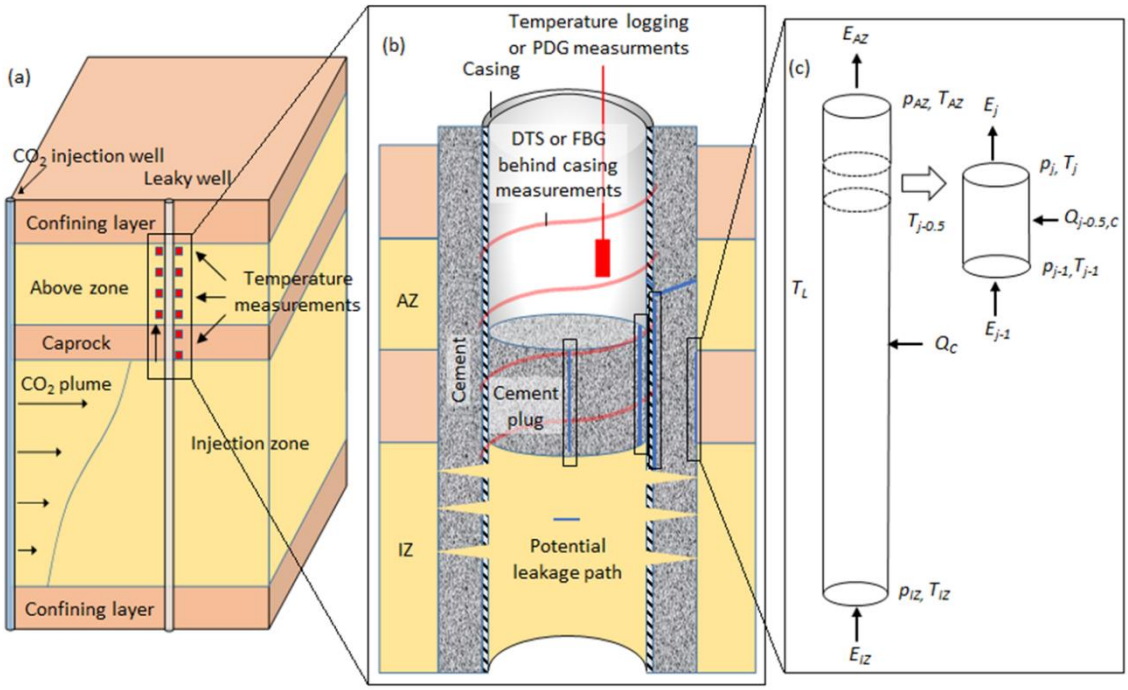

Figure 7. 12. A physical model description of the leaky well (b) and the mathematical control volume analysis on the wellbore leaks (c). This model is part of the IZ-leak-AZ model (a) developed in section 7.1, which provides synthetic data for this study.

This physical model of the leaky well is part of a leakage simulation model (IZ-leak-AZ) developed in section 7.1, which is illustrated in Figure 7.12 a. This IZ-leak-AZ model provides the leakage thermal signal and rate to serve as model input and validation, which will be presented in section 7.2.2.

7.2.1.2 Control volume analysis (leakage thermal model)

For each wellbore leak in the physical model, a control volume analysis (leakage thermal model illustrated in Figure 7.12 c) can be constructed to investigate the fluid flow and heat transfer behavior in the leak. The leakage thermal model presents the energy balance to derive an analytical solution to estimate the leakage rate from the measured temperature signal. In this model, Q_c is the conduction heat transfer into the system, E is the total energy in the system, p is the pressure, and T is the temperature. The leak is indexed by L. To perform accurate control volume analysis, the integrated model is discretized. In the case of a long leakage path, the leak can be discretized into multiple control volumes (cells). For *j*-cell, *j-1* indicates the adjacent upstream cell, and *j-0.5* indicates the arithmetic mean value of these two cells.

For the integrated control volume, energy balance is achieved between the total energy accumulation in the control volume and conductive heat transfer to the control volume, which forms an energy balance given by:

$$E_{AZMI} - E_{IZ} = Q_C \tag{7.5}$$

The conductive heat transfer to the control volume has been investigated by Kutasov (2003). The resulting equation for the control volume wall temperature under constant heat flow rate can be replaced by the leakage temperature in this study:

$$\dot{Q}_c = \frac{2\pi HK\left(T_{i,L} - T_L\right)}{\ln\left[1 + \left(c - \frac{1}{a + \sqrt{t_D}}\right)\sqrt{t_D}\right]} \tag{7.6}$$

where ρ_r, c_r, and K are the density, specific heat, and thermal conductivity of the caprock, respectively. $T_{i,L}$ is the initial temperature of the caprock, $t_D = Kt / \rho_r c_r r_L^2$ is the dimensionless starting time of conduction, a and c are constants with values of 2.7010505 and 1.4986055, respectively.

The total energy is the sum of kinetic, potential, and internal energy. The kinetic energy remains relatively constant in AZ and IZ due to almost identical fluid velocities. Thus, the total energy reduces to the sum of potential and internal energies:

$$\left(E_p + E_i\right)_{AZ} - \left(E_p + E_i\right)_{IZ} = Q_C \tag{7.7}$$

or:

$$m\left(\hat{H} + gz\right)_{AZ} - m\left(\hat{H} + gz\right)_{IZ} = Q_C \tag{7.8}$$

where m is the mass of leaking fluid, $\hat{H}$ is the enthalpy of the system, z is the vertical distance from leakage origin (IZ). To investigate the leakage rate, the derivative of Equation 7.8 with respect to time is required for which the enthalpy derivative is given by:

$$d\hat{H} = \left(\frac{\partial \hat{H}}{\partial p}\right)_T dp + \left(\frac{\partial \hat{H}}{\partial T}\right)_p dT = -\mu_{JT} c dp + c dT \tag{7.9}$$

Combining Equations 7.6, 7.8, and 7.9 gives:

$$\begin{aligned} &\dot{m}c\left(T_{AZ} - T_{IZ}\right) - mc\mu_{JT}\frac{d\left(p_{AZ} - p_{IZ}\right)}{dt} + mc\frac{d\left(T_{AZ} - T_{IZ}\right)}{dt} + \dot{m}gH \\ &= \dot{m}c\mu_{JT}\left(p_{AZ} - p_{IZ}\right) + \frac{2\pi HK\left(T_{i,L} - T_L\right)}{\ln\left[1 + \left(c - \frac{1}{a + \sqrt{t_D}}\right)\sqrt{t_D}\right]} \end{aligned} \tag{7.10}$$

where c is the specific heat and μ_{JT} is the JT coefficient of the leaking fluid. The condition of CO_2 phase change, which is possible to occur through the leak, is considered in Equation 7.10. The over-dot indicates the derivative with respect to time. Based on our previous investigations in section 7.1, the temperature changes associated with pressure derivative with respect to time (the second term on the LFS of Equation 7.10) is negligible. Also, after sufficiently long time, leakage becomes dominated by CO_2, resulting in relatively constant temperature signals in both IZ and AZ. These observations make the third term in Equation 7.10 negligible, which produces:

$$\dot{m}cT_{AZ} - \dot{m}cT_{IZ} + \dot{m}gH = \dot{m}c\mu_{JT}\left(p_{AZ} - p_{IZ}\right) + \frac{2\pi HK\left(T_{i,L} - T_L\right)}{\ln\left[1 + \left(c - \frac{1}{a + \sqrt{t_D}}\right)\sqrt{t_D}\right]} \tag{7.11}$$

Further simplification of Equation 7.11 gives:

$$\dot{m} = \frac{2\pi HK\left(T_{i,L} - T_L\right)}{\left[c\mu_{JT}\left(p_{IZ} - p_{AZ}\right) + c\left(T_{AZ} - T_{IZ}\right) + gH\right]\ln\left[1 + \left(c - \frac{1}{a + \sqrt{t_D}}\right)\sqrt{t_D}\right]} \tag{7.12}$$

Similar energy balance can be derived for each control volume over a long leakage pathway. As a result, the leakage rates for *j*-indexed control volume can be estimated by:

$$\dot{m}_j = \frac{2\pi h_j K_{j-0.5}\left(T_{i,j-0.5} - T_{j-0.5}\right)}{\left[c_j\mu_{JT,j-0.5}\left(p_{j-1} - p_j\right) + c_j\left(T_j - T_{j-1}\right) + gh_j\right]\ln\left[1 + \left(c - \frac{1}{a + \sqrt{t_{D,j}}}\right)\sqrt{t_{D,j}}\right]} \tag{7.13}$$

where *h* is the height of this control volume.

Assumptions made in developing the above leakage thermal model include negligible temperature changes associated with mass/chemical interactions between leaking fluids and rock matrix, negligible heat conduction in the vertical direction, and considering leakage in the vertical direction only. The effect of heat conduction in the direction of fluid flow has been extensively investigated in LaForce, Ennis-King, and Paterson (2014), which presents minimum effect. Similar assumptions were made in Zeng, Zhao, and Zhu (2012) as well. Considering the possible leakage laterally (in addition to the vertical direction) is a more complex problem and beyond the scope of this research. However, if the estimated leakage rate decreases in the upper cell through the discretized model, the results indicate the possibility of radial leakage through the caprock.

In the following, the method presented in this section is applied to example problems to investigate its application and limitation.

7.2.2 Results

Using the analytical leakage thermal model presented in section 7.2.1, the leakage rate can be estimated and validated with the synthetic results from IZ-leak-AZ model. First, we introduce an example problem of the IZ-leak-AZ model and the associated leakage temperature signal. Second, the leakage thermal model is applied to estimate the late-time leakage rates for steady-state analysis. We validate the estimations and develop criteria to properly apply the leakage thermal model to other cases. Third, the leakage rate estimation from the leakage thermal model is extended to the transient period to explore a further application of the developed analytical solution. Finally, another output of this model, leakage transmissibility, is presented for a high leakage rate scenarios. To summarize the results from leakage thermal model, a procedure to estimate leakage rate and transmissibility is presented for implementing this approach in the field.

7.2.2.1 Synthetic temperature profiles and leakage rates from IZ-leak-AZ model

It is important to understand the complex nature of the thermal signals associated with wellbore leaks. We present the synthetic temperature signals to serve this purpose and as a validation data set, which are generated from the IZ-leak-AZ model. The model details are provided in section 7.1.1. The major mechanisms driving the leakage thermal signals are revealed to be JT effect and conductive heat transfer with surrounding formations.

The leakage temperature profiles are strongly influenced by the leakage rates, as well as properties of the wellbore leak and the leaking fluid. Based on the leakage thermal model constructed in section 7.2.1 (Equations 7.12 and 7.13), the leakage rate depends on temperature

and pressure profiles along the leak, specific heats and JT coefficients of the leaking fluids, the thermal conductivity of the rock, and the conduction time span. Except for the latter two properties, these variables are functions of the leakage temperature and pressure. On the other hand, the leakage rate is not constant after CO_2 injection. Understanding the relationship between the leakage rates, the temperature and pressure signals are essential to estimate the leakage rate, which is the main theme of this section.

Figure 7.13 presents the synthetic temperature variation and leakage rate in the lowermost layer of AZ at the location of the wellbore leak. Two temperature profiles are illustrated in this figure: one signal profile of the combined JT effect and heat conduction, and the other mainly due to the JT effect. The temperature profiles and associated leakage rates can be classified into three periods: brine leakage, mixed leakage, and CO_2 leakage. The CO_2 starts flowing through the wellbore leak and induces temperature cooling signals due to JT effect right after CO_2 breakthrough. CO_2 leakage rates reach a plateau at the end of mixed leakage period while the magnitude of temperature cooling correspondingly extends to the maximum, indicating the leaking fluid is single-phase CO_2. The temperature changes due to JT effect remain relatively constant shortly after mixed leakage, suggesting the pressure drop across the leak barely changes, which have been extensively discussed in section 7.1. Given the temperature signals and leakage rate behavior, estimation of leakage rate from the leakage thermal signal should be conducted during mixed leakage and CO_2 leakage periods. The properties of the leaking fluid, specific heat, and JT coefficient can be limited to CO_2 properties due to the single-phase CO_2 leakage during CO_2 leakage period. Therefore, we start with estimating the CO_2 leakage rate during CO_2 leakage period.

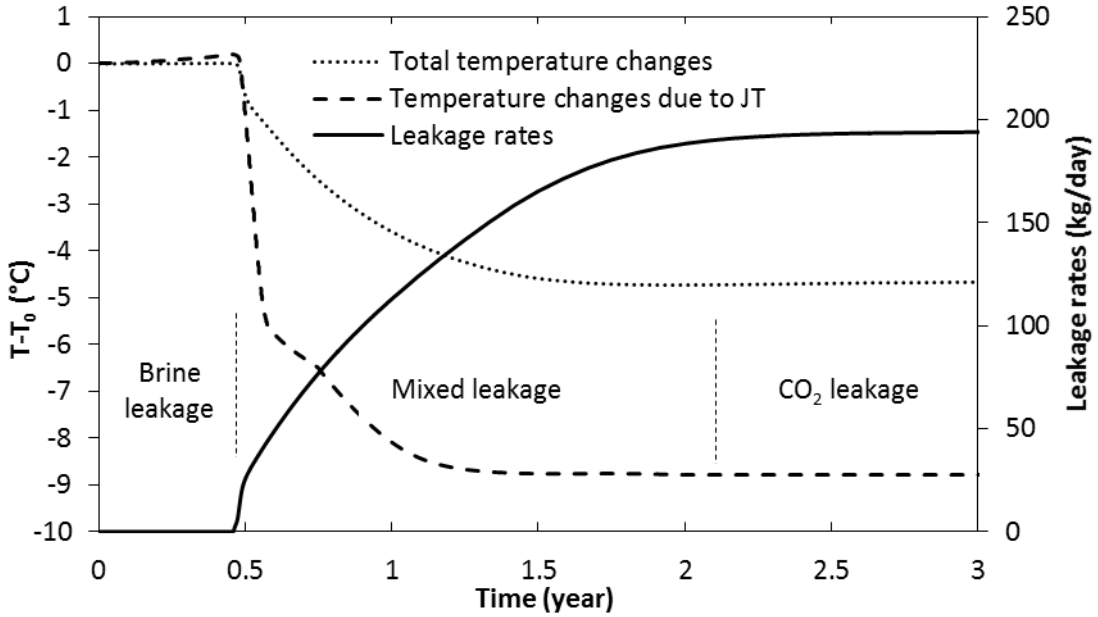

Figure 7. 13. Synthetic temperature variations and leakage rates in the lowermost layer of AZ at the location of the wellbore leak with leakage permeability of 1 md.

In the following, the effect of varying leakage rates on temperature signal is addressed. This effect is investigated by varying the leakage permeability, which is the main parameter affecting the leakage rate (Lu et al. 2012). Six cases with different leakage permeabilities from 0.1 md to 5 md are investigated, which demonstrate the impact of various leakage rates on the temperature signals. Figure 7.14 illustrates the temperature variations under different leakage rates in the lowermost layer of AZ at the location of the leaky well. The temperature profiles for various leakage rates eventually reach a plateau, the magnitude of which ranges from 0 to

7 degC below the geothermal AZ temperature. Smaller magnitude of plateau temperature changes indicates the effect of conduction is dominant over the JT effect, and vice versa. In extreme cases, one effect prevails if the magnitude of plateau temperature change is too small or too large. The temperature signals associated with these six leakage permeabilities are studied in section 7.2.2.2 since neither the conduction nor the JT effect is negligible in these conditions. Before reaching a plateau, the temperature decreases during the mixed leakage period with CO_2 and brine two-phase flow. CO_2 leakage rate estimation for this period will be presented in section 7.2.2.3.

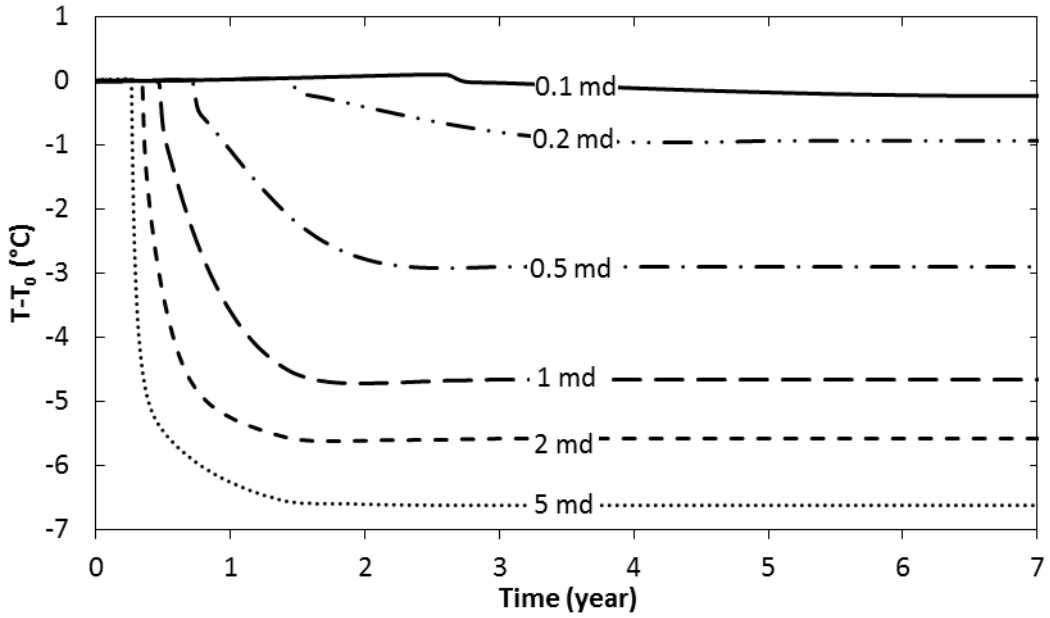

Figure 7. 14. Synthetic temperature changes and in the lowermost layer of AZ at the location of the wellbore leak for various leakage rates (leakage permeability).

7.2.2.2 Leakage rates estimation during CO_2 leakage period

The leakage rate estimation from the leakage thermal model introduced in section 7.2.1 starts with the simple case of steady-state analysis during CO_2 leakage period and extends to a transient analysis during mixed leakage period presented in section 7.2.2.3. We validate the developed leakage thermal model in various wellbore leakage scenarios by comparing with the synthetic results generated by IZ-leak-AZ model. These scenarios are carefully selected to ensure that the wellbore leaks modeled in the research are realistic. Table 7.4 presents a comparison between this study and existing research/data on several wellbore leakage properties. This comparison illustrates that the wellbore leakage property presented in this study comply with most of references/data. Therefore, we will proceed with these settings throughout this section.

To estimate the leakage rates from the leakage thermal model introduced in section 7.2.1, all the variables in Equations 12 and 13 need to be acquired. From section 7.2.2.1, the leakage temperature signals are simulated by the IZ-leak-AZ model for six different leakage permeabilities and should be measured by the downhole temperature monitoring system in the leaky well for practical purposes. The pressure drop across the wellbore leak remains relatively constant, which can be estimated from the injection pressure and the initial AZ pressure, or measured if the pressure monitoring system is available at the leaky well. We evaluate the specific heat and JT coefficient of the leaking fluid by CO_2 properties obtained from Linstrom and Mallard (2008). The thermal conductivity of the caprock can be estimated by the

geothermal gradient (Askari, Taheri, and Hejazi 2015). The conduction time intervals in Equations 12 and 13 include the beginning of mixed leakage until the current measurement time step, which is the heat conduction propagation period from the wellbore leak. The time span of leakage can be easily identified from the duration of the cooling temperature signals.

Table 7. 4. Wellbore leakage property comparison.

Leakage properties	References	Values	This study
Permeability (md)	Cameron, Durlofsky, and Benson (2016)	0.005 - 100	0.1 - 5
	Gasda et al. (2013)	1 - 1000	
	Sun et al. (2016)	1	
	Tao and Bryant (2014)	0.01 - 10	
Transmissibility ($md \times m^2$)	Ebigbo, Class, and Helmig (2007)	71	0.04 - 25
	Nordbotten et al. (2005)	62	
	Zeidouni and Vilarrasa (2016)	3142	
	Zeng, Zhao, and Zhu (2012)	0.3 - 1571	
Rates (kg/day)	Cameron, Durlofsky, and Benson (2016)	7400 - 189000	8 - 2593
	Ebigbo, Class, and Helmig (2007)	960 - 1600	
	Nordbotten et al. (2005)	1600 - 16000	
	Shakiba and Hosseini (2016)	17500 - 25620	
	Sun et al. (2016)	1728 - 86400	
	Tao and Bryant (2014)	3×10^{-7} – 0.3	
	Zeng, Zhao, and Zhu (2012)	1.2 - 5500	
Temperature signals (degC)	Ebigbo, Class, and Helmig (2007)	1.5	0.1 - 7
	Zeng, Zhao, and Zhu (2012)	0.1 - 15	

Table 7.5 presents the leakage rate estimation from Equations 12 and 13 for various permeabilities and compared with synthetic results from IZ-leak-AZ model. The estimated leakage rates from both models increase with increasing wellbore leak permeability. The accuracies of the estimated leakage rates vary for different permeabilities and different numbers of control volumes analyzed. The lower (0.1 md) and higher (5 md) end permeability cases for wellbore leak produce the most unreliable leakage rate estimation. The inaccuracies for these cases arise from the dominance of heat conduction over JT effect, or the opposite. In low permeable wellbore leak, the leakage rates are very small, leaving minor temperature drop at the leak allowing heat conduction to dominate. On the contrary, if the leakage rates are

enhanced by the more permeable leak, the conductive heat transfer only slightly affects the measured temperature signals, resulting significant inaccuracy in estimating the leakage rate.

Table 7. 5. Estimation of leakage rates from integrated (Equation 12) and discretized (Equation 13) leakage thermal models in comparison to synthetic leakage rates from IZ-leak-AZ model.

Leakage permeability (md)	Synthetic leakage rates (kg/day)	Integrated leakage rate estimation (kg/day)	Integrated leakage rate estimation error (%)	Discretized leakage rate estimation (kg/day)	Discretized leakage rate estimation error (%)
0.1	8.356	12.193	45.9	9.078	23.6
0.2	35.734	18.686	47.7	32.72	11
0.5	96.204	78.13	18.8	89.512	9.3
1	198.984	92.082	53.7	211.65	4.3
2	432.145	143.244	66.9	496.785	13.3
5	946.654	436.41	53.9	1154.858	20.8

For the 20-m wellbore leaks presented in this IZ-leak-AZ model, discretized leakage thermal model (Equation 13) is more accurate on the leakage rate estimation compared to the integral model (Equation 12). The improvements on the accuracy are most obvious for the high and low permeability leaks. Therefore, it is essential to apply multiple control volume analysis for the cases potentially producing inaccurate results. Figure 7.15 presents the comparison between the leakage rate estimations from the leakage thermal model developed in this study and the empirical equation presented by Zeng, Zhao, and Zhu (2012) given by:

$$\log \dot{m} = 1.1784 \log\left(\left|\Delta T_{\max}\right|\right) + 1.8074 \tag{7.14}$$

For all six cases of leakage rate estimation, the results obtained from this study show denoting improvement over those from Zeng, Zhao, and Zhu (2012). This improvement is more significant when the discretized model is used, which is also shown by the results in Table 7.5.

The accuracies of the estimated leakage rates are not only affected by the fluid properties of the leaking fluid, but also by the cell location of the discretized model. Figure 7.16 illustrates the leakage rate estimation from each cell in multiple control volume analysis for leakage permeability of 0.5 md the comparison with IZ-leak-AZ model results. The estimated leakage rates vary from 60 to 110 kg/day for the discretized control volume analysis while the synthetic results vary from 91 to 98 kg/day. The leakage rates at the inlet and outlet of the leak are underestimated while those at the middle of the leak are overestimated. Significant temperature variations at the inlet and outlet of the leak induce drastic changes in leaking fluid properties (specific heat, JT coefficient, etc.), which result in inaccurate leakage rate estimation. To improve the quality of the leakage thermal model, the number of discretization should be increased in these locations.

In the cases presented in Table 7.5, applying leakage thermal model to estimate leakage rate results in good accuracy (less than 15 %) under low to moderately permeable wellbore leak (0.1 to 2 md), the corresponding leakage rates of which range from 10 - 400 kg/day. Based on the energy balance in developing the leakage thermal model, the balance between the JT effect and conductive heat transfer is the main determinant of the accuracy of the leakage rate

estimation. An evaluation of this balance is introduced below in terms of a dimensionless number to identify the application limit of the leakage thermal model.

The magnitudes of JT effect and heat conduction are evaluated from Equation 7.12, the ratio of which is:

$$ratio = \frac{2\pi HK_r\left(T_L - T_{i,L}\right)}{\dot{m}c\mu_{JT}\left(p_{AZ} - p_{IZ}\right)} \frac{1}{\ln\left[1+\left(c-\frac{1}{a+\sqrt{t_D}}\right)\sqrt{t_D}\right]} \tag{7.15}$$

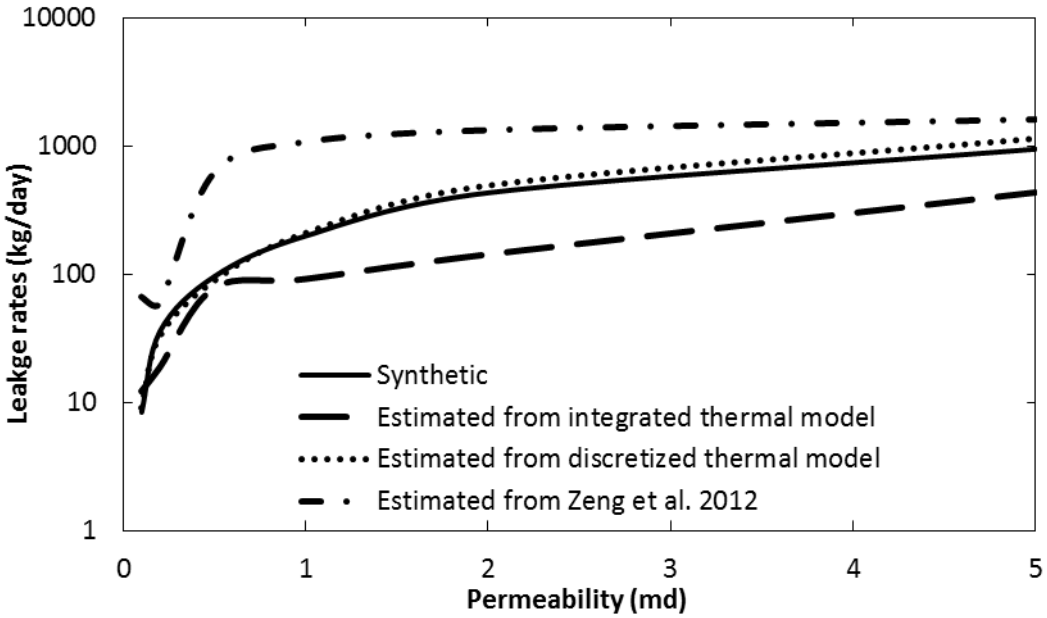

Figure 7. 15. Estimation of leakage rate from leakage thermal model in comparison to the empirical equation developed in Zeng, Zhao, and Zhu (2012).

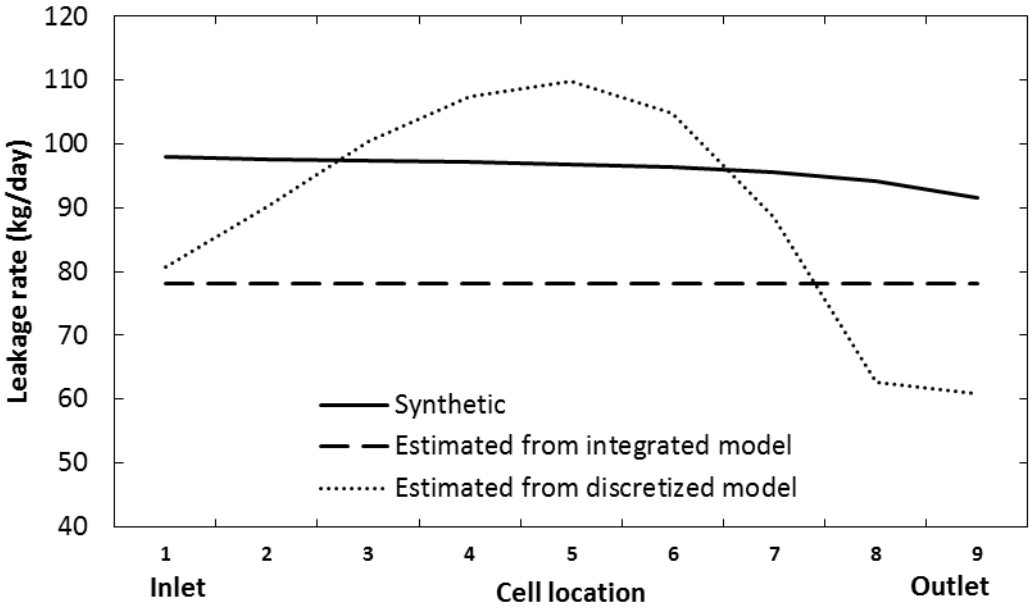

Figure 7. 16. Estimation of leakage rate from the discretized leakage thermal model in comparison to synthetic leakage rate under leakage permeability of 0.5 md.

Since the leakage rate estimation is performed relatively long time after CO_2 breakthrough, the logarithmic term in the denominator of Equation 7.15 can be assumed constant. Therefore, we can define a dimensionless number to represent the ratio in Equation 7.15, which we refer to as the JT/cond number:

$$N_{JT/cond} = \frac{\dot{m}c\mu_{JT}\Delta p}{K_r L \Delta T} \tag{7.16}$$

where L is the characteristic length of the heat transfer channel. For the discretized model, L is identical to cell height h.

Table 7.6 presents the magnitude ratio of heat conduction over JT effect and JT/cond Number for various leakage rates estimation. The accuracies of the leakage rate estimation are least reliable for low and high leakage rate cases. For the case with leakage permeability of 0.1 md, the magnitude ratio of heat conduction over JT effect is more than 90 percent, which indicates the conductive heat transfer from the caprock can warm back over 90 percent of the cooling induced by JT effect. On the contrary, this ratio is less than 40 percent suggesting the heat conduction is too weak compared to JT effect in the high leakage rate cases. Therefore, to obtain decent accuracy for leakage rate estimation using leakage thermal model, the analysis needs to be performed under the magnitude ratio of heat conduction over JT effect of 40-90 percent, and JT/cond Number of 1.6-4. To further explore the validity of these ranges, we present another example problem below.

Table 7. 6. The magnitude ratio of heat conduction over JT effect and JT/cond Number under various leakage rates estimation.

Leakage permeability (md)	Leakage rate estimation (kg/day)	Leakage rate estimation error (%)	Conduction/JT ratio (%)	$N_{JT/cond}$
0.1	9.078	23.6	91.6	1.216
0.2	32.72	11	86.7	1.628
0.5	89.512	9.3	78.6	2.099
1	211.65	4.3	69.2	2.272
2	496.785	13.3	56.2	2.788
5	1154.858	20.8	38.8	3.994

Table 7.7 demonstrates the magnitude ratio of heat conduction over JT effect and JT/cond Number for another example. For the example problems in Table 7.7, the leakage rates are varied by changing the leakage area while the leakage permeability is fixed at 1 md. In the first and last cases, the operating ranges for both parameters are violated, and the estimated leakage rates are in errors larger than 20 percent. On the contrary, high accuracies are achieved by other cases which lie within the presented ranges of parameters. While this example indicates that the ranges of the parameters established in this work are extendable to other leakage scenarios, further works may be required to ensure that these ranges are applicable for any CO_2 leakage scenario regardless of the leakage environment.

The negligible cooling effect for low permeability wellbore leakage, which is out of the applicable range of the developed thermal model, makes the leakage detection and rate estimation from thermal signals impractical. For the case of high permeability wellbore leakage, an alternative can be established to enhance the quality of the estimation, which will be presented in section 7.2.2.4.

Table 7. 7. Validation example of magnitude ratio of heat conduction over JT effect and JT/cond Number under various leakage rates estimation.

Leakage area (m^2)	Leakage rate estimation (kg/day)	Leakage rate estimation error (%)	Conduction/JT ratio (%)	$N_{JT/cond}$
0.04	9.91	25.4	99.2	1.369
0.25	57.47	12.4	85.4	1.838
1	211.65	4.3	69.2	2.272
4	812.6	2.6	47.9	3.282
25	2593	49.2	31.4	5.155

7.2.2.3 Leakage rate estimation during mixed leakage period

Given the two-phase CO_2 and brine leakage during mixed leakage period, the leakage rate estimation during this period is more complex compared to that over late-time single-phase CO_2 leakage period. The analysis in section 7.2.2.2 indicates that leakage rates can be reliably estimated under the assumption of CO_2 single-phase flow. Though this assumption is not valid during mixed leakage period, the leakage rate can still be estimated by the thermal balance between the JT effect and conductive heat transfer. Theoretically, Equation 7.10 should be used here to estimate the leakage rate due to the transient behavior of the temperature signal. However, we still apply simplified Equation 7.13 in the mixed leakage period to compare with synthetic data. After the comparison, this assumption will be further discussed.

The thermal behavior of brine leakage has been investigated in section 7.2.1. The observations suggested that the JT heating effect induced by brine leakage is weak compared to those from CO_2 leakage due to the magnitude of the JT coefficient for these two fluids. And the brine leakage rate during mixed leakage period is significantly lower compared to CO_2 leakage rate as a result of the CO_2/brine relative permeability and viscosity contrast. From these two observations, one can propose that the thermal balance during mixed leakage period is mainly contributed by the CO_2 leakage, and the leakage rate estimation can be achieved considering only the CO_2 leakage despite the existence of two-phase flow in this period.

Based on this presumption, we estimate the leakage rate during mixed leakage period on the example problem presented in Table 7.5. Figure 7.17 illustrates the comparison between the leakage rate estimations from leakage thermal model and the synthetic data. The estimated CO_2 leakage rate is in relatively good agreement with the corresponding synthetic leakage rate during the mixed leakage period. The largest discrepancies among the five cases come from the estimation during the CO_2 leakage period (except for the 0.2 md case). This observation confirms the possibility of treating the thermal balance during mixed leakage period as CO_2 leakage only.

For the cases with low permeability leak, the stronger resistance to flow in the leak requires a longer injection period to obtain a measurable leakage cooling effect. The prolonged injection activity affects the geothermal temperature at the caprock, which introduces more uncertainties to apply the thermal leakage model to estimate the leakage rate. This error is most significant at the beginning of the mixed leakage period since the small cooling signal is initially very sensitive to any changes in the geothermal temperature. Therefore, applying the leakage thermal model during mixed leakage period is more accurate for short injection period and high permeability leak. Although we applied the simplified analytical solution (Equation

7.13), which assumed steady state temperature behavior, the leakage rate estimations in mixed leakage period are acceptable. In fact, the effect of transient temperature behavior should be more significant in high permeability leak due to the larger temperature gradient with time. However, the results indicate the estimation is better in higher permeability leak. Therefore, the effect of transient temperature behavior on leakage rate estimation is not significant and can be safely neglected in the mixed leakage region for leakage rate estimation purpose.

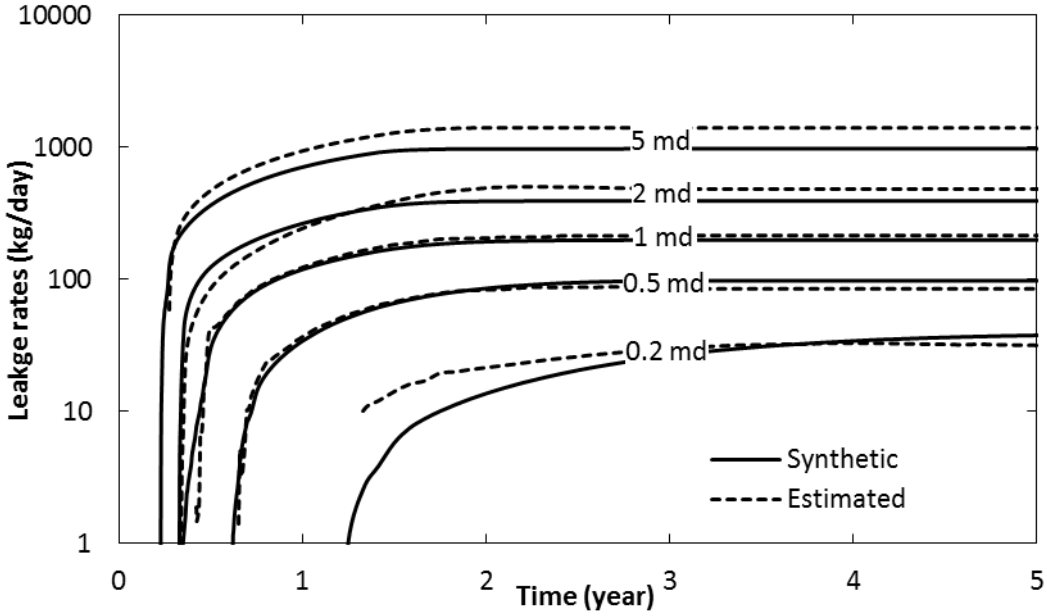

Figure 7. 17. CO_2 leakage rates estimation from leakage thermal model during mixed leakage period.

7.2.2.4 Leakage transmissibility estimation from leakage thermal model

The most important parameter for assessing the risks of leakage along a wellbore is the transmissibility, the product of leakage permeability and leakage area, of the leakage pathway (Tao et al. 2014, Zeidouni and Pooladi-Darvish 2012a). This estimation is essential, particularly for pressure signals associated with wellbore leak. The CO_2 leakage rate through the wellbore leak are governed by the flow properties of the leak, as well as the properties of the leaking fluid, which can be represented by Darcy's law:

$$\frac{\dot{m}}{\rho} = \frac{kk_r A}{\mu} \frac{p_{IZ} - p_{AZ}}{H} \tag{7.17}$$

where ρ, μ, and k_r are the density, viscosity, and relative permeability of the leaking fluid respectively. k and A are the permeability and area of the leak. The density and viscosity of the leaking fluid can be obtained from the equation of state and/or correlations for any given pressure and temperature. The relative permeability curves of CO_2 and brine mixture suggests that the relative permeability of CO_2 will approach to 1 shortly after CO_2 breakthrough (Mao, Zeidouni, and Askari 2017). Thus, with the estimated leakage rate, the transmissibility of the leak can be assessed.

The accuracy of leakage transmissibility estimation from Equation 7.17 seems to be directly related to those for leakage rate estimation. We compare these results in Table 7.8 and analyze any improvement made by estimating the leakage transmissibility. The estimated and input values to the IZ-leak-AZ are in relatively acceptable agreement, especially for transmissibility range of 0.5-5 md·m^2. Based on Equation 7.17, the leakage transmissibility is a function of leakage rates, leaking fluid density and viscosity, and pressure drop along the

leak. Therefore, the accuracy of the estimated leakage transmissibility should closely follow those for leakage rates. However, the estimation of a high transmissibility leak (5 md·m^2) is more accurate compared to the corresponding leakage rate estimation. As a result, we can estimate the leakage transmissibility from the leakage thermal model with higher accuracy compared to the direct estimation of leakage rate for high leakage rate cases.

Table 7. 8. Estimation of leakage transmissibility and the corresponding accuracy.

Leakage transmissibility (md·m^2)	Synthetic leakage rates (kg/day)	Discretized leakage rate estimation (kg/day)	Discretized leakage rate estimation error (%)	Leakage transmissibility estimation (md·m^2)	Leakage transmissibility estimation error (%)
0.1	8.356	9.078	23.6	0.0359	64.1
0.2	35.734	32.72	11	0.153	23.5
0.5	96.204	89.512	9.3	0.416	16.8
1	198.984	211.65	4.3	0.977	2.3
2	432.145	496.785	13.3	2.135	6.7
5	946.654	1154.858	20.8	5.387	7.7

So far (in sections 7.2.2.2 - 7.2.2.4), two methods to estimate the leakage rates were presented. The leakage thermal model directly estimating the leakage rates are most favorable in the leakage transmissibility range of 0.1-2 md·m^2. If higher leakage rates are encountered, applying the leakage transmissibility assessed from the leakage thermal model to pressure signals should be the proper way to achieve higher accuracy. According to Table 7.4, the detection ranges for these models are varied. The sustained casing pressure monitoring (Tao et al. 2014) appears to be capable of detecting very small leakage rate and the majority of pressure-based model aim for very high leakage rate. Therefore, the first approach in this study is a perfect candidate to estimate the moderate leakage rates that are too small or too strong to be obtained using pressure signals. Even at higher leakage rates, the leakage thermal model is useful to obtain the leakage transmissibility as a complement to the existing pressure-based approaches.

7.2.2.5 Procedures to estimate leakage rate and transmissibility from temperature data

Based on the developed leakage thermal model and its leakage rate and transmissibility estimation results, the following procedures for wellbore leakage rate and transmissibility estimation are presented:

1. Obtain field measurements of time-dependent leakage temperature and pressure data from IZ, AZ, and the wellbore leak.
2. Plot the leakage temperature and pressure signals versus time, identify the periods of mixed leakage and CO_2 leakage.
3. Define the discretized control volumes for leakage thermal model based on the leak length, and pressure and temperature variations along the leak.
4. Perform the leakage rate estimation during CO_2 leakage period using Equation 7.13.
    a. For each control volume, evaluate CO_2 JT coefficient and specific heat, the thermal conductivity of the caprock, and the conductive time interval from

pressure and temperature condition and geothermal gradient of the control volume.

b. Calculate the leakage rate using Equation 7.13 for each control volume and average the results to obtain leakage rate estimation.
c. Calculate the JT/conduction ratio and JT/cond Number by Equations 7.14 and 7.15 to determine if this given case is within the scope of applying temperature signals to estimate the leakage rates. The applicable ranges for these two parameters are 40-90 percent and 1.6-4 respectively. If the estimated rate is higher than the range, estimate the leak transmissibility instead of rate using step 6.

5. Perform the leakage rate estimation during mixed leakage period using Equation 7.13.
   a. For each control volume and each time step, evaluate the time-dependent CO_2 JT coefficient and specific heat, the thermal conductivity of the caprock, and the conductive time interval from pressure and temperature condition and geothermal gradient of the control volume.
   b. Calculate the time-dependent leakage rate using Equation 7.13 for each control volume and average these estimations.
6. Perform the leakage transmissibility estimation for those cases with higher leakage rate estimation from step 4c.
   a. For each control volume, evaluate the viscosity and density of CO_2 from pressure and temperature conditions.
   b. Calculate the leakage transmissibility using Equation 7.17 for each control volume using discretized leakage rate estimation and average these values to obtain the estimated leak transmissibility.

This procedure is summarized in a flowchart presented in Figure 7.18. The discretization in the procedure can be ignored for integrated analysis to enable quick and preliminary analysis.

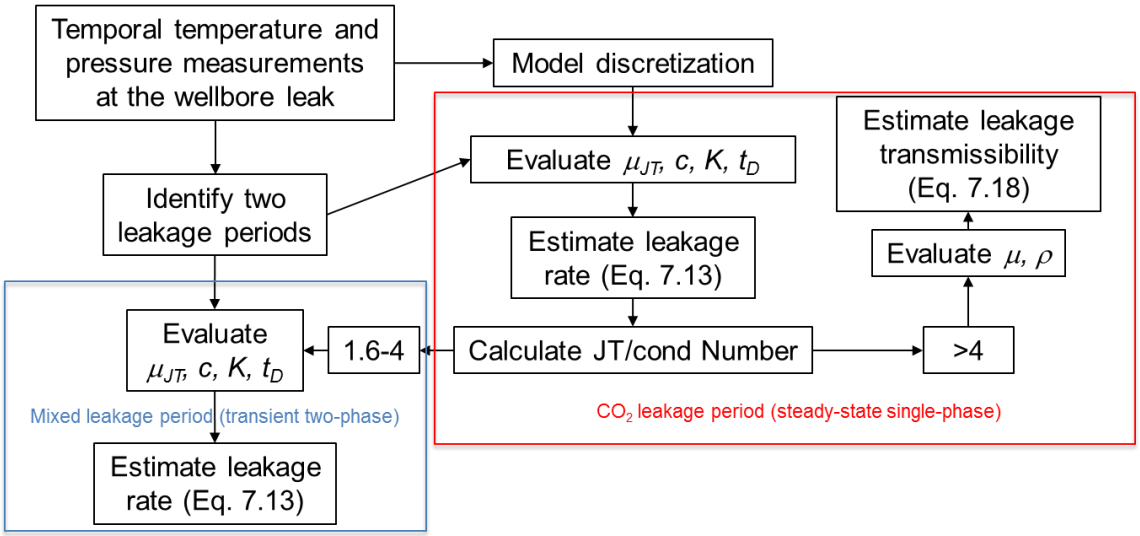

Figure 7. 18. Flowchart to apply leakage thermal model for leakage rate and transmissibility estimations.

7.2.3 Discussion

In this section, the developed analytical model and the leakage rate estimation results are further discussed. First, we discuss the leakage rate estimations in absence of pressure measurements. Next, we extend the leakage rate estimations to the post-injection period to

characterize leaky wells that are encountered after the CO_2 injection was terminated. Furthermore, we deliberate practical limitations and alternatives to estimate the wellbore leakage rates from leakage temperature signals. In the end, the effect of temperature monitoring locations on the leakage rate estimation is elaborated as the practical requirement of this research.

7.2.3.1 Pressure profile estimations

Pressure is an important input for the leakage thermal model. However, the analyst may not always have access to pressure data. If so, the pressure drop across the leak needs to be estimated. The AZ pressure remains relatively constant during the leakage, according to section 7.1. Meanwhile, the IZ pressure has been investigated and estimated through IZ pressure models (Mathias, McElwaine, and Gluyas 2014). The simplest estimation of IZ pressure at the leak is the pressure at the injection well (13 MPa). We take this assumption as well as assuming constant AZ pressure (8 MPa) to perform leakage rate estimation through the leakage thermal model. Compared with the case with pressure measurements, the introduced errors from the pressure profile estimations are illustrated in Figure 7.19.

According to the results presented in Figure 7.19, the leakage rate estimations in the presence and absence of pressure data can be close. The results with pressure estimations show slightly more errors compared to those from pressure measurements. The additional errors introduced from pressure estimations are less than 6 % of the cases presented in Figure 7.19, which is acceptable considering the modeling errors presented in Table 7.5. Therefore, simply assigning the AZ and IZ pressure to initial AZ and injection well pressure is very reasonable when the pressure measurement is not available at the wellbore leak.

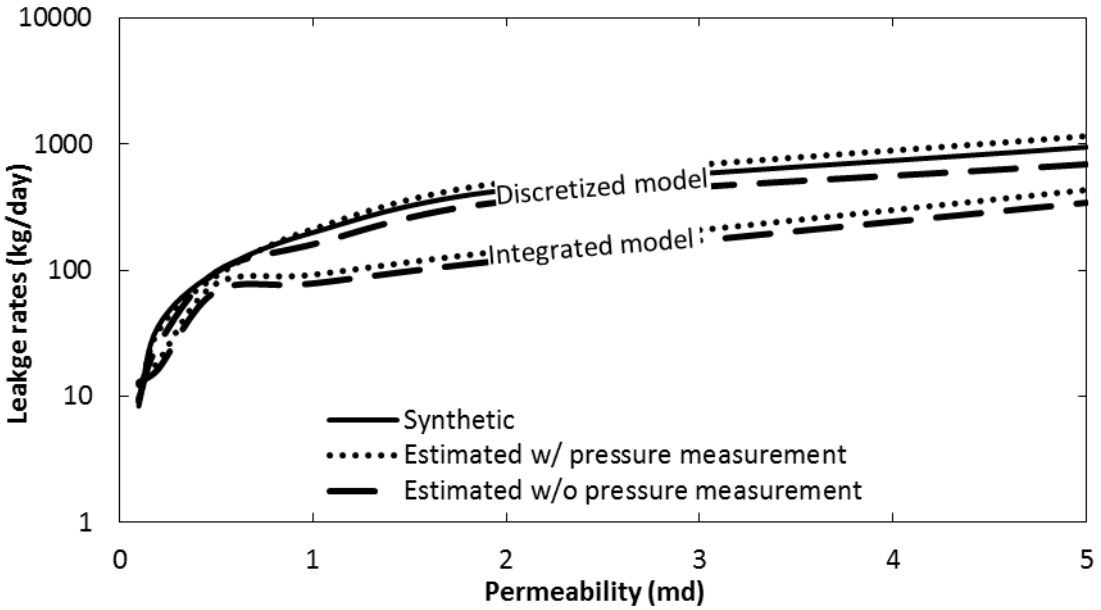

Figure 7. 19. Estimations of leakage rate from actual pressure measurements in comparison to those from pressure profile estimations.

7.2.3.2 Application of the leakage thermal model to the post-injection period

The developed leakage thermal model in this study has only been applied during the injection period to detect wellbore leakage. However, the leakage rate and transmissibility

estimation can be also applied over the post-injection period. This application can address the major concern of wellbore leakage from CO_2 sequestration sites where many more wells may be encountered by the CO_2 plume during the post-injection period.

The procedures to apply the leakage thermal model for the post-injection period are identical to those for the injection period, presented in section 7.2.2.5. In fact, the pressure drop across the leak should be easier to estimate since the IZ pressure stabilizes after the injection. The expected temperature signal during the post-injection period is weaker due to the slower CO_2 plume propagation and CO_2 solidification in the matrix during the post-injection period. These characteristics of the post-injection period also make the transient period (mixed leakage period) much longer compared to those in the injection period. Nonetheless, the same criteria for the JT/cond Number are applicable to the leakage thermal model.

7.2.3.3 Leakage rate estimation from breakthrough time

The estimates of elapsed time for the CO_2 breakthrough from wellbore leaks affect the leakage rates (Figures 7.14 and 7.17). Therefore, the elapsed time has the potential to estimate the CO_2 leakage rate with similar accuracy to our modeling of temperature signals. Table 7.9 presents the temperature response time after the CO_2 breakthrough (considering 0.1% CO_2 saturation threshold) in the AZ from wellbore leak. For all the cases presented, the cooling effect occurs as soon as the CO_2 starts leaking. However, it can be only detected after exceeding the resolution of the downhole temperature measurement tool. Assuming detectable thresholds of 0.1 and 0.5 degC, the times for leakage detection of various scenarios are 1-11 days and 3-38 days, respectively. In general, large leakage transmissibility results in shorter temperature response time. However, several issues need to be addressed before this method is feasible.

Table 7. 9. Temperature response time when leakage occurs.

Leakage transmissibility ($md \cdot m^2$)	Minimum cooling signals (days)	Detectable cooling signals (0.1 degC) (days)	Strong cooling signals (0.5 degC) (days)
0.2	+0	+11	-
0.25	+0	+2	+38
0.5	+0	+4	+15
1	+0	+2	+7
2	+0	+1	+3
4	+0	+2	+5

Unlike the leakage temperature signals in CO_2 leakage period, the CO_2 breakthrough time occurs while CO_2 and brine are both flowing through the leak. As a result of the two-phase flow, the CO_2 leakage rate is affected by the relative permeability of the CO_2 phase. The CO_2 saturation in the leak are also varying with time and location in the leak. The porosity of the leak is required to calculate the porous space, which is a general lack of information for practical purposes. Even if the above-mentioned variables are precisely obtained, the estimated leakage rate is not constant and increasing with time before and during the CO_2 breakthrough.

The numerical simulation of the IZ-leak-AZ model can simulate all the variables and estimate the leakage rates. Future works are required on modeling the variables to analytically capture the leakage rates or transmissibility from CO_2 breakthrough time.

7.2.3.4 Effect of temperature monitoring location on the leakage rate estimation

Leakage rate and transmissibility estimations performed in this research are based on the measurement of leakage temperature signals, which are obtained at the location of the wellbore leak. Wellbore leakage can be accommodated by weaknesses in the cement and/or the cement plug (Figure 7.12). Among several downhole temperature monitoring systems listed in the introduction, DTS and/or FBG can be implemented behind the casing (cemented) to monitor the thermal signals in all directions. In this case, the leakage temperature signals are probably accessible since the potential wellbore leakage paths can be covered by DTS and/or FBG. Other temperature measurements are currently limited inside the casing including PDG and well logging, which are ideal for detecting and estimating the leakage rates from cement plug inside the casing. If the leakage occurs outside the casing and temperature measurements behind the casing are unavailable, a more extensive wellbore thermal model is required to obtain leakage temperature signals from the wellbore temperature measurements. This process can introduce extra uncertainties and the leakage temperature signals may be masked by the low heat transfer coefficient of the wellbore. Therefore, temperature monitoring systems are recommended to cover the potential wellbore leakage. The available temperature measurements and the potential wellbore leak should be jointly assessed to apply this approach for practical purposes.

Chapter 8. Conclusions and Recommendation

8.1 Forward and Inverse Modeling in Conventional Reservoir

8.1.1 Single Layer Homogeneous Reservoir under Transient Flow

In section 3.1, we derived analytical solutions for temperature transient of slightly-compressible hydrocarbons produced from vertical wells and applied the solutions to oil and gas reservoirs. We used Laplace transform to solve the governing energy balance equation under infinite-acting reservoir and constant rate conditions. The temperature profiles calculated from the analytical solutions were illustrated and verified against numerical simulation results for an oil reservoir and a gas reservoir. The analytical solutions were in good agreements with the numerical simulation for both cases. The temperature profiles are a function of a similarity variable (r^2/t) in a homogeneous reservoir. The effects of Joule-Thomson and adiabatic expansion can be clearly identified from the temperature profiles. Considering the adiabatic expansion effect extends the radius of investigation of the temperature transient to be identical to the traditional pressure transient testing. The relevance of the assumptions made in the derivation of our analytical solutions including the negligible effect of heat loss to over- and under-burden was discussed. Restricted by the assumption of constant fluid property, analytical solutions are valid under 10% (gas reservoir) and 30% (oil reservoir) drawdown from initial reservoir pressure at the production well. Through identification of temperature responses induced by Joule-Thomson and adiabatic expansion effects, we provided interpretation techniques to determine the reservoir permeability (and porosity) from the temperature data in section 4.1.

8.1.2 Near Wellbore Damaged Single Layer Reservoir under Transient Flow

The transient flow analytical solutions developed in section 3.1 were extended to include the near-wellbore damage. In departures from existing solutions considering the damaged zone, we treated the damaged reservoir as a composite reservoir. The resulting analytical solution is no longer a function of the lumped skin factor. The damaged zone permeability and radius affect the temperature response separately. Development of the analytical solution considering damaged zone around the wellbore illustrated that the existence of a damaged zone can increase the temperature variations significantly. Unlike the pressure transient analysis that characterizes the damaged zone with a single skin factor lumping the effect of the damaged zone radius and its permeability, temperature transient analysis can determine these properties separately. Through identification of temperature responses induced by the damaged zone, we provided interpretation techniques to determine damaged zone radius and permeability from the temperature data in section 4.2.

8.1.3 Single Layer Reservoir with Near Wellbore Non-Darcy Effect under Transient Flow

Temperature transient analysis requires strong temperature signals which are often accompanied by non-Darcy flow effect in the near wellbore region. This effect is accounted for by the novel analytical solution developed in section 3.3. This analytical solution enables temperature modeling in the high drawdown well test, characterizing the non-Darcy flow effect, and modification of the current inversion procedures for temperature transient analysis.

The developed analytical solution was verified against numerical simulation results in the cases of vertical well production from non-damaged and damaged reservoirs. The temperature modeling results showed good agreements between the analytical solution and numerical simulation for all the cases presented in this study. Compared with cases neglecting

the non-Darcy flow effect, an additional heating effect occurs due to the non-Darcy flow effect. The more severe temperature and pressure dynamics considering the non-Darcy flow effect make the fluid property corrections essential to be implemented in temperature transient analysis.

According to the analytical solution, the temperature increments are directly proportional to the Forchheimer number and only affected by the non-Darcy flow effect in the near wellbore region. We conducted sensitivity analyses on two parameters in the Forchheimer number, production rate and non-Darcy flow coefficient, to identify their impacts on the temperature signals. In semi-log plots of temporal sandface temperature profiles, we found the late-time slope values are only related to the production rates, not to the non-Darcy flow coefficient. This finding indicates that the reservoir properties can be evaluated from the slope values regardless of the existence of non-Darcy flow effect, which is purely associated with the magnitude of the temperature signals at the late time. We identified two criteria to apply TTA for non-Darcy flow effect identification: critical Forchheimer number and accuracy of the downhole temperature monitoring system.

The temperature increments due to the non-Darcy flow effect evolve in the early time as a transition period and reach a nearly constant value in the sandface temperature modeling. Based on the analytical solution, we derived the slope of late time sandface temperature profiles in a semi-log plot after the start of non-Darcy flow transition period. If the production continues for a longer period, the slope can be identical to the case without non-Darcy flow effect. In the transition period, the slope is affected by the production time as well as the Forchheimer number. In the case of existing near wellbore damaged zone, its property should be estimated from the sandface temperature signals after the transition period of non-Darcy flow effect. However, if the damaged zone is regionally too small, its effect may be masked by the non-Darcy flow effect rendering difficulty in estimating the damaged zone radius.

Based on the findings in the forward temperature modeling, we modified the inversion process developed in sections 4.1-4.2 considering the non-Darcy flow effect. The outputs of the revised procedures are permeability and non-Darcy flow coefficient, and for the damaged reservoir, damaged zone radius and permeability. For the cases investigated, the reservoir characterization results can estimate (with less than 10% errors) the reservoir and damaged zone permeabilities, as well as damaged zone radius. The estimations of non-Darcy flow coefficients achieve less than 30% errors and the same order of magnitude compared to the reference values. By incorporating the non-Darcy flow effect, we extended the scope of temperature transient analysis to high flow rate well tests with up to 30-40 degC sandface temperature signals.

8.1.4 Single Layer Reservoir under Boundary Dominated Flow

Boundary dominated flow is an important flow period in the life of a reservoir for production analysis and reservoir characterization since most of the hydrocarbons (in conventional reservoirs) are recovered during this long-lasting period compared to its preceding transient period. During this period, production induced temperature signal may still behave transiently, but requires taking the boundary dominated pressure behavior into consideration to enable temperature transient analysis. To address this knowledge gap, a novel analytical solution was developed to model the temperature profiles under boundary dominated flow and its applications for temperature transient analysis were illustrated.

We applied Laplace transform to derive this transient temperature analytical solution from energy balance equation considering pseudo-steady state pressure profile. This solution presented similar Joule-Thomson effect in sections 3.1-3.3 and an additional production time-dependent term representing the effect of boundary dominated flow on temperature profile,

referred to as boundary dominated adiabatic expansion. Hence, an extended temperature transient analytical solution was developed by combining this new solution under boundary dominated flow with existing solutions. This integrated solution was verified against numerical simulation results in multiple cases.

For all the cases presented in section 3.4, the analytical temperature modeling results were in close agreement with those obtained numerically. The characteristic of boundary dominated flow displayed a quasi-linear cooling effect on temporal temperature profiles plotted in a Cartesian plot, which can be clearly differentiated from the linear heating Joule-Thomson effect in a semi-log plot. Based on the analytical solution, the slope of this linear behavior is a function of multiple reservoir parameters, including total compressibility and drainage area. According to the parametric analysis on the temperature modeling results, eight reservoir, production, and fluid properties were categorized, in which total compressibility and drainage area were only sensitive to temperature profiles controlled by boundary dominated flow. In addition, observation wells away from the production well presented strong cooling effect under boundary dominated flow due to the elimination of the heating Joule-Thomson effect. The reservoir shape affected the temperature profiles when the pressure transient reached the boundaries, which can be used to estimate the distance to the closest boundary from the production well. Based on the findings from the temperature modeling results, we developed additional inversion procedures to estimate drainage area and reservoir shape from the temperature signals under boundary dominated flow presented in section 4.4, which were applicable to both production and observation well surveillance. Examples in which these procedures were applied illustrated acceptable estimation accuracies (more than 93%), while the estimations from the observation well demonstrated fewer errors (< 0.5%).

Long-term monitoring of boundary dominated flow makes thermal conduction and heat loss to surroundings more significant on temperature modeling. They can introduce errors on drainage area estimations for up to an additional 10%. We also modeled the temperature signals associated with a build-up test. With a production period of boundary dominated flow, the buildup temperature signals were identical to those under pressure transient period. Therefore, existing temperature transient analytical solutions for build-up test can be safely applied to the cases under boundary dominated flow.

The temperature transient analytical solution under radial boundary dominated flow introduced in section 3.4 extended the potential for further application of temperature transient analysis. With this solution, the observation well temperature transient analysis proved to be feasible for reservoir characterization.

8.1.5 Multi-Layer Reservoir

Temperature transient analysis can assist in reservoir management of multilayer reservoirs by characterization of individual layer properties Through late-time production rate estimations per layer and the single layer transient temperature analytical solution, we developed a novel analytical solution to predict the transient inflow temperature signals of each layer presented in section 3.5, while producing with the constant rate from a fully penetrating vertical well. Based on this analytical solution, the procedures to characterize layer properties are procured.

We validated this analytical solution by illustrating the temperature profiles obtained from this analytical solution on a multilayer oil reservoir and benchmarking against those from a commercially available numerical simulation. This comparison demonstrated that this analytical solution is in very good agreement with the numerical results. Sensitivity analyses of temperature profiles were performed on layer properties of permeability, porosity, damaged zone radius and permeability. Higher layer permeability increases the radius of investigation

of Joule-Thomson and adiabatic expansion effects by rising speeds of temperature propagation. Porosity variations result in changes of adiabatic expansion effect associated with the heat capacity of the saturated porous medium. The effects of damaged zone radius and permeability on temperature signals are analogous with those produced from a single layer reservoir.

Semi-log interpretation techniques were developed from observations of temperature signals to characterize individual layer properties of a multilayer reservoir in section 4.5. With adequate knowledge of other layer properties, detailed procedures were demonstrated and can lead to the interpretations of layer production rates, permeability, and damaged zone permeability for each layer. Even with no prior knowledge of other layer properties, simplified procedures obtain the ratios of layer production rates, permeabilities, and damaged zone permeabilities between layers. These interpretation techniques significantly simplify the complications associated with the inversion from numerical simulation while maintaining decent accuracy.

8.2 Effect of Fluid Property and Production Rate Variations on Temperature Transient Analysis in Conventional Reservoir

8.2.1 Accounting for Fluid Property Variation in Temperature Transient Analysis

Analytical solutions developed in section 3 assume constant fluid properties that limit the applications of the solutions and can result in significant errors when modeling temperature signals under high drawdown conditions. In section 5.1, we presented a method to account for the fluid property variations in temperature transient analysis. The proposed method could significantly improve the modeling accuracy of existing analytical solutions and was adopted to assist in analyzing temperature data for reservoir characterization.

We identified four major fluid properties contributing to the temperature signals, which include fluid density, specific heat, Joule-Thomson coefficient, and viscosity. A sensitivity analysis among the four revealed that the viscosity imposes the largest impact on the temperature data. We used the developed analytical solutions to show the sensitivity of the temperature response to the fluid properties, which is most pronounced at late-time for both drawdown and buildup tests. The temporal temperature profiles in this period present quasi-linear behavior on a semi-log plot, which pointed to the fluid property correction method. The algorithm to obtain the proper fluid properties involved arithmetic and harmonic averaging for various fluid properties along with corresponding iterative procedures. Due to the theory behind the fluid property correction method, the applicability and limitations of this method depend on the assumption made on the development of analytical solution as well as the occurrence of the quasi-linear behavior. Further investigations indicated that applying a viscosity only correction method can correctly model the temperature behavior.

With the inputs of the corrected fluid properties, the analytical solutions developed in section 3 were benchmarked against those from the numerical simulation for various scenarios, including drawdown and buildup temperature signals for non-damaged and damaged reservoirs with different production rates and reservoir fluid components. To ensure the fluid properties are correctly estimated, the pressure modeling also considered the corrected fluid properties and was validated against the numerical simulation results. The drawdown and buildup temperature profiles corrected for fluid property variations showed excellent agreements with those from numerical simulation, especially at the late time. The damaged zone permeability induced unique temperature signals apart from that in the reservoir. This required performing another independent fluid property correction method in a different time period to precisely model the temperature transient in the damaged reservoir.

The temporal temperature profiles with the input of corrected fluid properties were essential for the improvement of reservoir characterization procedures. Based on the advancements of the forward temperature modeling, we updated existing semi-log temperature interpretation techniques to improve the reservoir characterization with the fluid property correction method. Significant improvements were observed in permeability estimations for the non-damaged and damaged reservoirs, showing up to 60% higher accuracy compare to characterization based on constant fluid property assumption. The two-time-period fluid property correction approach adds additional 25% accuracy on the permeability estimations for the damaged reservoir. Applying this method to solutions developed in section 3 extends the scope of solutions from modeling small temperature signals to significant temperature transients in high drawdown conditions, which were mainly modeled by numerical simulation previously.

8.2.2 Dynamic Temperature Analysis under Variable Rate and Pressure Conditions for Transient and Boundary Dominated Flow

Constant production rate, as an assumption for solutions developed in section 3, is rarely valid for any practical cases with an extended period of production. To extend the scope of analytical temperature transient analysis for more complex and realistic production strategies, novel analytical approaches were proposed in section 5.2 to model temperature signals under variable rate and pressure conditions, i.e. dynamic temperature analysis.

We started addressing this issue by classifying the potential cases of complex variable rate and pressure conditions based on production strategy (step-rate or constant pressure production) and flow regime (early pressure transient or late boundary dominated flow period). For each scenario, suitable approaches were developed to account for production rate variation. To be specific, we proposed the approaches of superposition cumulative production, simplified superposition, and material balance time to analyze three scenarios. A novel analytical solution was derived from energy balance equation with the input of exponential rate decline for the last scenario. As a result, cases with complex production history can be transformed to analogous cases with a constant rate, which can be analyzed using existing temperature transient analysis procedures.

To verify the proposed methods, multiple sets of synthetic temperature data were generated for each production scenario as candidates for dynamic temperature analysis. The validations come from both graphical confirmations of qualitative evaluation and quantitative estimations of reservoir properties. After performing dynamic temperature analysis, the temperature data for each set are found to be in close agreement with the corresponding case. With detailed reservoir characterization procedure, the reservoir property estimations are in close agreement with the reference settings (for permeability, porosity, drainage area, and damaged zone properties)

Besides the extended scope and application, the approach built on the contributions from section 4. The fluid property correction method was extended to variable rate and pressure conditions and illustrated improved characterization results. The observation well surveillance was introduced for monitoring boundary dominated flow with better estimation precision. We also demonstrated the dynamic temperature analysis for two case studies reported in the literature.

8.3 Application of Temperature Transient Analysis in Unconventional Reservoir

8.3.1 Forward Numerical Modeling in Producing Unconventional Reservoir

Recent developments on horizontal well drilling and hydraulic fracturing make the exploration of shale reservoir technically feasible. Implementation of temperature downhole monitoring system has contributed to the unconventional reservoir characterization and fracture diagnostic in the past decade. Thermal modeling research in this area has often focused on the temperature profiling along the horizontal wellbores. We build a numerical model to predict temperature signals associated with shale gas reservoir production from a hydraulic fracture.

We perform numerical simulation on a single fracture model as the base case and vary the fracture permeability and half-length to conduct further parameter study. The model parameters are comparable with previously published models. The temperature data is obtained from the numerical model at the wellbore-fracture interface as the arriving temperature profile, which can be incorporated into a wellbore model separately.

We identify similar baro-thermal effect observed in producing conventional reservoir, including Joule-Thomson and adiabatic expansion effects, on the temperature signals associated with the unconventional reservoir. For production with a constant bottom-hole pressure, the cooling baro-thermal effect did not last long before being balanced by the heating effect due to the production rate decline.

The following parametric study addresses the controversial topic of the fracture conductivity impact on the thermal behavior as well as the advantage of temperature versus pressure signals. Higher fracture conductivity can amplify the maximum cooling by baro-thermal effect as well as warm back due to the production rate decline. Therefore, the effect of fracture conductivity on the temperature signals is not monotonic. On the other hand, longer fracture half-length leads to weaker warm back. As a result, temperature signals are sensitive to fracture half-length and conductivity independently, even if the fracture has a constant dimensionless fracture conductivity.

8.3.2 Fracture Diagnostic during Stimulation Fluid Flow-back

Stimulation fluid flow-back presents a distinct thermal signal due to the significant temperature difference between the fractured and non-fractured regions. This work presents the analysis of flow-back temperature profile to identify inflow temperature from each of the fractures, which is a critical input for PLT analysis. The results from preliminary simulation studies suggest that the inflow temperature is identical to the surrounding fractured region temperature, which is masked by the heating effect induced by the wellbore fluid flow after a shut-in (after-flow). With the quantified heating effect, one can obtain the inflow temperature for each fracture.

In section 6.2, an analytical solution to model the temperature signal associated with a shut-in period separating the flow-back and production periods is presented, the results of which can be used to evaluate the efficiency of each fracture. This analytical solution is derived using the Method of Characteristics applied to an existing governing equation with newly incorporated thermal boundary condition. As a validation set, a wellbore fluid simulation is constructed using a simplified finite element model, the results of which present good agreement with those from the analytical solution.

The results of the analytical solution are presented in terms of the temporal temperature variation in the fractured and non-fractured region for constant and variable after-flow rate conditions. We identify the major mechanisms contributing to the temperature signal: inflow velocity and its variation, flowing, geothermal, and inflow temperature of each fracture,

surrounding temperature field (boundary condition), and casing radius. Near the fractured region, wellbore fluid temperature is subject to a heating effect after shut-in due to the warmer fluid away from the perforation moving into the cooler region. Hours after the shut-in, the wellbore temperature reaches a constant value, which indicates the thermal balance (steady state) between convection due to after-flow and heat transfer to surrounding rock.

After the validation and analysis of forward modeling results, inversion procedures are introduced based on the derived analytical solution. By comparing the temperature profiles in the fractured and non-fractured region, one can estimate inflow fluid temperature, surrounding temperature field, and after-flow velocity of each fracture. The characterization results show good accuracies against the true values (less than 15% errors for all the cases). The estimations are very accurate for temperature profiling of the fractured region (less than 3% errors). This work presented a method to accurately estimate the inflow fluid temperature from the fractured well and present the main factors affecting the flowing temperature data. The estimated fracture properties from this work can be used to evaluate the stimulation efficiency per individual fractures and optimize the future fracturing treatment through production logging analysis.

8.4 Application of Temperature Transient Analysis in CO_2 Storage Leakage Detection and Characterization

8.4.1 Effect of Leakage Pathway Flow Properties on Thermal Signal Associated with the Leakage from CO_2 Storage Zone

We evaluated the potential of the temperature signal to detect leakage of fluids from the CO_2 storage zone, and the effect of leakage pathway flow properties on the thermal signal. For the conditions evaluated in this study, the thermal signals can clearly reveal the phase changes across the leak because of the drastic varying JT coefficient between the liquid and CO_2-rich gas phase compared to the pressure signals. The temperature signals, obtained from compositional hydrothermal numerical simulations, are investigated for two leakage pathways: leaky wells and leaky faults. The temperature signal associated with leakage from a leaky well is found to be much higher than that from the leaky fault. We also revealed that the JT effect and heat conduction are the two dominant heat transfer mechanisms procuring the leakage thermal signal, while the adiabatic expansion shows a moderate impact on the temperature profiles only in the leaky fault case. We observed that the trend of the temperature signal from the JT effect will be completely altered before and after the CO_2 leakage.

Analyses with miscellaneous IZ, leaks, and AZ properties were performed to examine the temperature signals in various conditions that may be encountered in practice. We found that the factors governing the temperature signals in AZ include the pressure drop across the leaks and the leakage flux rate. As a result, our study quantitatively confirmed the preferred conditions for significant temperature signal in AZ, which involve the leak properties such as less capillary pressure, and IZ properties such as shallower depth and thinner cap-rock thickness. In addition, we treated the leakage pathway as a fractured medium to investigate its impact on the temperature signal. Based on our results, the lower fracture permeability defers the CO_2 breakthrough time and amplifies the leakage thermal signal in the leaky fault. If IZ and/or AZ are naturally fractured reservoirs, the magnitude of the leakage thermal signal significantly decreases, and the CO_2 leaks into the IZ much sooner.

In short, we have confirmed the significance of the temperature signals at the leaks and examined the favourable conditions to induce significant temperature signals in AZ if CO_2 leaks from the storage zone. Temperature signals have the advantage on detecting low permeable leaks and phase changes on the leaking fluid compared to the pressure

measurements. Careful screening on a CO_2 storage site should reveal the effectiveness to implement the required temperature surveying to detect leakage.

8.4.2 Temperature Analysis for Early Detection and Rate Estimation of CO_2 Wellbore Leakage

In section 7.2, we developed an analytical leakage thermal model to estimate the CO_2 leakage rate and transmissibility of the wellbore leak using temperature measurements. This model is based on a control volume analysis of a wellbore leak through the cement inside and/or outside the casing. The model considers the energy balance between the major mechanisms driving the leakage temperature signal: Joule-Thomson (JT) effect and heat conduction. The integrated approach (in which leakage pathway was treated as single control volume) was discretized to multiple control volumes to incorporate the varying pressure, temperature, and fluid properties through the leak.

We estimated the CO_2 leakage rates using the leakage thermal model and validated its estimations with the synthetic data obtained from numerically simulated IZ-leak-AZ model constructed in section 7.1. The IZ-leak-AZ model simulated the fluid flow and heat transfer in the IZ and AZ connected by the wellbore leak through the impermeable cap-rock. Based on the nature of leakage and the associated temperature signals, periods in which CO_2 leaks have been identified as either mixed leakage period (with brine and CO_2 flowing through the leak) or single-phase CO_2 leakage period (occurring after the mixed leakage period). The balance between heat conduction and JT effect is well established during CO_2 leakage period, producing a nearly constant temperature signal. We identified this behavior as steady state and addressed it first.

We presented the leakage rate estimations during single-phase CO_2 leakage period for various wellbore leakage properties reported in the literature. Results of the discretized leakage thermal model achieved improved accuracy in estimating leakage rates compared to the single control volume analysis, which is essential at the inlet and outlet of the leak. We compared these results with those obtained from a previous thermal model and observed significant improvements. Overall, the discretized thermal model can perform rate estimation with more than 80% accuracy on a wide range of cases. To better evaluate uncertainties in the estimates, we introduced the magnitude ratio of heat conduction over JT effect and the newly-defined JT/cond Number. The application range of this approach was obtained as 40-90 % of the magnitude ratio and within a range of 1.6-4 on the JT/cond Number. These ranges were confirmed by analysis of example problems.

We extended the leakage rate estimation to the more complex mixed leakage period, by attributing the major thermal contribution to the leaking CO_2. The estimates of CO_2 leakage rate from the steady state solution during mixed leakage period achieved acceptable accuracies compared to synthetic data. The accuracies of the estimates increase in high permeability leakage pathways, which indicate that, surprisingly, the transient behavior in mixed leakage period marginally affects the estimation of the leakage rates. We explored an additional output of the leakage thermal model to include predicting leakage transmissibility. The transmissibility estimates can be used in existing pressure-based models for leakage rate estimation purposes. Since the pressure-based models are favorable for higher permeability leaks, this combination obtained more robust results for the rate estimations. The procedure and flow chart were presented to estimate the leakage rate and transmissibility for applications to real field data on both injection and post-injection periods for a CO_2 storage project.

This particular analytical solution provides significant improvements on leakage rate estimation from temperature measurements. It addresses more complex two-phase leakage behavior under transient and steady state conditions with simpler and faster analytical approach. The flexibility of this model accommodates using pressure estimations instead of

measurements and minimum temperature data with small errors. This leakage thermal model provides multiple outputs of leakage rate and transmissibility and offers more alternatives to serve as wellbore monitoring techniques for CO_2 storage project, which is also beneficial as a validation for other available approaches.

8.5 Recommendation for Future Works

The development of downhole temperature monitoring system will continue to grow with the improvement in temperature data quality and cost of implementation. Building on the works in this dissertation to increase value of information gained from transient temperature analysis is required. Several recommendations for future works are suggested below:

1. Temperature transient analysis in conventional reservoir: Near wellbore liquid drop out (condensate banking) has been identified as a major factor causing the loss of deliverability for condensate wells, which occurs once the reservoir pressure becomes lower than the dew point pressure of the condensate gas. Estimating the size of the condensate bank, which is difficult to achieve from pressure transient analysis, is critical to design the lean gas injection remediation of condensate drop out. Transient temperature analysis has proven the capability to identify the damaged zone size and properties. Therefore, the potential of applying transient temperature analysis to characterize the condensate banking is important.
2. Thermal modeling for the warm-back period of hydraulic fracturing: As we discussed in section 6.2, the temperature modeling of flow-back period depends on the surrounding region temperature field, which can be acquired from thermal modeling for the warm-back period of hydraulic fracturing. In addition, analyzing temperature data from the warm-back period can reveal fracture and reservoir properties. While research efforts cited in Chapter 1 focused on this area, more developments can be made from the forward modeling including identifying and characterizing the stimulated region from temperature data. Meanwhile, the development of inversion procedures in this research area is difficult. One may consider the analytical solution as a direct approach for forward modeling to obtain simple inversion procedures.
3. Temperature transient analysis for gas hydrate exploration: Natural gas hydrate has proved to be the largest amount of hydrocarbon natural reserve on the planet. Current exploration of methane hydrate remains at the field trial stage with pressure depletion and thermal dissociation. Controllable, economical, and environment-friendly production method needs to be developed for natural gas hydrate exploration. Thermal modeling can be a great asset to optimize this development.

Appendix A. Analytical Solution Derivation for Single Layer Homogeneous Reservoir under Transient Flow

Applying the Laplace transform, the Equations 3.7-3.9 become:

$$s\overline{T_D} = \frac{1}{r_D}\left[\frac{\partial \overline{T_D}}{\partial r_D} - \sqrt{\frac{C_2}{s}}K_1\left(r_D\sqrt{sC_2}\right)\right] - 2C_1K_0\left(r_D\sqrt{sC_2}\right) \tag{A.1}$$

$$\overline{T_D} = 0, r_D \to \infty \tag{A.2}$$

This ordinary differential equation (ODE) can be solved by implementing the integrating factor. The general form of an ODE and its solution are:

$$\frac{dy}{dx} + f(x)\,y = g(x) \tag{A.3}$$

$$\frac{d}{dx}\left[ye^{\int f(x)dx}\right] = e^{\int f(x)dx}g(x) \tag{A.4}$$

where f and g are random functions. Following the procedures provided by Equations A.3 and A.4, the derivations to arrive the solution for Equation A.1 are:

$$-\overline{T_D}e^{-\frac{sr_D^2}{2}} = \int_{r_D}^{\infty} e^{-\frac{sr_D^2}{2}}\sqrt{\frac{C_2}{s}}K_1\left(r_D\sqrt{sC_2}\right)dr_D + \int_{r_D}^{\infty} e^{-\frac{sr_D^2}{2}}2C_1r_DK_0\left(r_D\sqrt{sC_2}\right)dr_D \tag{A.5}$$

Here, we apply the late time approximations to replace the modified Bessel functions of the second kind of order 1 and 0 with the functions of the reciprocal and exponential integral for small values of $r_D\sqrt{sC_2}$ (Abramowitz and Stegun 1964). Based on final value theorem, the late time asymptotic solution is:

$$\begin{aligned} -\overline{T_D}e^{-\frac{sr_D^2}{2}} &= \int_{r_D}^{\infty} e^{-\frac{sr_D^2}{2}}\sqrt{\frac{C_2}{s}}\frac{1}{r_D\sqrt{sC_2}}dr_D \\ &+ \int_{r_D}^{\infty} e^{-\frac{sr_D^2}{2}}2C_1r_D\left[-\gamma - \ln\left(\frac{r_D\sqrt{sC_2}}{2}\right)\right]dr_D \end{aligned} \tag{A.6}$$

$$\begin{aligned} -\overline{T_D}e^{-\frac{sr_D^2}{2}} &= \frac{1}{2s}\int_{\frac{sr_D^2}{2}}^{\infty} e^{-\frac{sr_D^2}{2}}\frac{2}{sr_D^2}d\left(\frac{sr_D^2}{2}\right) + \frac{2C_1}{s}\int_{e^{-\frac{sr_D^2}{2}}}^{0}\ln(r_D)\,d\left(e^{-\frac{sr_D^2}{2}}\right) \\ &+ \frac{2C_1}{s}\left[\gamma + \ln\left(\frac{\sqrt{sC_2}}{2}\right)\right]\int_{-\frac{sr_D^2}{2}}^{-\infty} e^{-\frac{sr_D^2}{2}}d\left(-\frac{sr_D^2}{2}\right) \end{aligned} \tag{A.7}$$

The second term on the RHS of Equation A.7 can be solved by the method of integration by part:

$$\begin{aligned} &-\overline{T_D}e^{-\frac{sr_D^2}{2}} = \\ &\frac{1}{2s}E_1\left(\frac{sr_D^2}{2}\right) + \frac{2C_1}{s}\left[\gamma + \ln\left(\frac{\sqrt{sC_2}}{2}\right)\right]e^{-\frac{sr_D^2}{2}}\Big|_{r_D}^{\infty} + \frac{2C_1}{s}\left[e^{-\frac{sr_D^2}{2}}\ln(r_D)\Big|_{r_D}^{\infty} - \int_{\ln(r_D)}^{\infty} e^{-\frac{sr_D^2}{2}}d\left[\ln(r_D)\right]\right] \end{aligned} \tag{A.8}$$

$$-\overline{T_D}e^{-\frac{sr_D^2}{2}} = \frac{1}{s}(0.5 - C_1)E_1\left(\frac{sr_D^2}{2}\right) - \frac{2C_1}{s}e^{-\frac{sr_D^2}{2}}\ln(r_D) - \frac{2C_1}{s}\left[\gamma + \ln\left(\frac{\sqrt{C_2}}{2}\right) + \frac{1}{2}\ln s\right]e^{-\frac{sr_D^2}{2}} \tag{A.9}$$

The analytical solution for Equation A.1 is:

$$\overline{T_D} = \frac{1}{s}\left(C_1 - 0.5\right)e^{\frac{sr_D^2}{2}}E_1\left(\frac{sr_D^2}{2}\right) + \frac{2C_1}{s}\left[\gamma + \ln\left(\frac{\sqrt{C_2}}{2}\right) + \frac{1}{2}\ln s\right] + \frac{2C_1}{s}\ln\left(r_D\right) \tag{A.10}$$

Equation A.10 is the analytical solution in the Laplace domain. To invert it back to the time domain, several Laplace transform identities are adopted here:

$$L^{-1}\left\{\exp\left(-as\right)E_1\left(-as\right)\right\} = \frac{1}{t_D - a} \tag{A.11}$$

$$L^{-1}\left\{\frac{f\left(s\right)}{s}\right\} = \int_0^{t_D} F\left(u\right)du \tag{A.12}$$

$$L^{-1}\left\{\frac{\ln s}{s}\right\} = -\left(\ln t_D + \gamma\right) \tag{A.13}$$

Therefore, the solution in the time domain is:

$$T_D = -0.5\ln\left(1 + \frac{2t_D}{r_D^2}\right) + C_1\ln\left(1 + \frac{2t_D}{r_D^2}\right) + C_1\left[\gamma + 2\ln\left(r_D\right) + 2\ln\left(\frac{\sqrt{C_2}}{2}\right) - \ln t_D\right] \tag{A.14}$$

Appendix B. Analytical Solution Derivation for Single Layer Near Wellbore Damaged Reservoir under Transient Flow

Apply the Laplace transform, the Equations 3.23-3.25 become:

$$s\overline{T_D} = \frac{1}{r_D}\left[\frac{\partial \overline{T_D}}{\partial r_D} - \frac{k_{sD}}{sr_D}\right] - 2C_1 K_0\left(\sqrt{sC_4}\right) \tag{B.1}$$

$$\overline{T_D} = \overline{T}_{sD}, r_D = r_{sD} \tag{B.2}$$

Following the same procedures provided by Equations A.3 and A.4, the derivations to arrive the solution for Equation B.1 are:

$$\overline{T_D} e^{\int -sr_D dr_D}\Big|_{r_D}^{r_{sD}} = \int_{r_D}^{r_{sD}} e^{\int -sr_D dr_D}\left[\frac{k_{sD}}{sr_D} + 2C_1 r_D K_0\left(\sqrt{sC_4}\right)\right] dr_D \tag{B.3}$$

Assuming the production time is sufficiently long (Appendix A), based on final value theorem, the late time asymptotic solution is:

$$-\overline{T_D} e^{-\frac{sr_D^2}{2}} = \int_{r_D}^{r_{sD}} e^{-\frac{sr_D^2}{2}} \frac{k_{sD}}{sr_D} dr_D + \int_{r_D}^{r_{sD}} e^{-\frac{sr_D^2}{2}} 2C_1 r_D\left[-\gamma - \ln\left(\frac{\sqrt{sC_4}}{2}\right)\right] dr_D - \overline{T}_{sD} e^{-\frac{sr_{rD}^2}{2}} \tag{B.4}$$

The analytical solution for Equation B.1 is:

$$\overline{T_D} = \frac{k_{sD}}{2s}\left[E_1\left(\frac{sr_{sD}^2}{2}\right) - E_1\left(\frac{sr_D^2}{2}\right)\right] e^{\frac{sr_D^2}{2}} + \overline{T}_{sD} e^{-\frac{sr_{sD}^2}{2}+\frac{sr_D^2}{2}} - \frac{2C_1}{s}\left[\gamma + \ln\left(\frac{\sqrt{sC_4}}{2}\right)\right]\left(e^{-\frac{sr_{sD}^2}{2}+\frac{sr_D^2}{2}} - 1\right) \tag{B.5}$$

Equation B.5 is the analytical solution in the Laplace domain. To invert it back to the time domain, several Laplace transform identities are applied here including Equations A.11 to A.13:

$$L^{-1}\left\{\frac{e^{-as}}{s}\right\} = U'(t_D - a) \tag{B.8}$$

$$L^{-1}\left\{\exp(-as)\, f(s)\right\} = F(t_D - a) U'(t_D - a) \tag{B.9}$$

Therefore, the solution in the time domain is:

$$\begin{aligned} T_D = & -\frac{k_{sD}}{2}\ln\left(1 + \frac{2t_D}{r_D^2}\right) - C_1\left[\gamma - \ln(t_D) + \ln\left(\frac{C_4}{4}\right)\right] \\ & + T_{sD}\left(t_D + \frac{r_D^2 - r_{sD}^2}{2}\right) U'\left(t_D + \frac{r_D^2 - r_{sD}^2}{2}\right) \\ & - C_1\left[\frac{k_{sD}}{2}\ln\left(\frac{r_D^2 + 2t_D}{r_{sD}^2}\right) + \gamma + \ln\left(\frac{C_4}{4}\right) - \ln\left(t_D + \frac{r_D^2 - r_{sD}^2}{2}\right)\right] U'\left(t_D + \frac{r_D^2 - r_{sD}^2}{2}\right) \end{aligned} \tag{B.10}$$

Appendix C. Analytical Solution Derivation for Single Layer Reservoir with near Wellbore Non-Darcy Effect under Transient Flow

Applying the Laplace transform, the Equations 3.32-3.34 become:

$$s\overline{T_D} = \frac{1}{r_D}\left[\frac{\partial \overline{T_D}}{\partial r_D} - \frac{1}{sr_D} - \frac{Fo}{sr_D^2}\right] - 2C_1 K_0\left(r_D\sqrt{sC_2}\right) \tag{C.1}$$

$$\overline{T_D} = 0, r_D \to \infty \tag{C.2}$$

Following the same procedures provided by Equations A.3 and A.4, the derivations to arrive the solution for Equation C.1 are:

$$-\overline{T_D}e^{-\frac{sr_D^2}{2}} = \int_{r_D}^{\infty} e^{-\frac{sr_D^2}{2}}\left(\frac{1}{sr_D}\right)dr_D + \int_{r_D}^{\infty} e^{-\frac{sr_D^2}{2}}\left(\frac{Fo}{sr_D^2}\right)dr_D + \int_{r_D}^{\infty} e^{-\frac{sr_D^2}{2}} 2C_1 r_D K_0\left(r_D\sqrt{sC_2}\right)dr_D \tag{C.3}$$

Assuming the production time is sufficiently long, based on final value theorem (Appendix A), the late time asymptotic solution is:

$$\begin{aligned} -\overline{T_D}e^{-\frac{sr_D^2}{2}} &= \frac{1}{2s}\int_{\frac{sr_D^2}{2}}^{\infty} e^{-\frac{sr_D^2}{2}}\left(\frac{2}{sr_D^2}\right)d\left(\frac{sr_D^2}{2}\right) - \frac{Fo}{sr_D}e^{-\frac{sr_D^2}{2}}\Big|_{r_D}^{\infty} - \int_{r_D}^{\infty} e^{-\frac{sr_D^2}{2}}\left(-sr_D\right)\left(-\frac{Fo}{sr_D}\right)dr_D \\ &+ \int_{r_D}^{\infty} e^{-\frac{sr_D^2}{2}} 2C_1 r_D\left[-\gamma - \ln\left(\frac{r_D\sqrt{sC_2}}{2}\right)\right]dr_D \end{aligned} \tag{C.4}$$

The RHS of Equation C.4 can be solved by the method of integration by part. And the analytical solution for Equation C.1 is:

$$\begin{aligned} \overline{T_D} &= \frac{1}{s}\left(C_1 - 0.5\right)e^{\frac{sr_D^2}{2}}E_1\left(\frac{sr_D^2}{2}\right) - \frac{Fo}{sr_D} + Fo\sqrt{\frac{\pi}{2s}}e^{\frac{sr_D^2}{2}}erfc\left(\sqrt{\frac{s}{2}}r_D\right) \\ &+ \frac{2C_1}{s}\left[\gamma + \ln\left(\frac{\sqrt{C_2}}{2}\right) + \frac{1}{2}\ln s\right] + \frac{2C_1}{s}\ln\left(r_D\right) \end{aligned} \tag{C.5}$$

Equation C.5 is the analytical solution in the Laplace domain. To invert it back to the time domain, Equations A.11-A.13 and the below Laplace transform identity are used:

$$L^{-1}\left\{\sqrt{\frac{1}{s}}e^{as}erfc\left(\sqrt{as}\right)\right\} = \frac{1}{\sqrt{\pi\left(t_D + a\right)}} \tag{C.6}$$

Therefore, the solution in the time domain is:

$$\begin{aligned} T_D &= -0.5\ln\left(1 + \frac{2t_D}{r_D^2}\right) + C_1\ln\left(1 + \frac{2t_D}{r_D^2}\right) - Fo\left(\frac{1}{r_D} - \frac{1}{\sqrt{2t_D + r_D^2}}\right) \\ &+ C_1\left[\gamma + 2\ln\left(r_D\right) + 2\ln\left(\frac{\sqrt{C_2}}{2}\right) - \ln t_D\right] \end{aligned} \tag{C.7}$$

Appendix D. Analytical Solution Derivation for Single Layer Reservoir under Boundary Dominated Flow

Applying the Laplace transform, the Equations 3.45-3.47 become:

$$s\overline{T_D} = \frac{1}{r_D}\frac{\partial \overline{T_D}}{\partial r_D} + \frac{1}{sr_D^2} + \frac{C_3}{s} \tag{D.1}$$

$$\overline{T_D} = \frac{C_3}{s^2}, r_D = r_{eD} \tag{D.2}$$

Following the same procedures provided by Equations A.3 and A.4, the derivations to arrive the solution for Equation D.1 are:

$$\frac{d}{dr_D}\left(\overline{T_D}e^{-\frac{sr_D^2}{2}}\right) = -e^{-\frac{sr_D^2}{2}}\left(\frac{1}{sr_D} + \frac{C_3 r_D}{s}\right) \tag{D.3}$$

$$\frac{C_3}{s^2}e^{-\frac{sr_{eD}^2}{2}} - \overline{T_D}e^{-\frac{sr_D^2}{2}} = -\int_{r_D}^{r_{eD}} e^{-\frac{sr_D^2}{2}}\left(\frac{1}{sr_D} + \frac{C_3 r_D}{s}\right)dr_D \tag{D.4}$$

$$\frac{C_3}{s^2}e^{-\frac{sr_{eD}^2}{2}} - \overline{T_D}e^{-\frac{sr_D^2}{2}} = \frac{C_3}{s^2}\int_{r_D}^{r_{eD}} e^{-\frac{sr_D^2}{2}} d\left(-\frac{sr_D^2}{2}\right) - \frac{1}{2s}\int_{r_D}^{r_{eD}} e^{-\frac{sr_D^2}{2}}\frac{2}{sr_D^2}d\left(\frac{sr_D^2}{2}\right) \tag{D.5}$$

The last term represents the slow propagating JT effect. Therefore, it is safe to assume the outer boundary is infinite far from the wellbore for JT effect:

$$\frac{C_3}{s^2}e^{-\frac{sr_{eD}^2}{2}} - \overline{T_D}e^{-\frac{sr_D^2}{2}} = \frac{C_3}{s^2}\left(e^{-\frac{sr_{eD}^2}{2}} - e^{-\frac{sr_D^2}{2}}\right) - \frac{1}{2s}E_1\left(\frac{sr_D^2}{2}\right) \tag{D.6}$$

$$\overline{T_D} = \frac{1}{2s}e^{\frac{sr_D^2}{2}}E_1\left(\frac{sr_D^2}{2}\right) + \frac{C_3}{s^2} \tag{D.7}$$

Equation D.7 is the analytical solution in the Laplace domain. To invert it back to the time domain, Equations A.11 and A.12 and the below Laplace transform identity are used:

$$L^{-1}\left\{\frac{1}{s^2}\right\} = t_D \tag{D.8}$$

Therefore, the solution in the time domain is:

$$T_D = 0.5\ln\left(1 + \frac{2t_D}{r_D^2}\right) + C_3 t_D \tag{D.9}$$

Appendix E. Analytical Solution Derivation for Single Layer Reservoir with Constant Pressure Production under Boundary Dominated Flow

Assuming a curve *C(x, s)* as an integral curve for the vector field perpendicular to the solution plane of Equation 5.27, we can obtain the set of characteristic equations for Equation 5.27:

$$\begin{aligned}\frac{dt_D}{ds} &= C_1 \\ \frac{dr_D}{ds} &= -\frac{\exp\left(-t_D\right)}{r_D} \\ \frac{dT_D}{ds} &= -\frac{\exp\left(-2t_D\right)}{r_D^2}\end{aligned} \tag{E.1}$$

From the initial condition (Equation 5.28), the integral curve becomes:

$$t_D\left(x,0\right)=0; r_D\left(x,0\right)=x; T_D\left(x,0\right)=0 \tag{E.2}$$

Each of the characteristic equation (Equation E.1) can be solved by integration with the initial condition of Equation E.2:

$$\begin{aligned}\int dt_D &= \int C_1 ds \\ \int r_D dr_D &= -\int \exp\left(-t_D\right) ds \\ \int dT_D &= -\int \frac{\exp\left(-2t_D\right)}{r_D^2} ds\end{aligned} \tag{E.3}$$

$$\begin{aligned}t_D &= C_1 s \\ r_D^2 &= x^2 + \frac{\exp\left(-C_1 s\right)-1}{C_1} \\ T_D &= \frac{\exp\left(-C_1 s\right)-1}{2} + \frac{C_1 x^2 - 2}{4}\ln\left[\frac{C_1 x^2}{C_1 x^2 - 2 + 2\exp\left(-C_1 s\right)}\right]\end{aligned} \tag{E.4}$$

Therefore, the integral curve can be determined with t_D and r_D:

$$\begin{aligned}s &= \frac{t_D}{C_1} \\ x^2 &= r_D^2 - \frac{\exp\left(-t_D\right)-1}{C_1}\end{aligned} \tag{E.5}$$

Introducing Equation E.5 to last equation in Equation E.4, we arrived the final analytical solution for constant pressure production during BDF period:

$$T_D = \frac{\exp\left(-t_D\right)-1}{2} + \frac{C_1 r_D^2 - 2\exp\left(-t_D\right)}{4}\ln\left[\frac{C_1 r_D^2 + 2 - 2\exp\left(-t_D\right)}{C_1 r_D^2}\right] \tag{E.6}$$

Appendix F. Analytical Solution Derivation for Wellbore Fluid Temperature During Flow-back Period Associated with After-flow

Assuming a curve *C(r, s)* as an integral curve for the vector field perpendicular to the solution plane of Equation 6.4, we can obtain the set of characteristic equations for Equation 6.4:

$$\begin{aligned}\frac{dt}{ds} &= 1 + C_T \\ \frac{dx}{ds} &= v \\ \frac{dT_f}{ds} &= vL_R\left[T_{ei}(x) - T_f\right]\end{aligned} \tag{F.1}$$

From the initial condition (Equation 6.5), the integral curve becomes:

$$t(r,0) = 0; x(r,0) = r; T_f(r,0) = T_p \tag{F.2}$$

Each of the characteristic equation (Equation F.1) can be solved by integration with the initial condition of Equation F.2:

$$\begin{aligned}\int dt &= \int (1 + C_T)\, ds \\ \int dx &= \int v ds \\ \int dT_f &= \int vL_R\left[T_{ei}(x) - T_f\right] ds\end{aligned} \tag{F.3}$$

$$\begin{aligned}t &= (1 + C_T)\, s \\ x &= vs + r \\ T_f &= T_i + (T_p - T_i)\exp(-vL_R s) \\ &+ \frac{aL_R(T_{\text{inflow}} - T_i)}{aL_R + 1}\left[\exp\left(\frac{vs + r - L}{a}\right) - \exp\left(-vL_R s + \frac{r - L}{a}\right)\right]\end{aligned} \tag{F.4}$$

Therefore, the integral curve can be determined with *t* and *x*:

$$\begin{aligned}s &= \frac{t}{1 + C_T} \\ r &= x - \frac{vt}{1 + C_T}\end{aligned} \tag{F.5}$$

Introducing Equation F.5 to last equation in Equation F.4, we arrived the final analytical solution for wellbore fluid temperature during flow-back period associated with after-flow:

$$\begin{aligned}T_f &= T_i + (T_p - T_i)\exp\left(-\frac{vL_R t}{1 + C_T}\right) \\ &+ \frac{aL_R(T_{\text{inflow}} - T_i)}{aL_R + 1}\exp\left(\frac{x - L}{a}\right)\left[1 - \exp\left(-\frac{vL_R t}{1 + C_T} - \frac{vt}{(1 + C_T)a}\right)\right]\end{aligned} \tag{F.6}$$

Reference List

Abramowitz, Milton, Stegun, Irene A. 1964. *Handbook of mathematical functions*, Vol. 55, Courier Corporation.

Agarwal, R. G., Gardner, D. C., Kleinsteiber, S. W. et al. 1999. Analyzing well production data using combined-type-curve and decline-curve analysis concepts. *Spe Reservoir Evaluation & Engineering* **2** (5): 478-486. 10.2118/57916-Pa.

Alves, I. N., Alhanati, F. J. S., Shoham, Ovadia. 1992. A Unified Model for Predicting Flowing Temperature Distribution in Wellbores and Pipelines. 10.2118/20632-PA.

App, J. 2017. Permeability, Skin, and Inflow-Profile Estimation From Production-Logging-Tool Temperature Traces. *Spe Journal* **22** (4): 1123-1133. Doi 10.2118/174910-Pa.

App, J. F. 2010. Nonisothermal and Productivity Behavior of High-Pressure Reservoirs. *Spe Journal* **15** (1): 50-63. SPE-114705-PA. 10.2118/114705-PA.

App, J. F., Yoshioka, K. 2013. Impact of Reservoir Permeability on Flowing Sandface Temperatures: Dimensionless Analysis. *Spe Journal* **18** (4): 685-694. SPE-146951-PA. 10.2118/146951-PA.

App, Jeffrey F. 2009. Field Cases: Nonisothermal Behavior Due to Joule-Thomson and Transient Fluid Expansion/Compression Effects. Proc., SPE-124338-MS, http://dx.doi.org/10.2118/124338-MS.

App, Jeffrey F. 2016. Influence of Flow Geometry on Sandface Temperatures During Single-Phase Oil Production: Dimensionless Analysis. *SPE Journal* **21** (03): 0928-0937. 10.2118/166298-pa.

Askari, R., Taheri, S., Hejazi, S. H. 2015. Thermal conductivity of granular porous media: A pore scale modeling approach. *Aip Advances* **5** (9): 097106. 10.1063/1.4930258.

Atkinson, P. G., Ramey, H. J., Jr. 1977. Problems Of Heat Transfer In Porous Media. Proc., SPE-6792-MS, http://dx.doi.org/10.2118/6792-MS.

Bachu, Stefan. 2003. Screening and ranking of sedimentary basins for sequestration of CO2 in geological media in response to climate change. *Environmental Geology* **44** (3): 277-289.

Bello, Rasheed Olusehun, Wattenbarger, Robert A. 2010. Multi-stage Hydraulically Fractured Horizontal Shale Gas Well Rate Transient Analysis. Proc., North Africa Technical Conference and Exhibition, Cairo, Egypt, 10.2118/126754-MS.

Blasingame, T. A., Lee, W. J. 1986. Variable-Rate Reservoir Limits Testing. Proc., 10.2118/15028-MS.

Blasingame, T. A., McCray, T. L., Lee, W. J. 1991. Decline Curve Analysis for Variable Pressure Drop/Variable Flowrate Systems. Proc., SPE Gas Technology Symposium, Houston, Texas, 10.2118/21513-MS.

Blaskovich, F. T., Cain, G. M., Sonier, Fernand et al. 1983. A Multicomponent Isothermal System for Efficient Reservoir Simulation. Proc., 10.2118/11480-MS.

Bostick, F. X., III. 2003. Commercialization of Fiber Optic Sensors for Reservoir Monitoring. Proc., OTC-15320-MS, http://dx.doi.org/10.4043/15320-MS.

Bourdet, D. 1985. Pressure Behavior of Layered Reservoirs With Crossflow. Proc., 10.2118/13628-MS.

Bourdet, Dominique, Ayoub, J. A., Pirard, Y. M. 1989. Use of Pressure Derivative in Well Test Interpretation. *SPE Formation Evaluation* **4** (02): 293-302. 10.2118/12777-pa.

Buckley, S. E., Leverett, M. C. 1942. Mechanism of fluid displacement in sands. *Transactions of the American Institute of Mining and Metallurgical Engineers* **146**: 107-116. http://dx.doi.org/10.2118/942107-G.

Cameron, D. A., Durlofsky, L. J., Benson, S. M. 2016. Use of above-zone pressure data to locate and quantify leaks during carbon storage operations. *International Journal of Greenhouse Gas Control* **52**: 32-43. 10.1016/j.ijggc.2016.06.014.

Chekalyuk, EB. 1965. *Thermodynamics of oil formation*, Vol. 1: Nedra, Moscow.

Cheng-Tai, Gao, Deans, H. A. 1983. *Single-Phase Flow In A Two-Layer Reservoir With Significant Crossflow - Pressure Drawdown And Buildup Behavior When Both Layers Are Completed At A Single Well*, Society of Petroleum Engineers.

Chevarunotai, N., Hasan, A. R., Kabir, C. S. 2015. Transient Flowing-Fluid Temperature Modeling in Oil Reservoirs for Flow Associated with Large Drawdowns. Proc., 10.2118/175008-MS.

Choi, E. S., Cheema, T., Islam, M. R. 1997. A new dual-porosity/dual-permeability model with non-Darcian flow through fractures. *Journal of Petroleum Science and Engineering* **17** (3-4): 331-344. Doi 10.1016/S0920-4105(96)00050-2.

Cicek, O. 2003. Compositional and Non-Isothermal Simulation of CO2 Sequestration in Naturally Fractured Reservoirs/Coalbeds: Development and Verification of the Model. Proc., 10.2118/84341-MS.

GEM - Compositional and Unconventional Oil and Gas Simulator, version 2015.10 2015. Calgary, Alberta, Canada, Computer Modelling Group Ltd.

STARS - Thermal & Advanced Processes Simulator, version 2015.10 2015. Calgary, Alberta, Canada, Computer Modelling Group Ltd.

WINPROP - Phase-behavior & fluid property program, version 2015.10 2015. Calgary, Alberta, Canada, Computer Modelling Group Ltd.

COMSOL, AB. 2015. COMSOL Multiphysics Ver. 5.0. *http://www.comsol.se*.

Corey, Arthur T. 1954. The interrelation between gas and oil relative permeabilities. *Producers monthly* **19** (1): 38-41.

Crafton, James W. 2008. Modeling Flowback Behavior or Flowback Equals "Slowback". Proc., SPE Shale Gas Production Conference, Fort Worth, Texas, USA, 10.2118/119894-MS.

Cui, J. Y., Yang, C. D., Zhu, D. et al. 2016. Fracture Diagnosis in Multiple-Stage-Stimulated Horizontal Well by Temperature Measurements With Fast Marching Method. *Spe Journal* **21** (6): 2289-2300. Doi 10.2118/174880-Pa.

Cui, Jingyuan, Zhu, Ding, Jin, Minquan. 2015. Diagnosis of Production Performance After Multistage Fracture Stimulation in Horizontal Wells by Downhole Temperature Measurements. *SPE Production & Operations*. 10.2118/170874-pa.

Denney, D. 2015. Manage Fields With Intelligent Surveillance, Production Optimization, and Collaboration. *Journal of Petroleum Technology* **64** (12): 98-100. SPE-1212-0098-JPT. http://dx.doi.org/10.2118/1212-0098-jpt.

Duru, O. O. 2011. Reservoir Analysis and Parameter Estimation Constrained to Temperature, Pressure and Flowrate Histories. PhD, Stanford University.

Duru, O. O., Horne, R. N. 2010a. Modeling Reservoir Temperature Transients and Reservoir-Parameter Estimation Constrained to the Model. *SPE Res Eval & Eng* **13** (6): 873-883. SPE-115791-PA. http://dx.doi.org/10.2118/115791-PA.

Duru, O. O., Horne, R. N. 2011a. Simultaneous Interpretation of Pressure, Temperature, and Flow-Rate Data Using Bayesian Inversion Methods. *SPE Res Eval & Eng* **14** (2): 225-238. SPE-124827-PA. http://dx.doi.org/10.2118/124827-PA.

Duru, Obinna Onyinye, Horne, Roland N. 2010b. Joint Inversion of Temperature and Pressure Measurements for Estimation of Permeability and Porosity Fields. Proc., 10.2118/134290-MS.

Duru, Obinna Onyinye, Horne, Roland N. 2011b. Combined Temperature and Pressure Data Interpretation: Applications to Characterization of Near-Wellbore Reservoir Structures. Proc., SPE-146614-MS, http://dx.doi.org/10.2118/146614-MS.

Dykstra, Herman, Parsons, RL. 1950. The prediction of oil recovery by waterflood. *Secondary recovery of oil in the United States* **2**: 160-174.

Ebigbo, A., Class, H., Helmig, R. 2007. CO2 leakage through an abandoned well: problem-oriented benchmarks. *Computational Geosciences* **11** (2): 103-115. 10.1007/s10596-006-9033-7.

Edwardson, M. J., Girner, H. M., Parkison, H. R. et al. 1962. Calculation of Formation Temperature Disturbances Caused by Mud Circulation. *Transactions of the Society of Petroleum Engineers of Aime* **225** (4): 416-426. http://dx.doi.org/10.2118/124-PA.

Ehlig-Economides, Christine A., Joseph, Jeffrey. 1987. A New Test for Determination of Individual Layer Properties in a Multilayered Reservoir. *SPE Formation Evaluation* **2** (03): 261-283. 10.2118/14167-pa.

Ennis-King, J, Paterson, L. Reservoir engineering issues in the geological disposal of carbon dioxide. Vol. 1, 290-295.

Evans, James P, Heath, Jason, Shipton, Zoe K et al. Natural leaking CO2-charged systems as analogs for geologic sequestration sites. *Alexandria, VA*.

Fenghour, A., Wakeham, W. A., Vesovic, V. 1998. The viscosity of carbon dioxide. *Journal of Physical and Chemical Reference Data* **27** (1): 31-44.

Fetkovich, M. J. 1980. Decline Curve Analysis Using Type Curves. *Journal of Petroleum Technology* **32** (6): 1065-1077. 10.2118/4629-Pa.

Forchheimer, P. 1901. Wasserbewegung durch boden. *Zeit. Ver. Deutsch. Ing.* **45**: 1781–1788.

Francis, P. G., McGlashan, M. L., Wormald, C. J. 1969. A vapour-flow calorimeter fitted with an adjustable throttle. The isothermal Joule-Thomson coefficient of benzene. The temperture-dependence of the second virial coefficient of benzene. *The Journal of Chemical Thermodynamics* **1** (5): 441-458. 10.1016/0021-9614(69)90003-2.

Gasda, Sarah E, Celia, Michael A, Wang, James Z et al. 2013. Wellbore permeability estimates from vertical interference testing of existing wells. *Energy Procedia* **37**: 5673-5680.

Gass, TE, Lehr, JH, Heiss, HW. 1977. Impact of abandoned wells on groundwater. *EPA-600/3-77-095*.

Glasbergen, G., Gualtieri, D., van Domelen, M. et al. 2009. Real-Time Fluid Distribution Determination in Matrix Treatments Using DTS. *Spe Production & Operations* **24** (1): 135-146. SPE-107775-PA. http://dx.doi.org/10.2118/107775-PA.

Gysen, Alain, Gysen, Michel, Zett, Adrian et al. 2010. Production Logging in Highly Deviated and Horizontal Wells: Moving From Qualitative to Quantitative Answers. Proc., SPE Annual Technical Conference and Exhibition, Florence, Italy, 10.2118/133479-MS.

Hannah, Robert R., Harrington, Larry J., Anderson, Robert W. 1977. Stimulation Design Applications Of A Technique To Locate Successive Fluid Segments In Fractures. Proc., 10.2118/6815-MS.

Harrington, Larry J., Hannah, Robert R., Robert, Beirute. 1978. Post Fracturing Temperature Recovery And Its Implication For Stimulation Design. Proc., 10.2118/7560-MS.

Hasan, A. R., Kabir, C. S. 1991. Heat Transfer During Two-Phase Flow in Wellbores; Part I--Formation Temperature. Proc., 10.2118/22866-MS.

Hasan, A. R., Kabir, C. S., Lin, D. 2005. Analytic wellbore-temperature model for transient gas-well testing. *Spe Reservoir Evaluation & Engineering* **8** (3): 240-247. Doi 10.2118/84288-Pa.

Hasan, A. R., Kabir, C. S., Wang, Xiaowei. 2013. Wellbore Two-Phase Flow and Heat Transfer During Transient Testing. *SPE Journal* **3** (02): 174-180. 10.2118/38946-pa.

Heller, J. P., Taber, J. J. 1986. Influence of Reservoir Depth on Enhanced Oil Recovery by CO2 Flooding. Proc., 10.2118/15001-MS.

Hill, A. C., Thomas, G. W. 1985. A New Approach for Simulating Complex Fractured Reservoirs. Proc., 10.2118/13537-MS.

Huckabee, Paul Thomas. 2009. Optic Fiber Distributed Temperature for Fracture Stimulation Diagnostics and Well Performance Evaluation. Proc., 10.2118/118831-MS.

Hurst, W. 1934. Unsteady flow of fluids in oil reservoirs. *Physics-a Journal of General and Applied Physics* **5** (1): 20-30. Doi 10.1063/1.1745206.

IPCC. 2005. Intergovernmental Panel on Climate Change, Special Report on Carbon Dioxide Capture and Storage.

Izgec, B., Cribbs, M. E., Pace, S. V. et al. 2009. Placement of Permanent Downhole-Pressure Sensors in Reservoir Surveillance. *Spe Production & Operations* **24** (1): 87-95. Doi 10.2118/107268-Pa.

Jung, Y. J., Zhou, Q. L., Birkholzer, J. T. 2013. Early detection of brine and CO2 leakage through abandoned wells using pressure and surface-deformation monitoring data: Concept and demonstration. *Advances in Water Resources* **62**: 555-569. 10.1016/j.advwatres.2013.06.008.

Kabir, C. S., Hasan, A. R., Kouba, G. E. et al. 1996. Determining circulating fluid temperature in drilling, workover, and well-control operations. *Spe Drilling & Completion* **11** (2): 74-79. 10.2118/24581-PA.

Kabir, C. S., Hasan, A. R., Lin, D. et al. 2002. Heat-transfer models for mitigating wellbore solids deposition. *Spe Journal* **7** (4): 391-399. 10.2118/81368-PA.

RUBIS - Multi Purpose Numerical Model, version 5.12.02 2015. Houston, TX, USA, KAPPA Engineering.

Kazemi, H., Merrill, L. S., Jr., Porterfield, K. L. et al. 1979. Numerical Simulation of Water-Oil Flow in Naturally Fractured Reservoirs. 10.2118/5719-PA.

King, George Everette, Valencia, Randy L. 2014. Environmental Risk and Well Integrity of Plugged and Abandoned Wells. Proc., 10.2118/170949-MS.

Kutasov, I. M. 2003. Dimensionless temperature at the wall of an infinite long cylindrical source with a constant heat flow rate. *Geothermics* **32** (1): 63-68. 10.1016/S0375-6505(02)00045-7.

LaForce, T., Ennis-King, J., Paterson, L. 2014. Semi-analytical solutions for nonisothermal fluid injection including heat loss from the reservoir: Part 1. Saturation and temperature. *Advances in Water Resources* **73**: 227-241. http://dx.doi.org/10.1016/j.advwatres.2014.08.008.

Lee, John. 1982. *Well testing*. Richardson, TX: SPE textbook series, Society of Petroleum Engineers.

Lefkovits, H. C., Hazebroek, P., Allen, E. E. et al. 1961. A Study of the Behavior of Bounded Reservoirs Composed of Stratified Layers. *Society of Petroleum Engineers Journal* **1** (01): 43-58. 10.2118/1329-g.

Li, Dacun, Engler, Thomas W. 2001. Literature Review on Correlations of the Non-Darcy Coefficient. Proc., 10.2118/70015-MS.

Li, Y. R., Cheng, B. K., Zhu, W. G. et al. 2017. Development and evaluation of the coaxial cable casing imager: a cost-effective solution to real-time downhole monitoring for CO2 sequestration wellbore integrity. *Greenhouse Gases-Science and Technology* **7** (5): 927-941. 10.1002/ghg.1691.

Linstrom, P.J. , Mallard, W.G. 2008. *NIST Chemistry WebBook, NIST Standard Reference Database Number 69,*. Gaithersburg MD,, National Institute of Standards and Technology,.

Lu, C. H., Sun, Y. W., Buscheck, T. A. et al. 2012. Uncertainty quantification of CO2 leakage through a fault with multiphase and nonisothermal effects. *Greenhouse Gases Sci Technol* **2** (6): 445-459. 10.1002/ghg.1309.

Mao, Y., Zeidouni, M., Askari, R. 2017. Effect of leakage pathway flow properties on thermal signal associated with the leakage from CO2 storage zone. *Greenhouse Gases-Science and Technology* **7** (3): 512-529. 10.1002/ghg.1658.

Marquardt, D. W. 1963. An Algorithm for Least-Squares Estimation of Nonlinear Parameters. *Journal of the Society for Industrial and Applied Mathematics* **11** (2): 431-441. http://dx.doi.org/10.1137/0111030.

Mathias, S. A., Gluyas, J. G., Oldenburg, C. M. et al. 2010. Analytical solution for Joule–Thomson cooling during CO2 geo-sequestration in depleted oil and gas reservoirs. *International Journal of Greenhouse Gas Control* **4** (5): 806-810. 10.1016/j.ijggc.2010.05.008.

Mathias, S. A., McElwaine, J. N., Gluyas, J. G. 2014. Heat transport and pressure buildup during carbon dioxide injection into depleted gas reservoirs. *Journal of Fluid Mechanics* **756**: 89-109. http://dx.doi.org/10.1017/jfm.2014.348.

Mattar, L., Anderson, D. M. 2003. A Systematic and Comprehensive Methodology for Advanced Analysis of Production Data. Proc., 10.2118/84472-MS.

Mattar, L., Anderson, D., Stotts, G. 2006. Dynamic material balance - oil- or gas-in-place without shut-ins. *Journal of Canadian Petroleum Technology* **45** (11): 7-10. 10.2118/06-11-TN.

Maxwell, S. C., Rutledge, J., Jones, R. et al. 2010. Petroleum reservoir characterization using downhole microseismic monitoring. *Geophysics* **75** (5): A129-A137. 10.1190/1.3477966.

Meyer, B. R. 1989. Heat Transfer in Hydraulic Fracturing. *SPE Prod Eng* **4** (04): 423-429. SPE-17041-PA. http://dx.doi.org/10.2118/17041-pa.

Mosaheb, M., Zeidouni, M. 2018. Above zone pressure interpretation for leaky well characterization and its identification from leaky caprock/fault. *Journal of Petroleum Science and Engineering* **171**: 218-228. 10.1016/j.petrol.2018.07.035.

Mosaheb, Mojtaba, Zeidouni, Mehdi. 2017a. Above-Zone Pressure Response to Distinguish Between Fault and Caprock Leakage. Proc., 10.2118/185698-MS.

Mosaheb, Mojtaba, Zeidouni, Mehdi. 2017b. Pressure Transient Analysis for Characterization of Lateral and Vertical Leakage through Faults. Proc., Carbon Management Technology Conference, Houston, Texas, USA, 10.7122/502924-MS.

Mosaheb, Mojtaba, Zeidouni, Mehdi. 2017c. Pressure Transient Analysis for Leaky Well Characterization and Its Identification from Leaky Fault. Proc., 10.2118/184440-MS.

Mosaheb, Mojtaba, Zeidouni, Mehdi, Shakiba, Mahmood. 2018. Pressure Pulse Testing Method for Caprock Characterization. Proc., SPE Annual Technical Conference and Exhibition, Dallas, Texas, USA, 10.2118/191524-MS.

Muradov, K., Davies, D. 2012a. Early-time Asymptotic, Analytical Temperature Solution for Linear Non-adiabatic Flow of a Slightly Compressible Fluid in a Porous Layer. *Transport in Porous Media* **91** (3): 791-811. 10.1007/s11242-011-9873-z.

Muradov, K., Davies, D. 2012b. Temperature transient analysis in horizontal wells: Application workflow, problems and advantages. *Journal of Petroleum Science and Engineering* **92-93**: 11-23. 10.1016/j.petrol.2012.06.012.

Muradov, K. M., Davies, D. R. 2011. Novel Analytical Methods of Temperature Interpretation in Horizontal Wells. *SPE J.* **16** (3): 637-647. SPE-131642-PA. http://dx.doi.org/10.2118/131642-PA.

Nield, D. A., Bejan, A. 2013. *Convection in porous media*, 4th edition. New York Springer.

Nobakht, M., Clarkson, C. R., Kaviani, D. 2012. New and Improved Methods for Performing Rate-Transient Analysis of Shale Gas Reservoirs. *Spe Reservoir Evaluation & Engineering* **15** (3): 335-350. Doi 10.2118/147869-Pa.

Nojabaei, B., Hasan, A. R., Kabir, C. S. 2014. Modelling Wellbore Transient Fluid Temperature and Pressure During Diagnostic Fracture-Injection Testing in Unconventional Reservoirs. *Journal of Canadian Petroleum Technology* **53** (3): 161-167. Doi 10.2118/166120-Pa.

Nordbotten, J. M., Celia, M. A., Bachu, S. et al. 2005. Semianalytical solution for CO2 leakage through an abandoned well. *Environmental Science & Technology* **39** (2): 602-611. DOI 10.1021/es035338i.

Nordbotten, Jan Martin, Celia, Michael A., Bachu, Stefan. 2004. Analytical solutions for leakage rates through abandoned wells. *Water Resour. Res.* **40**.

Nygaard, R., Salehi, S., Weideman, B. et al. 2014. Effect of Dynamic Loading on Wellbore Leakage for the Wabamun Area CO2-Sequestration Project. *Journal of Canadian Petroleum Technology* **53** (1). 10.2118/146640-PA.

Oldenburg, Curtis M. 2007. Joule-Thomson cooling due to CO2 injection into natural gas reservoirs. *Energy Conversion and Management* **48** (6): 1808-1815. http://dx.doi.org/10.1016/j.enconman.2007.01.010.

Onur, M., Cinar, M. 2017a. Analysis of Sandface-Temperature-Transient Data for Slightly Compressible, Single-Phase Reservoirs. *Spe Journal* **22** (4): 1134-1155. Doi 10.2118/180074-Pa.

Onur, Mustafa, Cinar, Murat. 2017b. Modeling and Analysis of Temperature Transient Sandface and Wellbore Temperature Data from Variable Rate Well Test Data. Proc., 10.2118/185802-MS.

Onur, Mustafa, Çinar, Murat. 2016. Temperature Transient Analysis of Slightly Compressible, Single-Phase Reservoirs. Proc., 10.2118/180074-MS.

Palabiyik, Y., Onur, M., Tureyen, O. I. et al. 2016. Transient temperature behavior and analysis of single-phase liquid-water geothermal reservoirs during drawdown and buildup tests: Part I. Theory, new analytical and approximate solutions. *Journal of Petroleum Science and Engineering* **146**: 637-656. 10.1016/j.petrol.2016.08.003.

Palacio, J. C., Blasingame, T. A. 1993. Decline-Curve Analysis With Type Curves - Analysis of Gas Well Production Data. Proc., 10.2118/25909-MS.

Park, Heungjun. 1989. Well Test Analysis of a multilayered reservoir with formation crossflow. PhD, Stanford University.

Peacock, D. R. 1965. Temperature Logging. Proc., SPWLA 6th Annual Logging Symposium (Volume I), Dallas, Texas.

Peng, D., Robinson, D. B. 1976. A New Two-Constant Equation of State. *Industrial & Engineering Chemistry Fundamentals* **15** (1): 59-64. DOI 10.1021/i160057a011.

Prats, M., Vogiatzis, J. P. 1999. Calculation of Wellbore Pressures and Rate Distribution in Multilayered Reservoirs. *Spe Journal* **4** (4): 307-314. Doi 10.2118/57241-Pa.

Prensky, Stephen. 1999. Temperature Measurements in Boreholes - An Overview of Engineering and Scientific Applications.

Pruess, K. 2005. Numerical studies of fluid leakage from a geologic disposal reservoir for CO2 show self-limiting feedback between fluid flow and heat transfer. *Geophysical Research Letters* **32** (14). 10.1029/2005gl023250.

Pruess, K. 2008. Leakage of CO2 from geologic storage: Role of secondary accumulation at shallow depth. *International Journal of Greenhouse Gas Control* **2** (1): 37-46. 10.1016/S1750-5836(07)00095-3.

Pruess, K. 2011. Integrated modeling of CO2 storage and leakage scenarios including transitions between super- and subcritical conditions, and phase change between liquid and gaseous CO2. *Greenhouse Gases Sci Technol* **1** (3): 237-247. 10.1002/ghg.024.

Pruess, Karsten. 2007. On CO2 fluid flow and heat transfer behavior in the subsurface, following leakage from a geologic storage reservoir. *Environmental Geology* **54** (8): 1677-1686. 10.1007/s00254-007-0945-x.

Quintero, Luis Fernando, Manrique, Eduardo José, Linares, José Albeno et al. 1993. Permeability Measurement Through Temperature Logging. Proc.

Ramazanov, A. S., Nagimov, V.M. 2007. Analytical model for the calculation of temperature distribution in the oil reservoir during unsteady fluid inflow. *Oil and Gas Business Journal*.

Ramazanov, A. S., Parshin, A. V. 2006. Temperature distribution in oil and water saturated reservoir with account of oil degassing. *Oil and Gas Business Journal*.

Ramazanov, A., Valiullin, R. A., Shako, V. et al. 2010. Thermal Modeling for Characterization of Near Wellbore Zone and Zonal Allocation. Proc., SPE-136256-MS, http://dx.doi.org/10.2118/136256-MS.

Ribeiro, Priscila M., Horne, Roland N. 2016. Detecting Fracture Growth Out of Zone by Use of Temperature Analysis. *SPE Journal*. 10.2118/170746-pa.

Rohmer, J., Seyedi, D. M. 2010. Coupled Large Scale Hydromechanical Modelling for Caprock Failure Risk Assessment of CO2 Storage in Deep Saline Aquifers. *Oil & Gas Science and Technology-Revue D Ifp Energies Nouvelles* **65** (3): 503-517. 10.2516/ogst/2009049.

Salina Borello, Eloisa, Fokker, Peter A., Viberti, Dario et al. 2016. Harmonic-Pulse Testing for Non-Darcy-Effects Identification. *SPE Reservoir Evaluation & Engineering*. 10.2118/183649-pa.

Sclater, K. C., Stephenson, B. R. 1929. Measurements of original pressure, temperature and gas-oil ratio in oil sands. *Transactions of the American Institute of Mining and Metallurgical Engineers* **82**: 119-131. 10.2118/929119-G.

Shakiba, M., Hosseini, S. A. 2016. Detection and characterization of CO2 leakage by multi-well pulse testing and diffusivity tomography maps. *International Journal of Greenhouse Gas Control* **54**: 15-28. 10.1016/j.ijggc.2016.08.015.

Sierra, Jose R., Kaura, Jiten D., Gualtieri, Dan et al. 2008. DTS Monitoring of Hydraulic Fracturing: Experiences and Lessons Learned. Proc., 10.2118/116182-MS.

Slider, H. C. 1966. Application of Pseudo-Steady-State Flow to Pressure-Buildup Analysis. Proc., 10.2118/1403-MS.

Spindler, R. 2011. Analytical Models for Wellbore-Temperature Distribution. *Spe Journal* **16** (1): 125-133. Doi 10.2118/140135-Pa.

Spivey, J.P., Lee, W.J. 2013. *Advanced well test interpretation*, 26. Richardson, TX: SPE Textbook Series, Society of Petroleum Engineers.

Su, HoJeen. 2004. A Three-Phase Non-Darcy Flow Formulation in Reservoir Simulation. Proc., 10.2118/88536-MS.

Sui, W., Ehlig-Economides, C., Zhu, D. et al. 2012. Determining Multilayer Formation Properties From Transient Temperature and Pressure Measurements. *Petroleum Science and Technology* **30** (7): 672-684. 10.1080/10916466.2010.514581.

Sui, Weibo, Zhu, Ding, Hill, A. D. et al. 2008a. Model for Transient Temperature and Pressure Behavior in Commingled Vertical Wells. Proc., SPE-115200-MS, http://dx.doi.org/10.2118/115200-MS.

Sui, Weibo, Zhu, Ding, Hill, Alfred Daniel et al. 2008b. Determining Multilayer Formation Properties from Transient Temperature and Pressure Measurements. Proc., 10.2118/116270-MS.

Sumnu-Dindoruk, D., Dindoruk, B. 2008. Analytical solution of nonisothermal Buckley-Leverett flow including tracers. *Spe Res Eval & Eng* **11** (3): 555-564. SPE-102266-PA. http://dx.doi.org/10.2118/102266-PA.

Sun, A. Y., Lu, J. M., Freifeld, B. M. et al. 2016. Using pulse testing for leakage detection in carbon storage reservoirs: A field demonstration. *International Journal of Greenhouse Gas Control* **46**: 215-227. 10.1016/j.ijggc.2016.01.015.

Sun, Alexander Y., Zeidouni, Mehdi, Nicot, Jean-Philippe et al. 2013. Assessing leakage detectability at geologic CO2 sequestration sites using the probabilistic collocation method. *Advances in Water Resources* **56** (0): 49-60. http://dx.doi.org/10.1016/j.advwatres.2012.11.017.

Sun, He, Yu, Wei, Sepehrnoori, Kamy. 2017. A New Comprehensive Numerical Model for Fracture Diagnosis with Distributed Temperature Sensing DTS. Proc., 10.2118/187097-MS.

Tabatabaei, M., Zhu, D. 2012. Fracture-Stimulation Diagnostics in Horizontal Wells Through Use of Distributed-Temperature-Sensing Technology. *Spe Production & Operations* **27** (4): 356-362. 10.2118/148835-PA.

Tan, Xuehao, Almulla, Jassim Mihammed, Zhu, Ding et al. 2012. Field Application of Inversion Method to Determine Acid Placement with Temperature Profiles. Proc., 10.2118/159296-MS.

Tao, Q., Bryant, S. L. 2014. Well permeability estimation and CO2 leakage rates. *International Journal of Greenhouse Gas Control* **22**: 77-87. 10.1016/j.ijggc.2013.12.022.

Tao, Q., Checkai, D. A., Huerta, N. J. et al. 2014. Estimating CO2 Fluxes Along Leaky Wellbores. *Spe Journal* **19** (2): 227-238. 10.2118/135483-PA.

Tardy, P. M. J., Ramondenc, P., Weng, X. et al. 2012. Inversion of Distributed-Temperature-Sensing Logs To Measure Zonal Coverage During and After Wellbore Treatments With Coiled Tubing. *Spe Production & Operations* **27** (1): 78-86. 10.2118/143331-PA.

Theis, C. V. 1935. The relation between the lowering of the piezometric surface and the rate and duration of discharge of a well using ground water storage. *Transactions-American Geophysical Union* **16**: 519-524.

Thiercelin, M. J., Dargaud, B., Baret, J. F. et al. 1998. Cement design based on cement mechanical response. *Spe Drilling & Completion* **13** (4): 266-273. Doi 10.2118/52890-Pa.

Tiab, Djebbar, Donaldson, Erle C. 2015. *Petrophysics: theory and practice of measuring reservoir rock and fluid transport properties*, Gulf professional publishing.

Tiab, Djebbar, Donaldson, Erle C. 2012. *Petrophysics - Theory and Practice of Measuring Reservoir Rock and Fluid Transport Properties (3rd Edition)*, Elsevier.

Trivedi, J. J., Babadagli, T. 2009. Oil Recovery and Sequestration Potential of Naturally Fractured Reservoirs During CO2 Injection. *Energy & Fuels* **23** (8): 4025-4036. 10.1021/ef900361n.

Valiullin, R., Ramazanov, A., Sadretdinov, A. et al. 2014. Field Study of Temperature Simulators Application for Quantitative Interpretation of Transient Thermal Logging in a Multipay Well. Proc., 10.2118/171233-MS.

Van Genuchten, M Th. 1980. A closed-form equation for predicting the hydraulic conductivity of unsaturated soils. *Soil science society of America journal* **44** (5): 892-898.

Vilarrasa, V., Bolster, D., Dentz, M. et al. 2010. Effects of CO2 Compressibility on CO2 Storage in Deep Saline Aquifers. *Transport in Porous Media* **85** (2): 619-639. 10.1007/s11242-010-9582-z.

Vinsome, P. K. W., Westerveld, J. 1980. A Simple Method for Predicting Cap and Base Rock Heat-Losses in Thermal Reservoir Simulators. *Journal of Canadian Petroleum Technology* **19** (3): 87-90. http://dx.doi.org/10.2118/80-03-04.

Wang, Y., Zhang, C., Wei, N. et al. 2013. Experimental study of crossover from capillary to viscous fingering for supercritical CO2-water displacement in a homogeneous pore network. *Environ Sci Technol* **47** (1): 212-8. 10.1021/es3014503.

Wang, Zan, Small, Mitchell J. 2014. A Bayesian approach to CO 2 leakage detection at saline sequestration sites using pressure measurements. *International Journal of Greenhouse Gas Control* **30**: 188-196.

Waples, Douglas W., Waples, Jacob S. 2004. A Review and Evaluation of Specific Heat Capacities of Rocks, Minerals, and Subsurface Fluids. Part 1: Minerals and Nonporous Rocks. *Natural Resources Research* **13** (2): 97-122. 10.1023/B:NARR.0000032647.41046.e7.

Warren, JE, Root, P Jj. 1963. *The behavior of naturally fractured reservoirs*, SPE Journal.

Winestock, A. G., Colpitts, G. P. 1965. Advances in Estimating Gas Well Deliverability. *Journal of Canadian Petroleum Technology* **4** (03): 111-119. 10.2118/65-03-01.

Wisian, K. W., Blackwell, D. D., Bellani, S. et al. 1998. Field comparison of conventional and new technology temperature logging systems. *Geothermics* **27** (2): 131-141. Doi 10.1016/S0375-6505(97)10013-X.

Wu, X. R., Xu, B. Y., Ling, K. G. 2015. A semi-analytical solution to the transient temperature behavior along the vertical wellbore after well shut-in. *Journal of Petroleum Science and Engineering* **131**: 122-130. 10.1016/j.petrol.2015.04.034.

Yildiz, Turhan. 1991. Analytical Treatment of Transient Non-Darcy Flow. Proc., SPE-22678-MS, http://dx.doi.org/10.2118/22678-MS.

Yoshida, N., Zhu, D., Hill, A. D. 2014. Temperature-Prediction Model for a Horizontal Well With Multiple Fractures in a Shale Reservoir. *Spe Production & Operations* **29** (4): 261-273. 10.2118/166241-PA.

Yoshioka, K., Zhu, D., Hill, A. D. et al. 2009. A New Inversion Method To Interpret Flow Profiles From Distributed Temperature and Pressure Measurements in Horizontal Wells. *SPE Prod & Oper* **24** (4): 510-521. SPE-109749-PA. http://dx.doi.org/10.2118/109749-PA.

Zeidouni, M., Nicot, J.-P., Hovorka, S.D. 2014a. Monitoring above-zone temperature variations associated with CO2 and brine leakage from a storage aquifer. *Environmental Earth Sciences* **72** (5): 1733-1747. http://dx.doi.org/10.1007/s12665-014-3077-0.

Zeidouni, M., Pooladi-Darvish, M. 2012a. Leakage characterization through above-zone pressure monitoring: 1-Inversion approach. *Journal of Petroleum Science and Engineering* **98-99**: 95-106. 10.1016/j.petrol.2012.09.006.

Zeidouni, M., Pooladi-Darvish, M. 2012b. Leakage characterization through above-zone pressure monitoring: 2-Design considerations with application to CO2 storage in saline aquifers. *Journal of Petroleum Science and Engineering* **98-99**: 69-82. 10.1016/j.petrol.2012.09.005.

Zeidouni, M., Vilarrasa, V. 2016. Identification of above-zone pressure perturbations caused by leakage from those induced by deformation. *Environmental Earth Sciences* **75** (18): 1271. 10.1007/s12665-016-6090-7.

Zeidouni, Mehdi. 2016. Semi-Analytical Model of Pressure Perturbations Induced by Fault Leakage in Multilayer System. *Journal of Hydrologic Engineering* **21** (6): 04016011. 10.1061/(asce)he.1943-5584.0001359.

Zeidouni, Mehdi, Nicot, Jean-Philippe, Hovorka, Susan D. 2014b. Monitoring above-zone temperature variations associated with CO2 and brine leakage from a storage aquifer. *Environmental Earth Sciences*: 1-15. 10.1007/s12665-014-3077-0.

Zeng, F. H., Zhao, G., Zhu, L. J. 2012. Detecting CO2 leakage in vertical wellbore through temperature logging. *Fuel* **94** (1): 374-385. 10.1016/j.fuel.2011.11.012.

Zeng, Z. W., Grigg, R. 2006. A criterion for non-Darcy flow in porous media. *Transport in Porous Media* **63** (1): 57-69. 10.1007/s11242-005-2720-3.

Zhang, C., Oostrom, M., Grate, J. W. et al. 2011. Liquid CO2 displacement of water in a dual-permeability pore network micromodel. *Environ Sci Technol* **45** (17): 7581-8. 10.1021/es201858r.

Zhang, M., Singh, M., Ayala, L. F. 2016. Rate forecasting during boundary-dominated multiphase flow: The rescaled exponential model. *Journal of Petroleum Science and Engineering* **143**: 199-210. 10.1016/j.petrol.2016.02.010.

Zhang, Shuang, Zhu, Ding. 2017. Inversion of Downhole Temperature Measurements in Multistage Fracture Stimulation in Horizontal Wells. Proc., 10.2118/187322-MS.

Zhang, Y. Q., Jung, Y., Freifeld, B. et al. 2018. Using distributed temperature sensing to detect CO2 leakage along the injection well casing. *International Journal of Greenhouse Gas Control* **74**: 9-18. 10.1016/j.ijggc.2018.04.011.

Zhang, Zhishuai, Jafarpour, Behnam. 2013. Joint Inversion of Production and Temperature Data for Identification of Permeability Distribution with Depth in Deep Reservoirs. Proc., 10.2118/166512-MS.

Publications

Peer-Reviewed Journal:

Mao, Y. Zeidouni, M. and Duncan, I. "Temperature Analysis for Early Detection and Rate Estimation of CO_2 Wellbore Leakage." International Journal of Greenhouse Gas Control 67, 20-30, 2017.

Mao, Y., Zeidouni, M., and Askari, R., "Effect of Leakage Pathway Flow Properties on Thermal Signal Associated with the Leakage from CO_2 Storage Zone." Greenhouse Gases: Science and Technology 7, 512-529. 2017

Mao, Y. and Zeidouni, M. "Accounting for Fluid Property Variations in Temperature Transient Analysis." SPE Journal, 23, 03, 868-884, SPE-187465-PA, 2018.

Mao, Y. and Zeidouni, M. "Temperature Transient Analysis for Boundary Dominated Pressure Response." International Journal of Thermal Science, 130, 457-470, 2018.

Mao, Y. and Zeidouni, M. "Dynamic Temperature Analysis under Variable Rate and Pressure Conditions for Transient and Boundary Dominated Flow." In Review, 201x.

Conference Proceedings:

Mao, Y. and Zeidouni, M. "Fracture Diagnostic using Distributed Temperature Measurements during Stimulation Fluid Flow-back." SPE Oklahoma City Oil and Gas Symposium, SPE-195221-MS, 2019.

Mao, Y. and Zeidouni, M. "Transient and Boundary Dominated Flow Temperature Analysis under Variable Rate Conditions." SPE Trinidad and Tobago Section Energy Resources Conference, SPE-191353-MS, 2018.

Mao, Y. and Zeidouni, M. "Temperature Transient Analysis During Boundary Dominated Flow Period." SPE Western Regional Meeting, SPE-190022-MS, 2018.

Mao, Y. and Zeidouni, M. "Near Wellbore Characterization from Temperature Transient Analysis: Accounting for Non-Darcy Flow Effect." SPE Symposium: Production Enhancement and Cost Optimisation, SPE-189234-MS, 2017.

Mao, Y. and Zeidouni, M. "Analytical Solutions for Temperature Transient Analysis and Near Wellbore Damaged Zone Characterization." SPE Reservoir Characterisation and Simulation Conference, SPE-185990-MS, 2017.

Mao, Y. and Zeidouni, M. "Temperature Transient Analysis for Characterization of Multilayer Reservoirs with Crossflow." SPE Western Regional Meeting, SPE-185654-MS, 2017.

Mao, Y. and Zeidouni, M. "Accounting for Fluid Property Variations in Temperature Transient Analysis." SPE Intelligent Oil & Gas Symposium and Exhibition, SPE-187465-MS, 2017.

Vita

Yilin Mao is a graduate assistant and doctoral candidate in Craft & Hawkins Department of Petroleum Engineering at Louisiana State University, expected to graduate in May 2019. Previously, he worked for Schlumberger as a drilling and measurement field engineer from 2008 to 2011. His research interests include analytical and numerical modeling of coupled flow and heat transfer in porous media with applications to reservoir characterization and leakage detection. Yilin received his Bachelor of Science in physics from Fudan University in 2008 and Master of Science in Petroleum Engineering from Missouri University of Science and Technology in 2012. He is a member of SPE and the second place recipient of Eastern North America Regional SPE paper contest (Philosophy of Doctor division) in 2016 and 2017.